

STATUS OF THESIS

Title of thesis

DEVELOPMENT AND VALIDATION OF COMPUTATIONAL
MODELS FOR SAND EROSION AND CORROSION
PREDICTION IN PIPES AND FITTINGS

I MYSARA EISSA MOHYALDINN ELHAJ,

hereby allow my thesis to be placed at the information Resource Center (IRC) of
Universiti Teknologi PETRONAS (UTP) with the following conditions:

1. The thesis becomes the property of UTP
2. The IRC of UTP may make copies of the thesis for academic purposes only.
3. This thesis is classified as

Confidential

Non-confidential

If the thesis is confidential, please state the reason:

The contents of the thesis will remain confidential for _____ years.

Remarks on disclosure:

Signature of Author

Permanent address:

College of Petroleum Eng. And Tech.,

Sudan Univ. of Science and Tech.,

P.O. Box 72 - Khartoum,

Sudan.

Date: 24-01-2011

Endorsed by

Signature of Supervisor

Prof. Dr. Noaman Elkhatib

Date: 24-01-2011

UNIVERSITI TEKNOLOGI PETRONAS

DEVELOPMENT AND VALIDATION OF COMPUTATIONAL MODELS FOR
SAND EROSION AND CORROSION PREDICTION IN PIPES AND FITTINGS

By

MYSARA EISSA MOHYALDINN ELHAJ

The undersigned certify that they have read, and recommend to the Postgraduate Studies Programme for acceptance this thesis for the fulfillment of the requirements for the degree stated.

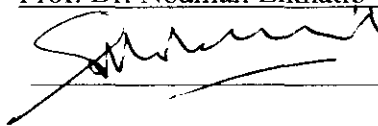
Signature:



Main Supervisor:

Prof. Dr. Noaman Elkhatib

Signature:



Co-Supervisor:

Assoc. Prof. Ir. Dr. Mokhtar Che Ismail

Signature:



Head of Department:

Assoc. Prof. Ir. Abdul Aziz Bin Omar

Date:

24/1/11

DEVELOPMENT AND VALIDATION OF COMPUTATIONAL MODELS FOR
SAND EROSION AND CORROSION PREDICTION IN PIPES AND FITTINGS

By

MYSARA EISSA MOHYALDINN ELHAJ

A Thesis

Submitted to the Postgraduate Studies Programme
as a Requirement for the Degree of

DOCTOR OF PHILOSOPHY

GEOSCIENCE AND PETROLEUM ENGINEERING DEPARTMENT

UNIVERSITI TEKNOLOGI PETRONAS

BANDAR SRI ISKANDAR

PERAK

JANUARY 2011

DECLARATION OF THESIS

Title of thesis

DEVELOPMENT AND VALIDATION OF COMPUTATIONAL
MODELS FOR SAND EROSION AND CORROSION
PREDICTION IN PIPES AND FITTINGS

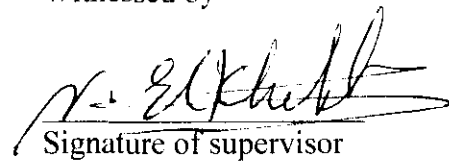
I MYSARA EISSA MOHYALDINN ELHAJ,

hereby declare that the thesis is based on my original work except for quotations and citations which have been duly acknowledged. I also declare that it has not been previously or concurrently submitted for any other degree at UTP or other institutions.

Witnessed by



Signature of Author



Signature of supervisor

Permanent address:

College of Petroleum Eng. And Tech.,
Sudan Univ. of Science and Tech.,
P.O. Box 72 - Khartoum,
Sudan.

Name of supervisor:

Prof. Dr. Noaman Elkhatib

Date: 24-1-2011

Date: 24-01-2011

Acknowledgements

I am heartily thankful to my supervisor, Prof Noaman Elkhatib, and co-supervisor, AP Dr Mokhtar Che Ismail, whose encouragement, guidance and support enabled me accomplish this work.

I would like to show my gratitude to my ex-supervisor, AP DR Razali Hamzah, under whose supervision the research topic was determined and the work was initiated.

My thank goes to Sudan University of Science and Technology for nominating me for PETRONAS scholarship, PETRONAS company for offering me the scholarship, and Universiti Teknologi PETRONAS for funding the project.

Special thanks to my wife, Gamila Ali, whose love and concern encourage me to accomplish this work.

Lastly, I offer my regards and blessings to all of those who supported me in any respect during the completion of the work.

Abstract

The primary objective of this research is to develop computational models for predicting sand erosion and CO₂ corrosion and their co-action (erosion-corrosion) in pipelines and pipe components (elbows and tees). The motivation behind this objective is to replace the sophisticated and time-consuming computational fluid dynamics (CFD) software used for erosion simulation with an accessible, faster, and cheaper predictive tool while maintaining the prediction accuracy, and to group the erosion prediction model with CO₂ corrosion prediction model in one package to serve as a comprehensive erosion-corrosion predictive tool. Two models have been used to build the erosion prediction code. The Salama model, a simple empirical model, was used to predict erosion rate in elbows and tees, assuming that sand particles velocity is the same as fluid velocity. This assumption makes the model more applicable to gas flow and high gas-liquid-ratio flow. An attempt has been made to increase the accuracy of the Salama model using a set of experimental data from a number of publications. As a result, three sand erosion models according to gas-liquid-ratio have been proposed. .

Direct Impingement Model (DIM) from University of Tulsa, a semi-empirical sand erosion model, was selected for application in all kinds of fluids due to its account of particle velocity instead of fluid velocity. In employing DIM model, a numerical algorithm was used to solve the simplified equation of particles motion, proposed by University of Tulsa, to track sand particles within a predetermined length (so-called stagnation zone). The particle impingement velocity was calculated, accordingly, and substituted in an empirical sand erosion equation to calculate erosion rate. An ad hoc equation was used with the DIM model to model temperature dependency of particle impingement velocity and erosion rate.

NORSOK CO₂ corrosion rate prediction model, an empirical model proposed by NORSOK, was selected for prediction of corrosion rate due to CO₂ presence in fluids. Since the original model is applicable to straight pipes, it was firstly extended to application in elbows by introducing elbow equivalent length before integrating it with the Salama model and Wood model to calculate erosion-corrosion in elbows. As another improvement, the NORSOK model was also coupled to selected thermal/hydraulic equations to predict corrosion rate along pipelines. This modification facilitates prediction of corrosion rate at any point along any pipeline, provided that flow and corrosion parameters at the pipeline inlet are known. The modified model was used, first, to simulate the temperature profile, which in turn was used to simulate the profiles of pressure and corrosion-related parameters.

A comparison of the original Salama model and DIM model with experimental data results has shown good agreement with the DIM model, whereas the Salama model highly overestimated the experimental results. This is further emphasized by comparing the two models with a CFD model created for erosion rate simulation in a 2-in elbow. Based on comparison with published data, three forms of improved Salama models (for pure gas, high gas-liquid-ratio, and low gas-liquid-ratio) have been proposed to increase the accuracy of the original Salama model, but their accuracy requires further verification. As another improvement, the effect of viscosity has been introduced to Salama model by comparison with the DIM model. As a result, the accuracy of Salama model has been increased and its applicability has been extended to liquids.

The results of CO₂ corrosion model for straight pipes were validated by comparison with published field data and good agreement was found. The code results of corrosion rate in elbow were compared with measured data. A flow loop was designed and fabricated for this purpose and corrosion rate was measured at different flow velocity and pH using electrochemical noise measurement (ENM) readings from three electrodes. Good agreement was found between the measured and predicted corrosion rate.

Abstrak

Tujuan utama kajian ini adalah untuk membangunkan model pengkomputeran untuk memprediksi hakisan pasir dan CO₂ korosi dan rakan-aksi (hakisan-korosi) pada paip dan bahagian-bahagian paip (siku dan tee). Motivasi di balik tujuan ini adalah untuk menggantikan dinamik canggih dan memakan masa pengkomputeran bendalir (CFD) software yang digunakan untuk simulasi hakisan dengan alat ramalan dicapai, lebih cepat, dan lebih murah dengan tetap mempertahankan ketepatan ramalan, dan untuk kumpulan model ramalan hakisan dengan CO₂ model ramalan korosi dalam satu pakej untuk melayani sebagai alat ramalan yang menyeluruh hakisan-korosi. Dua model telah digunakan untuk membina kod ramalan hakisan. Model Salama, model empirik yang sederhana, digunakan untuk memprediksi tingkat hakisan di siku dan tee, dengan andaian bahawa kelajuan zarah pasir adalah sama dengan kelajuan bendalir. Asumsi ini membuat model lebih berlaku untuk aliran gas dan tinggi aliran gas-cecair-nisbah. Suatu usaha telah dilakukan untuk meningkatkan ketepatan model Salama menggunakan satu set data eksperimen dari sejumlah penerbitan. Akibatnya, tiga model hakisan pasir sesuai dengan nisbah gas-cecair-telah dicadangkan. . Lompat pelampiasan Model (DIM) dari University of Tulsa, model pasir hakisan semi-empirik, dipilih untuk dilaksanakan di semua jenis cecair kerana akaun atas kelajuan zarah bukan kelajuan bendalir. Dalam menggunakan model DIM, algoritma berangka digunakan untuk menyelesaikan persamaan gerak partikel sederhana, yang dicadangkan oleh University of Tulsa, untuk mengesan zarah pasir dalam panjang yang telah ditetapkan (zon stagnasi disebut). Kelajuan pelampiasan zarah dikira, sesuai, dan diganti dalam sebuah persamaan hakisan pasir empirik untuk mengira laju hakisan. Persamaan ad hoc digunakan khususnya dengan model DIM untuk model pergantungan suhu kelajuan zarah menumbuk dan laju hakisan.

NORSOK CO₂ model ramalan laju korosi, model empirik yang dicadangkan oleh NORSOK, dipilih untuk ramalan laju korosi akibat kehadiran CO₂ dalam cecair. Kerana model asli ini berlaku untuk paip lurus, itu pertama kali diperluas

untuk aplikasi di siku dengan memperkenalkan panjang siku setara sebelum mengintegrasikan dengan model Salama dan model Kayu untuk mengira hakisan-korosi di siku. Sebagai pembaikan lain, model NORSOK juga digabungkan untuk dipilih persamaan terma hidrolik / untuk meramalkan laju korosi sepanjang paip. Modifikasi ini memudahkan ramalan laju korosi pada setiap titik sepanjang paip, asalkan aliran dan parameter korosi pada paip inlet diketahui. Model pengubahsuaian ini boleh digunakan, pertama, untuk mensimulasikan profil suhu, yang pada gilirannya digunakan untuk mensimulasikan profil tekanan dan parameter korosi-berkaitan.

Suatu perbandingan model Salama asli dan model DIM dengan hasil data eksperimen telah menunjukkan kesepakatan yang baik dengan model DIM, sedangkan model Salama sangat berlebihan keputusan eksperimen. Hal ini lebih ditekankan dengan membandingkan dua model dengan model CFD diciptakan untuk simulasi laju hakisan di 2-in siku. Berdasarkan perbandingan dengan data yang diterbitkan, tiga bentuk model Salama diperbaiki (untuk gas murni, gas-cecair-nisbah tinggi, dan gas-cecair-nisbah rendah) telah dicadangkan untuk meningkatkan ketepatan model Salama asli, tetapi mereka memerlukan ketepatan pengesahan lebih lanjut. Sebagai pembaikan lain, kesan viskositas telah diperkenalkan untuk model Salama berbanding dengan model DIM. Akibatnya, ketepatan model Salama telah dipertingkatkan dan pelaksanaan yang telah dipanjangkan sehingga cecair. Keputusan model korosi CO₂ untuk paip lurus telah diaktifkan dibandingkan dengan data lapangan diterbitkan dan perjanjian yang baik dijumpai. Kod Keputusan laju korosi pada siku dibandingkan dengan data pengukuran. Sebuah loop aliran direka dan dibuat untuk tujuan ini dan laju korosi diukur pada kelajuan aliran berbeza dan pH menggunakan elektrokimia pengukuran hingar (ENM) pembacaan dari tiga elektrod. Kecocokan ditemui antara laju korosi diukur dan diramal.

In compliance with the terms of the Copyright Act 1987 and the IP Policy of the university, the copyright of this thesis has been reassigned by the author to the legal entity of the university,

Institute of Technology PETRONAS Sdn Bhd.

Due acknowledgement shall always be made of the use of any material contained in, or derived from, this thesis.

© MYSARA EISSA MOHYALDINN ELHAJ, 2011

Institute of Technology PETRONAS Sdn Bhd

All rights reserved.

Dedication

This thesis is dedicated to

My parents

My wife

TABLE OF CONTENTS

ACKNOWLEDGEMENTS.....	V
ABSTRACT	VI
ABSTRAK	VIII
DEDICATION	XI
TABLE OF CONTENTS	XII
NOMENCLATURE	XXVI
CHAPTER 1	1
1.1 BACKGROUND.....	1
1.2 PROBLEM STATEMENT.....	2
1.3 SCOPE OF THE RESEARCH	5
1.4 THE RESEARCH OBJECTIVES	5
1.5 THESIS OVERVIEW.....	6
1.6 SUMMARY	7
CHAPTER 2	8
2.1 SAND PRODUCTION IN OIL AND GAS FACILITIES.....	8
2.2 SAND EROSION.....	10
2.3 CORROSION AND EROSION-CORROSION	10
2.4 SLURRY FLOW IN PIPES.....	12
2.5 EXPERIMENTAL SIMULATION OF EROSION AND CORROSION	13
2.5.1 <i>Flow loops</i>	13
2.5.2 <i>Jet impingement</i>	13
2.5.3 <i>Pot tester</i>	15
2.6 EROSION PREDICTION MODELS.....	15
2.6.1 <i>Prediction Models for General Applications</i>	16
2.6.2 <i>Prediction Models in Oil and Gas Applications</i>	22
2.6.2.1 Empirical methods	22

2.6.2.2 Semi-empirical Methods.....	24
2.6.2.3 Computational Fluid Dynamics (CFD) methods.....	27
2.6.2.3.1 Grid generation.....	28
2.6.2.3.2 Flow solution.....	29
2.6.2.3.3 Particle tracking.....	34
2.6.2.3.4 Erosion rate calculation.....	36
2.7 SUMMARY.....	37
 CHAPTER 3.....	 38
3.1 INTRODUCTION.....	38
3.2 THE MODELING METHODOLOGY.....	41
3.3 SAND EROSION MODELS.....	43
3.3.1.1 Salama empirical model.....	44
3.3.1.2 The Direct Impingement Model.....	45
3.3.1.3 Particle tracking using fluent software.....	54
3.4 CORROSION AND EROSION-CORROSION MODELS.....	56
3.4.1.1 Adoption of NORSOK model to predict corrosion and erosion- corrosion in elbow.....	59
3.4.1.2 Modifying NORSOK model to predict corrosion rate along pipelines.....	65
3.5 SUMMARY.....	71
 CHAPTER 4.....	 72
4.1 INTRODUCTION.....	72
4.2 GENERAL DESCRIPTION OF THE FLOW LOOP.....	72
4.3 THE MAIN TEST SECTION.....	73
4.4 THE FLOW LOOP DESIGN.....	75
4.4.1 <i>Critical velocity</i>	76
4.4.2 <i>Determination of the hydraulic gradient line</i>	78
4.4.3 <i>The pump selection</i>	85
4.5 THE PIPES AND FITTINGS SELECTION.....	86
4.6 EXPERIMENTS METHODOLOGY.....	86
4.7 SUMMARY.....	89

CHAPTER 5	90
5.1 INTRODUCTION.....	90
5.2 RESULTS FROM THE COMPUTATIONAL FLUID DYNAMICS (CFD) MODEL.....	91
5.3 MODEL CREATION AND GRID GENERATION.....	91
5.4 SOLUTION OF FLOW FIELD AND PARTICLES TRAJECTORIES	92
5.5 EROSION RATE CALCULATIONS	95
5.6 ANALYSIS OF RESULTS USING THE DEVELOPED CODE	99
5.6.1 Sand erosion prediction and simulation.....	100
5.6.1.1 Analysis of results from Salama model	101
5.6.1.2 Analysis of results from the DIM model	103
5.6.1.2.1 <i>Variation of particles impingement velocity with fluid type</i>	104
5.6.1.3 Effect of flow velocity on erosion rate	106
5.6.1.4 Effect of pipe diameter.....	109
5.6.1.5 Effect of sand production rate.....	112
5.7 VALIDATION AND EVALUATION OF SAND EROSION PREDICTION MODELS	115
5.7.1 <i>Validation and evaluation of Salama Empirical model</i>	115
5.7.2 <i>Validation and evaluation of Direct Impingement Model (DIM)</i>	120
5.8 EXTENSION OF SALAMA MODEL TO OILS FLOW (MYSARA (UTP) MODEL).....	124
5.8.1 <i>Development of Mysara (UTP) model</i>	124
5.8.2 <i>Validation of Mysara (UTP) model</i>	134
5.8.3 CO ₂ corrosion prediction and simulation.....	136
5.8.3.1 CO ₂ corrosion prediction and simulation in laminar flow	137
5.8.3.2 CO ₂ corrosion prediction and simulation in turbulent flow.....	141
5.8.3.2.1 <i>The effect of flow velocity on CO₂ corrosion</i>	143
5.8.3.3 The effect of fluid density on CO ₂ corrosion.....	146
5.8.3.4 The effects of fluid viscosity on CO ₂ corrosion.....	148
5.8.3.5 The effects of CO ₂ partial pressure on CO ₂ corrosion	150
5.8.3.6 Effect of pH and temperature on corrosion rate.....	152
5.8.3.7 Comparison of the model results with field data	155
5.8.4 Erosion-corrosion prediction and simulation.....	159
5.8.4.1 The effect of flow velocity on erosion-corrosion	160
5.8.4.2 The effect of fluid density on erosion-corrosion.....	162
5.8.5 Results of pipeline simulation.....	163

5.8.5.1 Prediction of corrosion rate and its related parameters along pipeline	164
5.9 ANALYSIS OF EXPERIMENTAL RESULTS	172
5.9.1 <i>Material characterization</i>	172
5.9.2 <i>Fluid preparation</i>	174
5.9.3 <i>Corrosion rate measurements</i>	178
5.10 SUMMARY	182
CHAPTER 6	183
6.1 CONCLUSIONS	183
6.2 RECOMMENDATIONS	184
6.3 CONTRIBUTIONS.....	185
REFERENCES	186
APPENDIX A.....	192
6.4 A.1 INTRODUCTION.....	192
6.5 A.2 THE SOFTWARE REQUIREMENT AND INSTALLATION PROCEDURE.....	192
6.6 A.3 THE SOFTWARE GRAPHICAL USER INTERFACE AND NAVIGATION FORMS.....	193
APPENDIX B.....	206
APPENDIX C.....	212

LIST OF FIGURES

FIGURE 2-1: A SCHEMATIC DIAGRAM OF THE JET IMPINGEMENT SETUP USED BY P. ANDREWS ET AL. (ANDREWS <i>ET AL.</i> 1999)	14
FIGURE 2-2: A SCHEMATIC DIAGRAM OF THE JET IMPINGEMENT SETUP USED BY G.A. ZHANG ET AL. (ZHANG <i>ET AL.</i> 2009)	15
FIGURE 2-3: THE FUNCTIONAL RELATIONSHIP FOR BRITTLE AND DUCTILE MATERIALS (BARTON 2003).....	18
FIGURE 2-5: THE CALCULATION PROCEDURE OF DIM (McLAURY 1996)	26
FIGURE 2-6: SAND EROSION SIMULATION USING FLUENT SOFTWARE.....	28
FIGURE 3-1: THE CODE DEVELOPMENT AND RESEARCH PROCEDURE.....	40
FIGURE 3-2: FLOW CHART FOR CALCULATION PROCEDURE FOR SALAMA MODEL .	45
FIGURE 3-3: STAGNATION ZONES IN ELBOW AND TEE (McLAURY 1996)	46
FIGURE 3-4: THE STAGNATION LENGTH OF ELBOW AND TEE VS. PIPE DIAMETER (McLAURY 1996)	46
FIGURE 3-5: VARIATION OF DIMENSIONLESS IMPACT VELOCITY WITH THE MASS RATIO FOR DIFFERENT PARTICLE REYNOLDS NUMBERS (McLAURY 1996)	49
FIGURE 3-6: ALGORITHM OF NUMERICAL SOLUTION FOR THE EQUATION OF PARTICLES MOTION	50
FIGURE 3-7: THE CALCULATION PROCEDURE FOR PREDICTING CORROSION RATE ALONG PIPELINES	70
FIGURE 4-1: GENERAL LAYOUT OF THE EROSION/CORROSION FLOW LOOP	74
FIGURE 4-2: THE FLOW LOOP	74
FIGURE 4-3: A SKETCH OF THE TEST SECTION	75
FIGURE 4-4: THE MAIN TEST SECTION	75
FIGURE 4-5: THE DESIGN PROCEDURE OF THE FLOW LOOP	76
FIGURE 4-6: THE GRAPHICAL USER INTERFACE OF THE CODE.....	82
FIGURE 4-7: HYDRAULIC GRADIENT LINE AT VELOCITY 0.5 M/S	83
FIGURE 4-8: HYDRAULIC GRADIENT LINE AT VELOCITY 1 M/S	83

FIGURE 4-9: HYDRAULIC GRADIENT LINE AT VELOCITY 1.5 M/S	84
FIGURE 4-10: HYDRAULIC GRADIENT LINE AT VELOCITY 2 M/S	84
FIGURE 4-11: CORROSION EXPERIMENTAL PROCEDURE	87
FIGURE 4-12: THE ELBOW TEST SECTION CONTAINING THE WIRED ELECTRODES.....	88
FIGURE 4-13: AN ELECTRODE	89
FIGURE 5-1: THE MODEL GENERATION AND MESHING.....	92
FIGURE 5-2: VELOCITY CONTOURS OF THE PRIMARY PHASE	93
FIGURE 5-3: PARTICLE VELOCITY TRACKING	94
FIGURE 5-4: ANGLE OF IMPINGEMENT OF DIFFERENT SAND PARTICLES.....	95
FIGURE 5-5: PARTICLE VELOCITY ALONG THE FLOW PATH.....	95
FIGURE 5-6: EROSION RATE VARIATION ALONG THE PATH (OUTER WALL)	98
FIGURE 5-7: VARIATION OF EROSION RATE WITH AIR VELOCITY (IN 2-IN ELBOW, SAND FLOW RATE=0.000886 KG/S)	99
FIGURE 5-8: THE CODE FORMS	100
FIGURE 5-9: INPUT DATA FORM OF SALAMA MODEL	101
FIGURE 5-10: VARIATION OF EROSION RATE WITH VELOCITY FOR WATER AND OIL (SALAMA MODEL).....	103
FIGURE 5-11: INPUT DATA FORM OF THE DIM MODEL	103
FIGURE 5-12: SAND TRAJECTORY ALONG THE STAGNATION ZONE FOR AIR, WATER, AND OIL.....	105
FIGURE 5-13: VARIATION OF SAND EROSION WITH IMPINGEMENT VELOCITY (AIR)	107
FIGURE 5-14: THE VARIATION OF EROSION RATE WITH VELOCITY (WATER).....	107
FIGURE 5-15: THE VARIATION OF EROSION RATE WITH VELOCITY (OIL).....	108
FIGURE 5-16: VARIATION OF EROSION RATE WITH VELOCITY FOR OIL WITH DIFFERENT VISCOSITY	108
FIGURE 5-17: VARIATION OF EROSION RATE IN CARBON STEEL ELBOW WITH FLOW VELOCITY FOR OIL WITH DIFFERENT DENSITY	109
FIGURE 5-18: THE VARIATION OF EROSION RATE WITH DIAMETER (AIR)	110
FIGURE 5-19: THE VARIATION OF EROSION RATE WITH DIAMETER (WATER)	110
FIGURE 5-20: THE VARIATION OF EROSION RATE WITH VELOCITY FOR DIFFERENT DIAMETERS (AIR)	111

FIGURE 5-21: THE VARIATION OF EROSION RATE WITH VELOCITY FOR DIFFERENT DIAMETERS (WATER).....	111
FIGURE 5-22: THE VARIATION OF EROSION RATE WITH SAND RATES (AIR).....	113
FIGURE 5-23: VALIDATION OF SALAMA MODEL.....	116
FIGURE 5-24: COMPARISON OF SALAMA MODEL PREDICTED VALUES WITH MEASURED DATA (PURE AIR).....	119
FIGURE 5-25: COMPARISON OF SALAMA MODEL PREDICTED DATA WITH MEASURED DATA (LOW GAS LIQUID RATIO).....	120
FIGURE 5-26: COMPARISON OF SALAMA MODEL PREDICTED DATA WITH MEASURED DATA (HIGH GAS LIQUID RATIO).....	120
FIGURE 5-27: VALIDATION OF DIRECT IMPINGEMENT MODEL.....	121
FIGURE 5-28: COMPARISON OF RESULTS OF SALAMA, DIM, AND CFD MODELS.....	122
FIGURE 5-29: COMPARISON BETWEEN SALAMA MODEL AND DIM MODEL (GAS).....	123
FIGURE 5-30: COMPARISON BETWEEN SALAMA MODEL AND DIM MODEL (WATER).....	123
FIGURE 5-31: COMPARISON BETWEEN SALAMA MODEL AND DIM MODEL (OIL).....	124
FIGURE 5-32: VARIATION OF EROSIONAL VELOCITY WITH VISCOSITY.....	125
FIGURE 5-33: VARIATION OF ABNORMAL VELOCITY WITH VISCOSITY.....	125
FIGURE 5-34: COMPARISON BETWEEN SALAMA AND DIM BELOW ABNORMAL VELOCITY (0.002 PA.S).....	127
FIGURE 5-35: COMPARISON BETWEEN SALAMA AND DIM BELOW ABNORMAL VELOCITY (0.005 PA.S).....	127
FIGURE 5-36: COMPARISON BETWEEN SALAMA AND DIM BELOW ABNORMAL VELOCITY (0.009 PA.S).....	128
FIGURE 5-37: VARIATION OF AL WITH VISCOSITY.....	128
FIGURE 5-38: VARIATION OF BL WITH VISCOSITY.....	129
FIGURE 5-39: COMPARISON BETWEEN SALAMA AND DIM ABOVE ABNORMAL VELOCITY (0.002 PA.S).....	129
FIGURE 5-40: COMPARISON BETWEEN SALAMA AND DIM ABOVE ABNORMAL VELOCITY (0.005 PA.S).....	130
FIGURE 5-41: COMPARISON BETWEEN SALAMA AND DIM ABOVE ABNORMAL VELOCITY (0.009 PA.S).....	130
FIGURE 5-42: VARIATION OF AU AND BU WITH VISCOSITY.....	131

FIGURE 5-43: FLOW CHART OF CALCULATION PROCEDURE USING MYSARAR (UTP) MODEL	133
FIGURE 5-44: COMPARISON OF MYSARA (UTP) MODEL WITH THE DIM MODEL.....	134
FIGURE 5-45: THE RESULT OF CALCULATION USING SHIRAZI ET AL DATA.....	135
FIGURE 5-46: VARIATION OF CORROSION RATE WITH VELOCITY (LAMINAR REGIME)..	139
FIGURE 5-47: VARIATION OF CORROSION RATE WITH DENSITY (LAMINAR REGIME)....	139
FIGURE 5-48: VARIATION OF CORROSION RATE WITH VISCOSITY (LAMINAR REGIME)	140
FIGURE 5-49: VARIATION OF CORROSION RATE WITH DIAMETER (LAMINAR REGIME).....	140
FIGURE 5-50: VARIATION OF SST WITH VELOCITY	142
FIGURE 5-51: VARIATION OF SST WITH VISCOSITY	142
FIGURE 5-52: VARIATION OF SST WITH DENSITY	143
FIGURE 5-53: THE VARIATION OF CO ₂ CORROSION RATE (MM/YEAR) WITH FLOW VELOCITY (M/S).....	144
FIGURE 5-54: THE VARIATION OF CO ₂ CORROSION RATE (MM/YEAR) WITH FLUID DENSITY (KG/M ³).....	146
FIGURE 5-55: THE EFFECT OF FLUID VISCOSITY (PA.S) ON CORROSION RATE (MM/YEAR)	148
FIGURE 5-56: THE EFFECT OF CO ₂ PARTIAL PRESSURE (BAR) ON CORROSION RATE (MM/YEAR)	150
FIGURE 5-57: VARIATION OF CORROSION RATE WITH FLOW VELOCITY AT DIFFERENT PH, T=60 °C	152
FIGURE 5-58: VARIATION OF CORROSION RATE WITH PH, V=10 M/S, T=60 °C.....	153
FIGURE 5-59: VARIATION OF CORROSION RATE WITH TEMPERATURE AT DIFFERENT VELOCITY, PCO ₂ =0.2 BAR, PH=5 (TURBULENT FLOW).	153
FIGURE 5-60: VARIATION OF CORROSION RATE WITH TEMPERATURE, V=10 M/S, PH=5 (TURBULENT FLOW).....	154
FIGURE 5-61: VARIATION OF CORROSION RATE WITH TEMPERATURE AT DIFFERENT VELOCITY PCO ₂ =0.2 BAR, PH=5 (LAMINAR FLOW).....	154
FIGURE 5-62: VARIATION OF CORROSION RATE WITH TEMPERATURE, V=0.04 M/S, PCO ₂ =0.2 BAR, PH=5 (LAMINAR FLOW)	155

FIGURE 5-63: COMPARISON OF NESIC ET AL. MODEL RESULTS (NESIC <i>ET AL.</i> 2005) WITH GUNALTUN FIELD DATA (GUNALTUN 1991)	157
FIGURE 5-64: VARIATION OF CORROSION RATE WITH VELOCITY USING GUNALTUN FIELD DATA (GUNALTUN 1991).....	157
FIGURE 5-65: COMPARISON OF THE CODE RESULTS WITH GUNALTUN FIELD DATA (GUNALTUN 1991).....	158
FIGURE 5-66: INPUT DATA FORM FOR EROSION-CORROSION.....	159
FIGURE 5-67: EFFECT OF FLOW VELOCITY ON EROSION, CORROSION AND EROSION-CORROSION RATES (SAND PRODUCTION RATE 500 KG/DAY)	161
FIGURE 5-68: EFFECT OF FLOW VELOCITY ON EROSION, CORROSION AND EROSION-CORROSION RATE (SAND PRODUCTION RATE 1500 KG/DAY)	161
FIGURE 5-69: THE EFFECT OF FLUID DENSITY (KG/M ³) ON PURE CORROSION AND EROSION-CORROSION RATE (MM/YEAR)	162
FIGURE 5-70: INPUT DATA FORM OF PIPELINE SIMULATION.....	163
FIGURE 5-71: CORROSION RATE VARIATION ALONG PIPELINE (VELOCITY=5 M/S)	165
FIGURE 5-72: CORROSION RATE VARIATION ALONG PIPELINE (VELOCITY=1 M/S)	166
FIGURE 5-73: TEMPERATURE VARIATION ALONG PIPELINE (VELOCITY=5 M/S) ...	166
FIGURE 5-74: TEMPERATURE VARIATION ALONG PIPELINE (VELOCITY=1 M/S) ...	167
FIGURE 5-75: VARIATION OF REYNOLDS NO ALONG PIPELINE (VELOCITY=1 M/S)	167
FIGURE 5-76: CORROSION RATE VARIATION ALONG PIPELINE (VELOCITY=0.5 M/S)	168
FIGURE 5-77: VARIATION OF REYNOLDS NO. ALONG PIPELINE (VELOCITY=0.5 M/S)	168
FIGURE 5-78: CORROSION RATE ALONG THE PIPELINE AT DIFFERENT VELOCITIES (D=0.2, PH=5, WC=30%)	169
FIGURE 5-79: TEMPERATURE ALONG THE PIPELINE AT DIFFERENT VELOCITIES...	170
FIGURE 5-80: WALL SHEAR STRESS ALONG THE PIPELINE AT DIFFERENT VELOCITIES	170
FIGURE 5-81: REYNOLDS NO. ALONG THE PIPELINE AT DIFFERENT VELOCITIES..	171

FIGURE 5-82: CORROSION RATE VARIATION ALONG PIPELINE AT DIFFERENT CO ₂ PARTIAL PRESSURE.....	171
FIGURE 5-83: CORROSION RATE VARIATION ALONG PIPELINE AT DIFFERENT pH.....	172
FIGURE 5-84: THE MICROSTRUCTURE OF THE SAMPLE MATEIAL (X720)	173
FIGURE 5-85: THE CHARACTERIZATION RESULT OF A SAMPLE (EDX)	173
FIGURE 5-86: THE SAMPLE SURFACE MICROSTRUCTURE USING EDX.	174
FIGURE 5-87: THE PH PROBE	175
FIGURE 5-88: THE CHANGE OF OCEAN CO ₂ PARTIAL PRESSURE AND PH WITH TIME(TURLEY <i>ET AL.</i> 2005)	175
FIGURE 5-89: THE CHANGE OF CO ₂ PARTIAL PRESSURE WITH PH	176
FIGURE 5-90: GILLAC POTENTIOSTAT	178
FIGURE 5-91: MEASURED AND PREDICTED CORROSION RATE AT pH=6.5.....	180
FIGURE 5-92: MEASURED AND PREDICTED CORROSION RATE AT pH=5.5.....	180
FIGURE 5-93: MEASURED AND PREDICTED CORROSION RATE AT pH=5.....	181
FIGURE 5-94: COMPARISON BETWEEN PREDICTED AND MEASURED CORROSION RATE	181

LIST OF TABLES

TABLE 1-1: EROSION PREDICTION METHODS	4
TABLE 2-1: THE CONSTANTS K AND N FOR SOME MATERIALS (HAUGEN ET AL.)	17
TABLE 2-2: A ₁ FACTORS IN EQUATION (2-3) (HAUGEN ET AL.).....	18
TABLE 2-3: THE CONSTANTS A, A, B, W, X, Y, AND Z IN EQUATION 2-14 (ALHERT, 1995)	21
TABLE 2-4: THE GEOMETRY-DEPENDENT CONSTANT S _M IN SALAMA EQUATION (SALAMA, 2000)	24
TABLE 2-5: THE TWO-EQUATION TURBULENCE MODELS AND THEIR PROPOSERS (KABIR, 2005)	33
TABLE 3-1: COMPARISON BETWEEN THE SECS PACKAGE AND CFD MODEL	42
TABLE 3-2: MATERIAL FACTORS F _M OF SOME MATERIAL (MCLAURY, 1996).....	52
TABLE 3-3: THE SHARPNESS FACTOR F _S FOR THREE PARTICLE SHAPES (MCLAURY, 1996)	52
TABLE 3-4: THE PENETRATION FACTOR F _P (MCLAURY, 1996).....	52
TABLE 3-5: VALUES OF K _T AT DIFFERENT TEMPERATURES (NORSOK 2005)	57
TABLE 3-6: f(pH) _i AT DIFFERENT TEMPERATURES AND PH VALUES (NORSOK 2005)	58
TABLE 3-7: ACTUAL LENGTH OF 45 ⁰ LONG RADIUS ELBOWS WITH DIFFERENT DIAMETERS	62
TABLE 3-8: EQUIVALENT LENGTH OF SOME FITTINGS	63
TABLE 3-9: THE RATIO OF EQUIVALENT LENGTH TO ACTUAL LENGTH (90 DEG ELBOW)	63
TABLE 3-10: THE EFFECT OF THE FOUR PARAMETERS ALONG THE PIPELINE.....	67
TABLE 4-1: CRITICAL VELOCITY OF DIFFERENT PIPE'S DIAMETERS.....	77
TABLE 4-2: THE FLOW PARAMETERS.....	77
TABLE 4-3: EQUIVALENT LENGTH (FT) FOR PVC FITTINGS	80
TABLE 4-4: EQUIVALENT LENGTH (FT) FOR STEEL FLANGED VALVES AND FITTINGS.....	81
TABLE 4-5: THE MAIN PUMP SPECIFICATION	85

TABLE 4-6: THE PUMP FLOW VELOCITY AT DIFFERENT PIPE SIZES	85
TABLE 4-7: PRESSURE RATINGS OF SDR 21 AND 26.....	86
TABLE 5-1: THE MAIN PARAMETERS OF THE PHASES.....	93
TABLE 5-2: VALUES OF ANGLE FUNCTION DEFINED TO THE MODEL	96
TABLE 5-3: VARIATION OF MAXIMUM EROSION RATE WITH VELOCITY	98
TABLE 5-4: VARIATION OF TOTAL EROSION RATE WITH VELOCITY	99
TABLE 5-5: VARIATION OF EROSION RATE WITH VELOCITY FOR GAS, WATER, AND OIL (SALAMA MODEL).....	102
TABLE 5-6: INPUT DATA FOR EROSION SIMULATION.....	104
TABLE 5-7: THE VARIATION OF EROSION RATE WITH ELBOW DIAMETER	112
TABLE 5-8: THE VARIATION OF EROSION RATE WITH VELOCITY AT DIFFERENT SAND PRODUCTION RATE	114
TABLE 5-9: VALUES OF CF FOR DIFFERENT UNIT OF SAND PRODUCTION RATE (W)	115
TABLE 5-10: VALIDATION OF THE CODE RESULTS (SALAMA MODEL) USING PUBLISHED DATA.....	116
TABLE 5-11: VALIDATION OF THE DIM RESULTS USING PUBLISHED DATA (MCLAURY AND SHIRAZI 1999).....	121
TABLE 5-12: COMPARISON OF SALAMA AND DIM RESULTS FOR OIL WITH DIFFERENT VISCOSITY	132
TABLE 5-13: INPUT DATA FOR CORROSION SIMULATION	136
TABLE 5-14: THE EFFECT OF FLOW VELOCITY ON CORROSION RATE IN STRAIGHT PIPES AND ELBOWS.....	145
TABLE 5-15: THE EFFECT OF FLUID DENSITY ON CORROSION RATE	147
TABLE 5-16: THE EFFECT OF FLUID VISCOSITY ON CORROSION RATE	149
TABLE 5-17: THE EFFECT OF CO ₂ PARTIAL PRESSURE ON CORROSION RATE FOR STRAIGHT PIPES AND ELBOWS	151
TABLE 5-18: THE FIELD DATA OF GUNALTUN (GUNALTUN 1991) (FROM NESIC ET AL. (NESIC <i>ET AL.</i> 2005)).....	156
TABLE 5-19: THE TUBING PREDICTED CORROSION RATE	158
TABLE 5-20: INPUT DATA FOR EROSION-CORROSION SIMULATION	160
TABLE 5-21: INPUT DATA FOR PIPELINE SIMULATION.....	165
TABLE 5-22: THE SAMPLE COMPOSITION (EDX).....	174
TABLE 5-23: CALCULATED SYSTEM PRESSURES AT DIFFERENT FLOW VELOCITIES	177

TABLE 5-24: CO ₂ PARTIAL PRESSURE AT DIFFERENT FLOW VELOCITIES AND PH VALUES	177
TABLE 5-25: MEASURED AND PREDICTED CORROSION RATES AT DIFFERENT VELOCITY AND PH	179

LIST OF ABBREVIATIONS

CFD	Computational Fluid Dynamics
DIM	Direct Impingement Model
DPM	Discrete Phase Model
E/CRC	Erosion/Corrosion Research Center
ENM	Electrochemical Noise Measurement
HGLR	High Gas Liquid Ratio
LGLR	Low Gas Liquid Ratio
LPR	Linear Polarization Resistance
SEM	Scanning Electron Microscope

NOMENCLATURE

Symbol	Description
a	Constant in equation 2-5
A	Constant in equation 2-5
b	Constant in equation 2-5
B	Brinell hardness
C	Constant in erosional velocity (API RP 14E) equation
C_1, C_2, C_3	Constants in equation 2-5
D	Pipe diameter (m)
d_p	Particle diameter (m)
E	Young's modulus
ER	Erosion rate, mm/year
f	Friction factor
f_{el}	Friction factor of elbow
f_p	Friction factor of straight pipe
$f(\text{CO}_2)$	Fugacity of CO_2 in equation 3-33
$f(\text{pH})_t$	The effect of pH at temperature T in equation 3-33
g	Gravity acceleration (m/s^2)
G	API gravity
K	Constant dependant of physical characteristics of material
k	Kinetic energy of turbulence (equation 2-37)
K_f	Resistance coefficient of pipes fittings
k_t	Temperature dependent constant in equation 3-33
k_{tot}	Overall heat transfer coefficient. $\text{W/m}^2\text{C}^\circ$
L_{act}	Actual length of elbow (m)
L_{eq}	Equivalent length of fitting (m)

L_o	Stagnation length (m)
m	Mass (kg)
m_p	Particle mass (kg)
n	Constant dependant of physical characteristics of material
P_{co2}	CO ₂ partial pressure, bar
p_f	Friction pressure (pascal)
Q	Volumetric flow rate, m ³ /s
R_c	Corrosion rate, mm/year
Re	Reynolds number
S_{el}	Wall shear stress of elbow
S_p	Wall shear stress of straight pipe
SG	Specific gravity
T	Temperature °C
T_L	Temperature at distance L along pipeline °C
T_o	Pipeline Surrounding temperature °C
u	Velocity in x-direction (m/s)
u'	Fluctuation velocity to account for turbulence (m/s)
v	Velocity in y-direction (m/s)
w	Velocity in z-direction (m/s)

Subscript

atm	atmosphere
C	Cutting
D	Deformation
el	elbow
eff	effective
f	fluid
g	gas
i	x-direction component
j	y-direction component
k	z-direction component
L	Liquid

m	Mixture
o	Oil
p	Particle
pg	Pressure gradient
s	Sand
sys	System
t	Turbulence

Greek

α	Angle of impingement
μ	Viscosity (Pa.s)
τ	Particle response time (s)
ε	Turbulence dissipation energy
ρ	Density (kg/m ³)
τ	Particle response time (s)

Chapter 1

INTRODUCTION

1.1 Background

Sand erosion can be defined as the material wear resulting from the presence of sand particulates with fluids. In the oil and gas industry, the sand is produced from a pay zone and the fluids are oil, gas, and water, in two-phase or multi-phase flows (Fajer *et al.* 1992).

Many factors affect the amount of wear (erosion) resulting from sand production with oil or gas. These factors are generally related to the characteristics of fluids, sand, and target material. The effects of some of these factors are still under investigations by many researchers.

In addition to wear that results from sand erosion, internal corrosion of pipes that transport oil and gas is highly expected when the transported fluids contain corrosive gases such as CO₂ and H₂S. The presence of both erosive and corrosive materials in a process causes the so-called erosion-corrosion phenomenon, which results in wear magnitude greater than the sum of that generated by pure erosion and pure corrosion. The erosion-corrosion is classified as erosion-enhanced-corrosion or corrosion-enhanced-erosion depending on the ratio of pure erosion to pure corrosion.

In order to avoid the consequences of erosion, corrosion, and erosion-corrosion at any particular condition; process parameters should always be controlled within safe operating limits. To do so, corrosion and erosion rates at different operating conditions are to be predicted to determine the critical value for each parameter. The process should then be operated below these critical values.

Many models have been developed for the prediction of erosion and corrosion rates. All these models, however, have limitations that restrict their applicability. Examples of these limitations are as follows:

- 1- Applicable for narrow range of parameters.
- 2- Involve few parameters.
- 3- Applicable to a specific case of flow (either one phase or two phases)
- 4- Applicable to a specific fluid (liquid or gas)
- 5- Applicable to a specific geometry (straight pipe, elbow, tee...etc)

In addition, the majority of the commercial softwares based on these models are applicable either to erosion or corrosion prediction and need license which mean extra cost. The erosion prediction using CFD software, in particular, is very complicated and time consuming.

1.2 Problem statement

The entrainment of sand particles in fluids flowing through horizontal or vertical pipes is frequently occurring during oil and gas production and transportation. In conventional oil production, sand is produced with oil and gas from a sandstone reservoir under certain conditions; such conditions include unconsolidated formation, high water cut, and high pressure drop. In unconventional oil or crude bitumen, which is a mixture of sand, bitumen, and water; sand is produced with a very high volume fraction (Tian 2007).

The entrainment of sand in fluids causes wear of pipes and fittings due to the impingement of sand particles on the internal surfaces of these pipes and fittings. The severity of the wear depends on many factors that are related to the fluid, sand particles, target material, and the flow velocity.

In addition to sand production, carbon dioxide (CO₂) may be contained in the oil and gas as a light impurity or CO₂ injection during enhanced oil recovery (EOR). The

presence of CO₂ with water in oil transported through a steel pipe forms a suitable environment for corrosion initiation. The corrosion propagation depends on the flow and chemical properties such as velocity, temperature, CO₂ partial pressure, and pH. At certain instant, a protection layer consisting of iron carbonate is formed on the pipe surface. This layer protects the steel from subsequent attack and decreases the corrosion rate. In the case of simultaneous presence of sand with CO₂, continuous impingements of the sand will remove the protection layer and lead to the so-called erosion-corrosion process.

The wear (erosion, corrosion, or erosion-corrosion) rate for a material used in any flow process can be determined either by field or laboratory tests under properly simulated conditions. It can also be calculated using a selected mathematical or computational model, provided that all the flow parameters are included in the model. Although field and laboratory tests guarantee more accurate results than modeling, they have some disadvantages such as:

1. The cost required to set up the experimental rig.
2. The difficulties of controlling the process parameters during the test.
3. Longer time required for a test run
4. The interruption of the process and destruction of the material in some field tests.

Modeling the erosion and corrosion requires proper selection of a model suitable for the specified process, on one hand, and provides acceptable accuracy, on the other.

For erosion, the models in the open literature can be grouped into three categories as shown in Table 1-1.

Table 1-1: Erosion prediction methods

Category	Advantages	Disadvantages	Examples
CFD models	The most accurate, provides erosion rate distribution, solve for the primary (fluid) and secondary (sand particles) phases	Costly (Mostly commercial software), time consuming, highly complicated	Fluent, Ansys
Semi-empirical models	Accuracy to be examined, solve for the secondary (sand particles) phase	Moderately complicated	Direct impingement model
Empirical models	Accuracy to be examined, very easy to implement	No solution for particles movement	API model, Salama model

For corrosion, the models available in literature are most likely empirical models based on flow or electrochemical data.

The problem to be tackled in this research is to develop a computational code to serve as a predictive tool for erosion, corrosion, and erosion-corrosion. The code is thought to eliminate the complexity and cost of the CFD models while maintaining the accuracy. The code, in addition, will serve as a comprehensive predictive tool for erosion, corrosion, and erosion-corrosion in pipes and fittings.

To guarantee the code accuracy for erosion prediction, a selected CFD model (namely Fluent) is used as a benchmark for examining the accuracy of selected empirical and semi-empirical models. In addition, published data gathered from literature is used for further examination and possible improvement of the empirical and semi-empirical models.

1.3 Scope of the research

This research mainly focuses on computational modeling of erosion, corrosion, and erosion-corrosion to develop a predictive tool that encompasses the features of accessibility, comprehensiveness, flexibility, simplicity, and accuracy. This aimed to be done by employing selected empirical and semi-empirical models to Visual Basic 6 programming. The research also covers investigation of the predictive tool by comparing the obtained results with experimental data as well as CFD results. The experimental data includes data collected from literature and lab measured data. A lab-scale flow loop will be constructed for the experimental measurements. The investigation process will be utilized to improve the models for better accuracy.

The developed code is applicable to prediction of erosion in elbows and tees, corrosion rate in elbows and straight pipes, and erosion-corrosion rate in elbows. The erosion prediction is applicable to sand particles entrained in gas, water, or oil flow. The corrosion prediction is applicable to single phase or multiphase flowing through an elbow or a pipe when CO₂ is present in the fluid. It is also applicable to prediction of CO₂ in long pipelines. The erosion-corrosion prediction is applicable to flow of fluids containing both sand particles and CO₂ taking into account the synergy effect.

The research will cover investigation of the factors affecting erosion and corrosion that are related to flow (velocity, viscosity, and density), sand (size, shape, and quantity) and geometry.

1.4 The research objectives

The main objective of this research is to develop a predictive tool for sand erosion and corrosion in elbows, tees, and straight pipes based on mathematical models from the open literature. The specific objectives of this research are to:

1. Develop a computational predictive tool for sand erosion, CO₂ corrosion and erosion-corrosion rate calculations in elbows, tees, and straight pipes.
2. Develop a computational fluid dynamics (CFD) model to simulate sand erosion in elbows.

3. Validate the developed predictive tool using published data from literature and measured data from a flow loop as well as the CFD results and improve the models if the accuracy is lacking.
4. Investigate the accuracy of different models used to develop the computational predictive tool and improve the models that lack accuracy.
5. Analyze the predictive tool results under different input data to investigate the effect of flow parameters on erosion and corrosion.

1.5 Thesis overview

This thesis contains six chapters as follows:

Chapter 1 is an introduction to the whole research and consists of a brief description of the research background, the scope of the research, the research objectives, and the research contributions.

Chapter 2 reviews the literature of topics relevant to the research area. The review covers literature related to sand production control and management, erosion and corrosion processes, erosion and corrosion testing, and the methods of erosion prediction and simulation.

Chapter 3 presents the theory and methodology that have been adopted in this work toward achieving the research goals. The chapter describes the erosion models used to develop the computational code and the CFD model. A detailed description of NOROK model implementation to simulate CO₂ corrosion in straight pipes, elbows, and long-distance pipelines is given. Summary of the experimental methodology including the techniques and devices used for corrosion measurements is given at the end of the chapter.

Chapter 4 presents the experimental setup design and fabrication. The chapter mainly focuses on the method followed to model the flow loop and size its components.

Chapter 5 presents and analyses the research results. The results include those obtained from computational code at specified process conditions (input parameters) and those obtained from experimental measurements. A thorough investigation of the code results is made to evaluate the models applicability and accuracy based on their comparison with measured and CFD results.

Chapter 6 summarizes the conclusions of the research along with recommendations and future work directions.

1.6 Summary

This chapter is a summary to the whole research. At the beginning, a brief description of the research background is given. And then, the motivation to carry on this research problem has been described. The scope of the research, the research objectives, and the research contributions are outlined at the end of the chapter.

Chapter 2

LITERATURE REVIEW

2.1 Sand production in oil and gas facilities

Fajaer and Risnes (Fajer *et al.* 1992) discussed sand production from petroleum reservoirs and detailed all the related matters including those related to rock stresses, flow, and the consequences of sand production. In addition, they proposed some prediction models for sand production calculations.

The conditions that lead to sand production have been discussed in many publications. John Carlson (Carlson *et al.* October 1992) stated four conditions that can cause sand production. These conditions are unconsolidated formation, water breakthrough, reservoir pressure depletion, and high lateral tectonics. The characteristics of the unconsolidated formation are pressure lower than 2000 psi (Salama 2000) and permeability of 0.5 to 8 Darcy (Carlson *et al.* October 1992). Hans Faziri et al. (Faziri *et al.* 2006) included more factors that affect sanding by focusing on sand properties rather than just the rock. They grouped these factors into two groups. The first group is the natural conditions related to the rock and sand particles, and the second group is the imposed conditions related to the sand face drilling, completion, and production strategies.

Sand production leads to subsequent problems in subsurface and surface petroleum production equipments. The problems related to subsurface and surface production facilities as stated by Fajaer and Risnes (Fajer *et al.* 1992) are:

- Equipment erosion
- Casing collapse

- Separation and handling of sand in produced fluids
- Sand precipitation in pipes and separators

The two methods which are used to prevent sand production or to solve the problems that arise due to it are sand control and sand management.

- Sand control: by applying sand control, sand production is avoided or minimized to an acceptable level. Sand control includes techniques like restricted hydrocarbon production, in-situ consolidation, gravel packing, high-rate water packing, frac packing, fracturing without screen, and drilling horizontal wells completed with screens (Carlson *et al.* October 1992). An ideal sand control should totally prevent production of sand from the pay zone to the well bore. However, this objective is difficult to achieve due to different reasons such as wrong sand control design, or failure of sand control screen due to erosion caused by sand impingement on the screen (Colwart *et al.* 2007). Sand control methods sometimes may be economically unfeasible for a project because of their high costs.
- Sand management: sand management allows sand production but avoids its consequences by the monitoring and controlling of well pressures, fluid rates and sand influx (Tronvoll *et al.* 2001). With sand management, tolerable amount of sand is allowed to be produced from the well. Appropriate design and analysis is then required to avoid and cure the consequences of sand production and transportation. The main advantage of applying sand management is that it saves the cost of sand control devices. Moreover it has been found that sand production improves well productivity by increasing its inflow performance (Servant *et al.* November 2007.).

During entrainment of sand particles in the flowing oil and gas, they continuously impact the internal surface of the pipe. As a result, the pipe is eroded leading to wall thinning and, in extreme conditions, fluids leakage and loss of production may occur.

2.2 Sand Erosion

Erosion is the process of material wear and thinning due to continuous hitting and impingement of solid particles. In petroleum production and transportation, the eroded material is normally the inner surface of a component such as pipe, elbow, or tee that contains a flowing fluid. The erodent material, on the other hand, is normally solid particles (most probably sand) moving with the flowing fluid as a secondary phase. The erosion in a ductile material takes a form of material removal due to localized plastic strain and fatigue; whereas in brittle materials, surface cracking and chipping take place as a result of particle impingement (Barton 2003).

Erosion may take place in different subsurface and surface components such as sand control screen (Colwart *et al.* 2007), choke (Haugen *et al.* 1995), valve (Mazur *et al.* 2004), plugged tee, and elbow (Chen *et al.* 2006)

The severity of the wear depends on many factors related to the fluid, sand particles, and target material (Finnie 1972) (Deng *et al.* 2005), (Barton 2003) (Ahlert 1995), (Karelin 2002). N A Barton (Barton 2003) has arranged the components, where the erosion takes place according to erosion vulnerability, in eight ranks ranging from chokes as the most vulnerable component to straight pipes as the least vulnerable component.

2.3 Corrosion and erosion-corrosion

corrosion is defined as “the deterioration of a material, usually metal, by the reaction with its environment” (Jones 1992). Internal corrosion of pipes transporting oil and gas is a common problem in petroleum production facilities. The problem is highly expected when corrosive gases such as CO₂ and H₂S are present in the transported fluids. In mature wells in many oil fields, water cut may be as high as 90% and the produced fluids may contain as high as 30% of CO₂. The presence of brine with CO₂ forms a suitable environment for corrosion initiation and growth.

Efforts have been made to predict and control corrosion in many oil fields worldwide. As a result, many models and measurement techniques have been proposed.

De Waard and Milliams (Waard and Milliams 1975) indicated that corrosion rate increases with CO₂ partial pressure and temperature until it reaches a maximum value at temperature 60-70 °C and then decreases until 90 °C.

De Waard, Lotz and Dugstad (Waard *et al.* 1995) proposed a semi-empirical model using data acquired from a high pressure test facility. Their model accounts for the contributions of kinetics of corrosion reaction and mass transfer of dissolved carbon dioxide. Their model, however, doesn't account for the oil composition.

In 1996, Jepson et al (Jepson *et al.* 1996) developed an empirical model for corrosion rate prediction in horizontal multiphase slug flow in pipelines. Their model relates the corrosion rate to the pressure gradient across the mixing zone, water cut, temperature, and CO₂ partial pressure. The model has been improved in 1997 (Jepson *et al.* 1997) to account for the effect of slug frequency and oil type.

A mechanistic model for CO₂ corrosion in horizontal multiphase slug flow has been proposed in 2002 by Hongwei Wang et al (Wang *et al.* 2002). Their model covers the electrochemical reactions on steel surface, the chemistry of fluid, and mass transfer between the metal surface and the fluid.

Srdjan Netic et al. (Netic *et al.* 2005) developed a comprehensive model for internal corrosion prediction in mild steel pipelines. The effects of many factors affecting the corrosion rate such as H₂S, water entrainment in multiphase flow, corrosion inhibition by crude oil components and localized attack have been taken into account in the model.

NORSOK Norwegian standard CO₂ prediction model (NORSOK 2005) predicts the corrosion rate due to presence of CO₂ in straight pipes that transport single phase or two-phase (oil-water) fluids. The model is a set of three equations for prediction of corrosion rate in straight pipe within temperature range of 5-150 °C. The effects of pH is introduced to the equations as a factor calculated at different temperatures and

within different pH ranges using simple empirical equations. The effect of CO₂ partial pressure is introduced to the model as CO₂ fugacity, which is calculated using a simple empirical equation. In this research, the model was extended for application in elbow and for predicting corrosion rate along heated pipelines before its employment to the code.

2.4 Slurry flow in pipes

Slurry is a fluid that consists of liquid and solid particles. The slurry flow can be classified in different ways; one of these ways is the classification according to flow patterns. A prerequisite for calculation of pressure losses and erosion in a specific slurry flow is the determination of its flow regime.

The slurry regime classification of Durand and Condolios (Durand and Condolios 1952) is considered as the pioneer of slurry flow classification. Since then, many classifications have been developed.

One of the established classifications is to classify the slurry flow into four regimes (Crowe 2006).

Identifying the flow pattern of slurry is important to gain information about particles supply and velocities, and hence predicting erosion distribution more accurately. Categorization of slurry flow patterns normally includes a stationary bed at the invert (bottom) of the pipe where particles are unmovable with flow. Above the stationary bed, flow can be subdivided into several layers, ranging from two layers as subdivided by Wilson (Wilson 1970, 1976), and five layers as subdivided by Goveir and Aziz (Govieir and Aziz 1972).

Wood et al. (Wood *et al.* 2004) considered the two-layer slurry flow by Wilson to propose three wear regions according to the circumferential position of a straight pipe or elbow. The first region is a high particle supply and low particle velocity at the bottom. The second region is a low particle supply and high particle velocity at the top. The third region is a high particle supply and high particle velocity in between.

2.5 Experimental simulation of erosion and corrosion

Different devices are used to measure erosion or corrosion rate for a target material. A piece of the target material known as specimen is usually subjected to simulated conditions of the real process using a selected device. The simulated conditions include the thermal condition which is normally simulated by heating the flowing medium and the flow condition which is simulated by rotating the specimen or by accelerating the fluid in a pipe. Among the devices used to simulate erosion and corrosion processes are flow loops, jet impingement, and pot testers.

2.5.1 Flow loops

Flow loops (also known as pilot plant test loops) are the most reliable devices for simulating a process hydrodynamic and the erosion/corrosion-related conditions. The flow loop, in addition, allows measurements in different geometries such as elbows (Salama and Venkatesh 1983), (Wood *et al.* 2004), (Mishra *et al.* 1998), (Deng *et al.* 2005), tees, straight pipes (Gupta *et al.* 1995), (McKibben 1992)), and coiled tubing (Shah and Samyak 2008). Yun Yao *et al.* (Yao *et al.* 2000) fabricated a specimen that made it possible to measure wear in both a straight pipe and a bend. Different measurement techniques can be used in the flow loop. R J K Wood (Wood *et al.* 2004) have used a combination of weight loss, ultrasonic, and visual inspection using endoscope techniques to measure material loss following every test run. T Deng *et al.* (Deng *et al.* 2005) have used an ultrasonic gage to measure the change of thickness during their measurements in a pneumatic conveyor bend.

2.5.2 Jet impingement

Jet impingements generate high velocities and allow measurements of wear at different angles of impingement. Jet impingements are more suitable for gases and they only measure erosion by impingements.

Figure 2-1 shows the jet impingement setup that was used by P. Andrews *et al.* (Andrews *et al.* 1999) to study erosion-corrosion of 13 Cr steel under sweet gas

environment. Their jet impingement setup consists of high pressure pump with a capability of delivering sweet or sour fluids with pressure up to 68.9 MPa. The jets can be regulated before the nozzles to provide velocities values between 100 and 350 m/s.

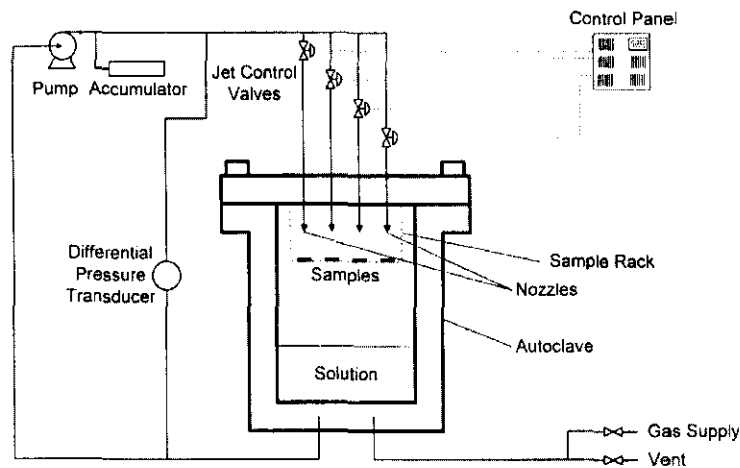


Figure 2-1: A schematic diagram of the jet impingement setup used by P. Andrews et al. (Andrews *et al.* 1999)

While P. Andrews et al. used weight loss technique for measuring erosion rate, G.A. Zhang et al. (Zhang *et al.* 2009) used both weight loss and electrochemical techniques to study erosion corrosion of 3003 aluminum (Al) alloy in ethylene glycol–water solutions. The electrochemical measurements were conducted by inserting reference, working, and counter electrodes inside a test chamber as shown in Figure 2-2.

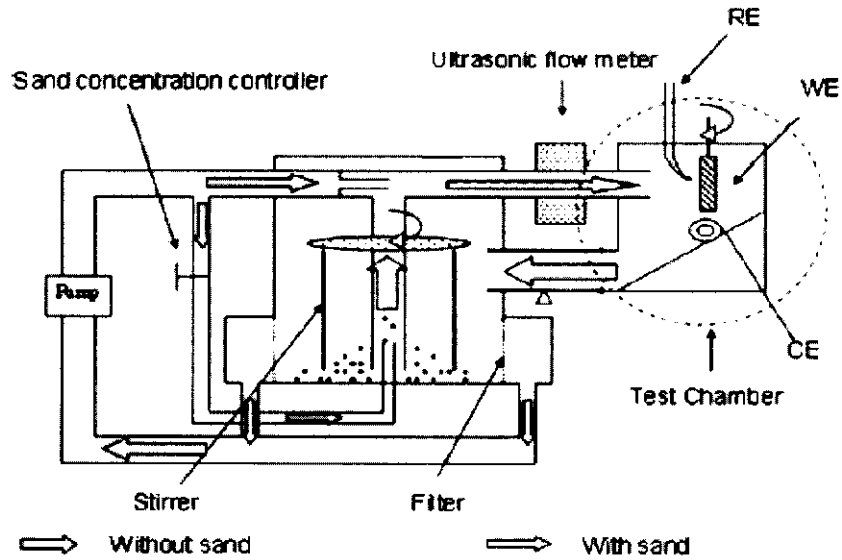


Figure 2-2: A schematic diagram of the jet impingement setup used by G.A. Zhang et al. (Zhang *et al.* 2009)

2.5.3 Pot tester

Pot tester consists of a small chamber (pot) through which slurry is pumped. A small impeller inside the chamber forces the slurry particles to hit samples of the target material that are arranged around the chamber (Hugget and Walker 1988).

An example of the Pot tester is that designed and fabricated by Gupta et al. (Gupta *et al.* 1992) and used by them (Gupta *et al.* 1995) to study sand erosion in a slurry pipeline. Their pot tester consists of a propeller attached to a shaft rotating inside a tank. The rotation of the propeller keeps the solid particles in suspension while specimens are fixed in four flat side arms fitted to a brass sleeve.

2.6 Erosion Prediction Models

Erosion modeling is an alternative to measurement to determine how severe a target material is eroded under specific conditions. Over the last decades, many models were proposed for erosion modeling. These models range from simple empirical models to

complicated computational fluid dynamics models. This section introduces some of these models:

2.6.1 Prediction Models for General Applications

Many models have been proposed for the prediction of material wear due to solid particles motion. The distinction of these models is due to many reasons such as the physical description of the phenomena, the considered parameters, and the range of parameters used to develop the model.

Basically the erosion rate generated by the flow of a particle depends on its velocity and the angle of impingement. This can be expressed mathematically as follows (Karelin 2002).

$$ER = KV_p^n f(\alpha) \tag{2-1}$$

Where ER is erosion rate in mm/year, K and n are constants dependent on the physical characteristics of the target material, and V_p is the particle velocity in m/s. The values of k and n for some materials have been proposed by Haugen and his co-workers as given in Table 2-1.

Table 2-1: The constants k and n for some materials (Haugen et al.).

Material	$K \times 10^9$	n
Steel	2	2.6
Hot sprayed WC-60%Ni	5.2×10^{-2}	3.4
Hot sprayed WC-40%Ni	1.2×10^{-2}	3.2
Degun WC, 0.25 mm	6.1×10^{-1}	2.7
Detonation gun WC, thin	5.3×10^{-1}	3.2
Cobalt based coating	5.3×10^{-1}	3.1
WC, DC-05	1.1×10^{-1}	2.3
WC, CS-10	3.2×10^{-1}	2.2
WC, CR-37	8.8×10^{-2}	2.5
95 Al ₂ O ₃	68	2
99.5 Al ₂ O ₃	9.5×10^2	1.2
PSZ	4.1	2.5
ZrO ₂ -Y ₃	4×10^{-2}	2.7
SiC	6.5	1.9
Si ₃ N ₄	2×10^{-1}	2
TiB ₂	9.3	1.9
B ₄ C	30	0.9
SiSiC	7.2×10^{-2}	2.7

The functional relationship $f(\alpha)$ is given in equation (2-2) (Karelin 2002).

$$f(\alpha) = \begin{cases} \frac{1}{3} \sin^2 \alpha & 0 < \alpha < 0.4\pi \\ \sin 2\alpha - 3 \cos^2 \alpha & 0.4\pi < \alpha < 0.5\pi \end{cases} \quad 2-2$$

The functional relationship for brittle and ductile materials has been described graphically as shown in Figure 2-3 (Barton 2003). The figure indicates that, for ductile material, the angle function increases with impact angle to reach a maximum of one at 30° and then declines with the impact angle to reach 0.6 at 90°. For brittle material, the angle function increases linearly from 0 at 0° to 1 at 90°.

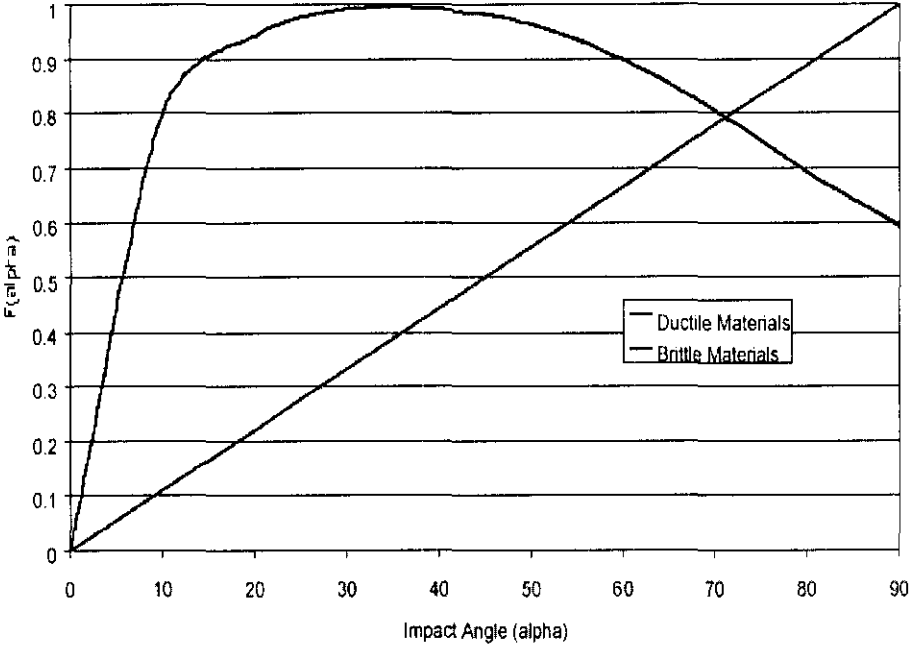


Figure 2-3: The functional relationship for brittle and ductile materials (Barton 2003)

The following relationship has been proposed by Haugen and co-workers for functional relationship $f(\alpha)$ calculation for carbon steel (Haugen *et al.* 1995).

$$f(\alpha) = \sum_{i=1}^8 (-1)^{(i-1)} A_i \left(\frac{\alpha\pi}{180} \right)^i \tag{2-3}$$

Where, values of A_i are given in Table 2-2.

Table 2-2: A_i factors in equation (2-3) (Haugen *et al.*)

A_1	A_2	A_3	A_4	A_5	A_6	A_7	A_8
9.37	42.295	110.864	175.804	170.137	98.298	31.211	4.170

The mechanism of wear has been classified by Bitter (Bitter 1963) into cutting wear and deformation wear. Cutting wear occurs at low angles of impingement at

which the collisions are more tangential and the particle tends to scratch the material surface and remove a small amount of the material. Deformation wear occurs at large angles with fatigue rupture due to so-called cold work and the subsequent impact leads to small fragments removal from the material surface.

Finnie (Finnie 1972) proposed equation 2-4 and Bitter (Bitter 1963) proposed equation 2-5 for prediction of cutting and deformation wears, respectively, which are expressed in the removed mass per single particle collision (kg/kg).

Cutting wear:

$$W_c = \begin{cases} \frac{\rho_m C_1 V_p^2}{K_2 \psi} \left[\sin 2\alpha - \frac{K_1}{C_2} \sin^2 \alpha \right] & \tan \alpha < \frac{C_1}{K_1} \\ \frac{\rho_m C_1 V_p^2}{K_2 \psi} \left[\frac{C_2}{K_1} \cos^2 \alpha \right] & \tan \alpha > \frac{C_1}{K_1} \end{cases} \quad 2-4$$

Deformation wear:

$$W_D = \frac{\frac{1}{2} \rho_m (V_p \sin \alpha - k_3)}{C_3} \quad 2-5$$

Where:

$$K_1 = 2 \left[1 - \frac{m_p d_p^2}{4I_p} \right] \quad 2-6$$

$$K_2 = \left[\frac{40}{\pi^4} \rho_p \left[\frac{1 - q_p^2}{E_p} + \frac{1 - q_m^2}{E_m} \right]^{-4} \right]^{\frac{1}{5}} (V_p \sin \alpha)^{2/5} \quad 2-7$$

$$K_3 = \frac{\pi^2}{2\sqrt{10}} (1.59Y)^{\frac{3}{2}} \left[\frac{1}{\rho_p} \right]^{\frac{1}{2}} \left[\frac{1 - q_p^2}{E_p} + \frac{1 - q_m^2}{E_m} \right]^2 \quad 2-8$$

$$E = \frac{4}{3} \left[\frac{1 - q_p^2}{E_p} + \frac{1 - q_m^2}{E_m} \right] \quad 2-9$$

C_1 , C_2 , and C_3 are empirical constants to account for all the subtle factors that affect the erosion process, such as the structures of particles and material, and shape of particles. The values of these constants obtained by the preliminary experiments were 0.15, 4 and 1.035×10^{-4} , respectively (Karelin 2002). E is the Young's modulus and the subscripts p and m denote particle and material; q is the Poisson's ratio, V_p is the particle velocity and α is the angle of impingement. I_p is the particle moment of inertia, which can be defined as the particle resistance to rotation; and can be written mathematically as follows (www.wikipedia.org):

$$I_p = m_p r^2 \quad 2-10$$

Where, r is the shortest distance from the axis of rotation to the particle.

Neilson and Gilchrist (Neilson and Gilchrist 1968) proposed a model that combined the brittle erosion model, as proposed by Bitter, to a simplified ductile erosion model. The proposed model is given as follows:

$$W_t = W_D + W_B = \begin{cases} \frac{M(V^2 \cos^2 \alpha - V_p^2)}{2\phi_c} + \frac{M(V \sin \alpha - V_{el})^2}{2\varepsilon_b} & \alpha \leq \alpha_o \\ \frac{MV^2 \cos^2 \alpha}{2\phi_c} + \frac{M(V \sin \alpha - V_{el})^2}{2\varepsilon_b} & \alpha > \alpha_o \end{cases} \quad 2-11$$

With the assumption that $W_B = 0$ when $V \sin \alpha < V_{el}$.

Where V_{el} is the threshold velocity, normal to the eroding surface; and V_p is the threshold velocity, parallel to the eroding surface given by:

$$V_p^2 = V^2 \cos^2 \alpha \sin[(n\alpha) - 1] \quad 2-12$$

Where n is an empirical constant and $\alpha_o = \frac{\pi}{2n}$.

The Erosion/Corrosion Research Centre (E/CRC) at the University of Tulsa developed a mechanistic model for a wide range of applications. The main

contribution of this model is the consideration of the parameters related to flow, material, and particles that affect the erosion rate. The sand erosion is calculated using the following semi-empirical equation (Ahlert 1995):

$$ER = AV_p^{1.73} f(\alpha) \quad 2-13$$

The angle function $f(\alpha)$ is calculated by the following equation (Wang and Shirazi 2003):

$$f(\alpha) = \begin{cases} a\alpha^2 + b\alpha & 0^\circ < \alpha \leq 15^\circ \\ x \cos^2 \alpha \sin(w\alpha) + y \sin^2 \alpha + z & 15^\circ < \alpha \leq 90^\circ \end{cases} \quad 2-14$$

The constants a, A, b, w, x, y, and z have been given by Ahlert as in Table 2-3 (Ahlert 1995).

Table 2-3: The constants a, A, b, w, x, y, and z in equation 2-14 (Ahlert, 1995)

Material	Carbon steel	Aluminium
A	$1.95 \times 10^{-5} B$	2.388×10^{-7}
δ	15	10
a	-3.84×10^{-8}	-34.79
b	2.27×10^{-8}	12.3
w	1	5.205
x	3.147×10^{-9}	0.147
y	3.609×10^{-10}	-0.745
z	2.532×10^{-9}	1

B is Brinell hardness which characterizes the indentation hardness of materials through the scale of penetration of an indenter, loaded on a material test-piece. (http://en.wikipedia.org/wiki/Brinell_scale).

The following model was also proposed by E/CRC for sand erosion prediction (McLaury *et al.* 1996). The model is one of many models developed by McLaury and co-workers based on direct impingement tests at different impingement angles and velocities.

For carbon steel:

$$ER = \left[\frac{1559}{B^{0.59}} \left[\frac{V}{0.3048} \right]^{1.73} f(\alpha) \right] \times 10^{-9} \quad 2-15$$

With

$$f(\alpha) = \begin{cases} 2.27 - 3.84\alpha^2 & \alpha < 15^\circ \\ 3.147 \cos^2 \alpha + 0.3609 \sin^2 \alpha + 2.532 & \alpha \geq 15^\circ \end{cases} \quad 2-16$$

For Aluminium,

$$ER = \left[2.388 \left[\frac{V}{0.3048} \right]^{1.73} f(\alpha) \right] \times 10^{-7} \quad 2-17$$

With

$$f(\theta) = \begin{cases} 12.3\alpha - 34.79\alpha^2 & \alpha < 10^\circ \\ 1 + 0.147 \cos^2 \alpha \sin(5.205\alpha) + 0.754 \sin \alpha & \alpha \geq 10^\circ \end{cases} \quad 2-18$$

Where α is in radians

2.6.2 Prediction Models in Oil and Gas Applications

Three methods have been used for prediction of sand erosion in oil and gas production and transportation the empirical, the semi-empirical, and the CFD models. Each of these methods will be described in the following subsections.

2.6.2.1 Empirical methods

In the empirical methods, erosion is predicted for a component (most probably elbow or tee) by using the fluid velocity (no particles or bubbles tracking). The methods are commonly based on simple empirical correlations that predict erosional threshold velocity (the velocity above which erosion occurs) and erosion rate, and are more

applicable to gas flow where the dispersed phase (particles or bubbles) is almost flowing at the fluid mean velocity. The erosional velocity, V_e is usually predicted using the American Petroleum Institute Recommended Practice equation (API RP 14 E) (API 1991).

$$V_e = \frac{c}{\sqrt{\rho_f}} \quad 2-19$$

Where C is constant, its value as proposed by API RP 14 E is 100 for continuous service and 125 for intermittent service, and ρ_f is the density of fluid.

Many investigators have questioned the accuracy of equation 2-19 on the ground of neglecting of some important factors such as particles size and shapes, component geometries and fluid viscosity. Therefore many attempts were made to enhance the accuracy, and to extend the applicability of API RP 14 E equation. Salama and Venkatesh proposed a model for prediction of penetration rate in elbows and tees (Salama and Venkatesh 1983). Assuming a sand density of 2650 kg/m³, their model can be written in SI units as follows:

$$ER = 37.585 \frac{WV^2}{PD^2} \quad 2-20$$

Where ER is the erosion rate (mm/year), W is sand production rate (kg/s), V is the fluid flow velocity (m/s), P is the hardness parameter (Bar), and D is the pipe diameter (m). Salama and Venkatesh used equation 2-20 to calculate the erosional velocity for steel pipes using value of P 1.05X10⁴ bar for allowable erosion rate of 0.254 mm/year. This resulted in the following equation for erosional velocity.

$$V_e = \frac{0.0152D}{\sqrt{W}} \quad 2-21$$

The shortcomings of Salama and Venkatesh model (equation 2-20) are its neglect of sand particle size and shape, and its inapplicability to two-phase (liquid-gas) flow.

Their model also neglects solid particles fragmentation and hardness, but since the model only deals with sand particulates where their hardness varies slightly, so we believe that neglecting the hardness is logical. The material hardness is also not considered due to the fact that the model only deals with carbon steel materials. Salama (Salama, 2000) incorporated the effect of two-phase mixture density and particle size into equation 2-20 and proposed the following equation.

$$ER = \frac{11.574 WV_m^2 d}{S_m D^2 \rho_m} \quad 2-22$$

Where V_m and ρ_m are mixture velocity (m/s) and density (kg/m^3), respectively. In equation 2-22, S_m is a geometry-dependant constant as given in Table 4-2..

Equation 2-22 was developed through numerous tests that were carried out using water and nitrogen gas. Since water and gas viscosities are almost constant, therefore the viscosity parameter has not been included in the equation. Salama, however, expected that higher viscosity will result in reduction of erosion rate (Salama, 2000).

Table 2-4: The geometry-dependent constant S_m in Salama equation (Salama, 2000)

Geometry	Elbow (1.5 and 5D)	Seamless and cast elbows (1.5 to 3.25 D)	Plugged tee (gas-liquid)	Plugged tee (gas flow)
S_m	5.5	33	68	1379

2.6.2.2 Semi-empirical Methods

An example of Semi-empirical methods is the direct impingement model (DIM) from University of Tulsa. In the DIM model, erosion is predicted by using simplified particles trajectory equations (the direct impingement model). This is a mechanistic model developed by Erosion/Corrosion research center (E/CRC) at University of Tulsa to predict the penetration rate of direct impingement in elbows and tees. The direct impingement model can predict the penetration rate after determining the direct

impact velocity, erosion ratio, and erosion rate. The data required for the direct impingement model are those relating to the component (geometry and size), flow (velocity, density and viscosity), and particle (density, size, and shape). To account for the particle trajectory along the flow stream, the concept of equivalent stagnation length has been introduced. The concept of equivalent stagnation length can be explained by the same way as the equivalent length used to predict local pressure loss in fittings, in which, different component geometries have different equivalent stagnation lengths. The calculation procedure is shown by the flow chart in Figure 2-4. More details of the model including the used equations and tables will be given in chapter 3.

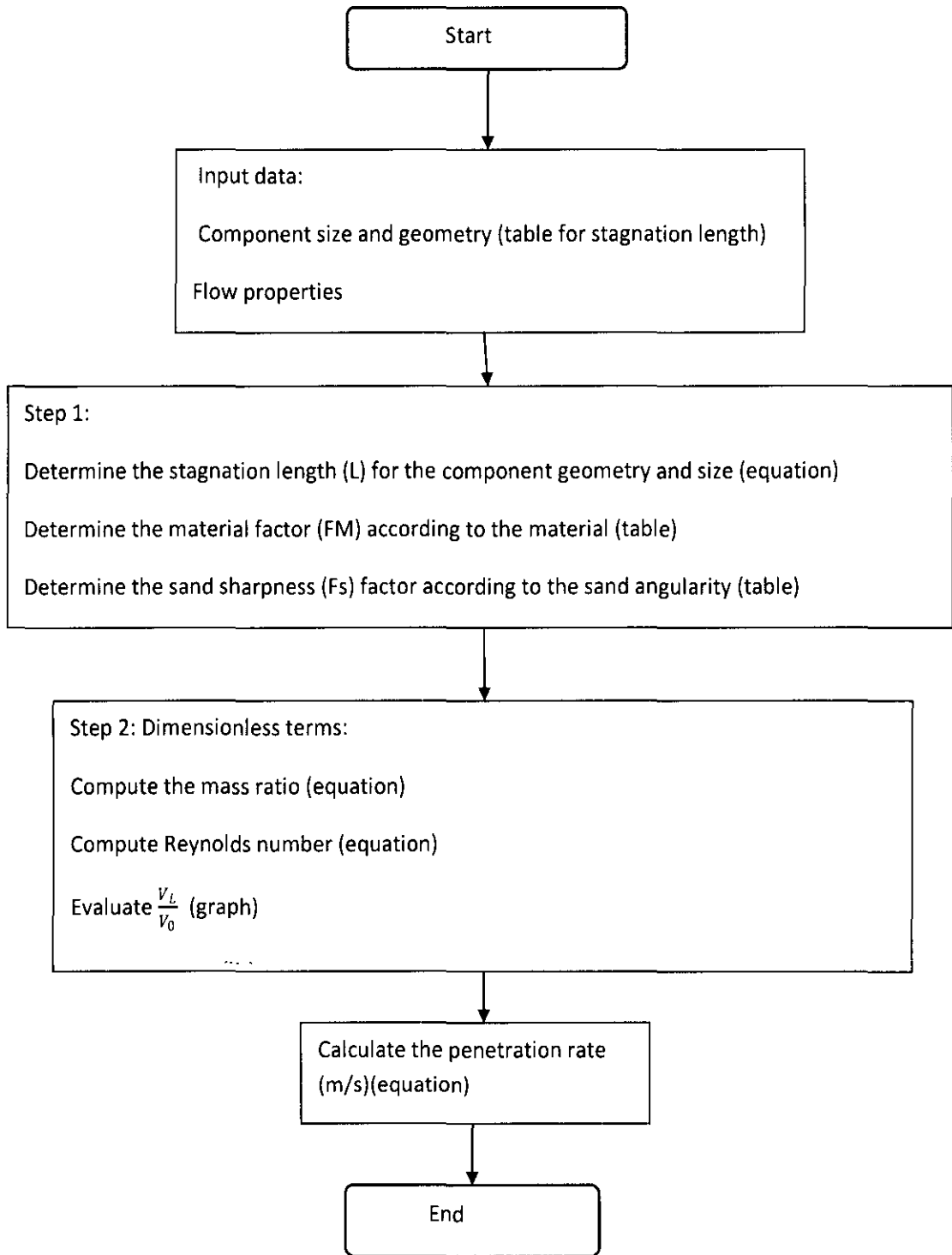


Figure 2-4: The calculation procedure of DIM (McLaury 1996)

2.6.2.3 Computational Fluid Dynamics (CFD) methods

The CFD is the simulation of fluids in dynamic (motion) state using numerical methods. Solutions are obtained using many models and techniques that suit several applications.

Simulation of sand erosion in different pipe components has been performed by many researchers. Huser and Kvernfold (Huser and Kvernfold 1998) outlined two procedures for predicting sand erosion using. The first procedure was proposed for the detailed assessment of sand erosion rates in complex process components using the CFD methods. The second procedure for standard pipe components has been developed based on extensive experiments and CFD modeling cases. Results are consolidated in correlation equations for different standard components such as bends, tees, straight pipes, welds, and reducers.

H. M. Badr and his co-worker (Badr et al. 2005) used a CFD commercial software with a FORTORAN subroutine to simulate erosion rate in a pipe with sudden contraction for two-phase (liquid and sand) turbulent flow with low particle concentration. In their study, they investigated the effects of flow velocity and particle size for one contraction geometry considering water flow in a steel pipe. They concluded a strong dependence of erosion on both flow velocity and particle size. Their results also indicated the presence of threshold velocity.

Habib and hisco-workers (Habib *et al.* 2005) have investigated erosion rate in tube entrance region of a shell and tube heat exchanger following the same procedure outlined by the same authors in (Badr *et al.* 2005). They found that the location and number of eroded tubes depend mainly on the particle size and velocity magnitude at the header inlet and the erosion rate depends exponentially on flow velocity. They found negligible effect of particle size on erosion rate at high velocity values and less erosion rate of the large-size particles than the small-size particles at low values of inlet velocities.

CFD simulation of sand erosion is generally performed in four steps. In the first step, the model is built and divided into sub domains using a grid generation

technique. In the second step, the fluid velocity is predicted along the flow direction by solving a flow model and a turbulence model. In the third step, sand particles velocity and angle of impingement are predicted using a particle equation of motion (Eulerian or Lagrangian). And finally, the data of particle velocity and angle of impingement are introduced to a selected erosion prediction model to predict the erosion rate.

Figure 2-5 shows the simulation procedure using the CFD Fluent software.

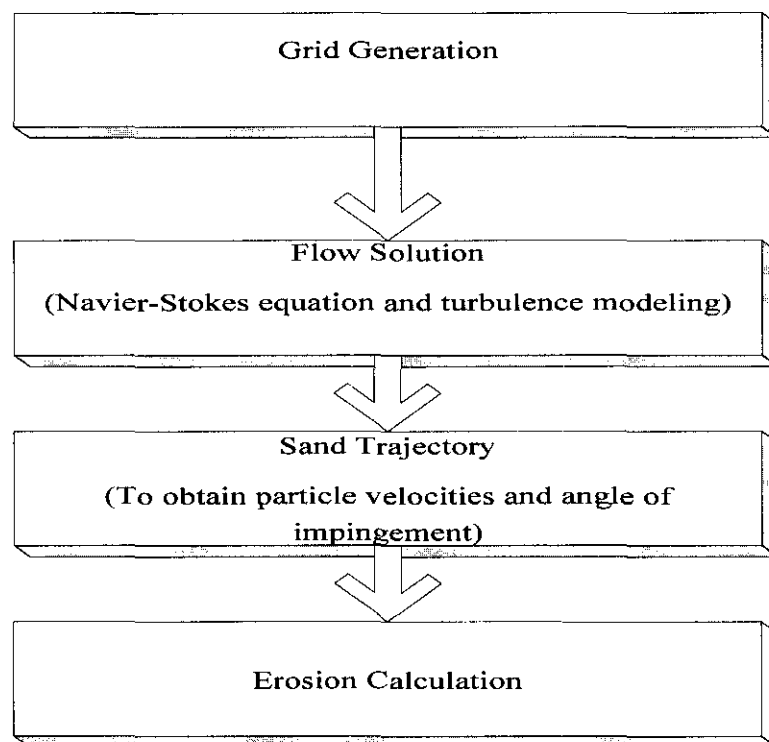


Figure 2-5: Sand Erosion Simulation Using Fluent Software

The four steps of erosion rate simulation using CFD software are detailed as follows:

2.6.2.3.1 Grid generation

Numerical grid (also called discretization) is a way to define the discrete locations at which the variables are to be calculated. It divides the solution domain into a finite number of subdomains (elements, control volumes etc.).

The grid elements in 2D can be quadrilaterals or triangles. While in 3D the elements can be 4-sides tetrahedral, 5-sides prisms, 5-sides pyramids, or six-sides hexahedra.

The elements in 2-D are planes produced from the connections of lines, whereas in 3D the elements are volumes that resulted from planes connections.

Some options of numerical grids are:

- A. **Structured grid:** structure grid contains two type, point-structured grid and block-structured grid. The point-structured grid consists of quadrilateral (2D) or hexahedral (3D) elements. Every element has a unique address in I, J, K spaces.

The block-structured grid consists of quadrilateral (2-D) or hexahedral (3-D) elements and have I, J, K structures in multi-cell blocks rather than across the entire domain (Paul *et al.* 2004).

- B. **Unstructured grid:** unstructured grids do not follow the I, J, K addressing rule. Hybrid grid is an example of unstructured grid in which different types of elements are contained.

Xianghui Chen and his co-workers (Chen *et al.* 2004) performed a grid sensitivity study for 1-in diameter elbow and plugged tee. In their study, they refined the grid in the plane normal to the flow direction in the first step, and along the axial flow direction in the second step.

2.6.2.3.2 Flow solution

In this step, the fluid parameters are obtained at every mesh element using flow solutions of the conservation equations. The conservation equations are the equations that describe the changes in fluids that result from convection (translation), diffusion (distortion related to velocity gradients), and sources or sinks of conserved or transported quantity. The main conservation equations are the continuity equation (mass conservation), momentum equation, and the energy equation (Paul *et al.* 2004).

Continuity (mass conservation)

The continuity equation states the conservation of mass of a transported quantity. The equation can be written for compressible unsteady state flow in three-dimension as follows:

$$\frac{\partial \rho}{\partial t} + \frac{\partial(\rho V_x)}{\partial x} + \frac{\partial(\rho V_y)}{\partial y} + \frac{\partial(\rho V_z)}{\partial z} = 0 \quad 2-23$$

Or, in vector form,

$$\frac{\partial \rho}{\partial t} + \nabla \rho V = 0 \quad 2-24$$

For incompressible fluids, density does not change with time and space, hence,

$$\nabla V = 0 \quad 2-25$$

Where ρ is the density and V is the velocity.

Momentum conservation

The momentum equation solves the momentum conservation by equating the momentum terms with other source and diffusion terms. In the three components (i, j, and k), the three equations of momentum are collected in the so-called Navier-Stokes equation form (Paul *et al.* 2004).

$$\frac{\partial \rho U_i}{\partial t} + \frac{\partial}{\partial x_j} (\rho U_i U_j) = -\frac{\partial P}{\partial x_i} + \frac{\partial}{\partial x_j} \left[\mu \left(\frac{\partial U_i}{\partial x_j} + \frac{\partial U_j}{\partial x_i} - \frac{2}{3} \frac{\partial U_k}{\partial x_k} \delta_{ij} \right) \right] + \rho g_i + F_i \quad 2-26$$

The right-hand terms in the above equation are the convection terms. The first term in the right hand is a source term describing the pressure gradient; the second term is the stress tensor divergence which is accountable for momentum diffusion; the third term is a source term describing gravitational force, and the last term is the source term for other forces.

Further simplification can be done by ignoring the gravitational force (for horizontal flow) and the additional forces.

Turbulence modeling

Different flow regimes occur during fluids motion in pipes or slurry mixing tanks. These regimes are well described based on a dimensionless term called Reynolds number, which is defined as the ratio of inertial forces to frictional forces. In pipes flow in pipes, Reynolds number can be written as follows:

$$Re = \frac{\rho U D}{\mu} \quad 2-27$$

And the flow regimes are normally described as follows:

Laminar flow: $Re < 2000$

Transitional flow: $2000 < Re \leq 4000$

Turbulent: $Re > 4000$

The above limitations are valid only for pure fluid flow in pipe. For spherical particles flow with fluid, the laminar regime occur somewhere between Reynolds number of 500 and 1000.

Several methods have been adopted to account for turbulence in the Navier-Stokes equation. In most of these methods, the velocity is assumed to be equal to the sum of equilibrium and fluctuation components $U + u'$, and time averaging is applied to the conservation equations. Then the Reynolds-averaged Navier–Stokes (RANS) equation for momentum is formed as follows:

$$\frac{\partial \rho U_i}{\partial t} + \frac{\partial}{\partial x_j} (\rho U_i U_j) = -\frac{\partial P}{\partial x_i} + \frac{\partial}{\partial x_j} \left[\mu \left(\frac{\partial U_i}{\partial x_j} + \frac{\partial U_j}{\partial x_i} - \frac{2}{3} \frac{\partial U_k}{\partial x_k} \delta_{ij} \right) \right] + \frac{\partial}{\partial x_j} (-\rho \overline{u'_i u'_j}) + \rho g_i + F_i \quad 2-38$$

With

$$\delta_{ij} = \begin{cases} 1 & i = j \\ 0 & i \neq j \end{cases}$$

The new term $\frac{\partial}{\partial x_j} (-\overline{\rho u_i u_j'})$ is called Reynolds stresses, which is time-averaged

value, indicated by the overbar.

The Reynolds stresses add new unknowns to the RANS equation that need to be related to other variables. This is achieved by using one of a variety of models known as turbulence models.

Boussinesq hypothesis

In this model, it is assumed that the Reynolds stresses can be related to the mean velocity gradient as follows:

$$\overline{\rho u_i u_j'} = \frac{2}{3} \rho k \delta_{ij} + \left[\mu_t \left(\frac{\partial U_i}{\partial x_j} + \frac{\partial U_j}{\partial x_i} \right) \right] \quad 2-29$$

μ_t is a constant known as eddy viscosity.

By combining the above equation with RANS equation, the velocity partial derivatives will be combined, and the sum of eddy viscosity and dynamic viscosity will be introduced as the effective viscosity.

$$\mu_{eff} = \mu + \mu_t \quad 2-30$$

k is another newly introduced variable known as the kinetic energy of turbulence.

is related to the fluctuation velocity in three directions as follows:

$$k = \frac{1}{2} (\overline{u'^2} + \overline{v'^2} + \overline{w'^2}) \quad 2-31$$

Some turbulence models with some levels of approximations can be used to calculate k and μ_t (or μ_{eff}) for computing Reynolds stresses, which in turn can be used to solve the Reynolds-averaged Navier–Stokes (RANS) equation. Examples of these models are the zero-equation models, one-equation model and two-equation

models. The zero-equation models are old models and are not included in the CFD software. There is a one –equation model called Spalart-Allamaras model designed for aerospace application. That leaves only the two-equation models relevant to our application.

The two-equation turbulence models

Muhammad Kabir (Kabir 2005) summarized the two-equation turbulence models and their proposers as shown in Table 2-6.

Table 2-5: The two-equation turbulence models and their proposers (Kabir, 2005)_

Turbulence model	Proposed by
Standard $k - \epsilon$ model	Jones and Launder (1973)
Renormalization group (RNG) $k - \epsilon$ model	Yakhot and Orszag (1986)
Realizable $k - \epsilon$ model	Shih et al. (1995)
$k - \omega$	Wilcox (1988)
RSM	Launder et al. (1975)

Standard $k - \epsilon$ model

The Standard $k - \epsilon$ model is a semi-empirical model that consists of two transport equations as follows:

The equation of the kinetic energy of turbulence (k):

$$\frac{\partial(\rho k)}{\partial t} + \frac{\partial}{\partial x_i}(\rho U_i k) = \frac{\partial}{\partial x_i} \left(\mu + \frac{\mu_t}{\sigma_k} \right) \frac{\partial k}{\partial x_i} + G_k - \rho \epsilon \quad 2-32$$

The equation of the rate of dissipation of turbulence (ε):

$$\frac{\partial(\rho\varepsilon)}{\partial t} + \frac{\partial}{\partial x_i}(\rho U_i \varepsilon) = \frac{\partial}{\partial x_i} \left(\mu + \frac{\mu_t}{\sigma_\varepsilon} \right) \frac{\partial \varepsilon}{\partial x_i} + C_1 \frac{\varepsilon}{k} G_k - C_2 \rho \frac{\varepsilon^2}{k} \quad 2-33$$

Depending on the system, other sources such as swirl, buoyancy, and compressibility can be added to the above transport equations.

C_1 , C_2 , σ_k , and σ_ε are empirical constants, their default values are 1.44, 1.92, 1, and 1.3, respectively. G_k is a generation term of turbulence given by:

$$G_k = \mu_t \left(\frac{\partial U_i}{\partial x_j} + \frac{\partial U_j}{\partial x_i} \right) \frac{\partial U_j}{\partial x_i} \quad 2-34$$

The turbulence viscosity μ_t can be calculated from the following equation:

$$\mu_t = \rho C_\mu \frac{k^2}{\varepsilon} \quad 2-35$$

C_μ is a constant with value equals to 0.09.

2.6.2.3.3 Particle tracking

By the end of the flow solution step, the continuous phase parameters are obtained along the flowstream at every grid element.

Particle tracking is the solution of the secondary phase (particles). Many parameters are aimed to be obtained from the particle tracking such as particle velocity, angle of impingement, and heat transfer to and from the particles.

Generally, two models are used for particles tracking. The first model is Eulerian model, also known as multi-fluid or continuum model (Brown 2003), in which particles are treated as a second continuous phase; the model is solved using a set of conservation equations. Eulerian model is more applicable to moderate and high particles concentrations.

The second model is the Lagrangian model in which the Newtonian equations of motion are solved to gain the trajectory of every individual particle (Patankar and Joseph 2001). The properties of particle (size, shape, and density) can be different, which makes it applicable to particles with large size distributions. This model is more applicable to dilute fluids where the volume fraction of the dispersed phase can be ignored in the continuous phase solution, and the coupling between phases can also be ignored.

In the Lagrangian model, the equation of motion in x-direction can be written as follows:

$$\frac{du_p}{dt} = \frac{1}{\tau}(u_f - u_p) + g \left(\frac{\rho_p - \rho_f}{\rho_p} \right) + F_{vm} + F_{pg} + F_{sl} \quad 2-36$$

The first term in the right hand of the equation of particles motion $\frac{1}{\tau}(u_f - u_p)$ represents the drag force, which is caused by the relative motion between a particle and a viscous fluid (Maniero and Canu 2006).

$u_p = \frac{dx_p}{dt}$ is the particle velocity in x-direction, $\tau = \frac{\rho_p d_p^2}{18\mu_f f}$ is the particle response time.

$$f = \frac{C_D \text{Re}_p}{24} \quad 2-37$$

Re_p is the relative particle Reynolds number given by:

$$\text{Re}_p = \frac{\rho_f d_p |u_p - u_f|}{\mu_f} \quad 2-38$$

C_D is the drag coefficient provided by

$$C_D = a_1 + \frac{a_2}{\text{Re}_p} + \frac{a_3}{\text{Re}_p^2}$$

Where a_1 , a_2 , a_3 are the coefficients given by Morsi and Alexander (Morsi and Alexander 1972) for smooth spherical particles over several ranges of Re_p (Badr *et al.* 2002). Other correlations for calculating drag coefficient are given by K. Hayashi and A. Tomiyama (Hayashi and Tomiyama 2009).

F_{vm} is the virtual mass force, which is the force required to accelerate fluid surrounding the particle; it can be calculated from the following equation (Mazur *et al.* 2004) :

$$F_{vm} = 1/2 \frac{\rho}{\rho_p} \frac{d}{dt} (u - u_p) \quad 2-40$$

F_{pg} is a force accounting for the effect of pressure gradient on particle motion given by:

$$F_{pg} = \frac{\rho}{\rho_s} u_p \frac{\partial u}{\partial x} \quad 2-41$$

F_{sl} is the Siffman lift force which occurs when particles are travelling across a velocity gradient such that different velocities occur on opposite sides of the particle (Maniero and Canu 2006).

2.6.2.3.4 Erosion rate calculation

By the end of the third step (particle trajectory), the velocity and angle of impingement of every particle is acquired. These values are then substituted in a selected erosion rate prediction model to calculate the erosion rate of every particle at any node.

The erosion simulation using the CFD method stated above is usually carried on using commercial software that are used for application in many CFD processes such as aerospace, multiphase flow etc. Mastering of the CFD software is essential for

application to erosion simulation. In addition, the CFD software is expensive, need computers with high specifications, and the simulation takes long time. All these limitations necessitate alternative computational tools for quick prediction of erosion rate with acceptable accuracy.

2.7 Summary

In this chapter the literature of the topics that are relevant to erosion and corrosion are reviewed. The review covers the literature related to sand production from oil and gas reservoirs. The main techniques used to prevent sand production, which include Sand control and management, have been reviewed. Literature related to flow of fluid/sand slurries in pipes including the slurry classification regimes has been covered. Thorough review of erosion and corrosion processes, including erosion and corrosion testing, and the methods of erosion predictions and simulations, has been given in details.

Chapter 3

THEORY AND RESEARCH METHODOLOGY

3.1 Introduction

Erosion and corrosion rates can be measured via means of either erosion/corrosion monitoring of the field process, or carrying out laboratory tests under simulated process conditions.

Lab scale flow loops give accurate results of erosion/corrosion rates in a petroleum production or transportation process due to its ability of simulating thermal and dynamic conditions of the flow.

The direct measurements of erosion and corrosion rate (field monitoring and laboratory tests), however, have many disadvantages such as the cost incurred due to the installation of a monitoring system or fabrication of the flow loops.

The erosion and corrosion prediction using computational models is available alternative for determination of erosion and corrosion rates. In these models, process conditions are used as input parameters in the simulation.

Many models have been published for prediction of erosion and corrosion rates in oil and gas systems, but no single model can be considered as reliable for all systems. Each model is applicable to a specific flow system depending on the fluid (liquid or gas), flow (single phase or multiphase), geometry (elbow, tee, straight pipe, or valve), and the ranges of pressure and temperature.

This research is primarily focused on developing predictive tools for sand erosion and CO₂ corrosion in petroleum production components. The tools enable calculations of pure erosion, pure corrosion, or erosion corrosion of a selected process by means of

navigating through a user-friendly graphical interface and input forms. The code also enables prediction of corrosion along a pipeline transporting fluid containing CO₂.

To validate the computational code, an erosion/corrosion flow loop has been designed and fabricated. The results of experiments carried out using the flow loop were used to validate corrosion prediction in elbows.

In addition to the measured data, selected published data from literature were used to validate the code. A CFD model has been created using the Discrete Phase Model (DPM) in Fluent software to simulate sand erosion in elbows at different conditions. The results of the CFD model were used to validate the code results for erosion rate.

The steps of developing the code and carrying the investigation is shown in

Figure 3-1.

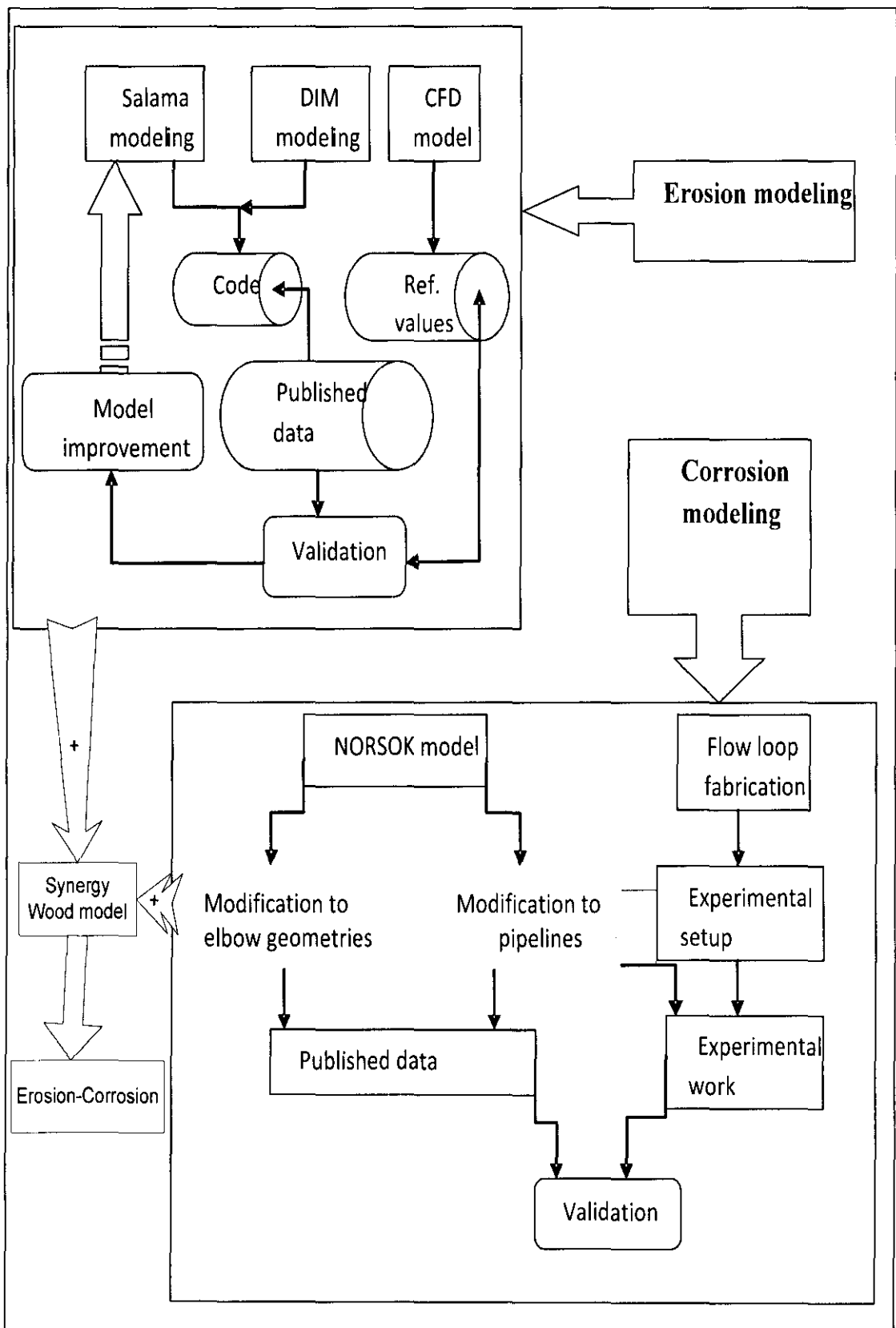


Figure 3-1: The code development and research procedure

3.2 The modeling methodology

The approach of developing the code was based on using visual basic programming language to employ selected empirical and mechanistic models for sand erosion and corrosion. Two models for sand erosion prediction and one model for CO₂ corrosion prediction were employed. The erosion prediction models are Salama model, which is an empirical model, and the direct impingement model (DIM), which is a semi-empirical model. The corrosion prediction model is the NORSOK model. Salama model (Salama 2000) assumes that the sand velocity is equal to the continuous fluid velocity. This assumption makes the model more applicable to gas flow or high gas-liquid-ratio two-phase flow. As an attempt to improve Salama model, the model results were compared with three groups of experimental data according to gas-liquid-ratio (GLR). As a result, three equations were proposed for predicting erosion rate in elbows.

The direct impingement model (DIM) from E/CRC at University of Tulsa takes into account the variation of sand velocity within a predetermined stagnation zone. Sand particles are tracked within the stagnation zone to calculate sand impingement velocity which is then used to calculate the erosion ratio (mass of material removed/mass of sand hitting the target kg/kg). The employment of the DIM model involved a numerical solution of the simplified equation of particles motion. This solution enables tracking particles and calculating the particles impingement velocity (the velocity at which sand particles hit the target). The consideration of sand velocity variation within the stagnation zone makes this model appropriate for applications in liquid and two-phase flows.

Beggs and Robinson correlations for viscosity-temperature (Arnold and Stewart 1998) were coupled to the equation of particles motion to study the temperature dependency of particles impingement velocity and erosion rate. By this, the temperature dependency of impingement velocity and erosion rate can be investigated.

For corrosion prediction, the NORSOK (NORSOK 2005) empirical model for corrosion prediction has been employed. This model is applicable to CO₂ corrosion

prediction in single phase and multiphase flows. The model was extended to application in elbows by introducing the equivalent length concept in the model. This modification allows the calculation of erosion-corrosion in elbows by coupling the modified model to Salama model. The synergic contribution to erosion corrosion has been considered by employing Wood models (Rajahram *et al.* 2009).

NORSOK model was also coupled to thermal/hydraulic equations to apply it for predicting corrosion rate along pipelines with varying temperature.

The code was developed as a software package given the name Sand Erosion and Corrosion Software (SECS). The SECS is easy to use and can be installed and run in any computer. Table 3-1 shows comparison between the SECS and CFD when applied for erosion prediction.

Table 3-1: Comparison between the SECS package and CFD model

	SECS package	CFD model
Accessibility	Can be installed in any computer	Need a license (cost)
Level of difficulty	Easy	Difficult
Application	Wide span of conditions	Wide span of conditions
Speed	Very fast	Slow (cost)
Output	The overall sand erosion and corrosion rates	Sand tracking, erosion rate distribution (axial path)
Accuracy	Validated for elbow and tee	Validated for different geometries

3.3 Sand Erosion Models

In this work, two models are used for sand erosion prediction. These two models are selected in order to make the developed software applicable to a wide span of fluids, geometries, and materials. Salama model is simple and requires fewer input data than the direct impingement model. It is not applicable to liquid flow because no account is taken to particles trajectory along the flowstreams. In addition to its consideration of particles motion, the direct impingement model furthermore accounts for the particle shape (angularity) and target material hardness. Therefore, by combining of the two models in one package the suitable model can be chosen according to the available data, the flow medium, and the desired output.

The package, however, is associated with some shortcomings including the followings:

- 1- Both of the two models employed to the package predict the overall erosion rate of the component and no distribution of the erosion rates on the surface of target material are obtained. The critical points susceptible to high erosion rate couldn't, therefore, be identified.
- 2- No flow solution is performed and flow velocity is assumed to be the same on the entire surface.
- 3- In reality, not all sand particles impinge the target material and even the particle impinge the target material does not impinge in the same angle. The developed package cannot determine the angle of impingement.
- 4- For simplifying the solution of the equation of particle motion, fluid velocity is assumed to be varied linearly within the stagnation zone.

The details of the two models are as follows:

3.3.1.1 Salama empirical model

This model is comparably simple and only predicts the overall erosion rate (no distribution is obtained along the flow stream) in elbows and tees. The Salama correlation used to develop the package is given in 2.6.2.1.

For two-phase flow, the mixture density can be calculated using the following equation:

$$\rho_m = \frac{\rho_g V_g + \rho_l V_l}{V_g + V_l} \quad 3-1$$

Where, V_g and V_l are the volume fraction of gas and liquid in the mixture.

The flow chart for calculation procedure using Salama model is shown in Figure 3-2.

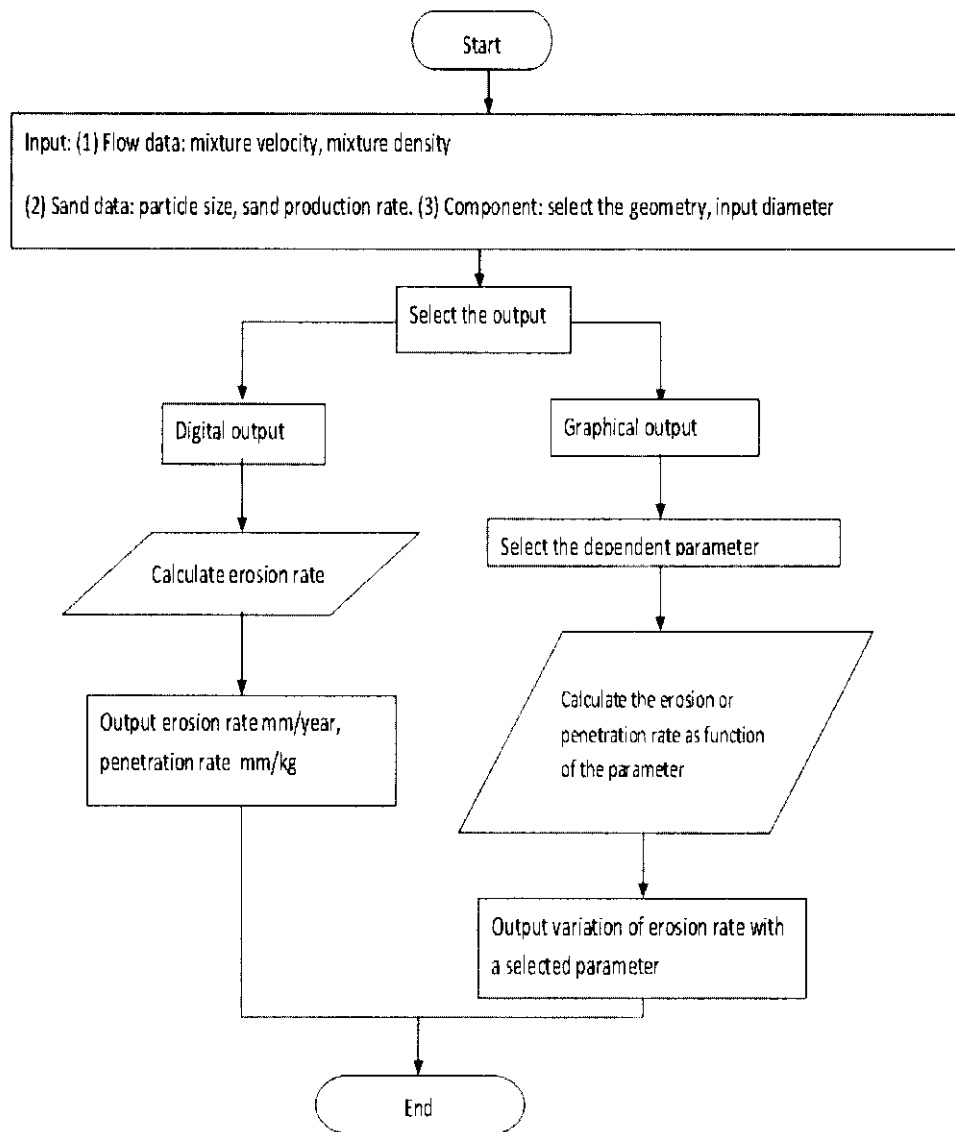


Figure 3-2: Flow chart for calculation procedure for Salama model

3.3.1.2 The Direct Impingement Model

The direct impingement model relates the erosion rate in common fittings such as elbows and tees to erosion rate occurring in direct (normal) impingement (McLaury 1996). A particle must firstly penetrate a so-called stagnation zone before it impinges the target wall. The stagnation zones for elbow and tee are shown in Figure 3-3.

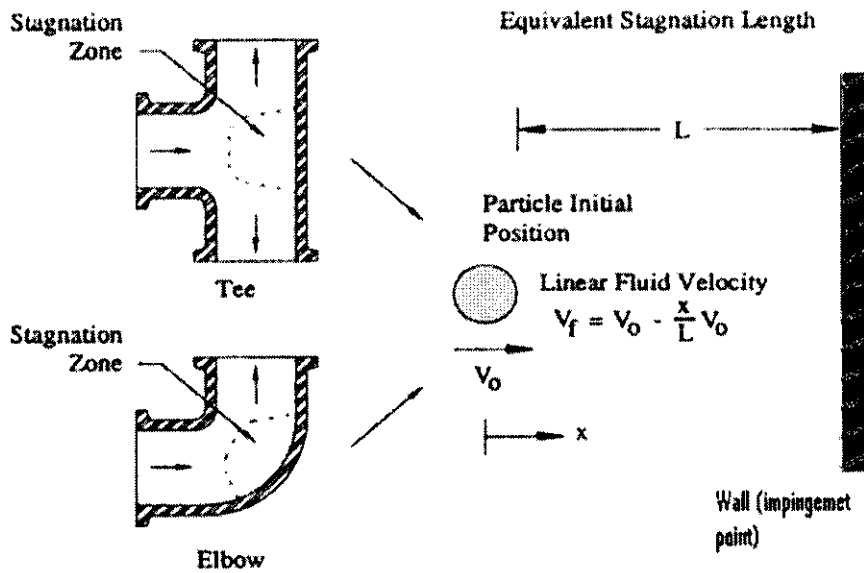


Figure 3-3: Stagnation zones in elbow and tee (McLaury 1996)

In the stagnation zone, the behavior of particle is strongly dependent on the geometry, and the properties of fluids and particles. The stagnation length value of an elbow or tee can be determined graphically using Figure 3-4.

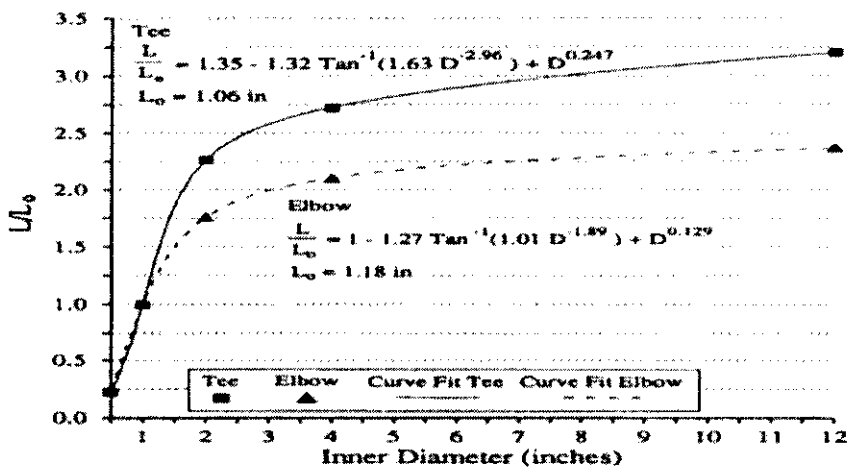


Figure 3-4: The stagnation length of elbow and tee vs. pipe diameter (McLaury 1996)

Alternatively, equations 3-3 and 3-4, which resulted from fitting of the curves of Figure 3-4 can be used to calculate the stagnation zone length.

For elbow:

$$\frac{L}{39.37L_0} = 1 - 1.27 \tan^{-1}(1.01D^{-1.89}) + D^{0.129}$$

3-2

$$L_0 = 0.029972 \text{ m}$$

For Tee

$$\frac{L}{39.37L_0} = 1.35 - 1.32 \tan^{-1}(1.01D^{-2.96}) + D^{0.247} \quad 3-3$$

$$L_0 = 0.02692 \text{ n}$$

Where, D is the pipe internal diameter in inch and L_0 the shape factor.

A simplified particle tracking model is used to determine the impingement velocity V_L . The simplified particle tracking model has the following four assumptions:

- 1: A linear velocity variation of the particle in direction of flow.
- 2: One-dimensional particle flow.
- 3: The initial values of the fluid and particle flow stream velocities are equal.
- 4: Only the drag force on the particle is considered, and the drag coefficient is defined from the following equation:

$$C_D = 0.5 + \frac{24}{\text{Re}_T} \quad 3-4$$

Where C_D is the drag coefficient and Re_T is the Reynolds number defined by the following equation:

$$\text{Re}_T = \frac{\rho_f |V_f - V_p| d_p}{\mu_f} \quad 3-5$$

By applying the assumptions above, the simplified equation of particle motion can be written as follows:

$$\frac{dV_p}{dx} = 0.75 \left(\frac{1}{d_p} \right) \left(\frac{\rho_f}{\rho_p} \right) \left[\frac{0.5(V_f - V_p)|V_f - V_p|}{V_p} + \frac{24\mu_f(V_f - V_p)}{V_p \rho_f d_p} \right] \quad 3-6$$

From the equation of particle motion, the following three dimensionless parameters can be identified:

$$\text{Dimensionless impact velocity} = \frac{V_L}{V_0} \quad 3-7$$

Particle Reynolds number

$$\text{Re}_o = \frac{V_0 d_p \rho_f}{\mu_f} \quad 3-8$$

The dimensionless parameter, ϕ , is related to the ratio of the mass of fluid displaced by the particles to the mass of the particles.

$$\phi = \left(\frac{L}{d_p} \right) \left(\frac{\rho_f}{\rho_p} \right) \quad 3-9$$

Figure 3-5 represents the relationship between the dimensionless impact velocity and the mass ratio for different Reynolds numbers.

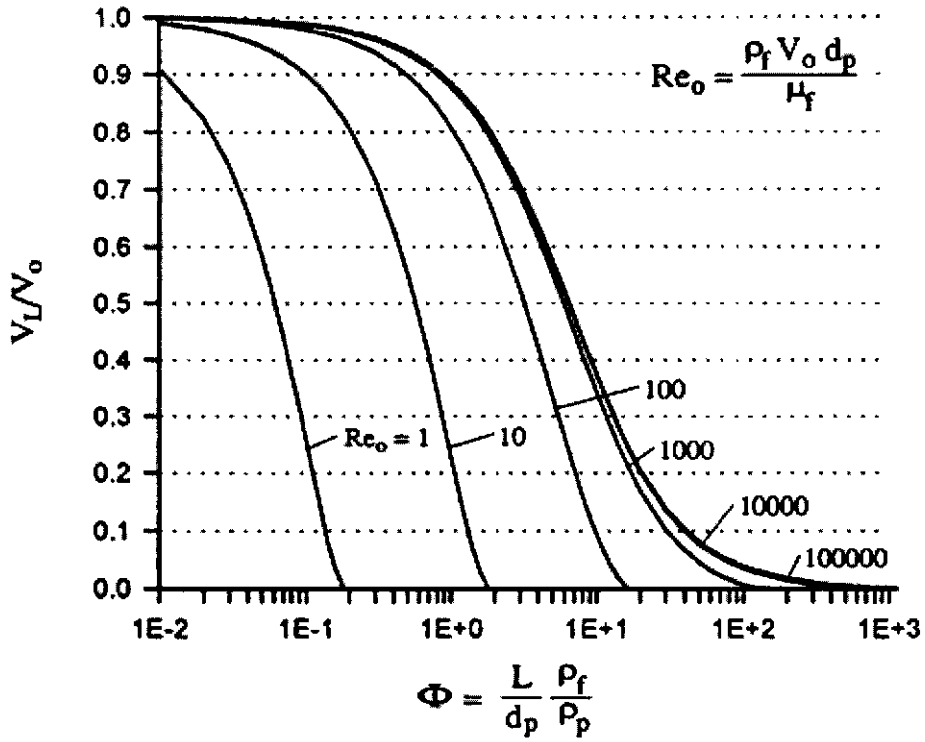


Figure 3-5: Variation of dimensionless impact velocity with the mass ratio for different particle Reynolds numbers (McLaury 1996)

The particle impact velocity V_L can be determined using Figure 3-5 after calculating the dimensionless mass ratio and Reynolds number.

In this work, the simplified equation of particles motion (equation 3-6) has been solved numerically

$$\text{Assume } \frac{V_p}{V_0} = VA \text{ and } \frac{V_f}{V_0} = 1 - \frac{x}{L} = 1 - X$$

Then, equation 3-7 can be written as follows:

$$\frac{dV_p}{dx} = \frac{0.75\phi(1 - X - VA)}{V_A} \left[0.5(1 - X - VA) + \frac{24}{Re} \right] \quad 3-10$$

The solution is then performed following the algorithm shown in

Figure 3-6. Re and ϕ in the algorithm are calculated using equations 3-8 and 3-9, respectively.

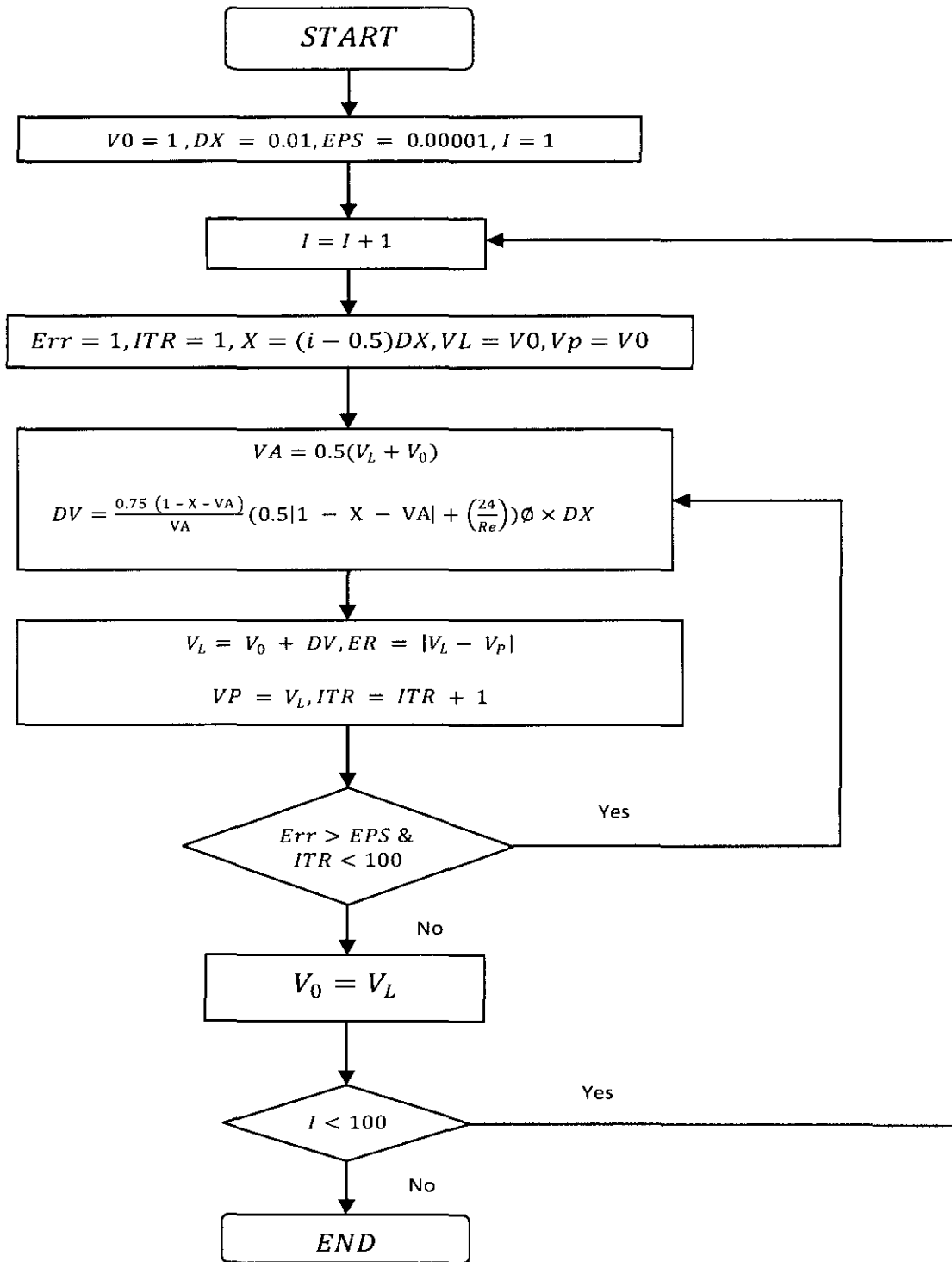


Figure 3-6: Algorithm of numerical solution for the equation of particles motion

The particle impact velocity is then used to calculate sand erosion rate using any erosion rate calculation model. Equation 3-11 is an example of the erosion rate model, which has been developed by E/CRC at U. of Tulsa Mclaury (McLaury and Shirazi 1999). The constant 4.687×10^6 is due to conversion of the units of erosion rate from m/s to mm/year and diameter from inch to mm.

$$ER = 4.687 \times 10^6 F_M F_s F_p F_{r/D} \frac{WV_i^{1.73}}{D^2} \quad 3-11$$

Where: ER = The erosion rate in mm/year.

D = The pipe diameter mm.

W = Sand production rate kg/s.

F_s = Shape factor

F_p = Empirical factor for material penetration

$F_{r/D}$ = Penetration factor for elbow radius

F_M = Empirical factor for material.

For steel pipe F_M can be calculated from the following formula:

$$F_M = \frac{1.95 \times 10^{-5}}{B^{-0.59}} \quad 3-12$$

F_M for other materials can be determined fromn Table 3-2.

F_s and F_p can be determined from Table 3-3 and Table 3-4, respectively.

Table 3-2: Material factors F_M of some material (McLaury, 1996)

Material type	Yield strength, Ksi	Tensile strength, Ksi	Brinell hardness, B	Material factor x106 (V=ft/s)	Material factor x106 (V=m/s)
CS AISI 1018	90	99.5	210	0.833	1.066
13 Cr annealed	61	105	190	1.267	1.622
13 Cr heat treated	77	93	180	1.089	1.394
13 Cr 5 Ni Duplex	74	111	217	0.788	1.009
316 SS	35	85	183	0.918	1.175
Incoloy 825	37	91	160	0.877	1.123

Table 3-3: The sharpness factor F_s for three particle shapes (McLaury, 1996)

Description	F_s
Sharp corners, Angular	1.0
Semi-rounded, rounded corners	0.53
Rounded, Spherical glass beads	0.2

Table 3-4: The penetration factor F_p (McLaury, 1996)

Shape	L_o		F_p (for steel)	
	mm	Inch	Mm/kg	In/lb
90° Elbow	30	1.18	206	3.68
Tee	27	1.06	206	3.68

$F_{r/D}$, the penetration factor for elbow radius can be calculated from Wang equation as follows (Wang *et al.* 1996):

$$F_{r/D} = \exp \left[- \left[\frac{0.1 \rho_f^{0.4} \mu_f^{0.65}}{d_p^{0.3}} + 0.015 \rho_f^{0.25} + 0.12 \right] \left(\frac{r}{D} - C_{std} \right) \right] \quad 3-13$$

Where C_{std} is r/D of standard elbow (assumed to be 1.5) (McLaury and Shirazi 1999).

For two-phase flow, the mixture density and viscosity can be pre-calculated using the following equations:

$$\rho_m = \frac{\rho_g V_g + \rho_l V_l}{V_g + V_l} \quad 3-14$$

$$\mu_m = \frac{\mu_g \mu_l}{X_g \mu_l + (1 - X_g) \mu_g} \quad 3-15$$

In this work we proposed a procedure to study temperature dependency of sand erosion and particle velocity. An ad hoc equation is used to predict particle velocity and erosion rate with respect to temperature instead of viscosity. This improvement eases erosion rate prediction in process with temperature fluctuation.

During production and transportation of crude oils, the rheological properties of the crude are highly affected by temperature. Since particle velocity depends on the Reynolds number of the particle, which in turn is a function of the fluid viscosity, the particle velocity at any temperature is proposed to be predicted based on the particle Reynolds number at that particular temperature. The Reynolds number of particles at any temperature T can be calculated using the following formula (the effect of temperature on density is neglected):

$$\text{Re}_o(T) = \frac{V_o d_p \rho_f}{\mu_f(T)} \quad 3-16$$

The viscosity at the temperature T can be calculated using Beggs and Robinson correlations (Arnold and Stewartt 1998) as follows:

$$\mu(T) = 10^{y \left(\frac{9T+160}{5} \right)^{-1.165}} - 1 \quad 3-17$$

Where

$$y = 10^{3.0324 - 0.02023G} \quad 3-18$$

$\mu(T)$ is the viscosity (cp) at temperature T ($^{\circ}\text{C}$).

G is the API gravity, which is given by

$$G = \frac{141.5 - 131.5SG}{SG} \quad 3-19$$

SG is the specific gravity of crude oil.

It is worth pointing out that the above procedure should only be applied to oil flow when no available data about viscosity or there is a significant fluctuation in temperature.

3.3.1.3 Particle tracking using fluent software

The commercial software package Fluent 6.0 is used to simulate erosion rate in an elbow. A model is built and meshed in Gambit software, and then transferred to Fluent for the simulation. The simulation steps discussed previously in chapter 2 will be followed. The continuous phase flow (velocity and pressure) will firstly be solved using Navier-Stokes equations and $k - \varepsilon$ turbulence model. The discrete phase model (DPM) in Fluent will be used to track the particles and to simulate the erosion rate.

Discrete phase model in Fluent is a Lagrangian-based model simulating two phase flow, which consists of a fluid as a continuous phase and spherical particles or droplets as a secondary phase. This model allows trajectories of the secondary phase, as well as calculating mass and heat transfer to and from it. The coupling of the phases can also be included. Many options are provided by the application of DPM such as the discrete phase trajectory using the Lagrangian equation, turbulent effects prediction, and heat/mass transfer prediction.

Trajectory calculations

The discrete phase (particles/droplets) trajectory is performed by applying Lagrangian method, which integrates the particle force balance equation (equation 3-20).

$$\frac{du_p}{dt} = F_D(u - u_p) + \frac{g_x(\rho_p - \rho_f)}{\rho_p} + F_x \quad 3-20$$

The first term on the right-hand of equation 3-21 is the drag force per unit of particle mass and

$$F_D = \frac{18\mu}{\rho_p d_p^2} \frac{C_D \text{Re}}{24} \quad 3-21$$

Re is the relative Reynolds number which is defined as follows:

$$\text{Re} = \frac{\rho d_p |u_p - u|}{\mu} \quad 3-22$$

C_D is the drag coefficient, which can be calculated by one of the following equations (equation 3-23 or equation 3-24).

$$C_D = a_1 + \frac{a_2}{\text{Re}} + \frac{a_3}{\text{Re}^2} \quad 3-23$$

Where a_1 , a_2 , and a_3 are constants.

$$C_D = \frac{24}{Re}(1 + b_1 Re^{b_2}) + \frac{b_3 Re}{b_4 + Re} \quad 3-24$$

Where,

$$\begin{aligned} b_1 &= \exp(2.3288 - 6.4581\phi + 2.4486\phi^2) \\ b_2 &= 0.0964 + 0.5565\phi \\ b_3 &= \exp(4.905 - 13.8944\phi + 18.4222\phi^2 - 10.2599\phi^3) \\ b_4 &= \exp(1.4681 + 12.2584\phi - 20.7322\phi^2 + 15.8855\phi^3) \end{aligned} \quad 3-25$$

$$\phi = \frac{s}{S}$$

s is the surface area of sphere having the same volume as the particle, and S is the actual surface area of the particle.

The second term on the right-hand of equation 3-20 is the gravity force on the particles; the default value in Fluent is zero.

The third term on the right-hand of equation 3-20 (F_x) is additional forces that can be considered under special conditions. These additional forces include virtual mass forces, rotating reference frame forces, thermophoretic forces, Brownian forces and Saffman's lift forces. Selected models for calculations of these forces are included in FLUENT software and described in its help manual.

3.4 Corrosion and Erosion-Corrosion Models

NORSK standard CO₂ corrosion model is proposed for this work. The model was developed by the Norwegian petroleum industry for calculation of corrosion rate due to CO₂ existence in hydrocarbon production and process systems.

The model that calculates corrosion rate in mm/year, consists of three empirical equations. The first equation is a general equation for calculating CO₂ corrosion rate for temperatures between 20 and 150 °C . The second and third equations are for

calculating CO₂ corrosion rate at 15 °C and 5 °C, respectively. The three equations can be combined as follows (NORSOK 2005) :

$$R_c = \begin{cases} k_t \times f_{CO_2}^{0.62} \times \left(\frac{S}{19}\right)^{0.146+0.0324\log(f_{CO_2})} \times f(pH)_t & 20^\circ C \leq T \leq 150^\circ C \\ k_t \times f_{CO_2}^{0.36} \times \left(\frac{S}{19}\right)^{0.146+0.0324\log(f_{CO_2})} \times f(pH)_t & T = 15^\circ C \\ k_t \times f_{CO_2}^{0.36} \times f(pH)_t & T = 5^\circ C \end{cases} \quad 3-26$$

k_t is a temperature-dependent constant given in Table 3-5.

Table 3-5: Values of k_t at different temperatures (NORSOK 2005)

Temperature °C	k_t
5	0.42
15	1.59
20	4.762
40	8.927
60	10.695
80	9.949
90	6.250
120	7.770
150	5.203

$f(pH)_t$ is the effect of pH at temperature T given in Table 3-6.

Table 3-6: $f(pH)$, at different temperatures and pH values (NORSOK 2005)

Temperature °C	pH	$f(pH)$
5	$3.5 \leq pH \leq 4.6$	$f(pH) = 2.0676 - 0.2309pH$
	$4.6 \leq pH \leq 6.5$	$f(pH) = 4.342 - 1.051pH + 0.0708pH^2$
15	$3.5 \leq pH \leq 4.6$	$f(pH) = 2.0676 - 0.2309pH$
	$4.6 \leq pH \leq 6.5$	$f(pH) = 4.986 - 1.191pH + 0.0708pH^2$
20	$3.5 \leq pH \leq 4.6$	$f(pH) = 2.0676 - 0.2309pH$
	$4.6 \leq pH \leq 6.5$	$f(pH) = 5.1885 - 1.2353pH + 0.0708pH^2$
40	$3.5 \leq pH \leq 4.6$	$f(pH) = 2.0676 - 0.2309pH$
	$4.6 \leq pH \leq 6.5$	$f(pH) = 4.986 - 1.191pH + 0.0708pH^2$
60	$3.5 \leq pH \leq 4.6$	$f(pH) = 1.836 - 0.1818pH$
	$4.6 \leq pH \leq 6.5$	$f(pH) = 15.444 - 6.1291pH + 0.8204pH^2$
80	$3.5 \leq pH \leq 4.6$	$f(pH) = 2.6727 - 0.3636pH$
	$4.6 \leq pH \leq 6.5$	$f(pH) = 331.68e^{-1.2618pH}$
90	$3.5 \leq pH \leq 4.57$	$f(pH) = 3.1355 - 0.4673pH$
	$4.57 \leq pH \leq 5.62$	$f(pH) = 21254e^{-2.1811pH}$
	$5.62 \leq pH \leq 6.5$	$f(pH) = 0.4014 - 0.0538pH$
120	$3.5 \leq pH \leq 4.3$	$f(pH) = 1.5375 - 0.125pH$
	$4.3 \leq pH \leq 5$	$f(pH) = 5.9757 - 1.157pH$
	$5 \leq pH \leq 6.5$	$f(pH) = 0.546125 - 0.071225pH$
150	$3.5 \leq pH \leq 3.8$	$f(pH) = 1$
	$3.8 \leq pH \leq 5$	$f(pH) = 17.634 - 7.0945pH + 0.715pH^2$
	$5 \leq pH \leq 6.5$	$f(pH) = 0.037$

f_{CO_2} is the fugacity of CO₂ calculated from the following equation:

$$f_{CO_2} = a \times P_{CO_2} \quad 3-27$$

Where P_{CO_2} is the partial pressure of CO_2 and a is the fugacity coefficient given by:

$$a = 10^{P(0.0031-1.4/T)} \quad 3-28$$

And the value of P is taken as 250 bar for pressures greater than 250 bar.

3.4.1.1 Adoption of NORSOK model to predict corrosion and erosion-corrosion in elbow

We consider a simultaneous erosive/corrosive process in an elbow. The erosive material is sand particles with different sizes, and the corrosive material is CO_2 gas supplied continuously to the process.

In this research, a model of predicting erosion-corrosion in elbows has been developed by using the Salama model for erosion rate calculation and NORSOK model for corrosion rate calculation.

To combine the NORSOK model with Salama model, it has been firstly modified to make it applicable to elbows geometry. The modification has been done by introducing the equivalent length concept to wall shear stress. The straight pipe wall shear stress is thereby converted to elbow wall shear stress which is substituted in the NORSOK model.

The wall shear stress of straight pipe is related to the friction pressure drop as follows:

$$S_p = \frac{D\Delta P_f}{4L} \quad 3-29$$

To make the above equation applicable for elbow, the friction pressure drop of the elbow can be substituted as follows:

$$\Delta P_{fel} = 4 f_p \frac{L_{eq}}{D} \rho \frac{V_m^2}{2} \quad 3-30$$

Where ΔP_{fel} is the friction pressure loss in elbow, f_p is the friction factor of straight pipe, and L_{eq} is the equivalent length of the elbow.

Accordingly, the geometry is firstly converted from an elbow to a straight pipe by using equivalent length.

The wall shear stress of a straight pipe S_p can be calculated using the following equation:

$$S_p = \frac{f_p \rho V_m^2}{2} \quad 3-31$$

Equation 3-31 can be re-written as follows:

$$\Delta P_{fel} = 4 f_p \frac{L_{eq}}{D} \rho \frac{V_m^2}{2} = 4 \frac{L_{act}}{D} S_{el} \quad 3-32$$

Where L_{act} is the actual length of the elbow and S_{el} is the average wall shear stress of the elbow, which can be related to the elbow friction factor as follows:

$$S_{el} = \frac{f_{el} \rho V_m^2}{2} \quad 3-33$$

From equation 3-33, the elbow average wall shear stress can be related to the straight pipe friction factor as follows:

$$S_{el} = \frac{4}{8} \left[\frac{f_p L_{eq}}{L_{act}} \right] \rho V_m^2 \quad 3-34$$

By equating equation 3-33 and equation 3-34, a relationship between the friction factor of straight pipe and elbow can be established as follows:

$$f_{el} = f_p \frac{L_{eq}}{L_{act}} \quad 3-35$$

The actual length of the elbow can be obtained from published standards or manufacturers documents. ASME B16.11 and B16.9 are examples of reliable published standards for elbow dimensions. Table 3-7 contains approximated actual length values of 45 deg long radius elbows obtained from ASME B16.9.

The equivalent length of elbows can be obtained from tables or empirical relationship.

Table 3-8 shows equivalent length of different fittings. W. Trimmer and H. Hassan (Trimmer and Hassan 1997) had proposed a rule for estimating the equivalent length (in feet) of the 90 deg elbow as the multiplication of the elbow diameter (in inch) by 2.5. Using this relationship, the ratio between the friction factors of elbows and straight pipes (using equation 3-36) for different diameters can be obtained as shown in Table 3-9.

Michael Swidzinski et al. (Swidzinski *et al.* 2000) established a relationship between the straight pipe shear stress and the elbow shear stress through numerous laboratory tests. They stated that, straight pipe shear stress can be converted to elbow shear stress by multiplying it by three.

By comparing Michael Swidzinski et al. model with the results in Table 3-9, it can be concluded that their proposal is not acceptable. Table 3-9 indicates that the straight pipe wall shear stress should be multiplied by 10 in order to convert it to elbow average wall shear stress.

Then, the modified NORSOK model for CO₂ corrosion prediction in straight pipes (equation 3-26) can be re-written for elbows as follows:

$$R_c = \begin{cases} k_t \times f_{CO_2}^{0.62} \times (0.5263 \times S)^{0.146+0.0324 \log(f_{CO_2})} \times f(pH)_t, & 20^\circ C \leq T \leq 150^\circ C \\ k_t \times f_{CO_2}^{0.36} \times (0.5263 \times S)^{0.146+0.0324 \log(f_{CO_2})} \times f(pH)_t, & T = 15^\circ C \\ k_t \times f_{CO_2}^{0.62} \times f(pH)_t, & T = 5^\circ C \end{cases} \quad 3-36$$

Table 3-7: Actual length of 45° long radius elbows with different diameters

Pipe diameter (mm)	Actual length (mm)
50	70
75	102
100	128
125	158
150	190
200	254
250	318
300	380
350	444
400	508
450	572
500	636

Table 3-8: Equivalent length of some fittings

Fittings		Nominal pipe size (mm)												
		12.5	18.75	25	31.25	37.5	50	62.5	75	100	150	200	250	275
Elb. Leq (m)	SR 90°	0.9	1.2	1.6	2.1	2.4	3.1	3.6	4.4	5.9	7.3	8.9	12	14
	LR 90°	1.1	1.3	1.6	2	2.3	2.7	2.9	3.4	4.2	5.	5.7	7	8
	LR 45°	0.5	0.6	0.8	1.1	1.3	1.7	2	2.6	3.5	4.5	5.6	7.7	9

Table 3-9: The ratio of equivalent length to actual length (90 Deg elbow)

Pipe diameter (mm)	Actual length (mm)	Equivalent length (mm)	$\frac{L_{eq}}{L_{act}}$
50	152	1524	10.026
75	228	2287	10.03
100	304	3049	10.03
150	458	4573	9.985
200	610	6098	10
250	762	7622	10

By integrating the modified NORSOK model with Salama model, the erosion-corrosion model for the temperature range 20 to 150 °C can be written for elbows as follows:

$$R_{EC} = \frac{1}{S_m} \frac{WV_m^2 d}{D^2 \rho_m} + k_t \times f_{CO_2}^{0.62} \times (0.5263 \times S)^{0.146 + 0.0324 \log(f_{CO_2})} \times f(pH)_t + EC_s \quad 3-37$$

EC_s is the wear rate due to synergy effect.

For slurry erosion, Wood et al ((Wood and Hutton 1990), (Wood 1992)) proposed two empirical models for predicting the wear due to synergic effect in medium and high synergy group. The models are as follows (Rajahram *et al.* 2009):

For medium synergy group:

$$EC_s = Exp \left[1.277 \ln \left(\frac{ER}{R_c} \right) - 1.9125 \right] R_c \quad 3-38$$

For high synergy group:

$$EC_s = Exp \left[0.755 \ln \left(\frac{ER}{R_c} \right) + 1.222 \right] R_c \quad 3-39$$

To calculate the friction factor, f , the flow regime should first be classified according to the Reynolds number (Re), which can be calculated using the following formula:

$$Re = \frac{\rho_m V_m D}{\mu_m} \quad 3-40$$

For laminar flow ($Re \leq 2000$), friction factor is calculated using the formula:

$$f = \frac{16}{Re} \quad 3-41$$

For turbulent flow ($Re > 2000$), Churchill (Churchill 1977) model is explicit in f and valid for both smooth and rough pipes. The model is written as follows:

$$f = 2 \left[\left(\frac{8}{Re} \right)^{12} + (A + B)^{-1.5} \right]^{1/12} \quad 3-42$$

Where,

$$A = \left[2.457 \ln \left(\frac{1}{C} \right) \right]^{16}$$

$$B = \left(\frac{37530}{\text{Re}} \right)^{16} \quad 3-43$$

$$C = \left(\frac{7}{\text{Re}} \right)^{0.9} + 0.27 \frac{e}{D}$$

e is the pipe roughness and D is the internal diameter.

3.4.1.2 Modifying NORSOK model to predict corrosion rate along pipelines

During oil transportation, temperature gradually decreases from the inlet temperature (at inlet) due to heat transfer from the heated oil to the surroundings. In pipelines where no intermediate heating stations are installed, the temperature will eventually decline to the surrounding temperature some kilometers after the inlet point depending on many factors such as the surrounding temperature, the overall heat transfer coefficient, velocity, and fluid heat capacity. The temperature at distance L along the pipeline can be calculated using the following equation (Huang and Chong 1995):

$$T_L = \left(T_o + \frac{giG}{k_{tot}\pi D} \right) + \left(T_i - \left(T_o + \frac{giG}{k_{tot}\pi D} \right) \right) e^{-\frac{k_{tot}\pi D}{Gc} L} \quad 3-44$$

For pipelines with short length, small diameter, low flow rate, and high temperature difference between fluid and environment; heat generation due to friction can be neglected, and hence, equation 3-44 can be simplified as follows:

$$T_L = T_o + (T_i - T_o) e^{-\frac{k_{tot}\pi D}{Gc} L} \quad 3-45$$

Where

T_i =The inlet temperature, °C.

T_o =The surrounding temperature, °C.

k_{tot} =The overall heat transfer coefficient, $W/m^2 \cdot ^\circ C$. s (a function of the fluid film heat transfer coefficient, and the pipe and coating heat conduction factor).

C =The heat capacity of the fluid, $W/kg \cdot ^\circ C$.

$G = \frac{\pi}{4} D^2 V \rho_f$ is the mass flow rate of the fluid, kg/s .

ρ_f =Fluid density, kg/m^3 .

V =Fluid velocity, m/s .

D =pipe diameter, m .

i =hydraulic gradient (due to friction), m/m .

Corrosion rate is a function of temperature because of the effect of temperature on k_t , $f(pH)$, and viscosity (and hence Reynolds number). Therefore different points along the pipeline are expected to corrode at different rates depending on the temperature at the specified point.

According to NORSOK model (equation (3-26)) (NORSOK 2005), CO_2 depends on four factors that in turn depend on temperature. These factors can be summarized as shown in Table 3-10.

Table 3-10: The effect of the four parameters along the pipeline

Parameter	Effect of temperature	The expected change along pipeline
K_i (temperature-dependant constant)	Increases from 5 to 60 °C and then decreases up to 150 °C (As shown in Table 3-5)	Decreases with distance if the inlet temperature is 60 °C or below. Otherwise it increases with temperature from the inlet up to the point where temperature is 60 °C and the decreases.
fCO_2 (Fugacity of CO ₂)	Decreases with temperature.	Decreases with distance due to stronger dependency on system pressure which decreases along the pipeline. $fCO_2 = a \times P_{CO_2}$ $a = 10^{P(0.0031-1.47)}$
S (Wall shear stress)	Increases with viscosity and density, which in turn decreases with temperatures.	Increases with distance.
$f(pH)_i$ (The effect of pH at any temperature)	As shown in Table 3-6	Not obvious

To calculate CO₂ corrosion rate along the pipeline, equation 3-45 is firstly used to calculate the temperature using a suitable length interval and assuming constant overall heat transfer coefficient and surrounding temperature. Tables (3-5) and (3-6) are then used to calculate k_i and $f(pH)$ along the pipeline.

To calculate fCO_2 , the total system pressure is calculated along the pipeline. If we assume a horizontal pipeline, the total pressure at the inlet should, at least, equals to all pressure losses from the inlet to the outlet. Darcy-Weisbach equation (Equation 3-51) (Huang and Chong 1995) is used to calculate friction pressure losses within every interval. The Reynolds number and friction factor in any interval are calculated using the fluid density and viscosity at the temperature at that interval.

As corrosion will only take place in the presence of water, we assume a two-phase (oil, water) system.

The density and viscosity of water at any temperature T is calculated as follows (assuming the water density at 20 °C is 998.2 kg/m³):

$$\begin{aligned} \mu_w(T) &= ((T + 273) - 225.4)^{-1.637} \\ \rho_w(T) &= \frac{998.2}{(1 + 0.0002(T - 20))} \end{aligned} \quad 3-46$$

The oil density at any temperature T is calculated as follows (Huang and Chong 1995):

$$\begin{aligned} \rho_o(T) &= \rho_{20} - \alpha(T - 20) \\ \alpha &= 1.825 - 0.001315\rho_{20} \end{aligned} \quad 3-47$$

Where ρ_{20} is the oil density at 20 °C, kg/m³.

Beggs and Robinson correlations for viscosity-temperature (Arnold and Stewartt 1998), Equations 3-18 to 3-20, are used for viscosity prediction at any temperature T.

The mixture viscosity and density at any temperature T are calculated as follows:

$$\frac{1}{\mu_m(T)} = \frac{\left(\frac{WC}{100}\right)}{\mu_w(T)} + \frac{\left(1 - \frac{WC}{100}\right)}{\mu_o(T)} \quad 3-48$$

$$\rho_m(T) = \rho_w(T) \times \frac{WC}{100} + \rho_o(T) \times \left(1 - \frac{WC}{100}\right) \quad 3-49$$

Where WC=water cut (%).

Reynolds number at any temperature T is calculated as follows:

$$Re(T) = \frac{\rho_m(T)VD}{\mu_m(T)} \quad 3-50$$

In the case of laminar flow ($Re(T) \leq 2000$) Equation 3-41 is used to calculate friction factor and in the case turbulent flow ($Re(T) > 2000$), friction factor is calculated using Churchill (Churchill 1977) (Equation 3-42).

The friction factor is introduced to the Darcy-Weisbach equation as follows (Huang and Chong 1995):

$$\Delta P_f(T) = 4f(T) \frac{\Delta L}{D} \rho_m(T) \frac{V^2}{2} \quad 3-51$$

If we divide a pipeline into N interval, then the total pressure at the inlet can be calculated as follows:

$$P_T = \sum_{i=1}^N \Delta P_f(T) \quad 3-52$$

And the pressure at the Mth interval is calculated using the following equation:

$$P_{TM} = \sum_{i=M}^N \Delta P_f(T) = P_T - \sum_{i=1}^M \Delta P_f(T) \quad 3-53$$

The wall shear stress at any temperature T is calculated using the following equation:

$$S(T) = \frac{f(T)\rho_m(T)V^2}{2} \quad 3-54$$

The calculation procedure is shown in Figure 3-7.

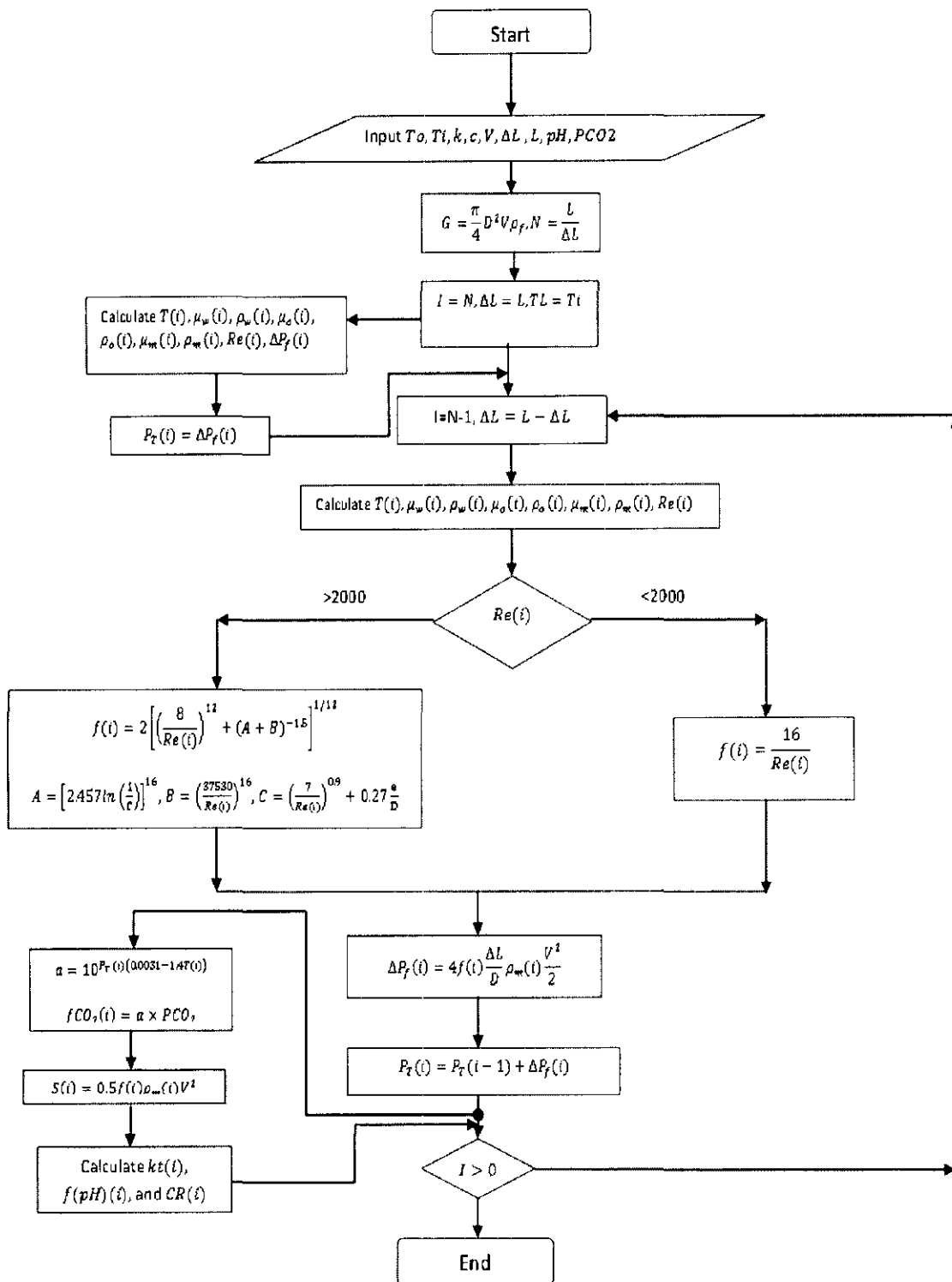


Figure 3-7: The calculation procedure for predicting corrosion rate along pipelines

3.5 Summary

This chapter summarizes the theory and methodology that have been adopted in this work for achieving the research goals. The chapter describes the two models (namely the Salama model and DIM model) employed in the computational code for erosion prediction including a proposed algorithm for numerical solution of the equation of particles motion and a proposed method for improving the equation to study temperature dependency of particles velocity and erosion rate . The discrete phase model (DPM) used for CFD erosion simulation is outlined in details. A detailed description of NORSOK model implementation to simulate CO₂ corrosion in straight pipes and the procedure followed to extend it to application to elbows and along pipelines is given.

Chapter 4

THE EXPERIMENTAL SET-UP AND MEASURING TECHNIQUES

4.1 Introduction

A lab-scale flow loop has been designed and fabricated for carrying out the erosion/corrosion experiments. The design of the flow loop has been performed using a developed computational code for predicting critical velocity, total pressure losses, and plotting the pressure profiles along the flow loop under different conditions.

This chapter describes the flow loop design and fabrication.

4.2 General description of the flow loop

Figure 4-1 and Figure 4-2 show the general layout and the real photo of the flow loop which consists of the following parts:

- 1- Mixing tank [1]: a 300-liter conical steel tank for mixing the liquid/sand slurry. The tank bottom is coned to avoid sand trapping in the bottom of the tank which may affect the mixing quality.
- 2- Pump [2]: a screw pump for pumping and circulating the slurry from and to the main tank.
- 3- Main line [3] is a 3-in PVC pipe.
- 4- Carbon steel elbow [4] for measuring pure erosion rate using weight loss.
- 5- The erosion/corrosion measurement specimen [5] is steel tee and elbow connected to each other and located downstream to the CO₂ injection point [6]. A 3" PVC pipe is branched from the tee to connect the main erosion/corrosion test section.

An ultrasonic flow meter is available for measuring flow rate. The flow meter should be calibrated before measurements.

4.3 The main test section

The main test section is an 84 mm section connected to a 40 mm section using a reducer. The 84 mm section is 500 mm length mild steel pipe divided into 4 big specimens with 90x5 mm (length X thickness) each and 5 small specimens with 10x5 (length X thickness) each. The big specimens are used for online measurement of erosion/corrosion using the potentiostat. In order to guarantee no electricity connection between the specimens, all the specimens are inserted into an acrylic pipe and separated from each other using O-rings. Every specimen is connected to the potentiostat by inserting a stainless steel bolt in a hole drilled through the acrylic pipe wall till it touches the specimen. The bolt is then connected to the working electrode wire of the potentiostat.

The 40-mm section is a 500 length mild steel pipe divided into 4 pieces 90x3 (length X thickness) each and 5 pieces 10x3 mm (length X thickness) each, inserted to an acrylic pipe and connected to the potentiostat in the same manner as previously described.

The two pipes are connected together using 80 mm length mild steel reducer. The design model of the test section is shown in Figure 4-3 and the test section after fabrication is shown in Figure 4-4.

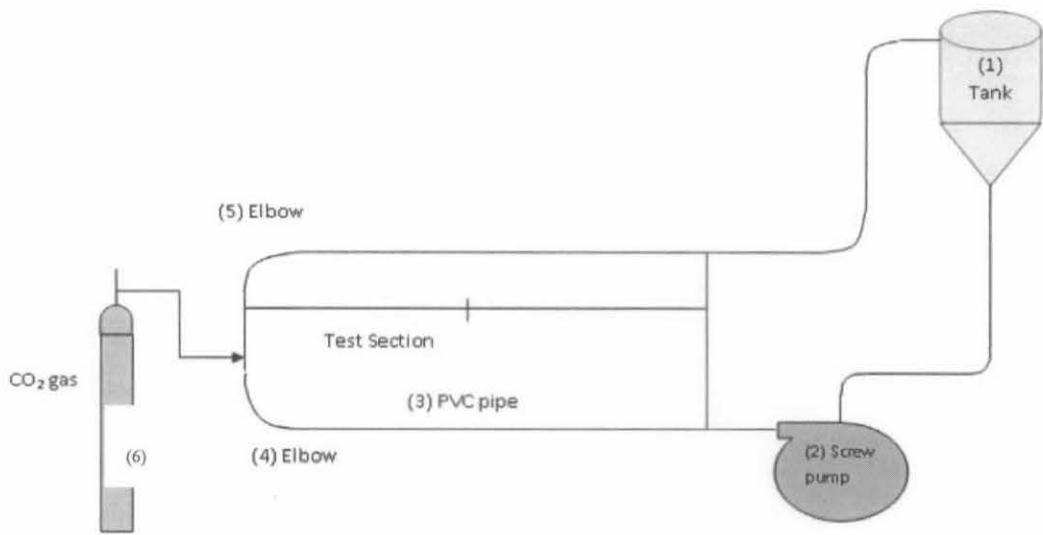


Figure 4-1: General layout of the erosion/corrosion flow loop



Figure 4-2: The flow loop

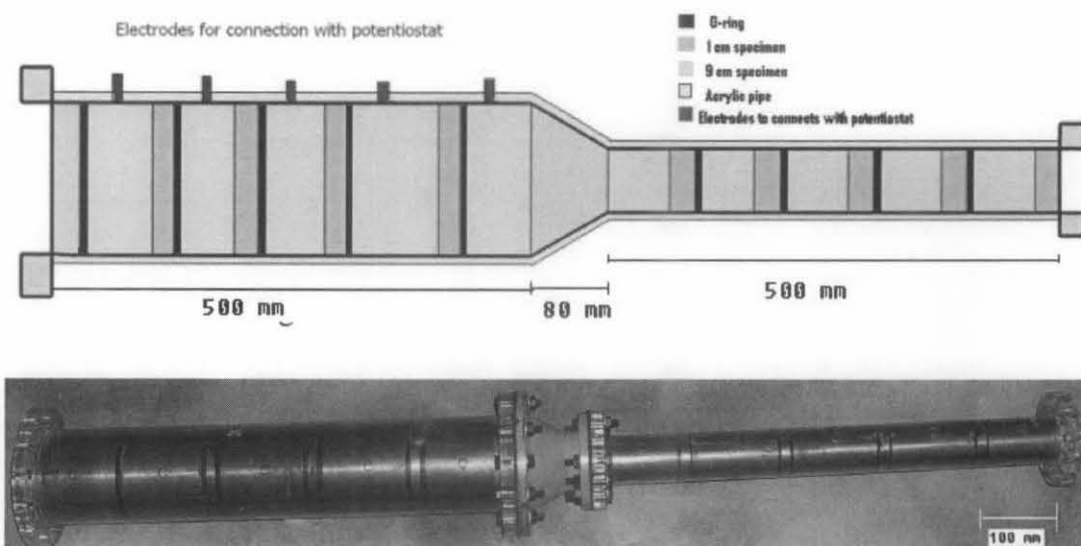


Figure 4-4: The main test section

4.4 The flow loop design

The design of the flow loop involves hydraulic calculations performed using a computational code that was developed by employing selected mathematical models described below. The flow loop was designed in accordance to the procedure in the flow chart shown in Figure 4-5.

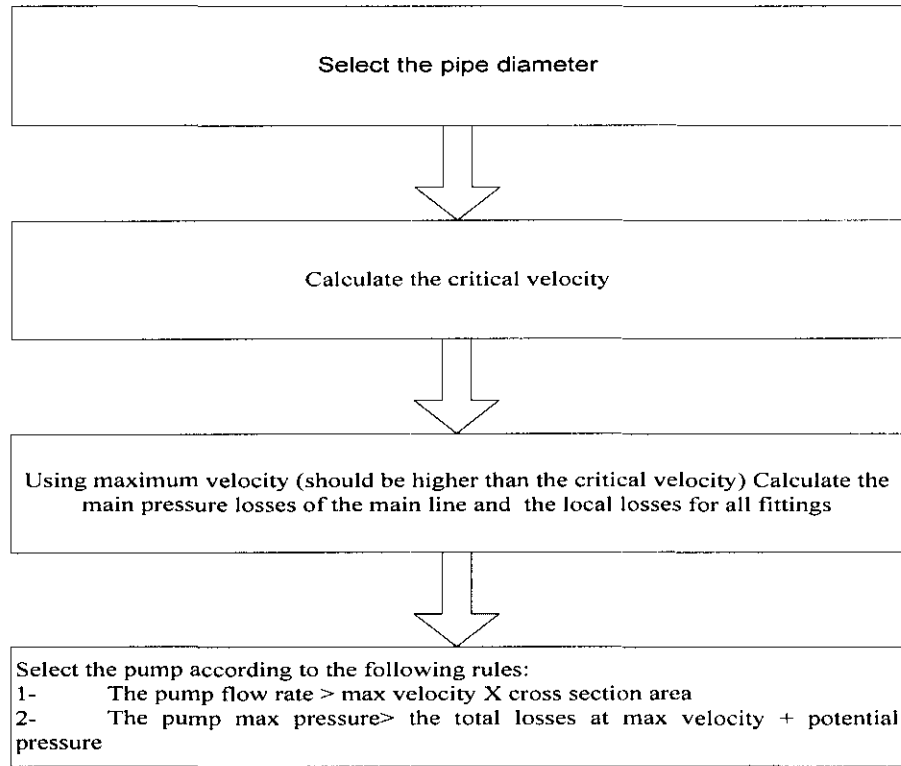


Figure 4-5: The design procedure of the flow loop

4.4.1 Critical velocity

Critical velocity is the velocity below which sand particles start to settle down on the pipe wall. The critical velocity is calculated according to Turian's empirical correlation (Turian et al. 1987) as follows

$$\frac{U_c}{[2gD(S-1)]^{0.5}} = x_1 \alpha_s^{x_2} (1 - \alpha_s)^{x_3} B \left(\frac{d_p}{D} \right)^{x_5} \quad 4-1$$

$$B = \left[\frac{D \rho_l (gD(S-1))^{0.5}}{\mu_l} \right]^{x_4}$$

Where x_1 to x_5 are constants given in the reference and S is the relative density of sand given as $S = \frac{\rho_s}{\rho_l}$.

Sand concentration α_s is expressed as volume fraction obtained by the following equation:

4-2

$$\alpha_s = \frac{Q_s}{Q_s + Q_l}$$

Where Q_s and Q_l are the volumetric flow rate of sand and liquid, respectively.

Table 4-1 shows the critical velocity for different pipe's diameters during flow of fluid with parameters shown in Table 4-2.

Table 4-1: critical velocity of different pipe's diameters

No	Pipe diameter (m)	Critical velocity (m/s)
1	0.025	1.013
2	0.05	1.37
3	0.075	1.64
4	0.1	1.86

Table 4-2: The flow parameters

Parameter	Unit	Value
Sand content	wt%	5
Mixture Viscosity	mPa.s	0.1
Liquid Density	kg/m ³	1025
Sand density	kg/m ³	2700

4.4.2 Determination of the hydraulic gradient line

For better description of the hydraulic behavior, the pressure profiles are drawn along the axial direction of the flow loop. The pressure profile is a measure of the energy (pressure) available at any point along the flow stream. In the case of a fluid flows in a pipe, this is the energy remaining after dynamics (friction and local) and potential (elevation) losses.

The mixture density is calculated using the following equation:

$$\rho_m = \rho_l(1 - \alpha_s) + \rho_s \alpha_s \quad 4-3$$

To calculate the pressure required to circulate slurry with specific properties, the flow is assumed to be homogeneous and Newtonian.

The viscosity of Newtonian slurry is generally referred to as relative viscosity and calculated using the following equation:

$$\mu_r = \frac{\mu_m}{\mu_l} \quad 4-4$$

Where, μ_m is the mixture viscosity and μ_l is the liquid viscosity.

μ_r Can be calculated using the following model (Thomas 1965)

$$\mu_r = 1 + 2.5\alpha_s + 10.05\alpha_s^2 + 0.0027\exp(\alpha_s) \quad 4-5$$

The total pressure required to circulate the slurry is calculated using the following equation:

$$\Delta P = \Delta P_f + \Delta P_{ft} + \Delta P_z \quad 4-6$$

Where ΔP_f is the main frictional pressure loss, ΔP_{fi} is the secondary frictional pressure losses (pressure losses in fittings), and ΔP_z is the pressure change due to elevation difference calculated using the following equation:

$$\Delta P_z = \rho_m g \Delta z \quad 4-7$$

The main frictional pressure loss is calculated using the following formula:

$$\Delta P_f = 4f \frac{L}{D} \rho_m \frac{V_m^2}{2} \quad 4-8$$

To calculate the friction factor, the flow regime should first be classified according to the Reynolds number (Re), which can be calculated using the following formula:

$$\text{Re} = \frac{\rho_m V_m D}{\mu_m} \quad 4-9$$

Friction factor calculations in laminar and turbulent regimes are calculated using equation 3-42 and equation 3-43, respectively.

The secondary fittings pressure losses are those arisen from tees, elbows, valves, reducers and expander, and entrance and exits.

The remaining pressure at any point i can be written mathematically as follows:

$$P_{av}(i) = P_{inlet} - \Delta P_{f(0,i)} - \sum \Delta P_{fi(0,i)} - \rho g (Z_i - Z_0) \quad 4-10$$

Where

$P_{av}(i)$ = The pressure remaining at point i, Pa.

P_{inlet} = The inlet pressure (at x=0), Pa.

$P_{f(0,i)}$ = The pressure losses due to friction between the inlet and point i, Pa.

$\sum P_{f(0,i)}$ = The local pressure losses due to all fittings between the inlet and point i, Pa.

ρ_m = Mixture density, kg/m³.

Z_i = The height of the point i, m.

Z_0 = The height of the inlet, m.

The local pressure losses in fittings can either be expressed in terms of the so-called resistance coefficient (k_f) as follows:

$$\Delta P_f = k_f \frac{\rho_m V_m^2}{2} \tag{4-11}$$

Or, it is expressed in terms of equivalent length (L_e), where:

$$\frac{L_e}{D} = \frac{k_f}{4f} \tag{4-12}$$

The equivalent length method has been followed in the flow loop design. Table 4-3 and Table 4-4 are used for PVC and steel fittings respectively (www.dultmeier.com) (www.engineeringtoolbox.com 2005).

Table 4-3: Equivalent length (ft) for PVC fittings

Fitting	Nominal pipe size (inch)												
	0.5	0.75	1	1.25	1.5	2	2.5	3	4	6	8	10	11
90° elbow	1.5	2	2.5	3.8	4	5.7	6.9	7.9	12	18	22	26	32
45° elbow	0.8	1.1	1.4	1.8	2.1	2.6	3.1	4	5.1	8	10.6	13.5	15.5
Gate valve	0.3	0.4	0.6	0.8	1	1.5	2	3					
Tee Flow run	1	1.4	1.7	2.3	2.7	4.3	5.1	6.2	8.3	12.5	16.5	17.5	20
Tee flow	4	5	7	8	12	15	16	22	32.7	49	57	67	
Male/female	1	1.5	2	2.8	3.5	4.5	5.5	9	14				

Table 4-4: Equivalent length (ft) for steel flanged valves and fittings

Fittings		Nominal pipe size (inch)												
		0.5	0.75	1	1.25	1.5	2	2.5	3	4	6	8	10	11
Elbows	R 90°	0.9	1.2	1.6	2.1	2.4	3.1	3.6	4.4	5.9	7.3	8.9	12	14
	LR 90°	1.1	1.3	1.6	2	2.3	2.7	2.9	3.4	4.2	5	5.7	7	8
	R 45°	0.5	0.6	0.8	1.1	1.3	1.7	2	2.6	3.5	4.5	5.6	7.7	9
Tees	Line flow	0.7	0.8	1	1.3	1.5	1.8	1.9	2.2	2.8	3.3	3.8	4.7	5.2
	Branch flow	2	2.6	3.3	4.45	5.2	6.6	7.5	9.4	12	15	18	24	30
Valves	Globe	38	40	45	54	59	70	77	94	120	150	190	260	310
	Gate						2.6	2.7	2.8	2.9	3.1	3.2	3.2	3.2
	Angle	15	15	17	18	18	21	22	28	38	50	63	90	120

The calculations of the available pressures at all points along the flow direction result in the pressure profile. The pressure at the zero-distance point of the pressure profile represents the pumping pressure.

The friction pressure of the whole flow loop has been calculated considering the data in Table 4-2 as the worst operation conditions.

A code has been developed for the critical velocity and hydraulic gradient line prediction of the flow loop. Figure 4-6 shows the graphical user interface of the code.

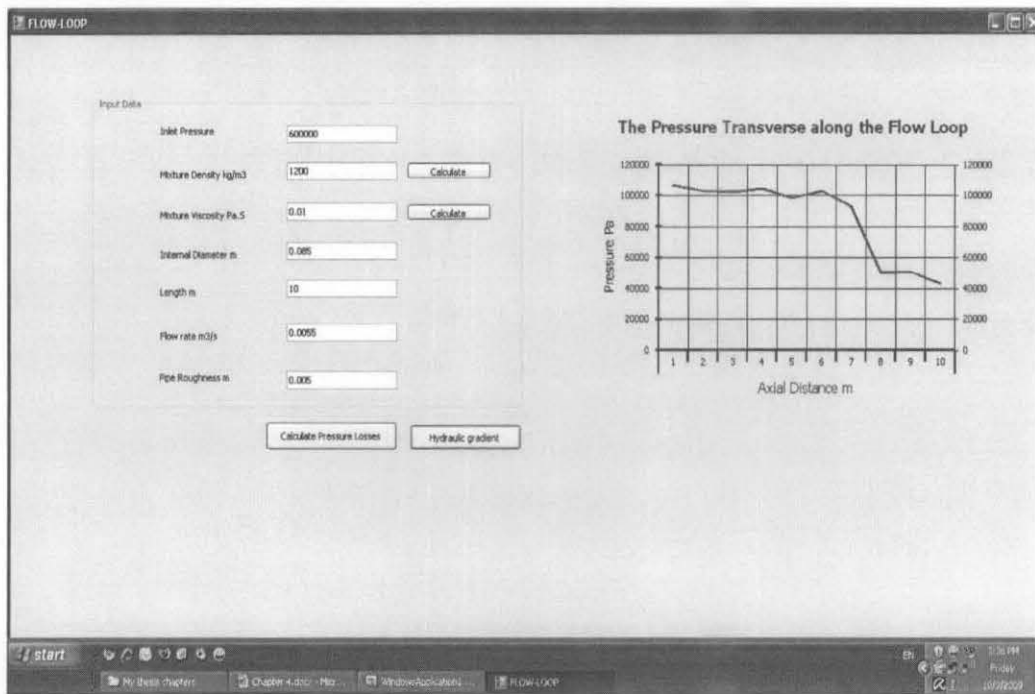


Figure 4-6: The graphical user interface of the code

The pressure profiles of the flow loop at flow velocities of 0.5, 1, 1.5, and 2 (m/s) are shown in Figure 4-7 to Figure 4-10. The other flow parameters are the worst expected operating parameters as listed in

Table 4-2 4-2. The terminal pressure of the flow loop (the remaining pressure at the end point) was assumed to be 5% of the total pressure.

The figures show that the pressure losses in the 3-in horizontal pipe (from 0 to 6 m) are very low. After 7 m the losses increase due to diameter change from 3-in to 2-in pressure highly decreases.

The Pressure Variation along the Flow Loop

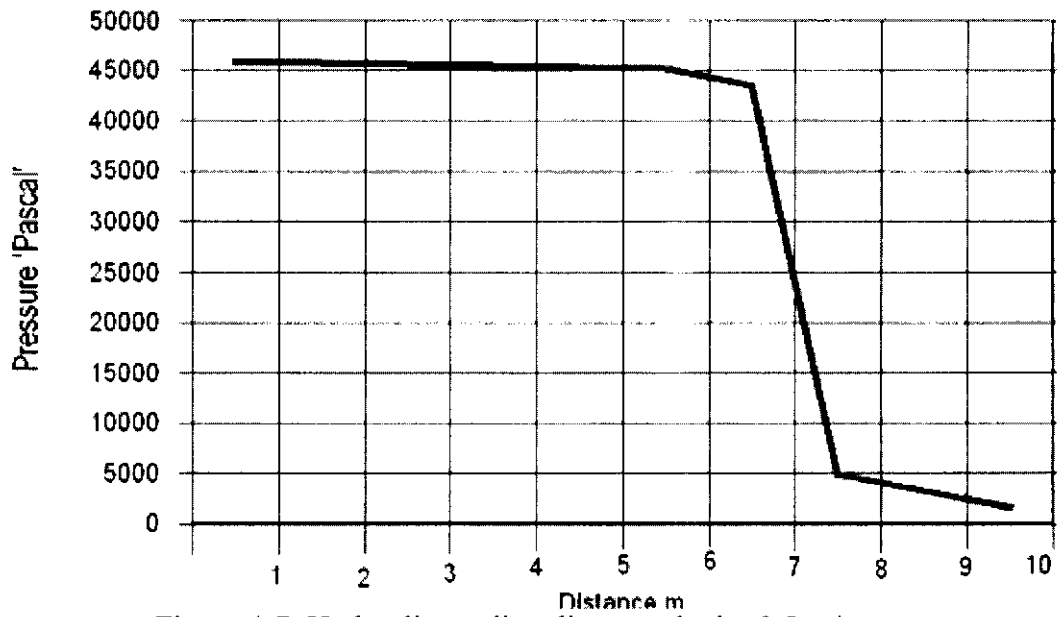


Figure 4-7: Hydraulic gradient line at velocity 0.5 m/s

The Pressure Variation along the Flow Loop

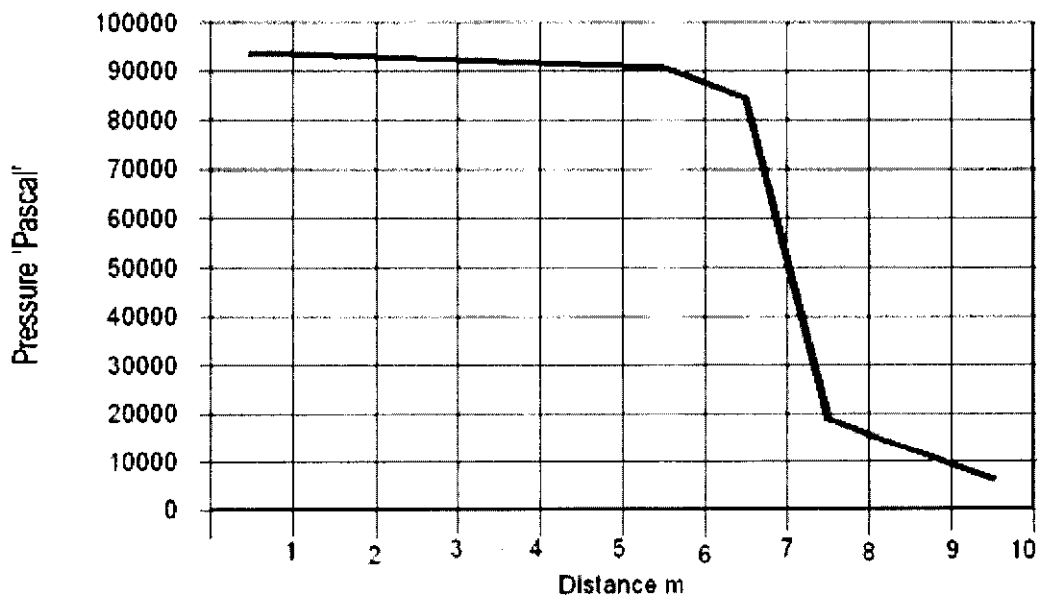


Figure 4-8: Hydraulic gradient line at velocity 1 m/s

The Pressure Variation along the Flow Loop

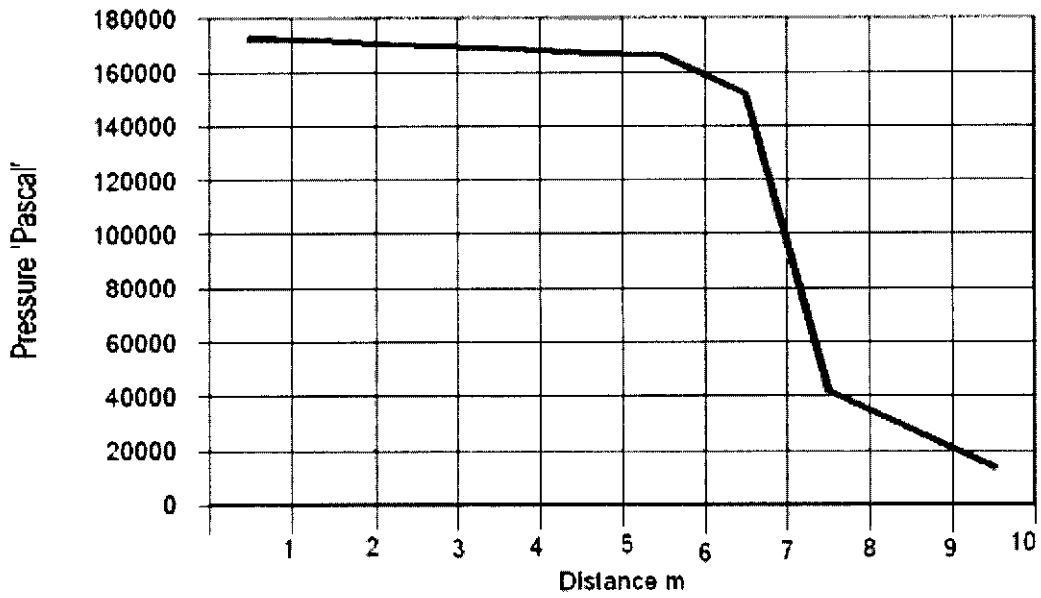


Figure 4-9: Hydraulic gradient line at velocity 1.5 m/s

The Pressure Variation along the Flow Loop

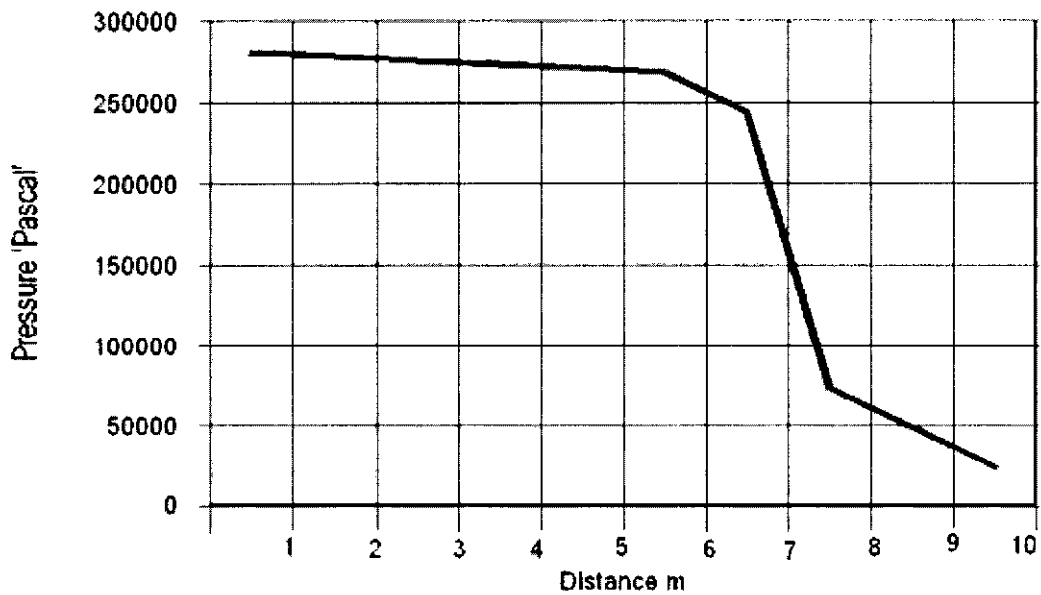


Figure 4-10: Hydraulic gradient line at velocity 2 m/s

From the hydraulic gradient line results, the required pumping pressure at velocity 2 m/s is 250000 Pa (2.5 Bar). Based on the above results, the pump must be selected with a maximum operating pressure greater than 2.5 Bar.

4.4.3 The pump selection

The pump selection is based on the following two requirements:

- 1- The pump can transport the (oil-water-sand) slurries.
- 2- The pump pressure is capable to circulate the slurry at the worst conditions included in Table 4-2.
- 3- A single screw pump with a capability of conveying grain and fiber media has been selected for the process circulation. The pump specifications are shown in Table 4-5.

Table 4-5: The main pump specification

Pump type	Speed r/min	Capacity m ³ /hr	Pressure MPa	Power kW	Inlet mm	Outlet mm
G35-1	960	8	0.6	3	65	50

The maximum velocity that can be provided by the pump can be calculated by substituting the maximum flow rate (8 m³/hr) into the following equation:

$$V(m/s) = \frac{4Q_{\max}(m^3/hr)}{3600\pi D^2}$$

4-13

The velocity rates at three different pipe sizes - 1" (0.025 m), 2" (0.05 m), and 3" (0.075 m) are listed in Table 4-6.

Table 4-6: The pump flow velocity at different pipe sizes

Diameter (inch)	Velocity (m/s)
1	4.52
2	1.13
3	0.5

4.5 The pipes and fittings selection

PVC pipes and fittings have been selected for the flow loop fabrication to avoid erosion, on one hand, and because of their low price, on the other hand. To select PVC pipes and fittings that can withstand a maximum pressure of 6 Bar, the standard dimension ratio (SDR) system has been adopted. SDR is defined using the following formula:

$$SDR = \frac{OD}{t}$$

4-14

Where OD is the pipe outer diameter and t is the thickness.

In the SDR system, pipes are grouped according to their SDR.

The pressure ratings (psi) of SDR 26 and SDR 21 are listed in the following table.

Table 4-7: Pressure ratings of SDR 21 and 26

Size (inch)	0.5	0.75	1	1.25	1.5	2	2.5	3	4	6	8
SDR 26				160	160	160	160	160	160	160	160
SDR 21	315	200	200	200	200	200	200	200	200	200	200

For example the outer diameter and thickness for the selected 3” pipe are 84 mm and 4 mm, respectively, and SDR is equal to 21. It means that, the maximum pressure that the pipe can withstand is 200 psi (13.6 Bar).

4.6 Experiments methodology

In this section, the methodology followed for corrosion measurement in elbow is discussed. The flow loop was designed for measurement of erosion in elbow, tee, and reducer and corrosion measurement in straight pipe and elbow. In this work, however, only corrosion in elbow is measured. For the flow loop to be used for erosion

measurement, another high speed pump should be installed to increase the flow velocity and enable generating wear.

Methodology for corrosion measurement in elbows

CO₂ gas was injected from a cylinder connected to the flow loop before the test section. The electrochemical noise measurement (ENM) technique was used for continuous online readings of potential and current fluctuations over time span. This technique allows corrosion rate monitoring without disturbances of the flow process. The monitoring of corrosion rate using ENM is achieved by converting the potential/current fluctuations into useful information of corrosion rate and type using different methods. Aballe and his co-workers (Aballe *et al.* 1999) proposed three methods for interpreting ENM signals into quantitative and qualitative corrosion rate information. These methods are statistical methods, spectral analysis, and the chaos theory-based method. The correlation between electrochemical noise and corrosion rate is given in Appendix B.

GillAC potentiostat is used to record and analyze the electrochemical noise measurements collected from a 3-in mild steel elbow.

The corrosion rate measurement procedure is shown in the following chart:

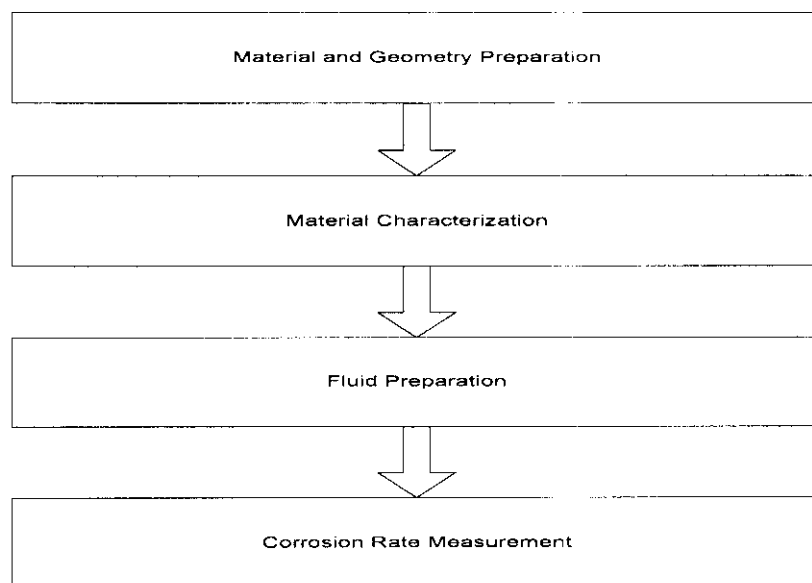


Figure 4-11: Corrosion Experimental Procedure

Material and geometry preparation

In this work the corrosion rate measurement was carried out in an elbow test section in order to, mainly, validate the modified NORSOK model. Three electrodes were fastened to the elbow and immersed in the flow medium as shown in Figure 3-9.

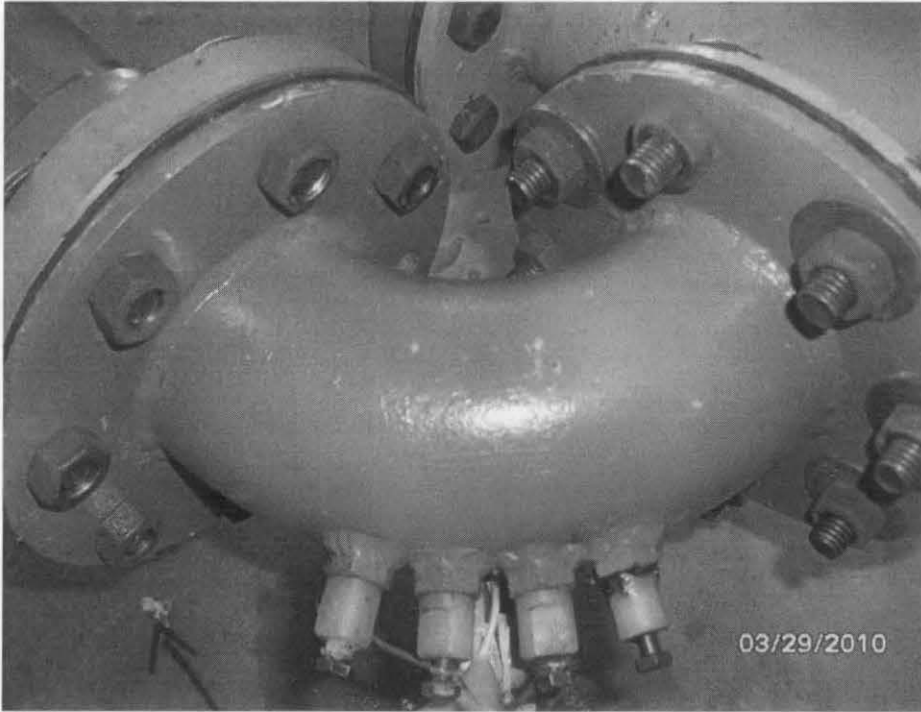


Figure 4-12: The elbow test section containing the wired electrodes

The three electrodes were well isolated to guarantee that there is no electrical connection. Two electrodes served as working electrodes whereas the third one is used as a reference electrode.

The similarity of the electrodes is a prerequisite to measure corrosion rates using the ENM technique. The similarity has been achieved by using the same material with the same dimensions for the three electrodes.

The three electrodes were 6x8 mm (Diameter x Height) cylindrical shapes. Every electrode was attached to a steel screw, which in turn was wired to the potentiostat. The electrical isolation between any electrode and the elbow was attained by using a plastic material through which the screw was fastened as shown in Figure 3-10.

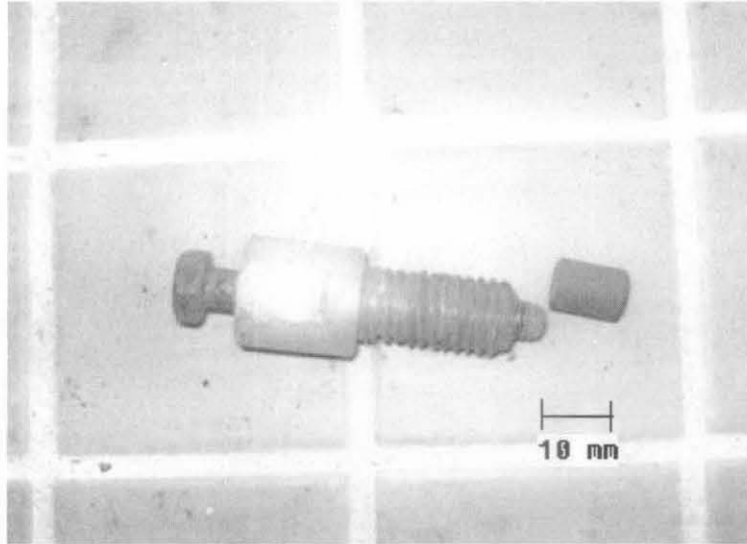


Figure 4-13: An electrode

4.7 Summary

This chapter described the experimental setup design and fabrication. The chapter mainly focuses on the method followed to model the flow loop and size its components. The procedure followed to design the flow loop, which is based on hydraulic calculations and depicting of pressure profiles along the axial direction of the flow loop, has been given in details. The calculations have been performed using a developed computational code to assist in the main pump selection. The rating of the selected pump, pipes, and fittings along with description of the flow loop components and flow process have been described.

Summary of the experimental methodology for measuring corrosion rate in elbow including the techniques and devices used for corrosion measurements is given at the end of the chapter.

Chapter 5

RESULTS AND DISCUSSION

5.1 Introduction

In this chapter different simulation and experimental results are illustrated. The simulation results include those obtained from the developed code and the CFD model. The experimental results are those obtained from the flow loop tests. The code results include sand erosion in elbows and tees, CO₂ corrosion in pipes and elbow, erosion-corrosion in elbows, and CO₂ corrosion prediction along pipelines for different input parameters. The CFD results include erosion rate simulation in an elbow due to transportation of fluid containing sand particles.

Sand erosion due to (gas + sand) dilute flow has been simulated using the CFD Fluent software under different fluid velocities. The CFD results were used as a benchmark to validate the Salama and DIM models used to develop the code. The validation shows good agreement of DIM model with the CFD whereas Salama model shows higher values. Salama model was then improved with comparison with DIM to increase its accuracy and extend its applicability to liquid flow. The main benefit of the improvement of Salama model is making it with the same accuracy and applicability of CFD and DIM models while avoiding the sophisticated solution of particles movement. The improvement results in including the effect of viscosity which is not taken into account in the original Salama model. This makes the modified model, called Mysara-UTP model, applicable to oils with varying viscosity. Salama model was also improved by comparing it with measured data from literature. The improvement resulted in three sub-models for pure gas, high gas liquid ratio (HGLR), and low gas liquid ratio (LGLR).

To investigate the developed code for prediction of CO₂ corrosion in elbows and straight pipes, erosion-corrosion in elbows, and CO₂ corrosion along pipelines; arbitrary selected input data sets are used and the output showing the effect of different parameters is presented. The corrosion results show significant difference of the effect of fluid characteristics on corrosion rate in laminar and turbulent flow and the corrosion rate in elbows is always significantly higher than that in straight pipe. The code results for corrosion prediction are validated using field and experimental data.

5.2 Results from the computational fluid dynamics (CFD) model

5.3 Model creation and grid generation

A 2-D geometry has been created and meshed in Gambit and then transferred to Fluent software for CFD solution. The geometry is 50 mm (2 in) internal diameter elbow ending with two straight pipes 100 mm each. The length of the elbow outer wall curvature is 157 mm. Quadratic mesh type with has been and denser grid is created near to walls and in the curvature region to obtain more accurate solution. Four boundaries have been selected as shown in Figure 5-1. The inflow boundary is the boundary at which the fluid and solid particles enter the flow domain and particles are tracked along the stream until the outflow boundary. The erosion is then simulated in the outer “Wall” boundary because it susceptible to more severe erosion than the inner wall.

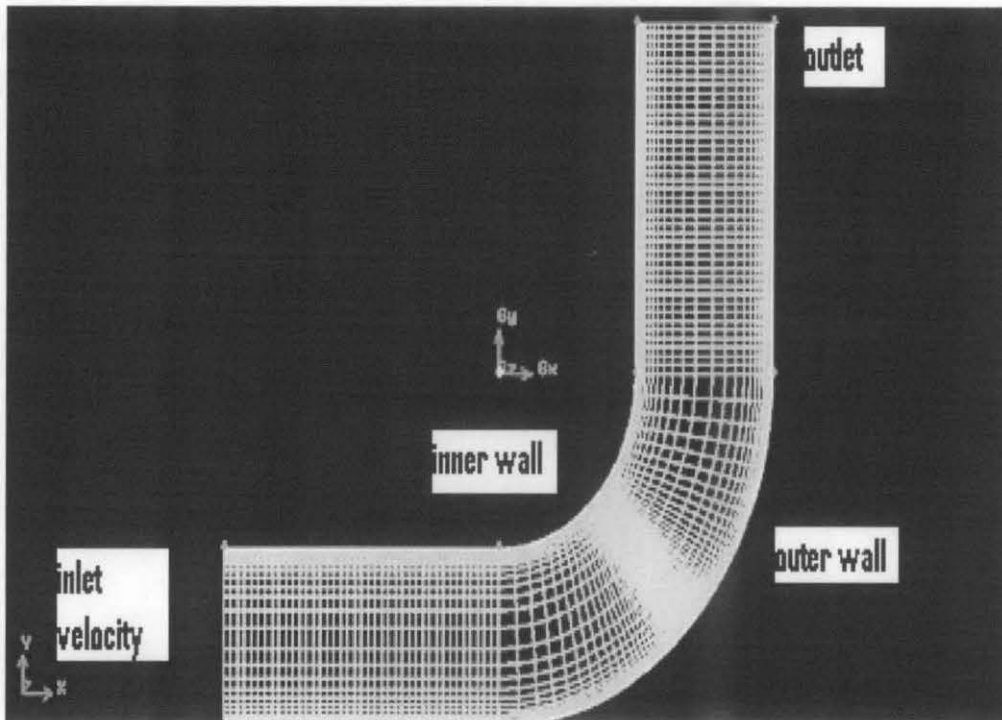


Figure 5-1: The model generation and meshing

5.4 Solution of flow field and particles trajectories

Sand erosion has been simulated using the computational fluid dynamics (CFD) Fluent V6.2.16 commercial software. Sand flow rate of 0.000886 kg/s was injected from the INLET VELOCITY boundary shown in the geometry. The sand erosion simulation has been performed following the flow solution and particle trajectory steps. In the flow solution, the $k - \varepsilon$ model was selected for turbulence solution. The fluid velocity at the inlet was set to 20 m/s. The solution was initialized, requesting 170 iterations; the solution converged after 157 iterations.

The flow is assumed to be two phases (air+ sand) dilute flow. The main parameters of the primary and dispersed phases are as shown in Table 5-1.

Table 5-1: The main parameters of the phases

Parameter	Unit	Value
Air (continuous phase)		
Density	kg/m ³	1.2015
Viscosity	Pa.s	0.0000182
Sand (dispersed phase)		
Density	kg/m ³	2650
Size	m	0.0003
Mass flow rate	kg/s	0.000886

Figure 5-2 shows the velocity contours of the primary phase in the elbow. The maximum fluid velocity is 26.7 m/s in the vicinity of curvature of the inner wall.

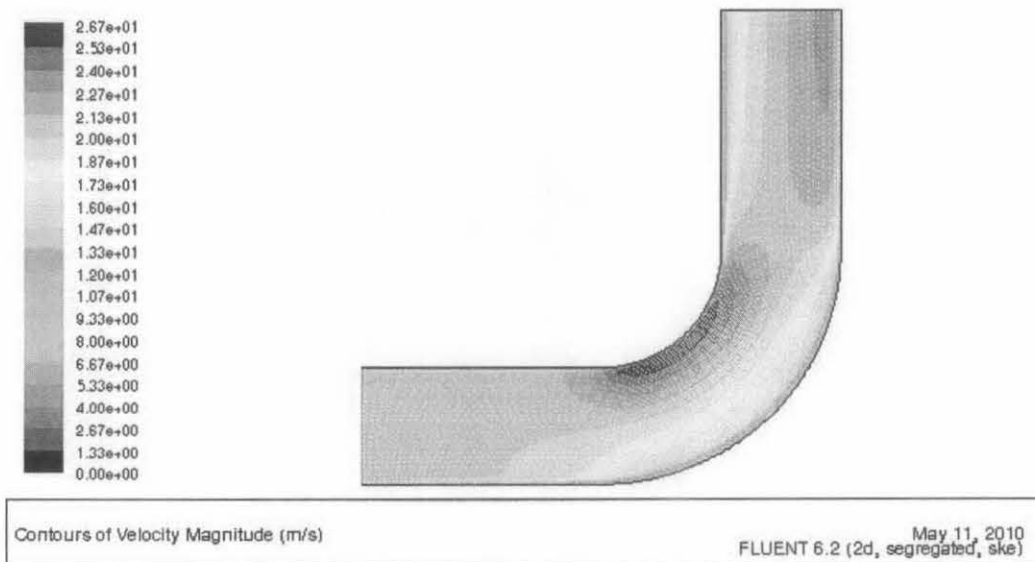


Figure 5-2: Velocity contours of the primary phase

After the solution of the primary phase, sand has been tracked along the axial position. The particle trajectory allowed acquiring of particles velocity (Figure 5-3 and Figure 5-5) and particles angles of impingement (Figure 5-4). The particles angle

of impingement as shown in Figure 5-4 remains constant at zero in the horizontal pipe until the start point of the elbow curvature, where it starts to increase to reach 90° at the end point of the elbow curvature and the start point of the vertical pipe to remain constant until the end of the vertical pipe. Figure 5-3 shows that no particles impinge the inner wall at this condition, and the impingement velocities at the outer wall are in the range from 16.34 to 20.14 m/s. The variation of the velocity of a single particle along the path length is shown in Figure 5-5.

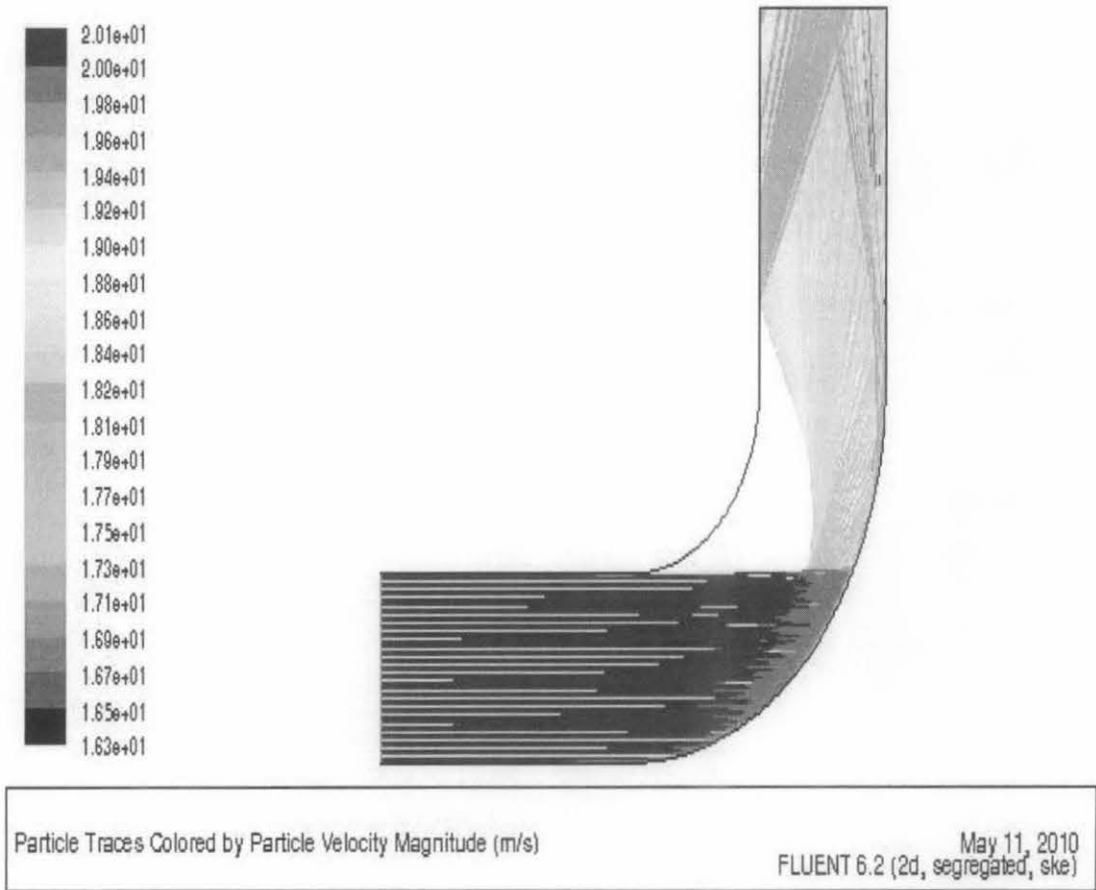


Figure 5-3: Particle velocity tracking

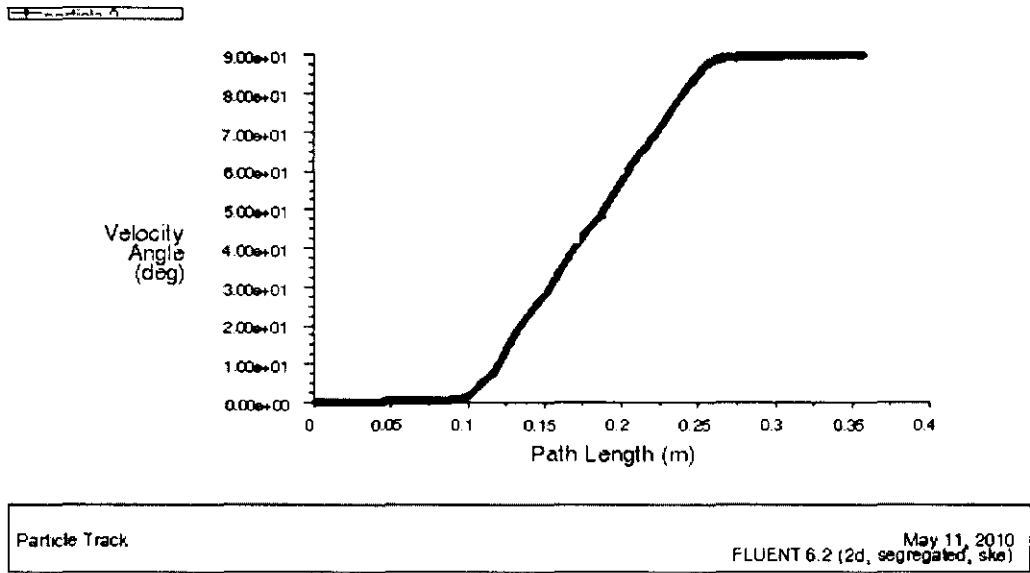


Figure 5-4: Angle of impingement of different sand particles

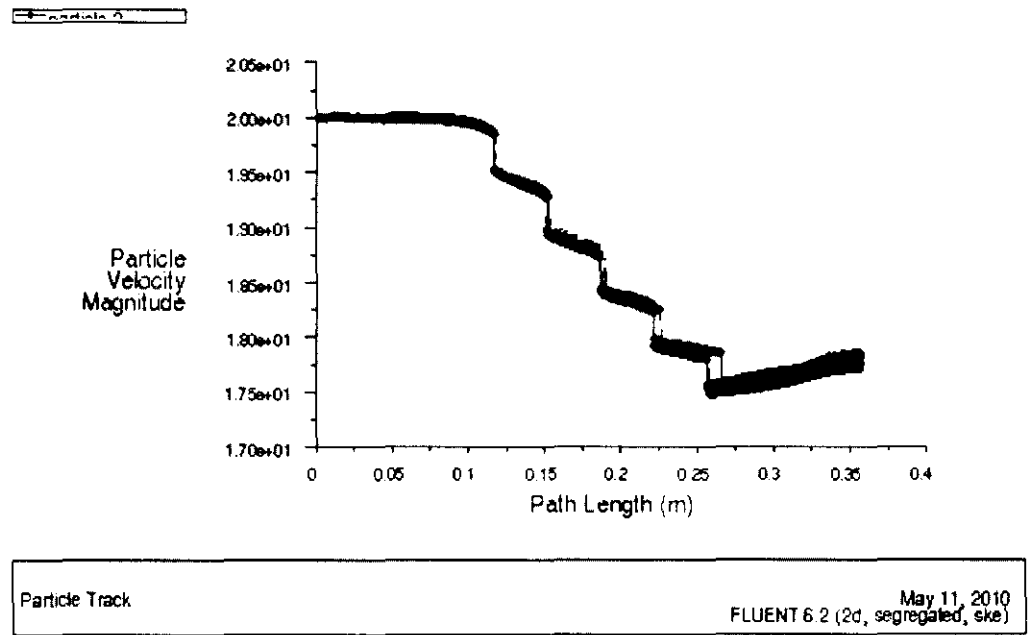


Figure 5-5: Particle velocity along the flow path

5.5 Erosion rate calculations

The calculated particle velocities and angles of impingement are substituted into the following equation to calculate the erosion rate at every node in the assigned wall.

$$ER = \sum_{p=1}^N \frac{m_p C(d_p) f(\alpha) v^{b(v)}}{A_{face}} \quad 5-1$$

Where m_p and d_p are particle mass flow rate and diameter, respectively, α is the angle of impingement, v is the particle velocity, and A_{face} is the area of target subject to erosion. C , f , and b are functions of particle size, angle of impingement, and velocity, respectively.

In this work, the impact angle function $f(\alpha)$ has been defined to Fluent using a piece-linear profile with values shown in Table 5-2. The diameter function $C(d_p)$ and velocity exponent function $b(v)$ were set to values of $1.8e-09$ and 2.6 , respectively.

Table 5-2: Values of angle function defined to the model

(degrees)	$f(\alpha)$
0	0
20	0.8
30	1
45	0.5
90	0.8

It is assumed that particle's velocity changes after hitting a solid wall. The particle velocity u_{p2} after the impingement is related to that before the impingement u_{p1} as follows:

$$u_{p2} = e u_{p1} \quad 55-2$$

Where e is the coefficient of restitution, the value of which depends on many factors such as the coefficient of kinetic friction, particle velocity, angle of impingement and the materials of particles and substrates (Sommerfeld 1992). Grant and Tapakof proposed two relationships between the coefficient of restitution in parallel and perpendicular directions, and angle of impingement. The relationships are expressed as follows (Chen *et al.* 2006):

$$e_{parallel} = 0.998 - 1.66\theta + 2.11\theta^2 - 0.67\theta^3 \quad 5-3$$

$$e_{perp} = 0.993 - 1.76\theta + 1.56\theta^2 - 0.49\theta^3 \quad 5-4$$

From Table 5-2, it is seen that the maximum angle of impingement function at $\alpha = 30^\circ$. From Figure 5-4 it can be concluded that this occurs at a position 150 mm of the path which is emphasized by the maximum erosion rate $7.56E-7$ kg/m².s. as shown in Figure 5-6. The particle velocity at the position of maximum erosion rate is 18.5 m/s as shown in Figure 5-5. Figure 5-6 shows the erosion rate at five points along the outer wall. These points are the points where angles of impingement match those given in Table 5-2. It can be noted that, although particle velocity before the point 100 mm of the path is very high (as shown in Figure 5-5), no erosion takes place because the angle of impingement (and so the angle function) is zero (as shown in Figure 5-4).

Erosion rate unit in Fluent is kg/m².s. The maximum erosion rate for the outer wall in mm/year can be obtained in mm/year as follows:

$$ER \left(\frac{mm}{year} \right) = \frac{ER \left(\frac{kg}{m^2 s} \right)}{\rho_s \left(\frac{kg}{m^3} \right)} \times 1000 \left(\frac{mm}{m} \right) \times 3600 \left(\frac{s}{hr} \right) \times 24 \left(\frac{hr}{day} \right) \times 365 \left(\frac{day}{year} \right)$$

$$= \frac{7.56E - 07 \times 1000 \times 3600 \times 24 \times 365}{7800} = 3.1 \text{ mm/year}$$

The total erosion rate is 5.512E-05 kg/m².s which is equivalent to 255.7 mm/year.

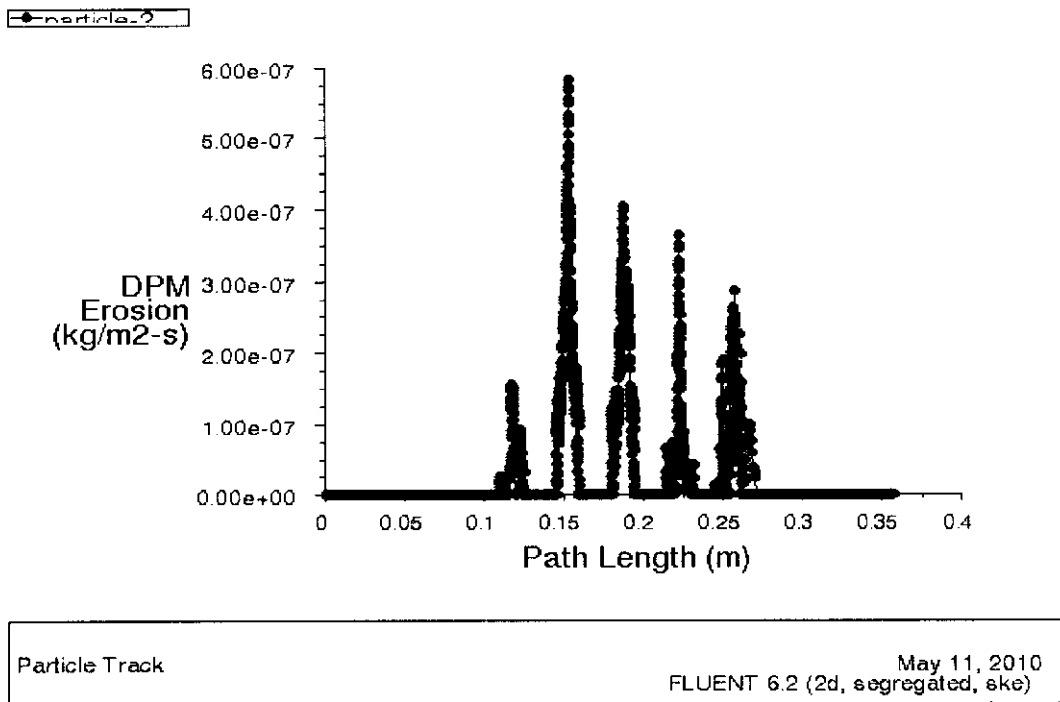


Figure 5-6: Erosion rate variation along the path (outer wall)

To analyze the effect of velocity on the maximum erosion rate and total erosion rate, different values of inlet velocity were entered. The variation of maximum erosion rate with velocity is shown in Table 5-3 and Figure 5-7; and the variation of total erosion rate with velocity is shown in Table 5-4.

Table 5-3: Variation of maximum erosion rate with velocity

Velocity m/s	Max Erosion rate	
	kg/m ² .s	mm/year
5	4.102377e-9	0.0166
10	1.053087e-7	0.426
15	3.29e-7	1.33
20	6.66027e-7	2.693
25	1.212146e-6	4.9
30	1.97e-6	7.97

Table 5-4: Variation of total erosion rate with velocity

Velocity m/s	Total Erosion rate	
	kg/m ² .s	mm/year
5	6.529167e-07	2.64
10	6.395296e-06	26
15	2.58961e-05	105
20	5.5120436e-05	222.4
25	9.6189249e-05	389
30	0.000156	631

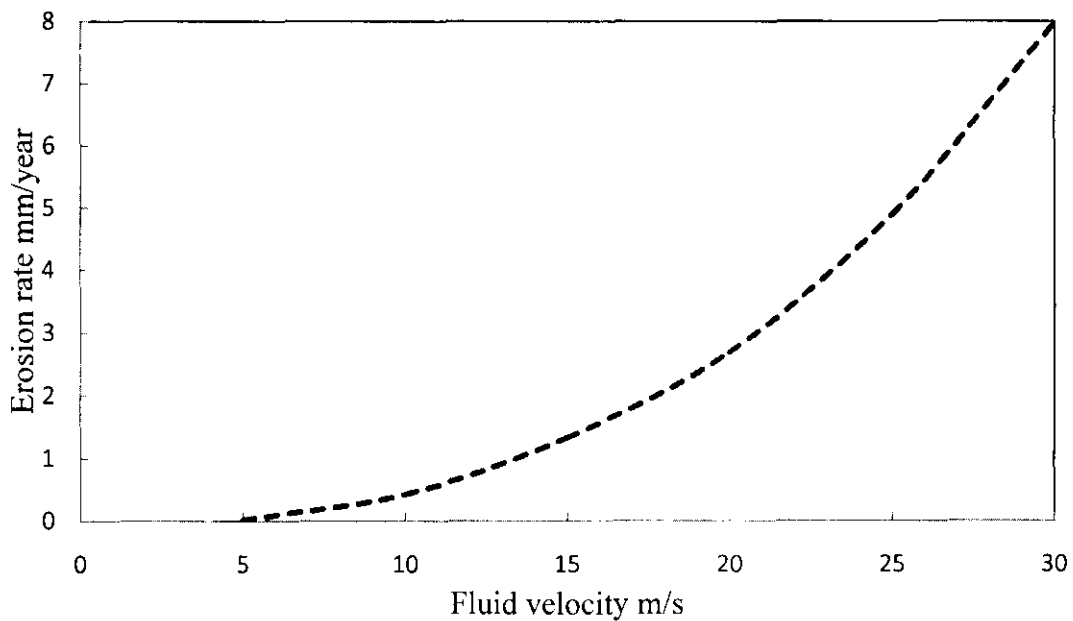


Figure 5-7: Variation of erosion rate with air velocity (in 2-in elbow, sand flow rate=0.000886 kg/s)

5.6 Analysis of results using the developed code

In this section different simulation results from the developed code will be presented and discussed. The code is designed to predict erosion rate for elbows and tees, and corrosion rate for straight pipes and elbows for different input data. The code

graphical user interface, navigation forms, and input data form are shown in Figure 5-8.

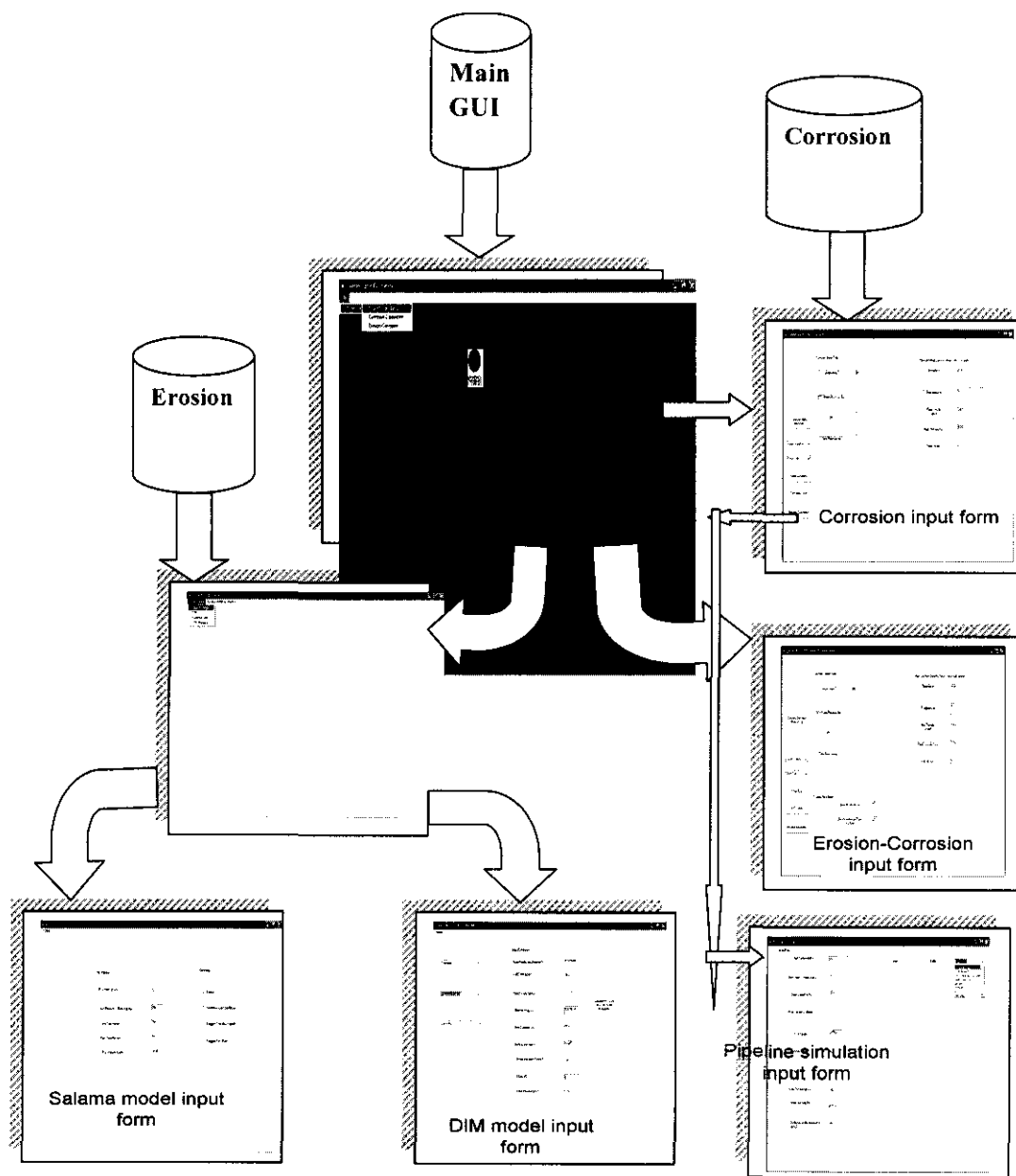


Figure 5-8: The code forms

5.6.1 Sand erosion prediction and simulation

Two erosion prediction models have been used to develop the code. The models formulae were discussed in chapter 3. In this chapter, results from the models are used to analyze the effects of different parameters on the predicted erosion rate.

5.6.1.1 Analysis of results from Salama model

In our code, the Salama model input data form appears as shown in Figure 5-9 . From this form, the user can select the geometry and input fluid and sand properties, which include flow velocity, sand production rate, sand size, pipe diameter, and fluid density. To examine the results of Salama model, the data shown in Figure 5-9 for velocity, sand production rate, sand size, and pipe diameter were used. Three values of density were used to predict erosion rate in gas (with density of 1.2015 kg/m^3), water (with density of 1000 kg/m^3), and oil (with density of 850 kg/m^3). The variation of erosion rate with velocity for the three fluids is shown in Table 5-5.

Input Data	Value	Geometry	Selected
Flow Velocity m/s	20	Elbow	Yes
Sand Production Rate Kg/day	76.55	Seamless and Cast Elbow	No
Sand Size micron	300	Plugged Tee (Gas-Liquid)	No
Pipe Diameter mm	50	Plugged Tee (Gas)	No
Fluid Density Kg/m3	850		

Figure 5-9: Input data form of Salama model

Table 5-5: Variation of erosion rate with velocity for gas, water, and oil (Salama model)

Velocity m/s	Erosion rate mm/year		
	Gas	water	oil
0	0	0	0
0.8	0.81551	0.00098	0.00115
1.6	3.26206	0.00392	0.00461
2.4	7.33963	0.00882	0.01037
3.2	13.0482	0.01568	0.01844
4	20.3879	0.0245	0.02882
4.8	29.3585	0.03527	0.0415
5.6	39.9602	0.04801	0.05648
6.4	52.1929	0.06271	0.07378
7.2	66.0566	0.07937	0.09337
8	81.5514	0.09798	0.11528
8.8	98.6772	0.11856	0.13948
9.6	117.434	0.1411	0.166
10.4	137.822	0.16559	0.19482
11.2	159.841	0.19205	0.22594
12	183.491	0.22046	0.25937
12.8	208.772	0.25084	0.2951
13.6	235.684	0.28317	0.33315
14.4	264.227	0.31747	0.37349
15.2	294.401	0.35372	0.41614
16	326.206	0.39194	0.4611
16.8	359.642	0.43211	0.50836
17.6	394.709	0.47424	0.55793
18.4	431.407	0.51834	0.60981
19.2	469.736	0.56439	0.66399
20	509.696	0.6124	0.72047

It is seen from the results the erosion rate is very high for the gas flow as compared to oil and water. By comparing column 3 and column 4 in Table 5-5, we can notice that the erosion rate for oil is greater than that of water, which is analogical result. This error is due to the fact that no account is taken for viscosity in the Salama model since it was developed mainly for gas (air) flow. In this model the erosion rate changes inversely with fluid density and since water density is higher than oil density the predicted erosion rate for water flow is lower than that for oil flow. This result is shown graphically in Figure 5-10.

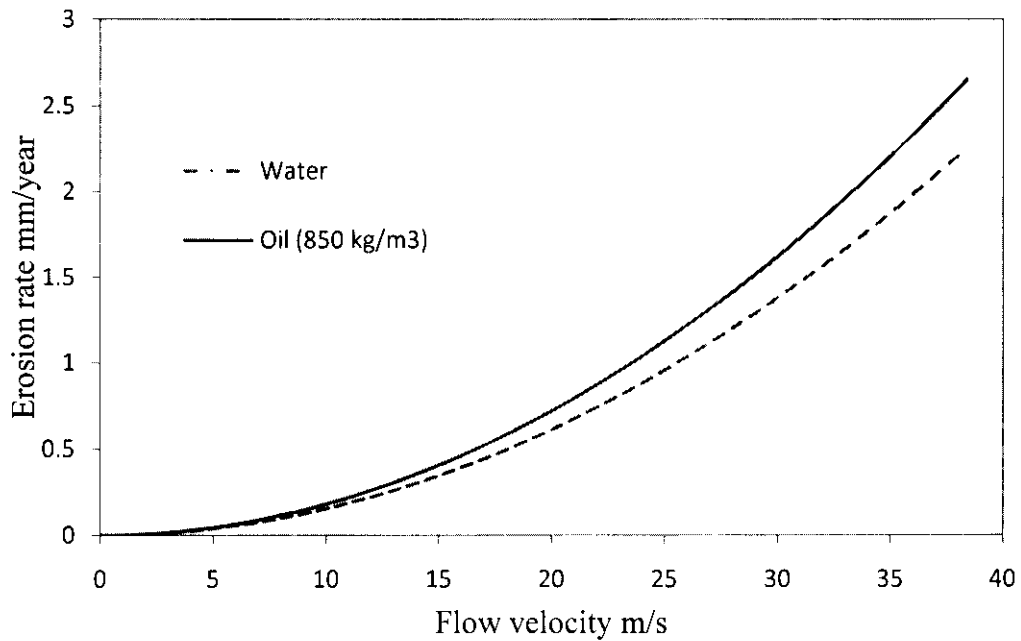


Figure 5-10: Variation of erosion rate with velocity for water and oil (Salama model)

5.6.1.2 Analysis of results from the DIM model

The DIM model input data form is shown in Figure 5-11. The user can input data related to the fluid, sand, and target material to this form; and select the geometry.

Figure 5-11: Input data form of the DIM model

5.6.1.2.1 Variation of particles impingement velocity with fluid type

When particles are entrained in a fluid, the velocity of the particles is always changing along the flow stream due to their interaction with the fluid. This interaction is usually described mathematically by using the equation of particles motion (equation 3-7), which equates the change of the particle momentum with the forces on it. A simplified form of the equation of particles motion is solved numerically considering the assumptions of the direct impingement model (DIM) proposed by E/CRC at University of Tulsa. The solution to the equation simulates the particles' velocities along the stagnation zone and calculates the particles impingement velocity. The change of the particle's velocity depends on many factors that are related to the carrier fluid, geometry of the particle and the properties of the dispersed particles.

Three fluids have been considered to analyze the effect of fluid properties on particle's velocity in elbow. These fluids are air, water, and crude oil with properties shown in Table 5-6. The same properties and geometry of sand are assumed for all fluids.

Table 5-6: Input data for erosion simulation

Property	Unit	Gas	Water	Oil
Density	kg/m ³	1.2015	1000	900
Viscosity	Pa.s	0.0000182	0.00018	0.009
Velocity	m/s	20		
Sand size	Micron	300		
Sand	kg/m ³	2650		
Elbow ID	m	0.05		

The results of sand trajectories for the three fluids are shown in Figure 5-12. The impingement velocities are 19.77 for air, 1.28 for water, and 0.39 for oil. In air, sand velocity changes very slightly to the extent that the impingement velocity can be assumed as equal to the air velocity. For liquids, sand decelerates rapidly to hit the target wall with very low velocity.

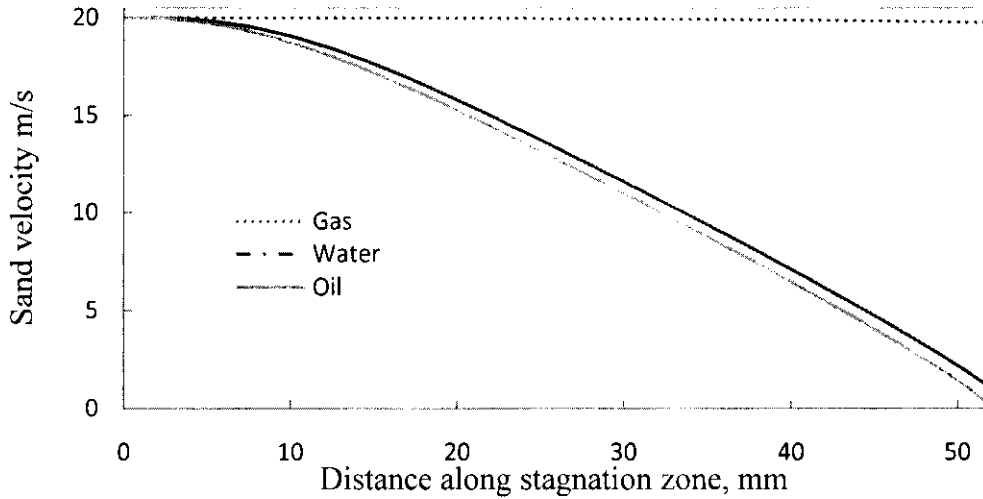


Figure 5-12: Sand trajectory along the stagnation zone for air, water, and oil

The rapid deceleration of liquids is mainly due to effect of viscosity, which is expressed mathematically by rewriting of the equation of particle motion (Equation 3-7) in the following form:

$$\frac{dV_p}{dx} = a + \frac{b}{\text{Re}_p} \quad 5-5$$

With

$$a = \left[\frac{0.375\rho_f}{d_p\rho_p} \right] \left[\frac{(V_f - V_p)|V_f - V_p|}{V_p} \right] \quad 5-6$$

$$b = \left[\frac{18\rho_f}{d_p\rho_p} \right] (V_f - V_p) \quad 5-7$$

$$\text{Re}_p = \frac{V_f\rho_f d_p}{\mu_f} \quad 5-8$$

It means that, $\frac{dV_p}{dx}$ for liquids with high viscosity (i.e. low Reynolds number) are high, in contrast to gases.

5.6.1.3 Effect of flow velocity on erosion rate

The relationship between sand erosion and flow velocity has been proposed quantitatively by many investigators. For carbon steel, the relationship is in the form $ER \propto V^n$ where V is the particle velocity; and the value of the exponent n ranges from 1 to 3. Typical proposed n values for carbon steel are 1.73 (Shirazi, et al.), 2.6 (Haugen, et al.), and 2.0 (Salama). In Salama model, sand particle's velocity is assumed to be identical to the fluid velocity. So the fluid velocity can be used to calculate sand erosion. In direct impingement, however, a simplified computational fluid dynamics equation (equation 3-7) is used to track the particles within the stagnation zone to get the exact value of the particle velocity on the surface of the target. Figure 5-13 to Figure 5-15 illustrate examples of the direct impingement model output showing the variation of erosion rate with the velocity due to angular sand for a carbon steel elbow in cases of flow of air, water, and oil, respectively, with properties similar to those given in Table 5-6. The sand mass flow rate is 0.000886 kg/s. The x-axis shows the velocity of both fluid and particles. In these figures, the x-axis shows both impingement velocity (between brackets) and fluid velocity (out of the brackets). i.e. the impingement velocity is firstly calculated at any fluid velocity and then erosion rate is calculated using the impingement velocity. It can be noted from Figure 5-13 and Figure 5-14, for gas and water that erosion exists regardless of the fluid velocity. The erosion by sand in water is, however, too low compared to that of gas. From Figure 5-15, for sand in oil, no erosion takes place for fluid velocity below 16 m/s. The higher viscosity of oil compared to water results in more

interaction between sand and oil, which results in decreasing the impingement velocity as indicated by Equation 5-6.

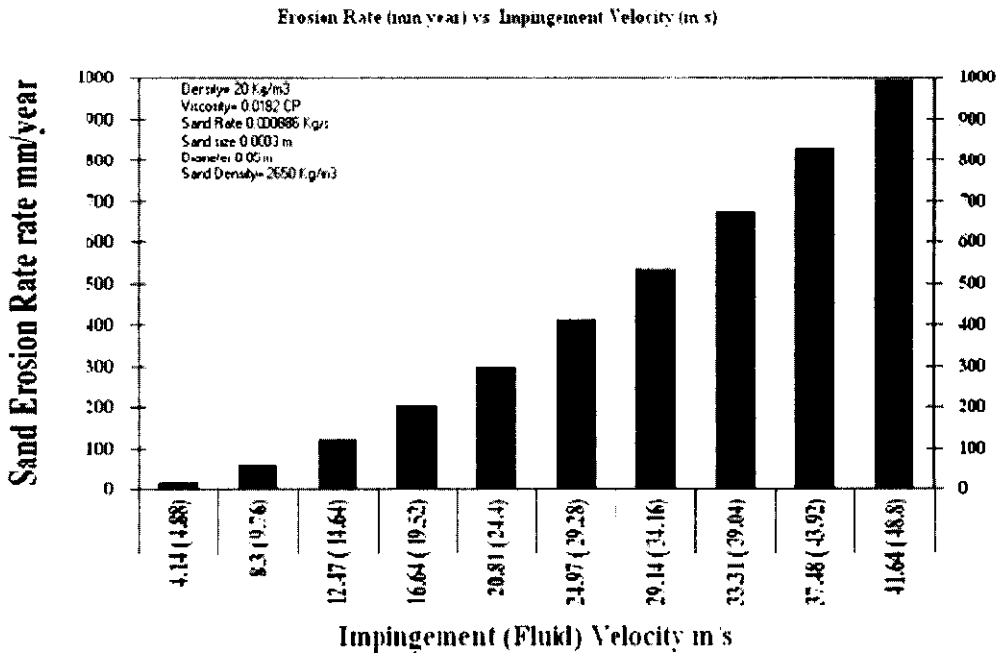


Figure 5-13: Variation of sand erosion with impingement velocity (air)

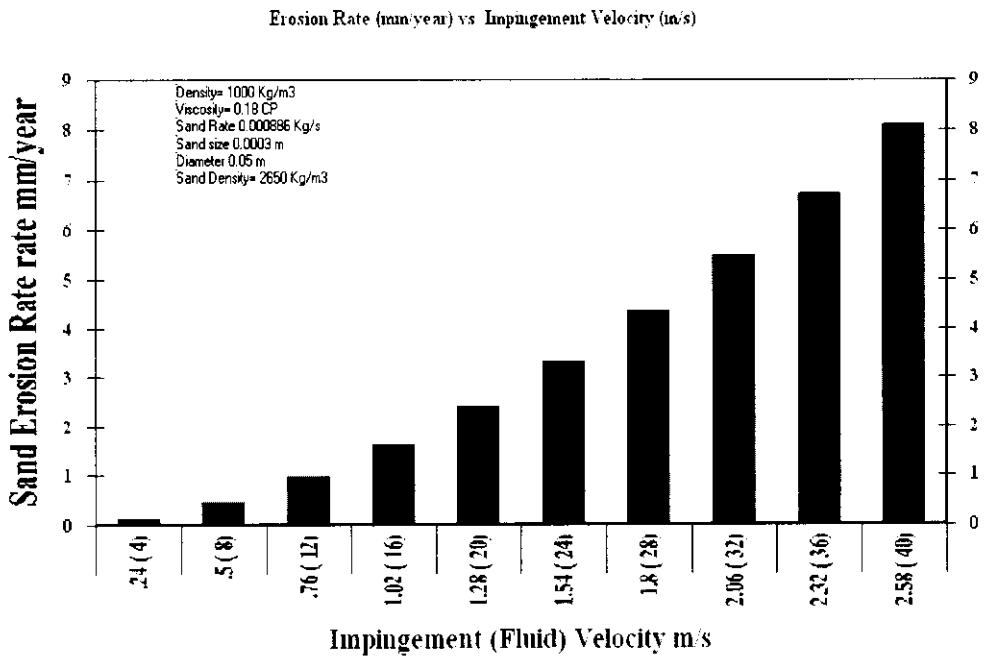


Figure 5-14: The variation of erosion rate with velocity (water)

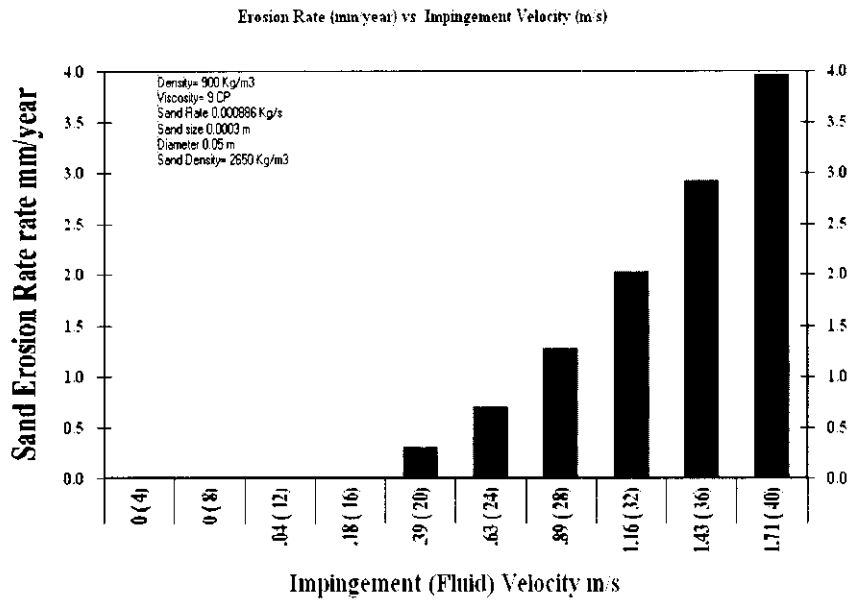


Figure 5-15: The variation of erosion rate with velocity (oil)

To further investigate the effect of viscosity and density on erosion rate, the variation of erosion rate with flow velocity for oil with density of 850 kg/m^3 at different viscosity is shown in Figure 5-16 and the variation of erosion rate with flow velocity for oil with viscosity of $0.009 \text{ Pa}\cdot\text{s}$ at different density is shown in Figure 5-17 (other parameters are the same as those used in Table 5-6). It is clear that erosion rate decreases with increase of both density and viscosity. The effect of viscosity, however, is more significant.

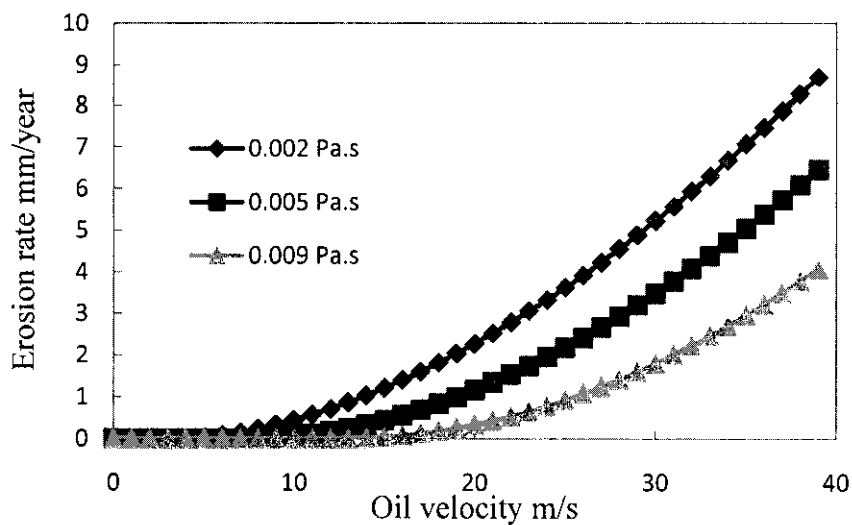


Figure 5-16: Variation of erosion rate with velocity for oil with different viscosity

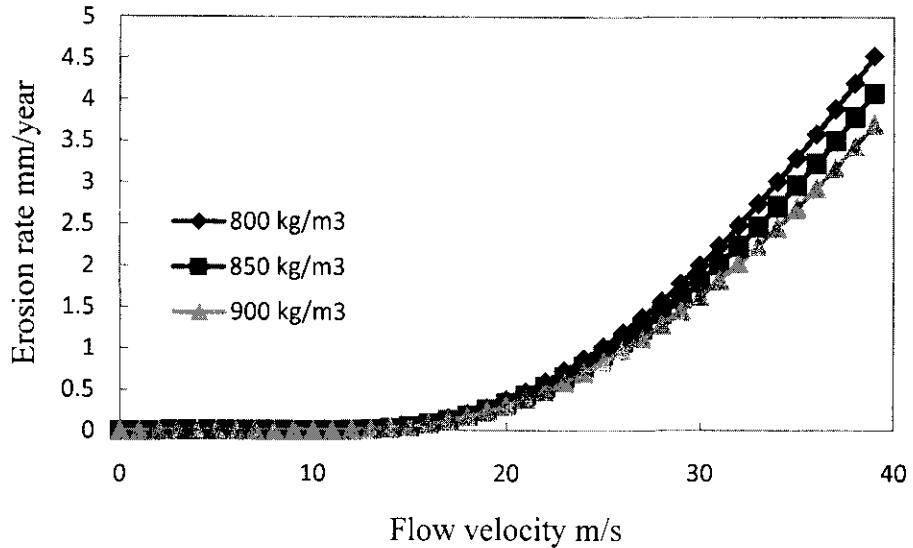


Figure 5-17: Variation of erosion rate in carbon steel elbow with flow velocity for oil with different density

5.6.1.4 Effect of pipe diameter

Figure 5-18 and Figure 5-19 illustrate examples of the direct impingement model output showing the variation of sand erosion with internal diameter for air and water flow. It is clear from the two figures that the erosion rate is markedly affected by the pipe size. The erosion rate can be mitigated by increasing the pipe diameter. This fact is emphasized by Figure 5-20 and Figure 5-21, which show the variation of erosion rate with particles and fluid velocity for different pipe diameters for air and water. Every curve in Figure 5-20 and Figure 5-21 represents a specified diameter as indicated in the legend. The same result of Figure 5-18 is shown in Table 5-7.

It is clearly shown that above diameter of 137.5 mm (5.5 in.), the erosion rate is very low as compared with the erosion rate at diameter of 25 mm (1 in.).

Erosion Rate vs Diameter, The Impingement Velocity= 19.7701202444563m/s

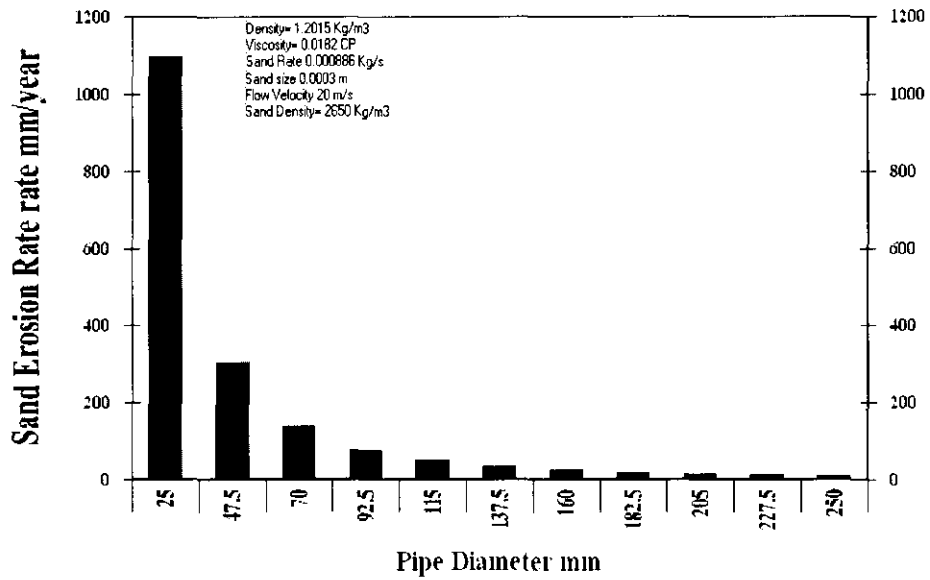


Figure 5-18: The variation of erosion rate with diameter (air)

Erosion Rate vs Diameter, The Impingement Velocity= 1.27915637849272m/s

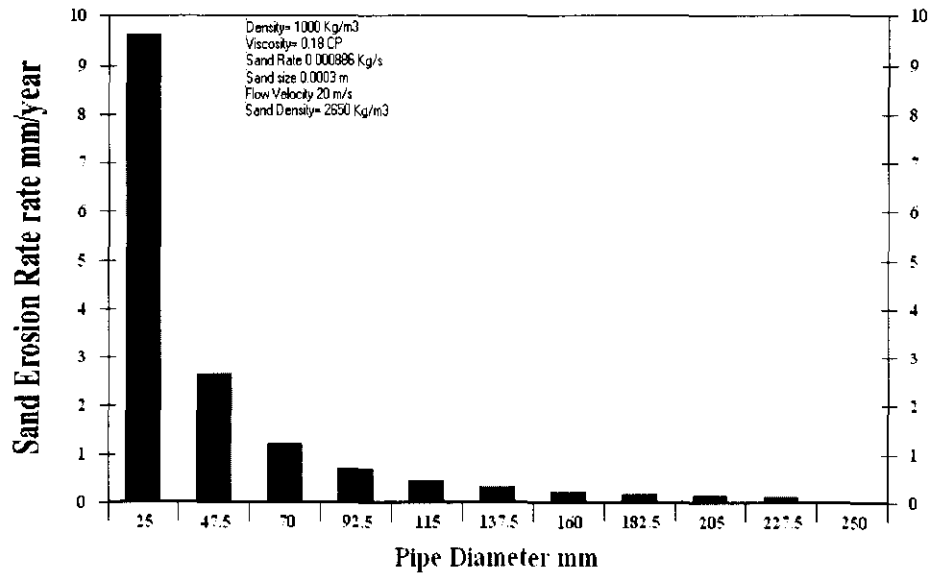


Figure 5-19: The variation of erosion rate with diameter (water)

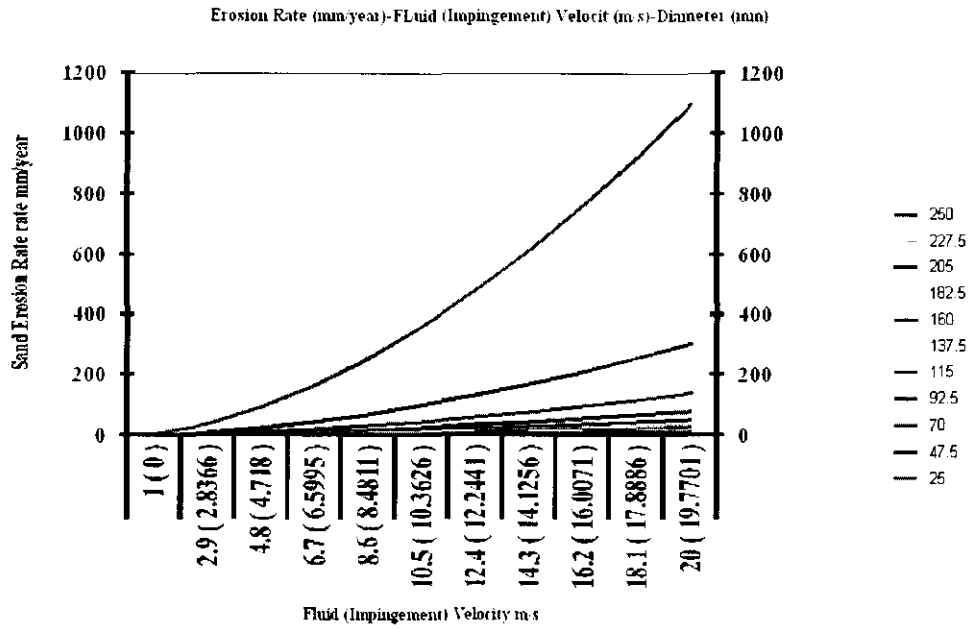


Figure 5-20: The variation of erosion rate with velocity for different diameters (air)

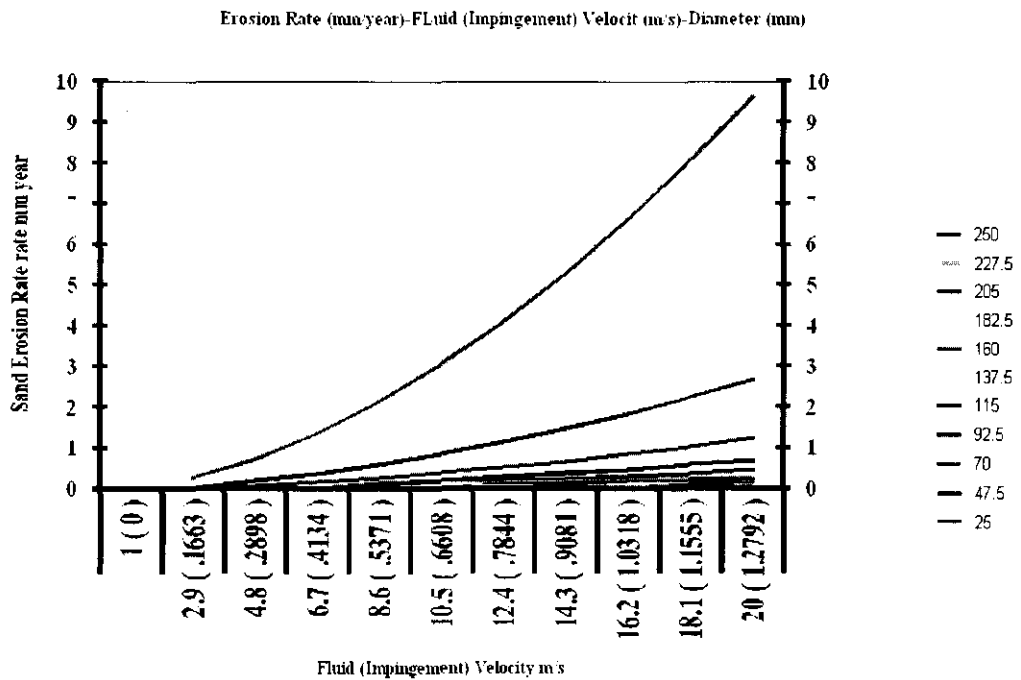


Figure 5-21: The variation of erosion rate with velocity for different diameters (water)

Table 5-7: The variation of erosion rate with elbow diameter

Diameter mm	Sand Erosion mm/year	Diameter mm	Sand Erosion mm/year
10	9835.19	105	89.21
15	4371.2	110	81.28
20	2458.8	115	74.37
25	1573.63	120	68.3
30	1092.8	125	62.95
35	802.87	130	58.2
40	614.7	135	53.97
45	485.69	140	50.18
50	393.41	145	46.78
55	325.13	150	43.71
60	273.2	155	40.94
65	232.79	160	38.42
70	200.72	165	36.13
75	174.85	170	34.03
80	153.67	175	32.11
85	136.13	180	30.36
90	121.42	185	28.74
95	108.98	190	27.24
100	98.35	195	25.87

5.6.1.5 Effect of sand production rate

Both Salama model and direct impingement model assume a linear proportional relationship between sand erosion and sand production rate in kg/s. The linear relationship, however, is only valid for low sand concentration. Salama proposed a

critical concentration of 500 ppm above which the linear relationship will no longer be valid and the effects will increase salama (Salama 2000). Sand production rate Q_s in kg/s can be converted into ppm using the following equation:

5-9

$$ppm = \frac{Q_s}{\pi D^2 V_f \rho_f} \times 10^6$$

Figure 5-22 shows the variation of erosion rate with sand production rate for air and Table 5-8 shows the variation of erosion rate with fluid and particles velocity for different sand flow rates for air.

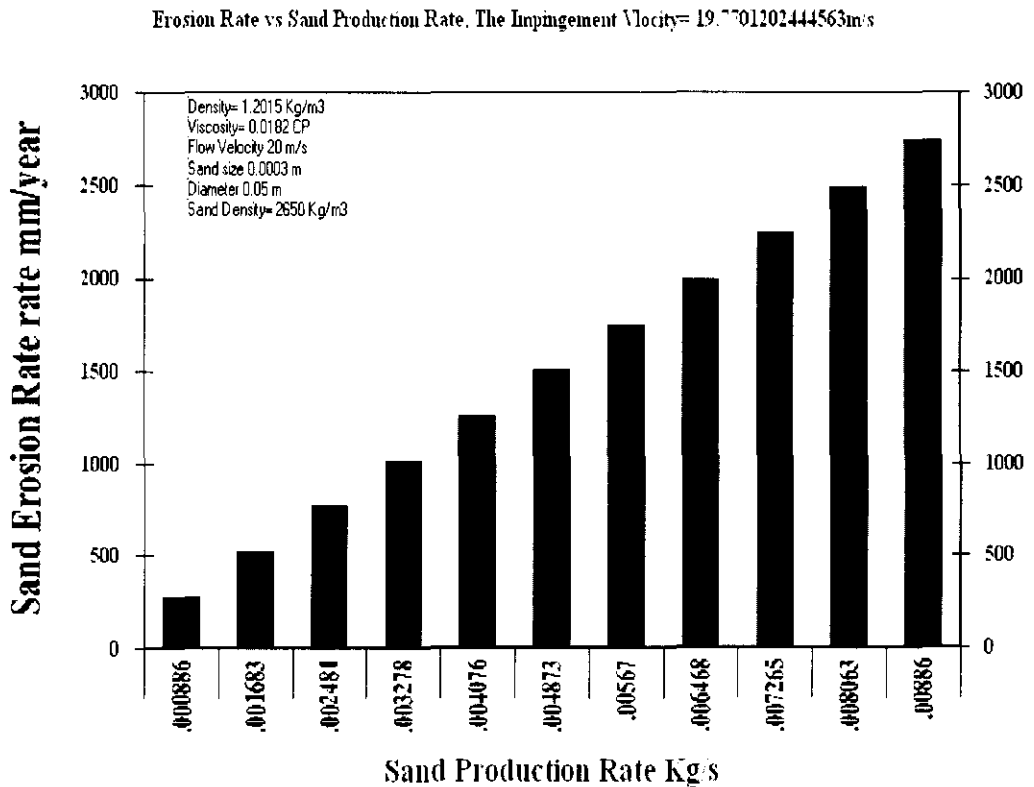


Figure 5-22: The variation of erosion rate with sand rates (air)

Table 5-8: The variation of erosion rate with velocity at different sand production rate

Sand Prod Rate Kg/s		0.000887	0.001774	0.002661	0.003547
Vf (m/s)	Vp (m/s)	Erosion Rate mm/year			
1	0.955189	1.450863	2.901725	4.352588	5.803451
2	1.945354	4.96637	9.93274	14.89911	19.86548
3	2.935589	10.120087	20.24017	30.360261	40.480348
4	3.925841	16.733053	33.46611	50.199158	66.932211
5	4.916101	24.693094	49.38619	74.079281	98.772375
6	5.906364	33.919974	67.83995	101.759921	135.679894
7	6.896629	44.352013	88.70403	133.056038	177.40805
8	7.886895	55.939563	111.8791	167.81869	223.758253
9	8.877162	68.641359	137.2827	205.924077	274.565436
10	9.86743	82.422274	164.8445	247.266822	329.689096
11	10.8577	97.251859	194.5037	291.755577	389.007436
12	11.84797	113.10333	226.2067	339.30999	452.41332
13	12.83824	129.952849	259.9057	389.858547	519.811396
14	13.8285	147.778988	295.558	443.336965	591.115953
15	14.81877	166.562327	333.1247	499.686982	666.249309
16	15.80904	186.285139	372.5703	558.855418	745.140557
17	16.79931	206.931144	413.8623	620.793432	827.724575
18	17.78958	228.485309	456.9706	685.455927	913.941236
19	18.77985	250.933689	501.8674	752.801066	1003.734755
20	19.77012	274.263291	548.5266	822.789873	1097.053164
21	20.76039	298.461967	596.9239	895.385901	1193.847868
22	21.75066	323.518318	647.0366	970.554954	1294.073272
23	22.74093	349.421616	698.8432	1048.264848	1397.686464
24	23.7312	376.161736	752.3235	1128.485209	1504.646945

5.7 Validation and evaluation of sand erosion prediction models

5.7.1 Validation and evaluation of Salama Empirical model

The code results have been compared with published measured data [Salama 2000, Shirazi et al. 1995]. The erosion rate in the published data is expressed in unit of mm/kg, which means material loss in mm for every kg of sand hits the target. The predicted erosion rate in mm/year is converted to mm/kg using the following relationship:

$$E(L/M) = \frac{1}{CF} \frac{ER(L/T)}{W(M/T)}$$

5-10

Where W is sand production rate and CF is a conversion factor for converting unit of sand production rate to kg/year. The value of CF for different unit of W is contained in Table 5-9 provided that ER unit is mm/year. L, M, and T denote dimensions of length, mass, and time respectively.

Table 5-9: Values of CF for different unit of sand production rate (W)

Unit of sand production rate (W)	CF
kg/s	31536000
kg/day	365
kg/hr	8760

Table 5-10 and Figure 5-23 show that the predicted results by Salama model overestimates the measured data.

Table 5-10: Validation of the code results (Salama model) using published data

	V_l m/s	V_g m/s	ρ_m kg/m ³	d sand micron	D pipe mm	Bend radius *Dpipe	ER measured	ER predicted	Relative error (%)	Average absolute relative error (%)
1	30	34.48	150	49	5	5.52E-04	8.83E-04	-6.0E+01	5.35E+01	
5.8	20	226.59	150	49	1.5	5.19E-05	9.16E-05	-7.65E+01		
6.2	9	413.5	250	26.5	5	1.80E-04	9.93E-05	4.48E+01		
0.5	34.3	24.1	250	26.5	5	7.20E-03	8.98E-03	-2.47E+01		
0.7	52	23	250	26.5	5	1.33E-02	2.15E-02	-6.17E+01		

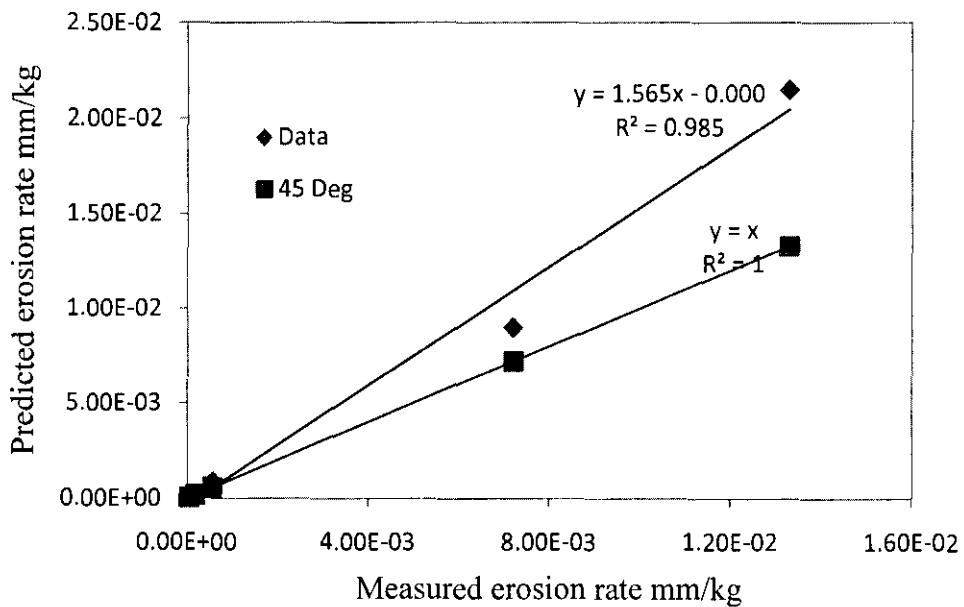


Figure 5-23: Validation of Salama model

An attempt is made to improve the accuracy of Salama model. Another set of data measured by Bourgoyne (Bourgoyne 1989) and Tolle and Greenwood (Tolle and Greenwood 1977) has been added to the data in Table 5-10. The whole data is included in Appendix C. The whole data is categorized into three groups according to the gas-liquid-ratio (GLR) as follows:

Pure gas flow at

$$\frac{V_{sl}}{V_{sg}} = 0$$

5-11

High Gas Liquid Ratio at

$$0 < \frac{V_{sl}}{V_{sg}} \leq 0.155$$

5-12

Low Gas Liquid Ratio at

$$\frac{V_{sl}}{V_{sg}} > 0.155$$

5-13

From

Figure 5-24 to

Figure 5-26, the measured values are related to the predicted values for the three types of flow as follows:

Pure gas flow:

$$\log ER_m = 0.296 \ln(ER_p) - 0.985$$

5-14

High gas liquid ratio flow:

$$\log ER_m = 0.462 \ln(ER_p) + 0.349$$

5-15

Low gas liquid ratio flow:

$$\log ER_m = 0.347 \ln(ER_p) - 0.99$$

5-16

The Salama model predicts the erosion rate in mm/year from the following equation:

$$ER = \frac{11.57WV_m^2 d_p}{S_m D^2 \rho_m}$$

Considering the value of S_m for elbow, the erosion rate (ER) unit is converted from mm/year to mm/kg (the unit of the collected data) as follows:

$$ER = \left[\frac{11.578WV_m^2 d_p}{5.5D^2 \rho_m} \right] \times \frac{1}{W} \times \frac{1}{3600 \times 24 \times 365}$$

$$ER = 6.66 \times 10^{-8} \left[\frac{V_m^2 d_p}{D^2 \rho_m} \right] \quad 5-18$$

By substituting ER in Equation 5-17 for ER_p in Equations 5-13 to 5-15, the modified erosion rate prediction equations can be written for the three flow types as follows:

$$\log(ER_{act}) = \begin{cases} 0.296 \ln \left[\frac{V_m^2 d_p}{D^2 \rho_m} \right] - 7.621 & \frac{V_{sl}}{V_{sg}} = 0 \\ 0.462 \ln \left[\frac{V_m^2 d_p}{D^2 \rho_m} \right] - 10.009 & 0 < \frac{V_{sl}}{V_{sg}} \leq 0.155 \\ 0.347 \ln \left[\frac{V_m^2 d_p}{D^2 \rho_m} \right] - 6.7895 & \frac{V_{sl}}{V_{sg}} > 0.155 \end{cases} \quad 5-19$$

Where:

ER_{act} = Actual erosion rate, mm/kg.

W = Sand production rate in kg/s.

V_m = Mixture flow rate, m/s.

D= Elbow diameter, m.

d= Particles size, micron.

ρ_m =Mixture density, kg/m³.

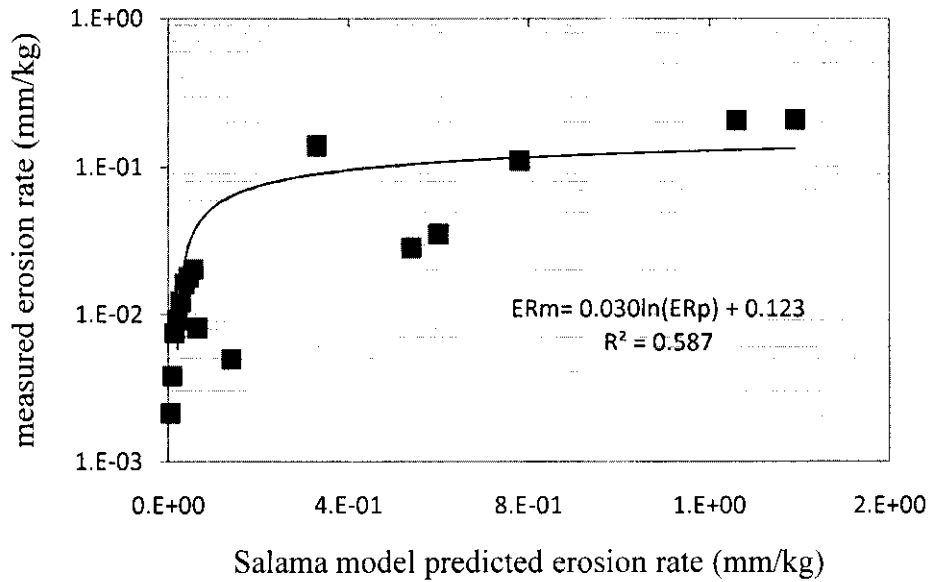


Figure 5-24: Comparison of Salama model predicted values with measured data (pure air)

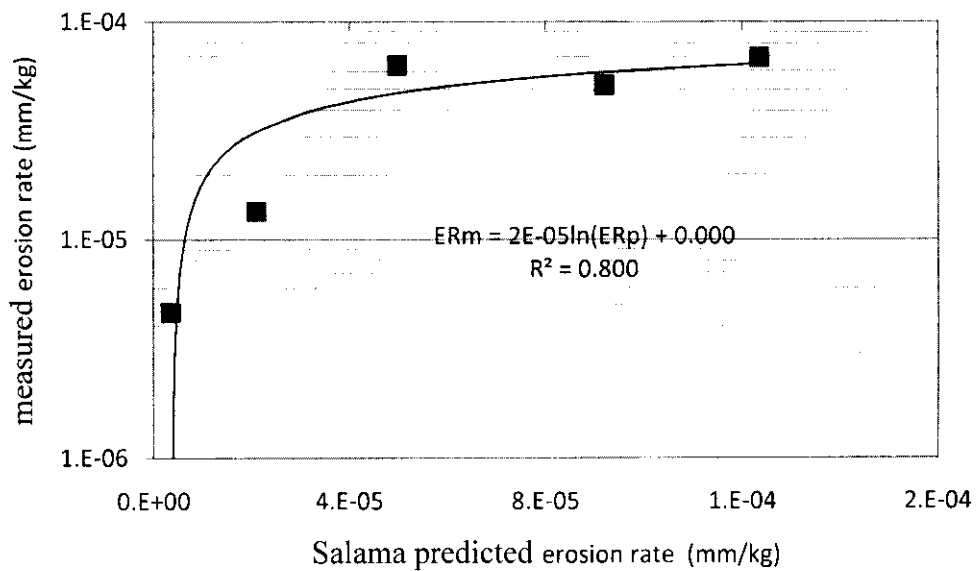


Figure 5-25: Comparison of Salama model predicted data with measured data
(low gas liquid ratio)

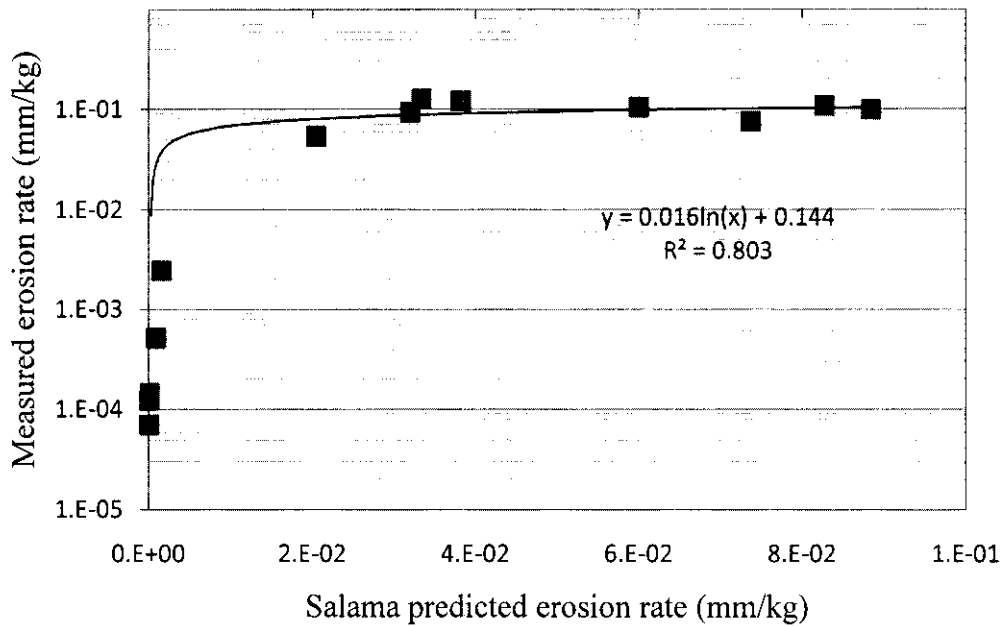


Figure 5-26: Comparison of Salama model predicted data with measured data (high gas liquid ratio)

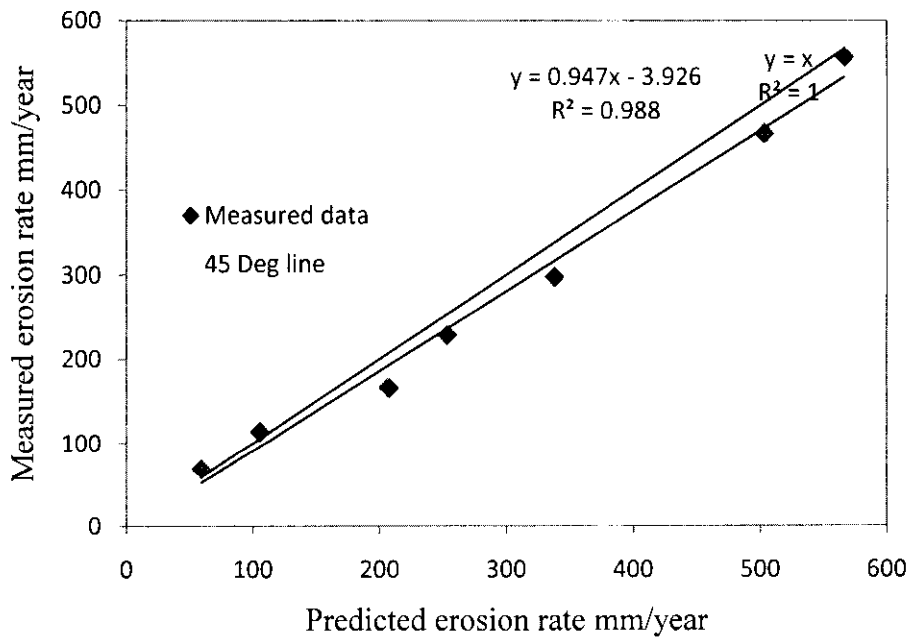
5.7.2 Validation and evaluation of Direct Impingement Model (DIM)

DIM model was verified using measured data from literature. Good agreement has been found between results from the direct impingement code and the published data as shown in Table 5-11 and Figure 5-27. This can be seen from the fitting curve equation in Figure 5-27. The DIM model slightly underestimates the measured data; however, its accuracy is acceptable since the predicted points are not far from the 45° straight line.

Table 5-11: Validation of the DIM results using published data (McLaury and Shirazi 1999)

V m/s	Sand rate kg/s	ρ_m kg/m ³	Viscosity Pa.s	d sand micron	D pipe mm	Sand shape	ER meas. mm/y	ER pr. mm/y	Relative error (%)	Average absolute relative error (%)
9.14	0.0008801	1.2015	0.0000182	300	50.8	angular	59.182	68.8848	-9.18269	7.3278
12.2	0.000881	1.2015	0.0000182	300	50.8	angular	105.664	113.64	-3.84823	
15.24	0.000875	1.2015	0.0000182	300	50.8	angular	207.264	165.862	16.31632	
18.29	0.0008797	1.2015	0.0000182	300	50.8	angular	253.746	229.006	7.323427	
21.34	0.000878	1.2015	0.0000182	300	50.8	angular	337.82	297.917	7.934264	
27.44	0.000886	1.2015	0.0000182	300	50.8	angular	502.92	466.954	6.349705	
30.49	0.000881	1.2015	0.0000182	300	50.8	angular	566.42	557.174	0.340202	

Figure 5-27: Validation of Direct Impingement model



The Salama and DIM models used to develop the code have been compared with the CFD results using the same parameters of the CFD simulation as input data to the code.

Figure 5-28 shows fair agreement between DIM and CFD models, whereas the Salama model predicts much higher erosion rate as compared to the other two models.

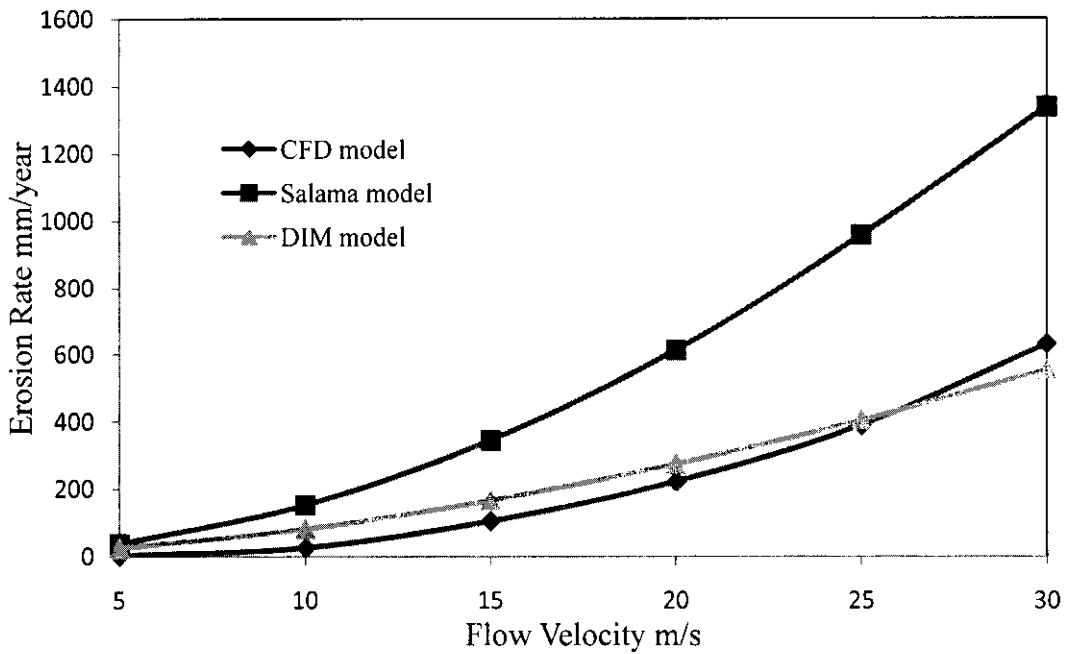


Figure 5-28: Comparison of results of Salama, DIM, and CFD models

The CFD model can be considered as a benchmark for evaluating the Salama and DIM models as it employs more sophisticated solutions for the primary and secondary phases before predicting erosion rate. As the DIM model agreed fairly with both the CFD results and measured data, the Salama model can then be improved further by comparing it with the DIM model.

Comparing the salama model with DIM model resulted in unexpected outcome. It was observed that the erosion rates from Salama model are higher than those from the DIM model for gas flow, whereas they are lower than the DIM model for water. For oil, the erosion rate from Salama model underestimates that of DIM model at low erosion rate and overestimates it for higher erosion rate. Figure 5-29 through Figure 5-31 show comparison between Salama model and DIM model for gas, water, and oil flow, respectively.

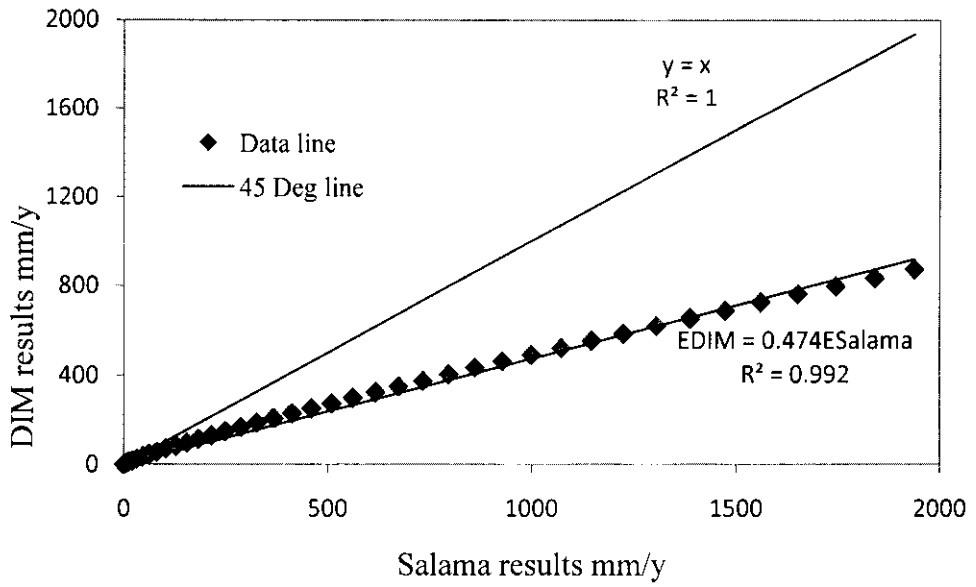


Figure 5-29: Comparison between Salama model and DIM model (gas)

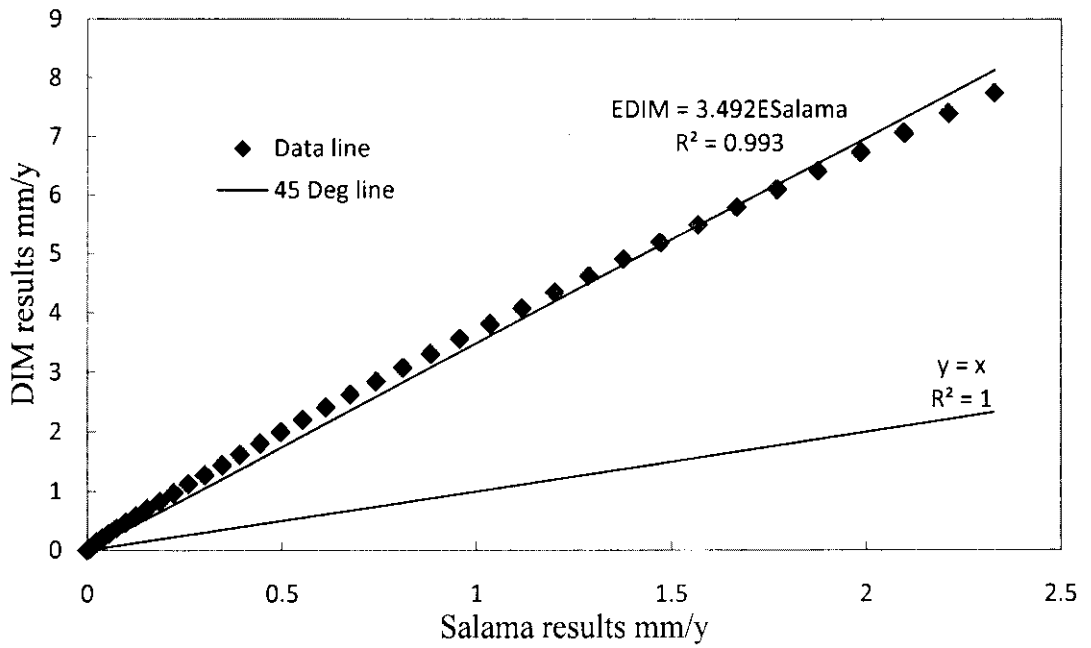


Figure 5-30: Comparison between Salama model and DIM model (water)

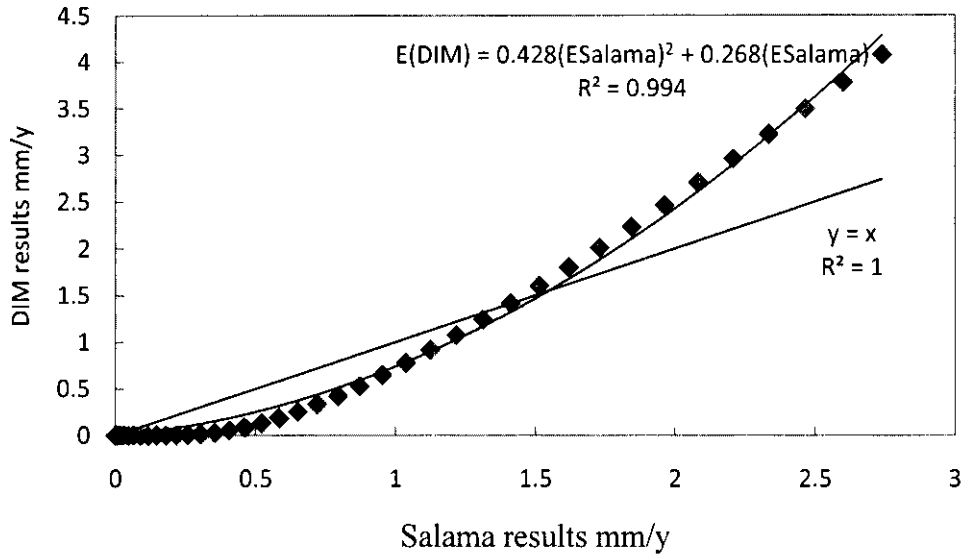


Figure 5-31: Comparison between Salama model and DIM model (oil)

5.8 Extension of Salama model to oils flow (Mysara (UTP) model)

In this section, we improve Salama model to include the effect of fluid viscosity to the original model. Doing so, a new model that combines the simplicity of Salama model and the accuracy of DIM model is proposed to be used for erosion prediction in elbows during flow of oil.

5.8.1 Development of Mysara (UTP) model

To improve Salama model to account for viscosity, its predicted erosion rate results were compared with the DIM model results for oil with different viscosity as shown in Table 5-11. From the table, Salama model predicts non-zero erosion rate for all flow velocities greater than zero, whereas DIM model predicts zero erosion rates as long as flow velocity is lower than a critical value, referred to as erosional velocity, which is proportionally related to viscosity. When plotting erosional velocity with viscosity as shown in Figure 5-32, the relationship can be written as follows:

$$V_{el} = 1227\mu$$

5-20

Where μ is the viscosity in Pa.s

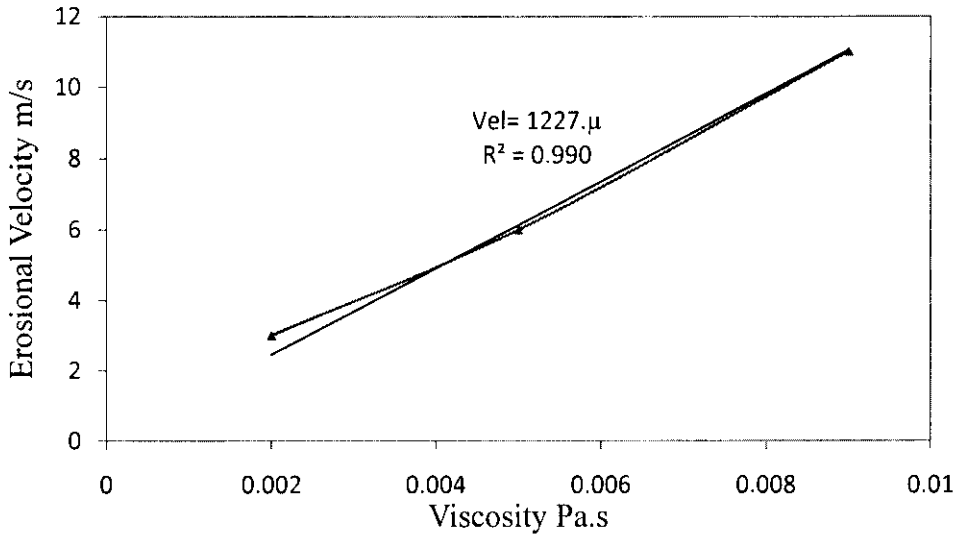


Figure 5-32: Variation of erosional velocity with viscosity

The erosion rates predicted by Salama model exceeds those predicted by DIM model for velocities lower than another critical value, referred to as abnormal velocity. From Figure 5-33, abnormal velocity is also proportionally related to viscosity as follows:

$$V_{ab} = 3081\mu$$

5-21

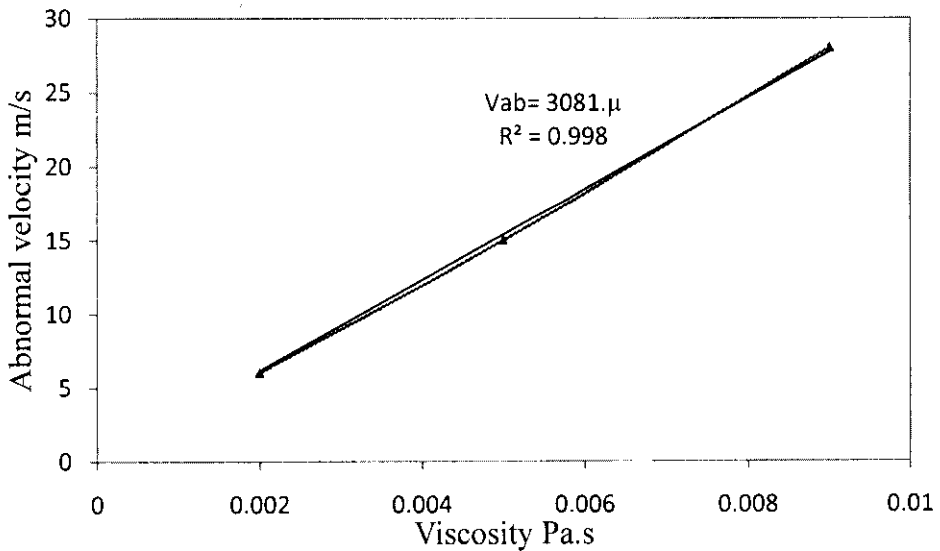


Figure 5-33: Variation of abnormal velocity with viscosity

Before the comparison between Salama model and DIM model, the unit of erosion rate is converted from mm/year to mm/kg (erosion rate in mm/year per every sand production rate in kg/year) using equation 5-10. As a result of the comparison between Salama model and DIM model, the following equation was developed for modification of Salama model:

$$E_m = \begin{cases} 0 & V < V_{el} \\ A_l E_s - B_l & V_{el} \leq V \leq V_{ab} \\ A_u E_s - B_u & V \geq V_{ab} \end{cases} \quad 5-22$$

Where

E_m is the modified mass loss rate (mm/kg)

E_s is the mass loss rate predicted by Salama model (mm/kg)

A_l, B_l, A_u and B_u are constants related to fluid viscosity as follows:

$$A_l = -47.06\mu + 1.522$$

$$B_l = 0.001\mu - 2E - 06 \quad 5-23$$

$$A_u = -175.6\mu + 3.556$$

$$B_u = 0.006\mu - 1E - 05$$

The relationship at $V_{el} \leq V \leq V_{ab}$ was developed from Figure 5-34 through 5-36 and then variation of the constants A_l and B_l is drawn against viscosity as shown in Figure 5-37 and Figure 5-38. Similarly, the relationship at $V \geq V_{ab}$ was developed from Figure 5-39 through 5-41 and the variation of the correction factors A_u and B_u with viscosity is obtained from Figure 5-42.

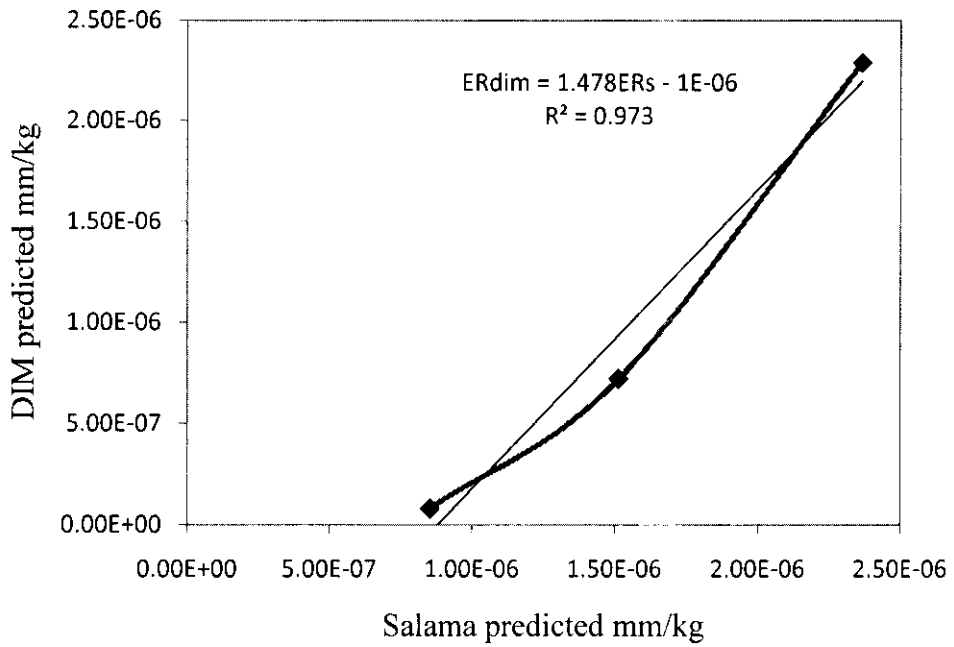


Figure 5-34: Comparison between Salama and DIM below abnormal velocity (0.002 Pa.s)

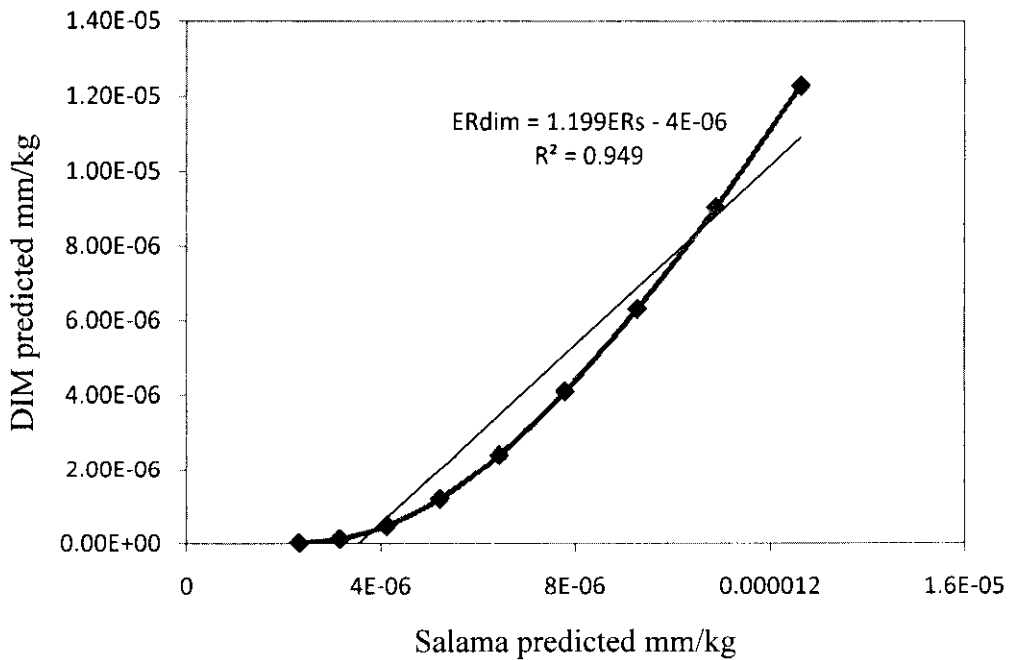


Figure 5-35: Comparison between Salama and DIM below abnormal velocity (0.005 Pa.s)

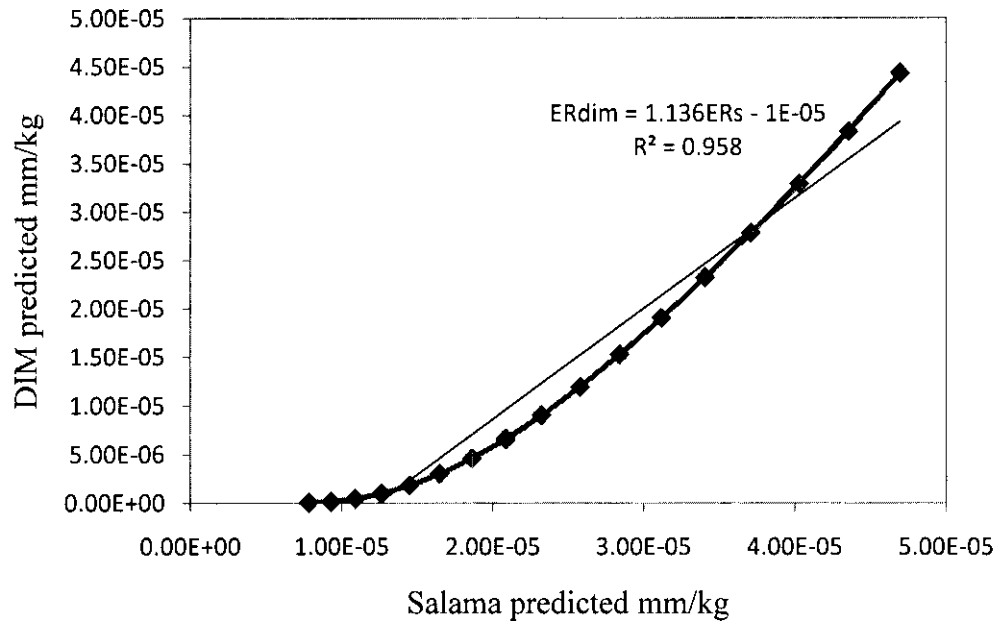


Figure 5-36: Comparison between Salama and DIM below abnormal velocity (0.009 Pa.s)

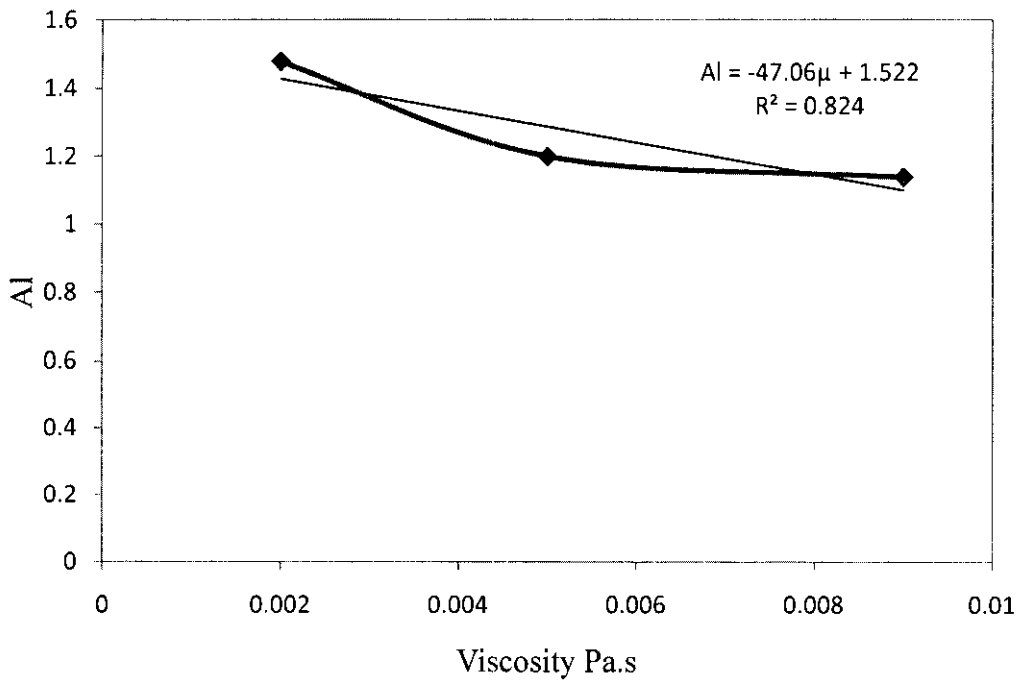


Figure 5-37: Variation of Al with viscosity

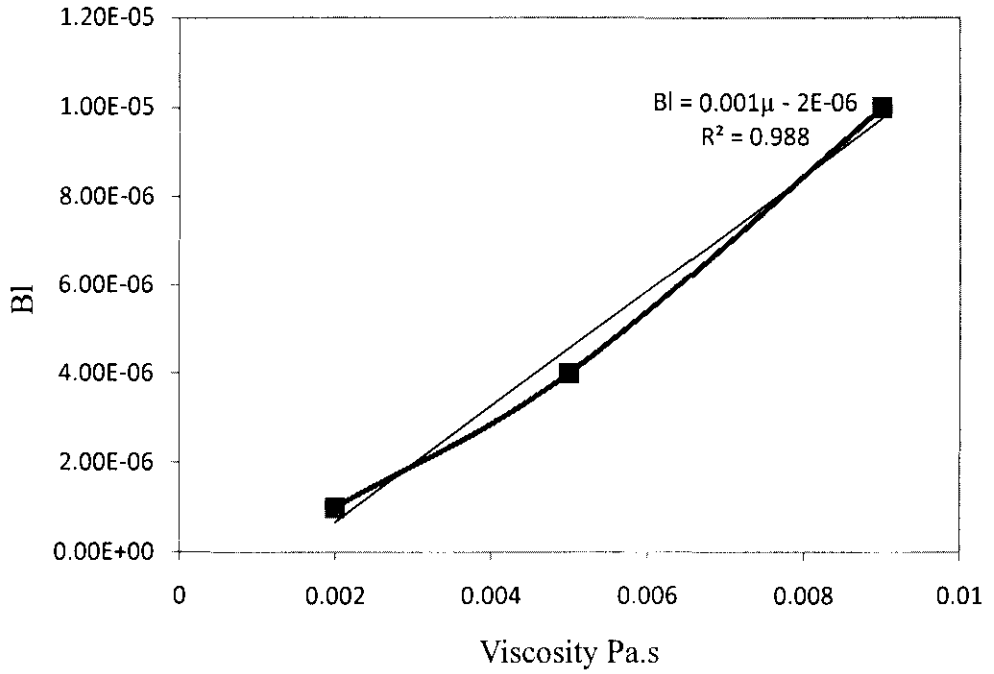


Figure 5-38: Variation of BI with viscosity

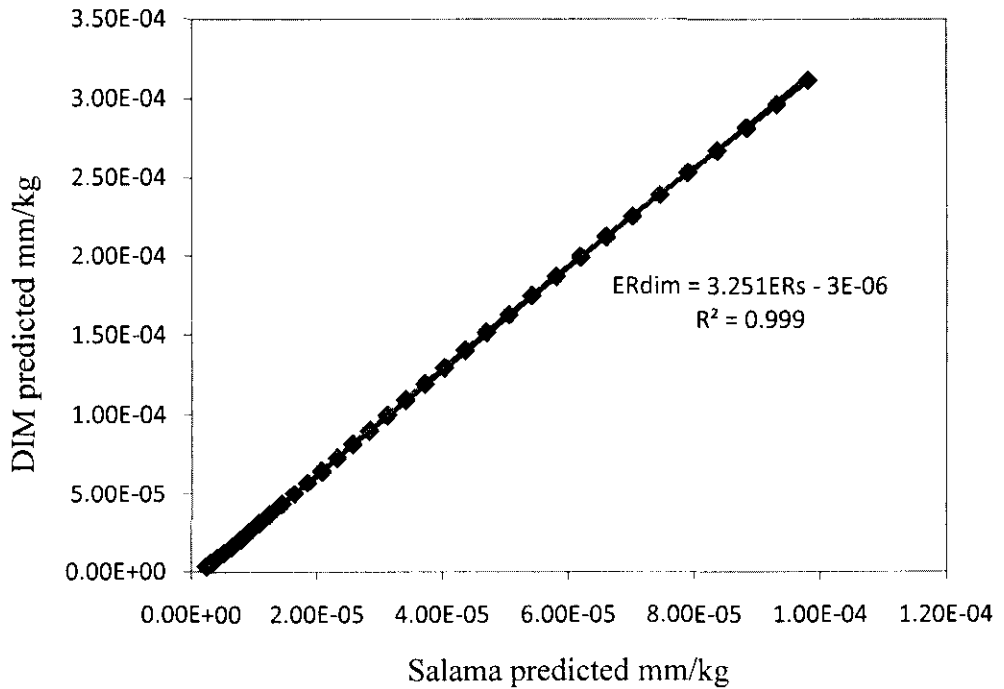


Figure 5-39: Comparison between Salama and DIM above abnormal velocity (0.002 Pa.s)

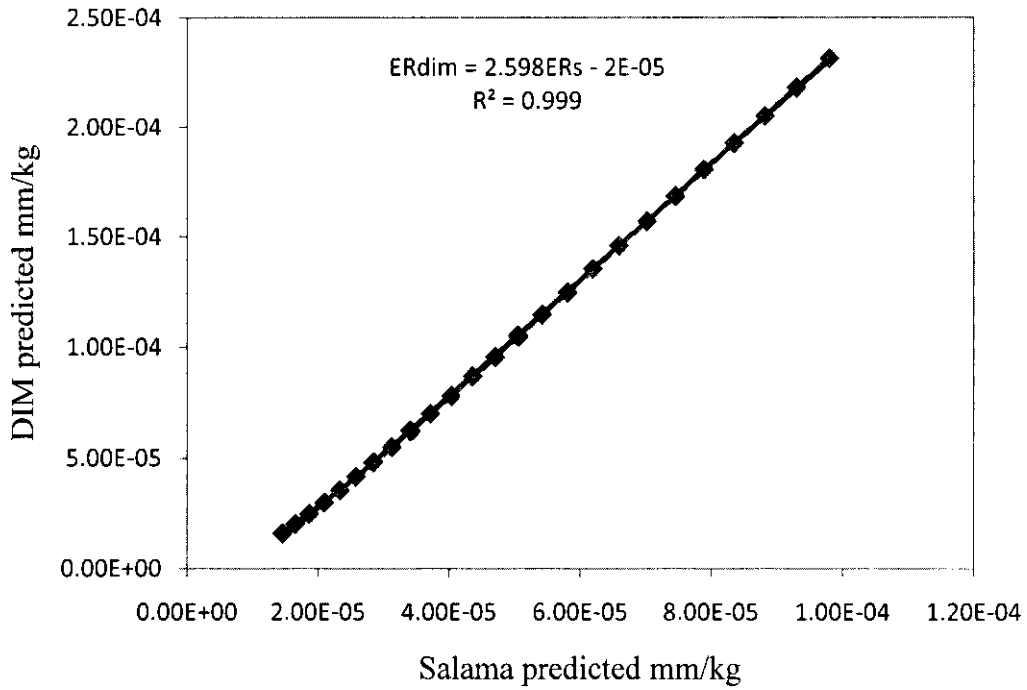


Figure 5-40: Comparison between Salama and DIM above abnormal velocity (0.005 Pa.s)

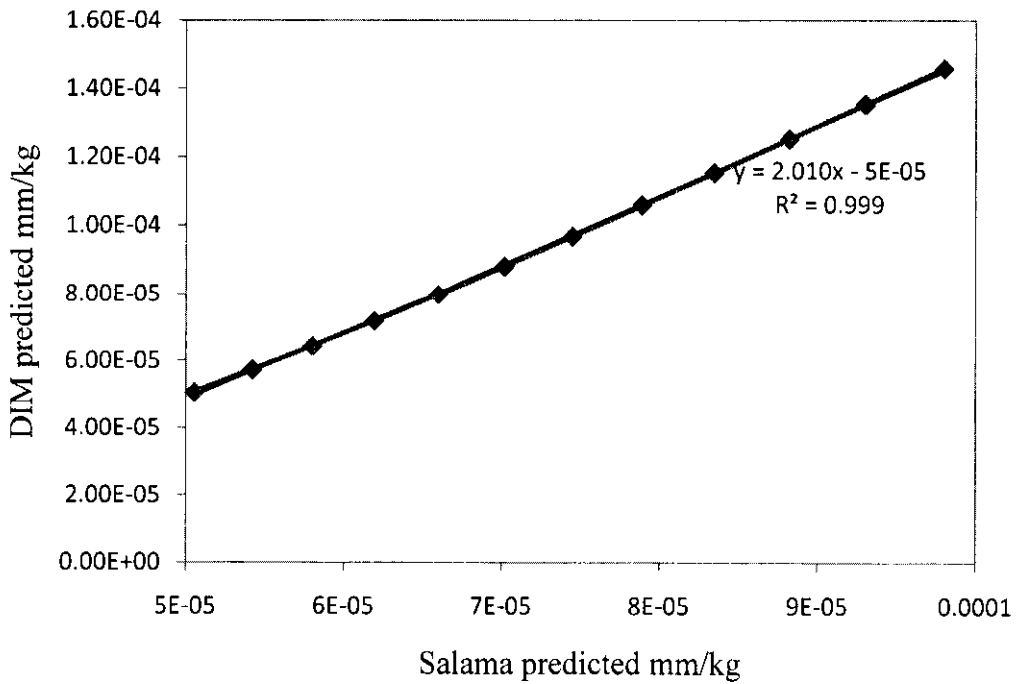


Figure 5-41: Comparison between Salama and DIM above abnormal velocity (0.009 Pa.s)

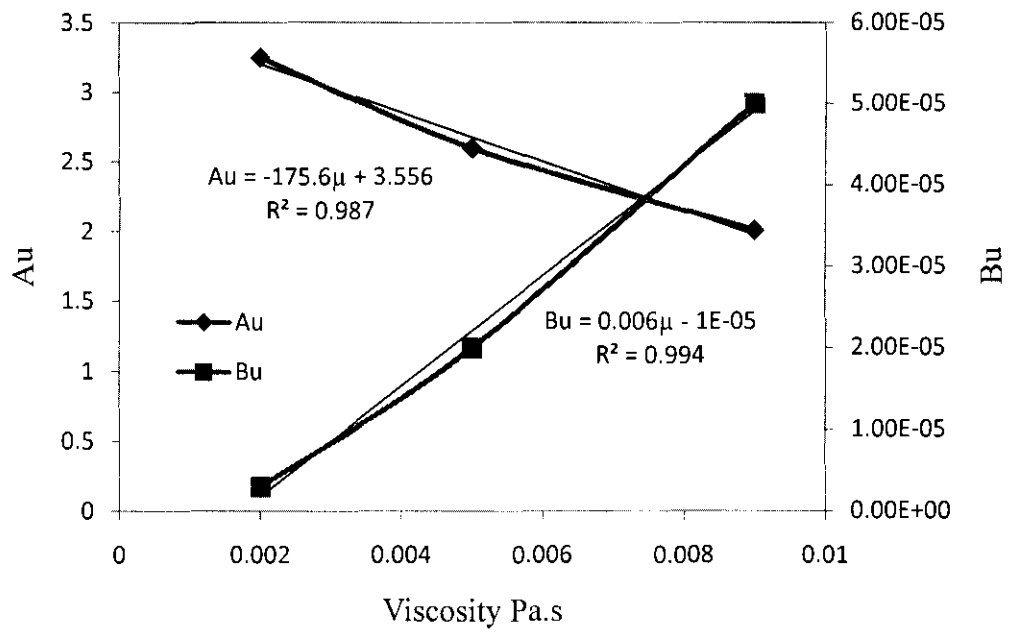


Figure 5-42: Variation of Au and Bu with viscosity

Table 5-12: Comparison of Salama and DIM results for oil with different viscosity

V m/s	Erosion rate mm/year				V m/s	Erosion rate mm/year			
	Salama	DIM				Salama	DIM		
		0.002 Pa.s	0.005 Pa.s	0.009 Pa.s			0.002 Pa.s	0.005 Pa.s	0.009 Pa.s
0	0	0	0	0	20	0.72	2.28	1.16	0.33
1	0.0018	0	0	0	21	0.79	2.53	1.35	0.43
2	0.0072	0	0	0	22	0.87	2.79	1.54	0.53
3	0.016	0.0015	0	0	23	0.95	3.055	1.74	0.65
4	0.029	0.0137	0	0	24	1.037	3.33	1.96	0.777
5	0.045	0.0436	0	0	25	1.125	3.62	2.2	0.92
6	0.065	0.092	0.00053	0	26	1.22	3.92	2.42	1.07
7	0.09	0.157	0.0036	0	27	1.31	4.23	2.67	1.23
8	0.115	0.24	0.013	0	28	1.41	4.555	2.9	1.4
9	0.146	0.336	0.034	0	29	1.51	4.9	3.2	1.6
10	0.18	0.448	0.067	0	30	1.62	5.22	3.48	1.8
11	0.218	0.574	0.115	0.002	31	1.73	5.57	3.777	2.01
12	0.26	0.714	0.176	0.0057	32	1.84	5.93	4.078	2.23
13	0.304	0.87	0.25	0.014	33	1.96	6.3	4.4	2.46
14	0.353	1.03	0.343	0.029	34	2.08	6.68	4.7	2.7
15	0.405	1.21	0.45	0.052	35	2.205	7.067	5.04	2.96
16	0.461	1.40	0.57	0.085	36	2.33	7.46	5.38	3.2
17	0.52	1.60	0.7	0.129	37	2.46	7.87	5.73	3.496
18	0.58	1.82	0.84	0.185	38	2.6	8.28	6.09	3.78

The set of Equations 5-21 and 5-22 (referred to as Mysara-UTP model) are employed to the computational package following the flow chart shown in Figure 5-43.

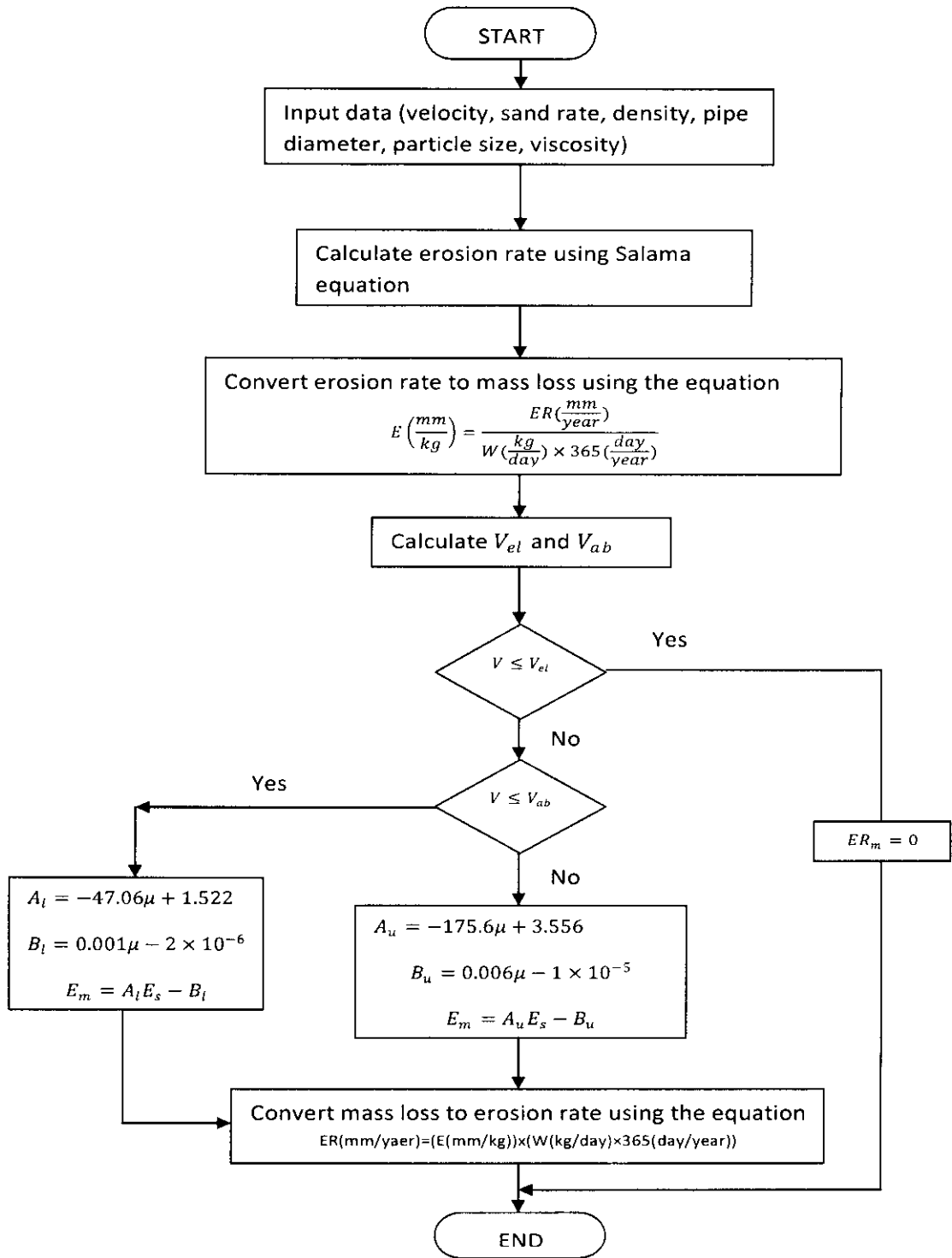


Figure 5-43: Flow chart of calculation procedure using Mysarar (UTP) model

5.8.2 Validation of Mysara (UTP) model

It is recommended that, the model is to be applied to oils with viscosities greater than 0.001 Pa.s (1 cp). For gas and water, the fitting equations of the curves in Figure 5-29 and Figure 5-30 are to be used instead.

To ensure that the model is as accurate as the DIM model, results from the model for erosion rate from oil flow in elbow were compared with results from DIM model under the same input data. Figure 5-44 shows good agreement between the two models.

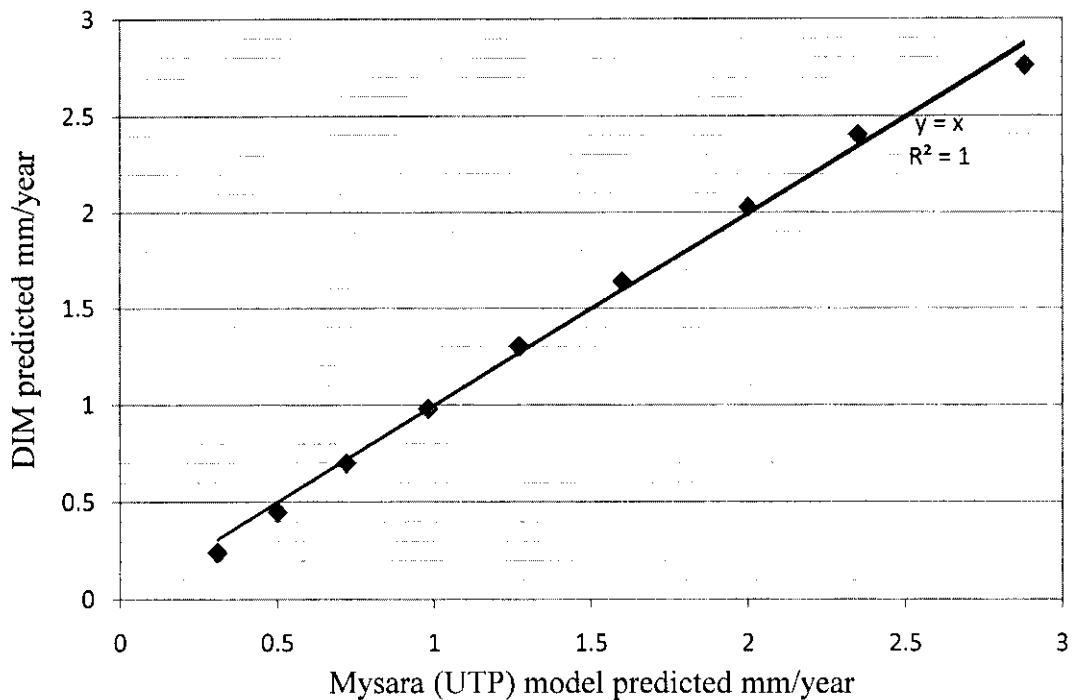


Figure 5-44: Comparison of Mysara (UTP) model with the DIM model (2-in elbow, sand rate=43.2 kg/day, viscosity=4 cp, density=900 kg/m³, particles size=300 micron)

Unfortunately, to our knowledge, no available data in open literature for sand erosion in oil flow. To validate our model, data from Shirazi et al (Shirazi *et al.* 1995) for clay/water mud with viscosity of 6 cp (0.006 Pa.s) are used. The geometry is a 2-in (0.05 m) elbow, the sand particle diameter is 350 micron, the sand flow rate is 1754 ft³/day (131720 kg/day (considering sand density of 2650 kg/m³)), the fluid velocity

31 ft/s (9.45 m/s), the fluid density is 68.7 b/ft³ (1101 kg/m³). The reported erosion rate is 4238 mil/year (105.95 mm/year).

The calculation output shown in Figure 5-45 gives the following results:

- ❖ The erosional velocity= 7.362 m/s
- ❖ The abnormal velocity= 18.486
- ❖ The erosion rate by Mysara (UTP) model= 116.8 mm/year
- ❖ The erosion rate by Salama model= 249.3 mm/year

By comparing the results obtained by Mysara (UTP) model and Salama model with the reported value, we conclude that Mysara (UTP) model is more accurate.

The input data form of Mysara (UTP) model shown in Figure 5-45 looks similar to the input data form of Salama model (Figure 5-9). In this form, however, viscosity is added to the input data and no geometry selection is included as the model is only applied to elbows.

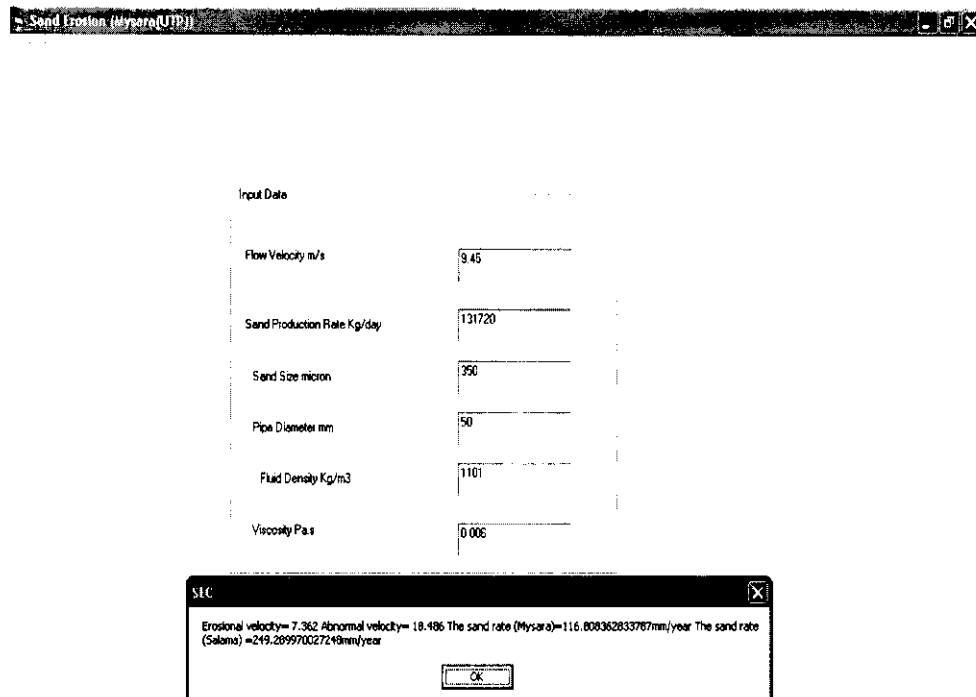


Figure 5-45: The result of calculation using Shirazi et al data

5.8.3 CO₂ corrosion prediction and simulation

Employing the original and modified NORSOK CO₂ corrosion prediction models detailed in section 3.4 to the developed code (software), allows prediction of CO₂ corrosion in straight pipes or elbows under any conditions (input data). In this section we will present and analyze results of the code for CO₂ corrosion in an elbow and a straight pipe under arbitrary selected input data.

Table 5-13 shows the input data entered into the computational code for CO₂ corrosion prediction and simulation. The asterisk * indicates that the parameter can be set as variable, while other parameters are kept constant. That is to say, the corrosion rate variation with velocity, density, viscosity, and CO₂ partial pressure can be obtained as output in tables or graphical forms.

Table 5-13: Input data for corrosion simulation

Parameter	Value
Temperature (°C)	20
CO ₂ partial pressure (Bar)	0.2*
pH	5
System total pressure (Bar)	10
Diameter (m)	0.075
Roughness (m)	0.0005
Fluid density (kg/m ³)	1000*
Fluid viscosity (Pa.s)	0.0015*
Velocity (m/s)	5*

5.8.3.1 CO₂ corrosion prediction and simulation in laminar flow

To investigate the contribution of the different flow parameters (Velocity, density, viscosity, and pipe diameter) on corrosion rate in laminar flow, the change of corrosion rate with respect to these parameters should be quantified. All these parameters implicitly affect the corrosion rate due to their direct relationship with shear stress. The shear stress, therefore, need to be substituted with these parameters. By substituting the Reynolds number (equation 3-38) into the friction factor for laminar flow (equation 3-39), the wall shear stress (using equation 3-30) can be given as follows:

$$S = \frac{16\mu}{\rho V D} \frac{\rho V^2}{2} = \frac{8\mu V}{D} \quad 5-24$$

From the above equation, in laminar flow, the shear stress (and so to the corrosion rate) is directly proportional to viscosity and velocity whereas it is inversely proportional to pipe diameter and not affected by the density.

We will consider the first NORSOK equation (equation 3-26) (which is applicable within $20^\circ C \leq T \leq 150^\circ C$) to obtain the effect of the three parameters on corrosion rate.

$$\text{Let } C_1 = K_i \times f_{CO_2}^{0.62} \times f(pH)_i, C_2 = 0.146 + 0.0324 \log(f_{CO_2}), C_3 = \left[\frac{0.42104\mu}{D} \right]^{C_2}$$

$$, C_4 = \left[\frac{0.421046V}{D} \right]^{C_2}, C_5 = [0.42104\mu V]^{C_2}$$

Then the first equation in the set of equations 3-25 ($20^\circ C \leq T \leq 150^\circ C$) can be written as follows:

$$R_c = C_1 \left[\frac{0.42104\mu V}{D} \right]^{C_2} = C_1 C_3 V^{C_2} = C_1 C_4 \mu^{C_2} = C_1 C_5 \left(\frac{1}{D} \right)^{C_2} \quad 5-25$$

And, the derivative of corrosion rate with respect to velocity, viscosity, and diameter can be obtained as follows:

$$\frac{dCR}{dV} = C_1 C_2 C_3 V^{C_2-1}$$

5-26

$$\frac{dCR}{d\mu} = C_1 C_2 C_4 \mu^{C_2-1}$$

5-27

$$\frac{dCR}{dD} = -C_1 C_2 C_3 D^{-C_2-1}$$

5-28

The above equations indicate that corrosion rate increases with velocity and viscosity while it decreases with pipe diameter.

Considering the parameters in Table 5-13, the velocity below which flow regime is laminar can be calculated by substituting $Re=2000$ as follows:

$$2000 = \frac{1000 \times V_c \times 0.075}{0.002}$$

$$V_c = \frac{2000 \times 0.002}{1000 \times 0.075} = 0.053 \text{ m/s}$$

By introducing velocity values less than 0.05, we obtained the change of corrosion rate with velocity, density, viscosity, and diameter as in Figure 5-46 to Figure 5-49. It is clear that corrosion rate increases with velocity and viscosity, decreases with pipe diameter, and remains constant when density changes, which agrees with the derivation above.

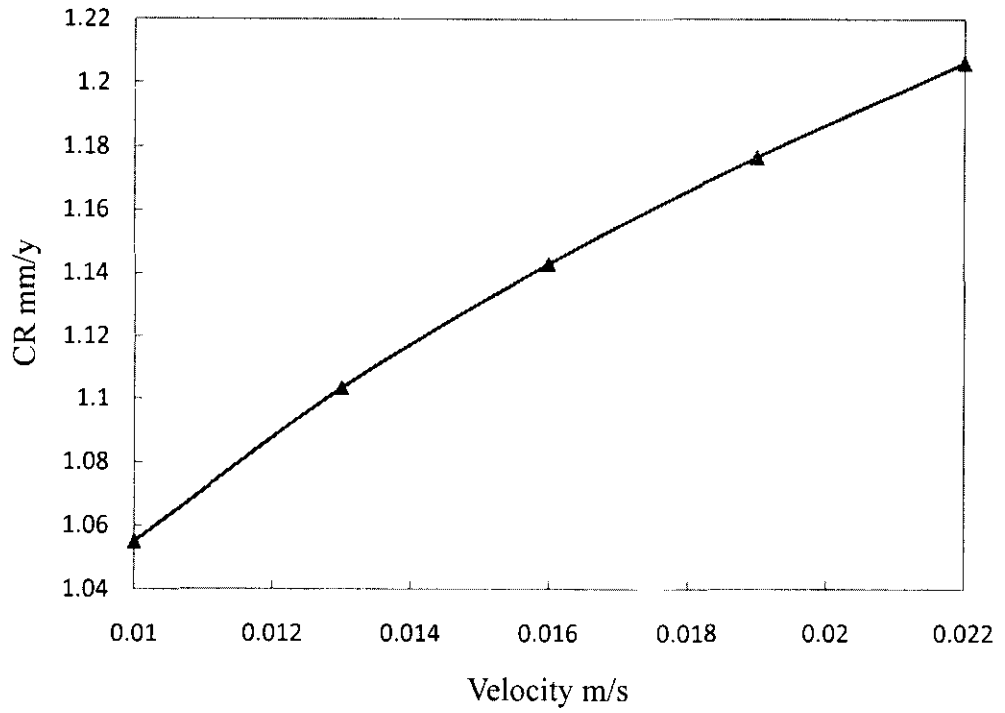


Figure 5-46: Variation of corrosion rate with velocity (laminar regime)

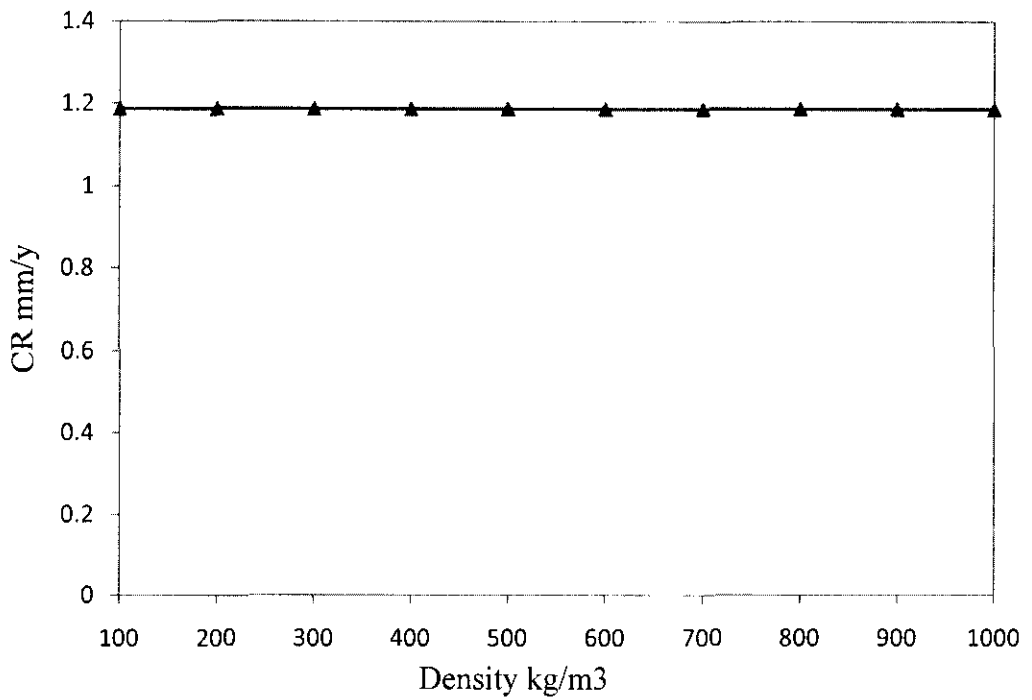


Figure 5-47: Variation of corrosion rate with density (laminar regime)

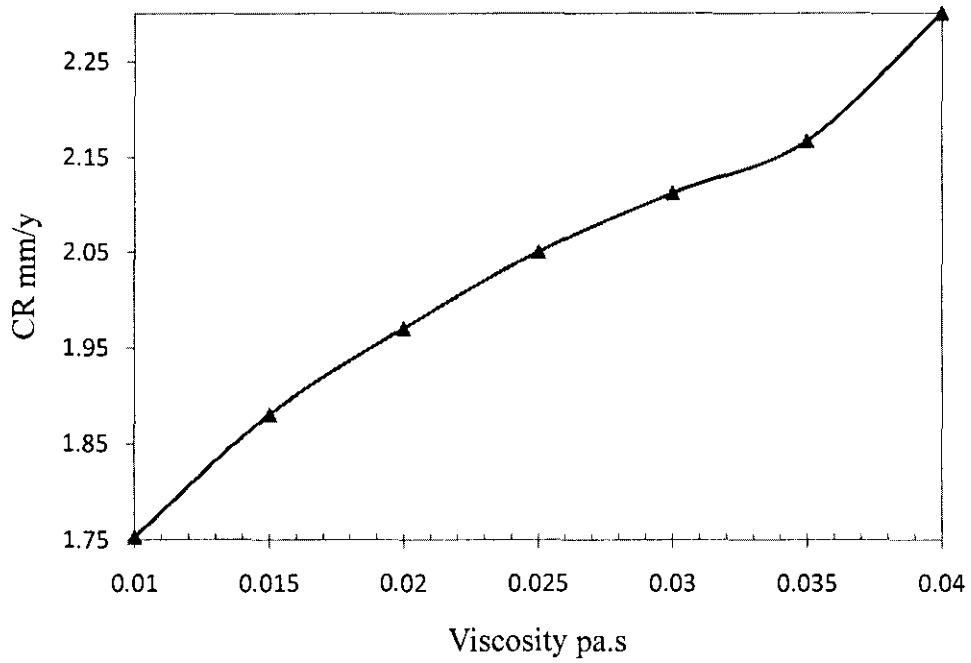


Figure 5-48: Variation of corrosion rate with viscosity (laminar regime)

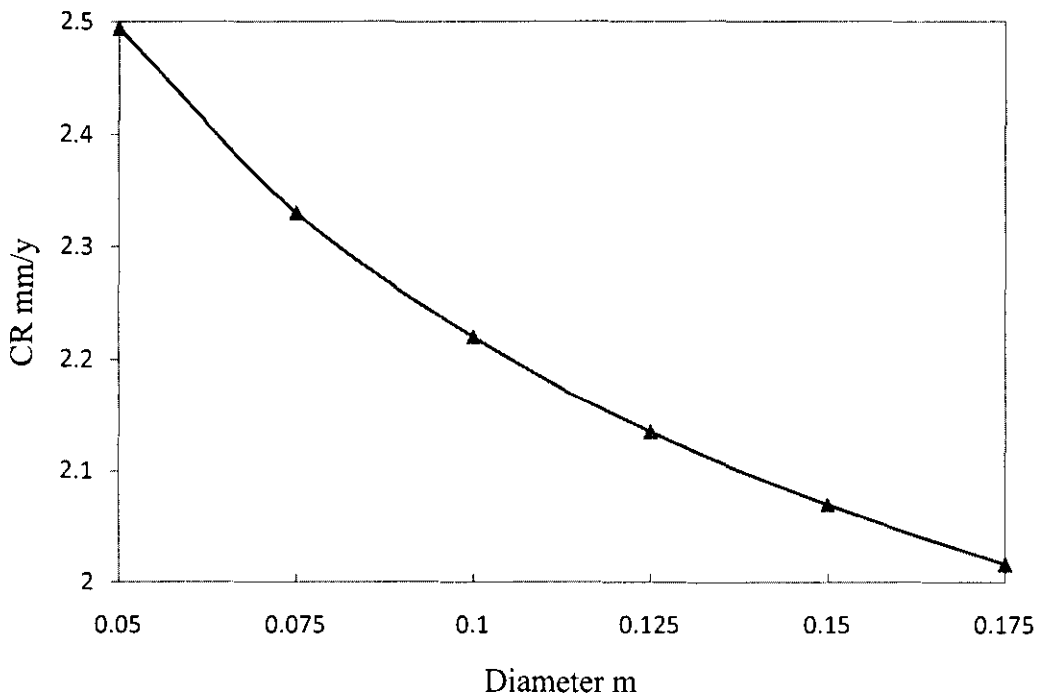


Figure 5-49: Variation of corrosion rate with diameter (laminar regime)

5.8.3.2 CO₂ corrosion prediction and simulation in turbulent flow

In turbulent flow, the friction factor is calculated using the following equation:

$$f = 2 \left[\left(\frac{8}{\text{Re}} \right)^{12} + \left[\left[2.457 \ln \left(\frac{1}{\left(\frac{7}{\text{Re}} \right)^{0.9} + 0.27 \frac{e}{D}} \right) \right]^{16} + \left(\frac{37530}{\text{Re}} \right)^{16} \right]^{-1.5} \right]^{1/12} \quad 5-29$$

By substituting Reynolds number (equation 3-41), we obtain the friction factor as

follows:

$$f = 2 \left[\left(\frac{8\mu}{\rho VD} \right)^{12} + \left[\left[2.457 \ln \left(\frac{1}{\left(\frac{7\mu}{\rho VD} \right)^{0.9} + 0.27 \frac{e}{D}} \right) \right]^{16} + \left(\frac{37530\mu}{\rho VD} \right)^{16} \right]^{-1.5} \right]^{1/12} \quad 5-30$$

And the wall shear stress can be obtained from equation 3-32 as follows:

$$S = \rho V^2 \left[\left(\frac{8\mu}{\rho VD} \right)^{12} + \left[\left[2.457 \ln \left(\frac{1}{\left(\frac{7\mu}{\rho VD} \right)^{0.9} + 0.27 \frac{e}{D}} \right) \right]^{16} + \left(\frac{37530\mu}{\rho VD} \right)^{16} \right]^{-1.5} \right]^{1/12} \quad 5-31$$

It is clear that the differentiation of the above equation is complicated. To quantify the effect of the flow parameters on shear stress (and hence on corrosion), we consider the term including the shear stress in NORSOK equation (Equation 3-27), giving it the name shear stress term (SST), as follows:

$$SST = \begin{cases} (0.05263 \times S)^{0.146+0.0324 \log(f_{CO_2})} & \text{Pipe} \\ (0.5263 \times S)^{0.146+0.0324 \log(f_{CO_2})} & \text{Elbow} \end{cases} \quad 5-32$$

The shear stress term includes the flow parameters (velocity, viscosity, and density). The effects of velocity, viscosity, and density on SST in turbulent flow are given in Figure 5-50, Figure 5-51, and Figure 5-52 respectively. It is clear that the shear stress term (and so corrosion rate) markedly increases with velocity and insignificantly increases with density and viscosity.

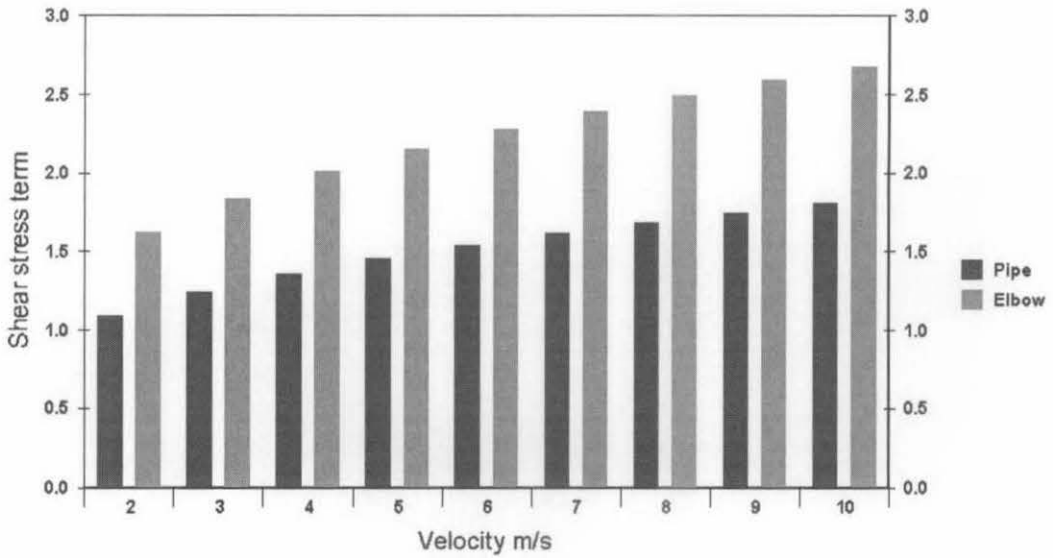


Figure 5-50: Variation of SST with velocity

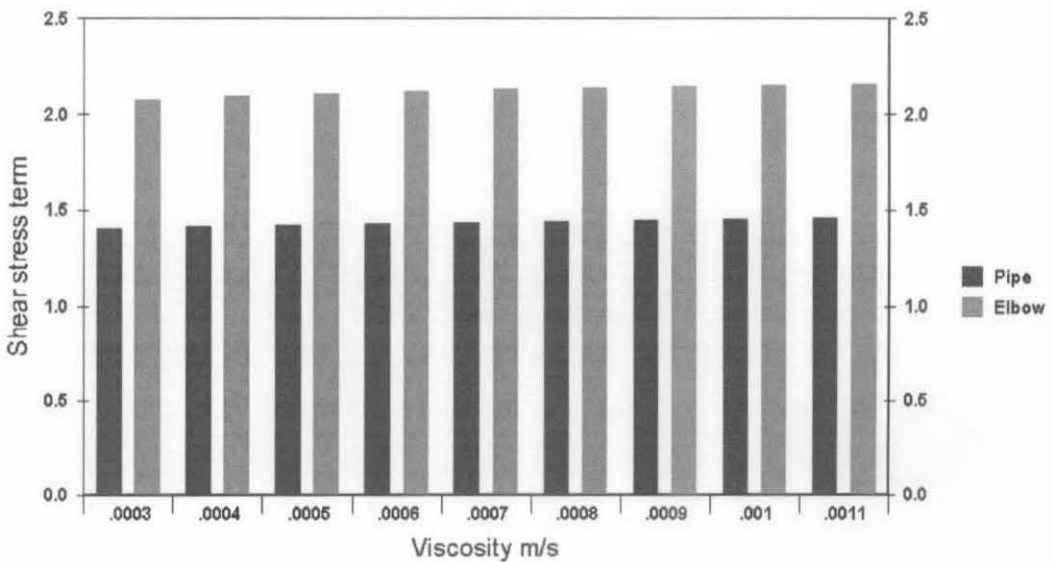


Figure 5-51: Variation of SST with viscosity

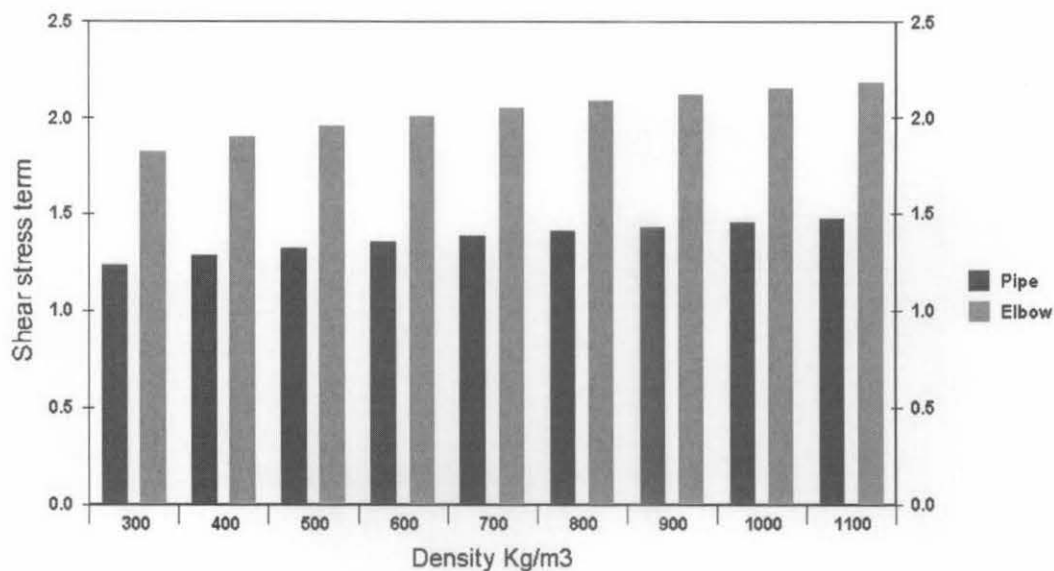


Figure 5-52: Variation of SST with density

5.8.3.2.1 *The effect of flow velocity on CO₂ corrosion*

In the NORSOK model, CO₂ corrosion is implicitly related to flow velocity due to its direct relationship with wall shear stress, which is proportionally related to the velocity raised to the power 2.

Figure 5-53 and Table 5-14 show how CO₂ corrosion rate (mm/year) changes with the flow velocity (m/s) for straight pipe and elbow with the same size using the input data shown in Table 5-13. It is clear that, corrosion rate markedly increases with velocity increase, and it is significantly higher in elbows than in straight pipe.

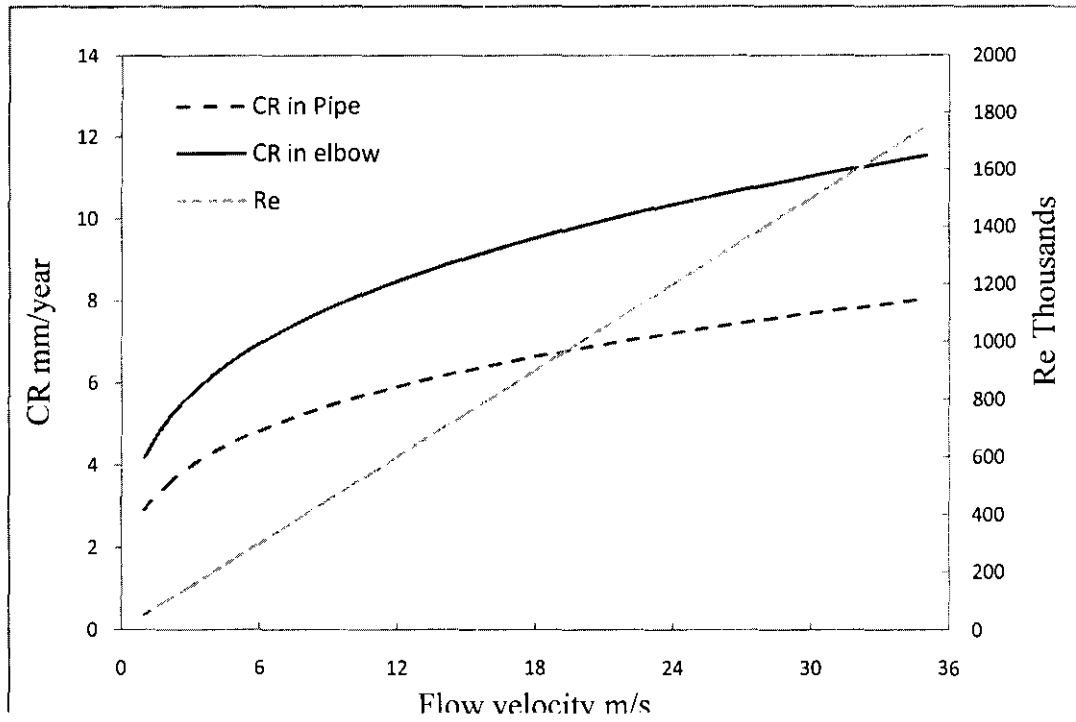


Figure 5-53: The variation of CO₂ corrosion rate (mm/year) with flow velocity (m/s)

Table 5-14: The effect of flow velocity on corrosion rate in straight pipes and elbows

Velocity m/s	Corrosion Rate (St Pipe) mm/year	Corrosion Rate (Elbow) mm/year	Reynolds No.
1	2.914	4.182	50000
2	3.542	5.083	100000
3	3.973	5.702	150000
4	4.311	6.188	200000
5	4.594	6.594	250000
6	4.84	6.946	300000
7	5.058	7.259	350000
8	5.255	7.542	400000
9	5.435	7.8	450000
10	5.602	8.04	500000
11	5.757	8.263	550000
12	5.903	8.472	600000
13	6.04	8.669	650000
14	6.17	8.856	700000
15	6.294	9.033	750000
16	6.412	9.203	800000
17	6.525	9.365	850000
18	6.633	9.52	900000
19	6.737	9.67	950000
20	6.838	9.814	1000000

5.8.3.3 The effect of fluid density on CO₂ corrosion

The fluid density also affects the wall shear stress proportionally. The density increase leads to higher corrosion rate. Again, the increase of corrosion rate is mainly due to the effect of density on wall shear stress. The effect, however, is very slight compared to that of the velocity. Figure 5-45 and Table 5-15 show examples of the effects of fluid density variation on the corrosion rate using the input data shown in Table 5-13. Taking into consideration that oil density is, normally, in the range of 700 to 1000 kg/m³, the effect of oil density on corrosion rate is negligible.

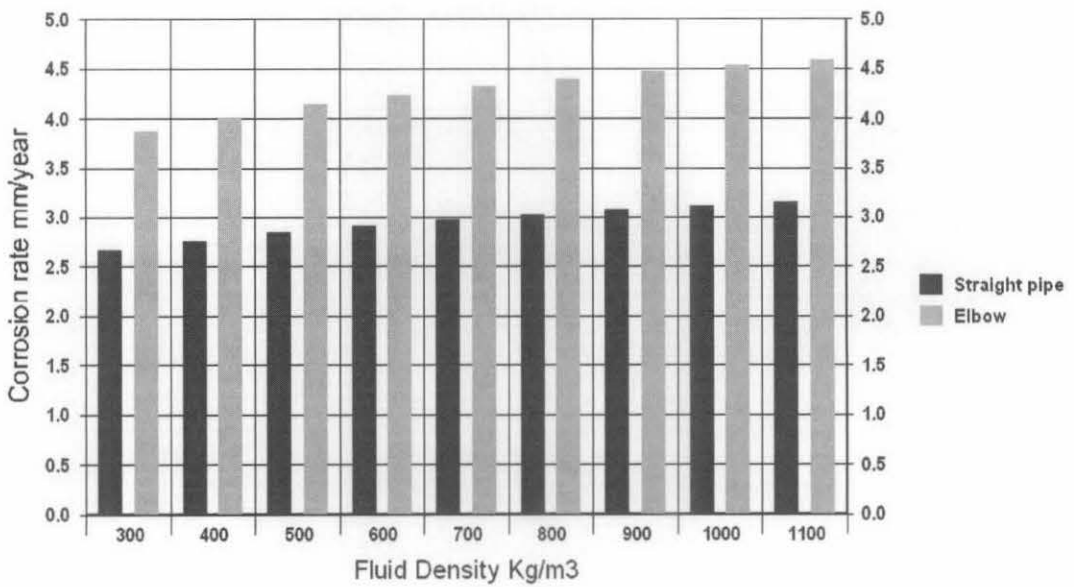


Figure 5-54: The variation of CO₂ corrosion rate (mm/year) with fluid density (kg/m³)

Table 5-15: The effect of fluid density on corrosion rate

Density k/m ³	Corrosion Rate (St Pipe) mm/year	Corrosion Rate (Elbow) mm/year
500	2.847	4.137
525	2.865	4.163
550	2.883	4.189
575	2.9	4.213
600	2.916	4.237
625	2.932	4.26
650	2.947	4.282
675	2.961	4.303
700	2.976	4.324
725	2.989	4.344
750	3.003	4.363
775	3.016	4.382
800	3.028	4.4
825	3.041	4.418
850	3.053	4.436
875	3.064	4.453
900	3.076	4.469
925	3.087	4.486
950	3.098	4.501
975	3.109	4.517
1000	3.119	4.532

5.8.3.4 The effects of fluid viscosity on CO₂ corrosion

Corrosion rate has been found to increase as the fluid viscosity increases. A fluid with higher viscosity generates higher friction factor, which in turns induces higher shear stress. The effect, however, is too low to the extent that it can be neglected; in particular for turbulent flow due to the fact that friction factor does not only depend on Reynolds number but also on roughness. The variation of corrosion rate with viscosity for turbulent flow is shown for straight pipes and elbows in Figure 5-55 and Table 5-16 using the input data shown in Table 5-13.

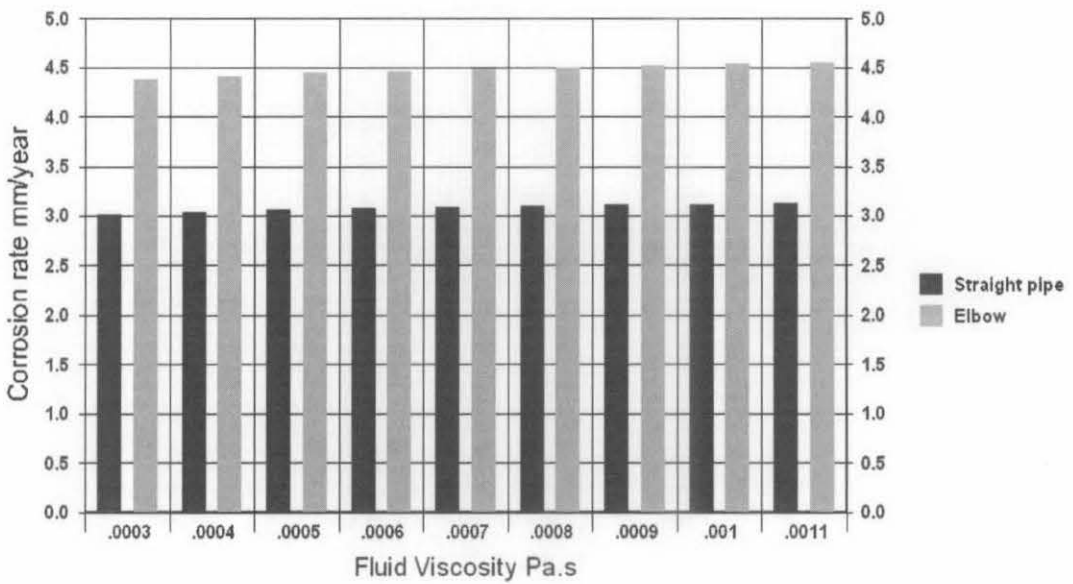


Figure 5-55: The effect of fluid viscosity (Pa.s) on corrosion rate (mm/year)

Table 5-16: The effect of fluid viscosity on corrosion rate

Viscosity mPa.s	Corrosion Rate (St Pipe) mm/year	Corrosion Rate (Elbow) mm/year
0.03	2.85	4.142
0.032	2.854	4.147
0.034	2.858	4.153
0.036	2.861	4.158
0.037	2.865	4.163
0.039	2.868	4.167
0.041	2.871	4.172
0.043	2.874	4.176
0.045	2.877	4.18
0.047	2.879	4.184
0.049	2.882	4.188
0.051	2.885	4.191
0.052	2.887	4.195
0.054	2.889	4.198
0.056	2.892	4.202
0.058	2.894	4.205
0.06	2.896	4.208
0.062	2.898	4.211
0.064	2.9	4.214
0.066	2.902	4.217
0.067	2.904	4.22

5.8.3.5 The effects of CO₂ partial pressure on CO₂ corrosion

The CO₂ partial pressure highly affects corrosion rate. The relationship is directly proportional. From NORSOK model (equation 3-27), CO₂ partial pressure contributes to corrosion rate as CO₂ fugacity which is calculated using equation 3-28 and equation 3-29. CO₂ fugacity affects corrosion rate directly (raised to the power 0.62) and implicitly as a part of wall shear stress exponent. Figure 5-56 and Table 5-17 show how the corrosion rate varies with the CO₂ partial pressure.

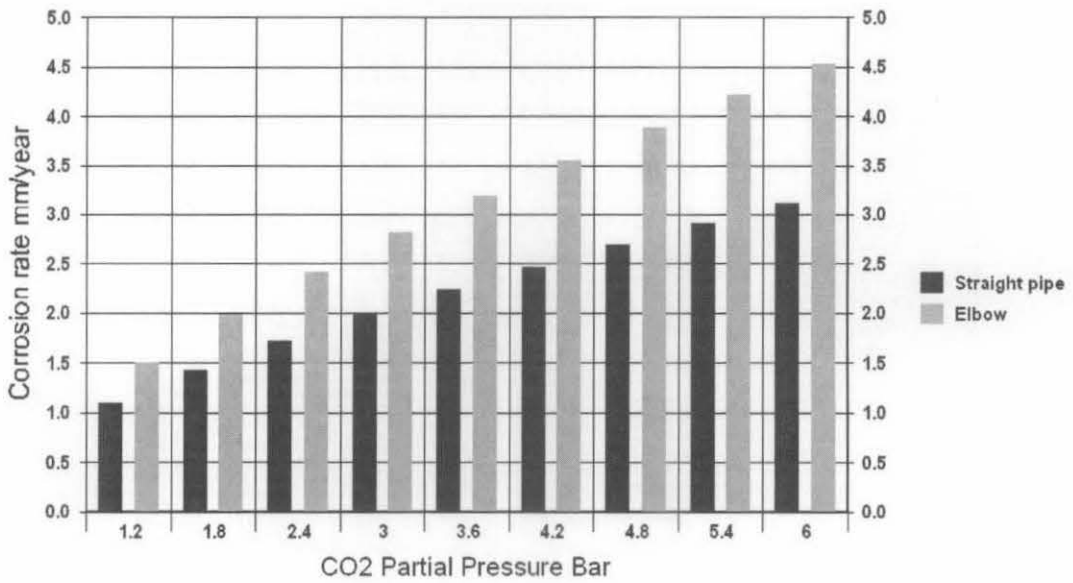


Figure 5-56: The effect of CO₂ partial pressure (Bar) on corrosion rate (mm/year)

Table 5-17: The effect of CO₂ partial pressure on corrosion rate for straight pipes and elbows

CO ₂ Partial Pressure Bar	Corrosion Rate (St Pipe) mm/year	Corrosion Rate (Elbow) mm/year
0.15	0.27	0.348
0.3	0.422	0.556
0.45	0.548	0.732
0.6	0.66	0.889
0.75	0.762	1.034
0.9	0.857	1.17
1.05	0.946	1.299
1.2	1.031	1.422
1.35	1.113	1.54
1.5	1.191	1.654
1.65	1.266	1.765
1.8	1.339	1.872
1.95	1.41	1.976
2.1	1.479	2.078
2.25	1.547	2.177
2.4	1.612	2.274
2.55	1.677	2.37
2.7	1.74	2.463
2.85	1.801	2.555

5.8.3.6 Effect of pH and temperature on corrosion rate

The effect of pH on corrosion rate as given by NORSOK model is dependent on the temperature. The effect of pH on corrosion rate is calculated at different temperature using the empirical models shown in Table 3-6. Figure 5-57 and Figure 5-58 show that corrosion rate increases while pH decreases. Lower pH is indicator of higher acidity of the fluid.

Temperature affects corrosion rate implicitly due to its direct relationship with kt (Table 3-5) and $f(\text{pH})$ (Table 3-6). Table 3-5 shows that kt increases with temperature up to 60 °C to decrease after that upto 150 °C. In reality, temperature also affects the shear stress due to its effect on viscosity and, to a lesser degree, density. These effects, however, are not taken into account in this calculation.

Figures 5-59 through 5-62 show that, in both laminar and turbulent flow, corrosion rate increases with temperature from 20 °C up to a maximum value between 60 °C and 80 °C to start declining after the maximum value. Anderzej Anderko and Robert D. Young (Anderko and Young 2001) obtained a similar result when calculating corrosion rate for carbon steel under a partial pressure of CO_2 equal to 30 bar. The maximum temperature they obtained, however, is between 80 °C and 100 °C. They explained that this maximum value results from the development of FeCO_3 surface layer which decelerate the attack of carbon steel by CO_2 .

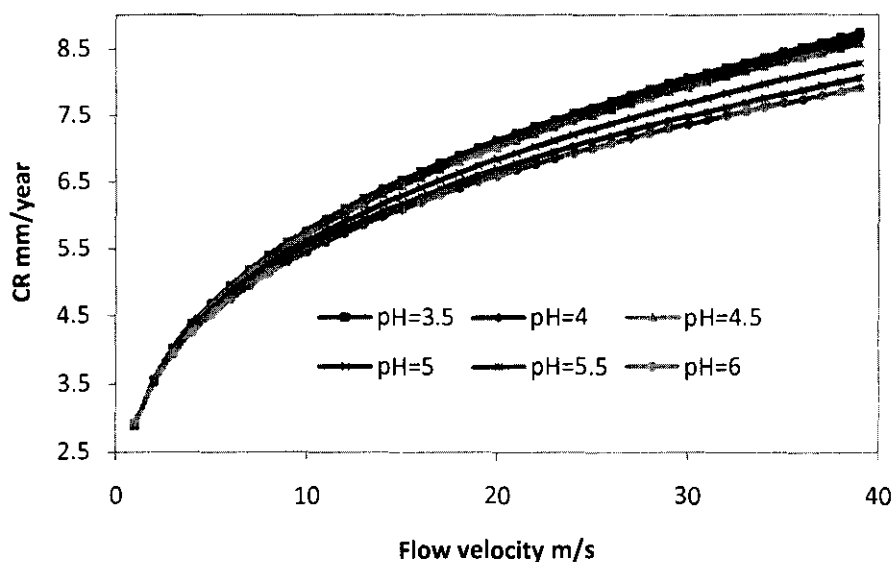


Figure 5-57: Variation of corrosion rate with flow velocity at different pH, T=60 °C

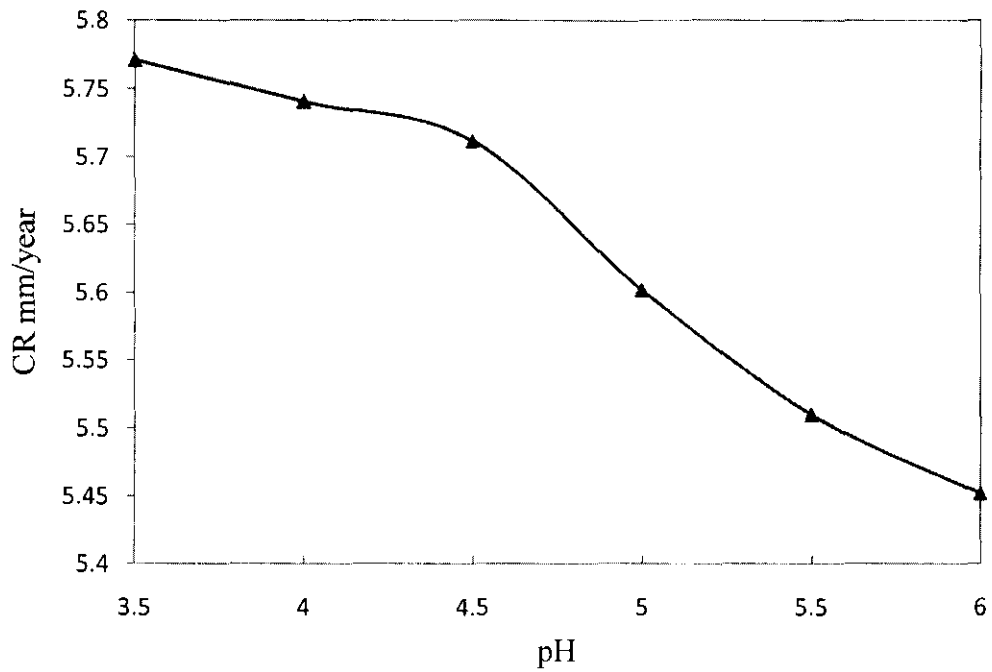


Figure 5-58: Variation of corrosion rate with pH, V=10 m/s, T=60 °C

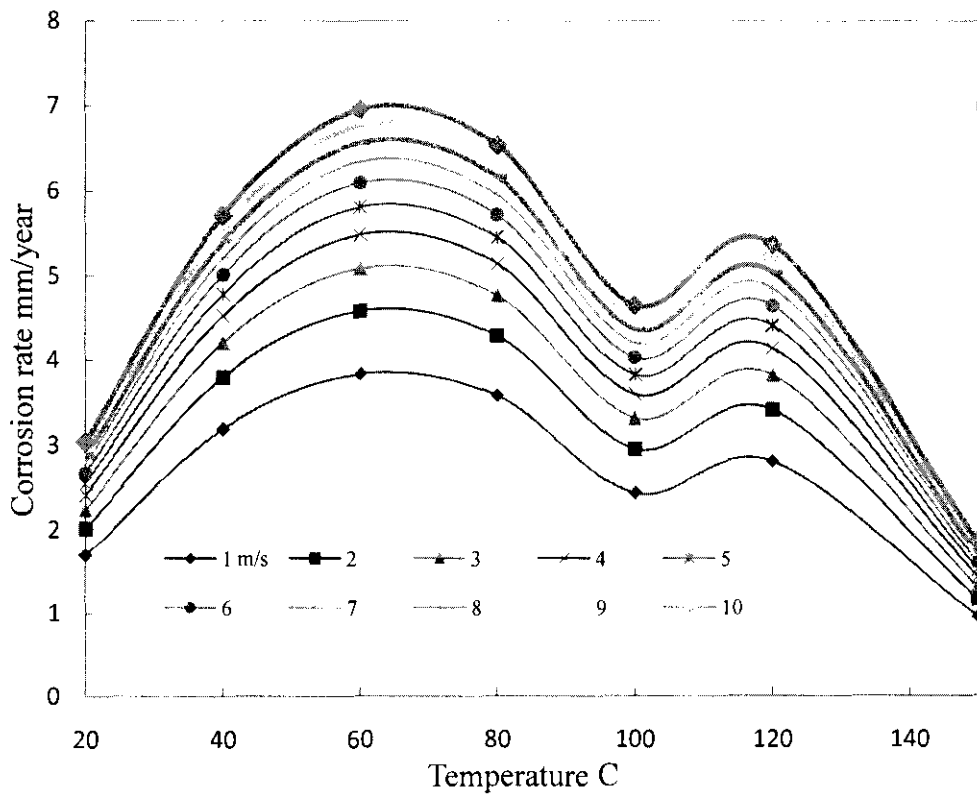


Figure 5-59: Variation of corrosion rate with temperature at different velocity, $PCO_2=0.2$ bar, pH=5 (turbulent flow).

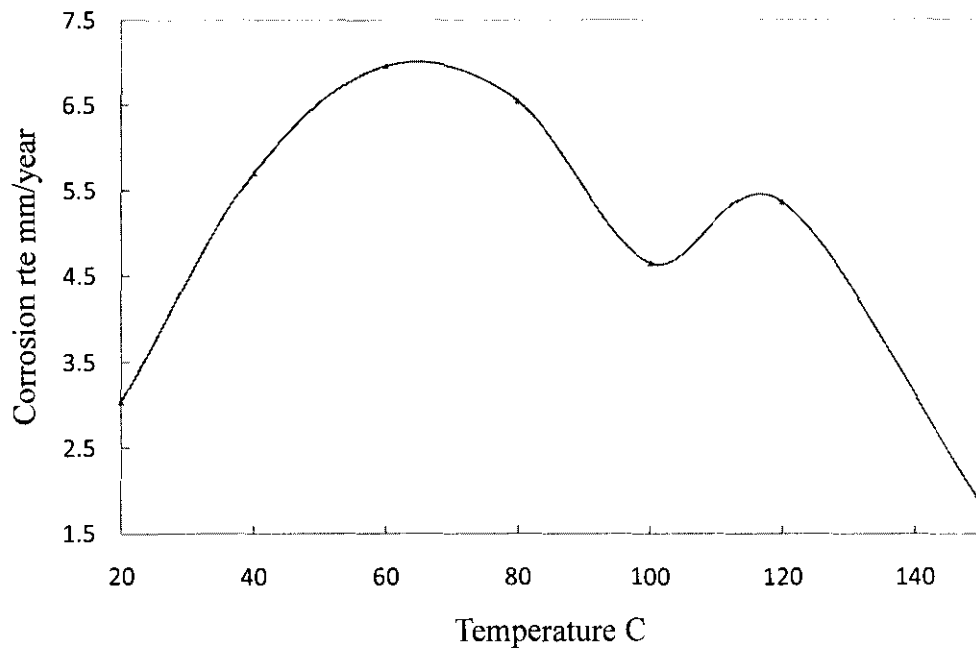


Figure 5-60: Variation of corrosion rate with temperature, $V=10$ m/s, $pH=5$ (turbulent flow)

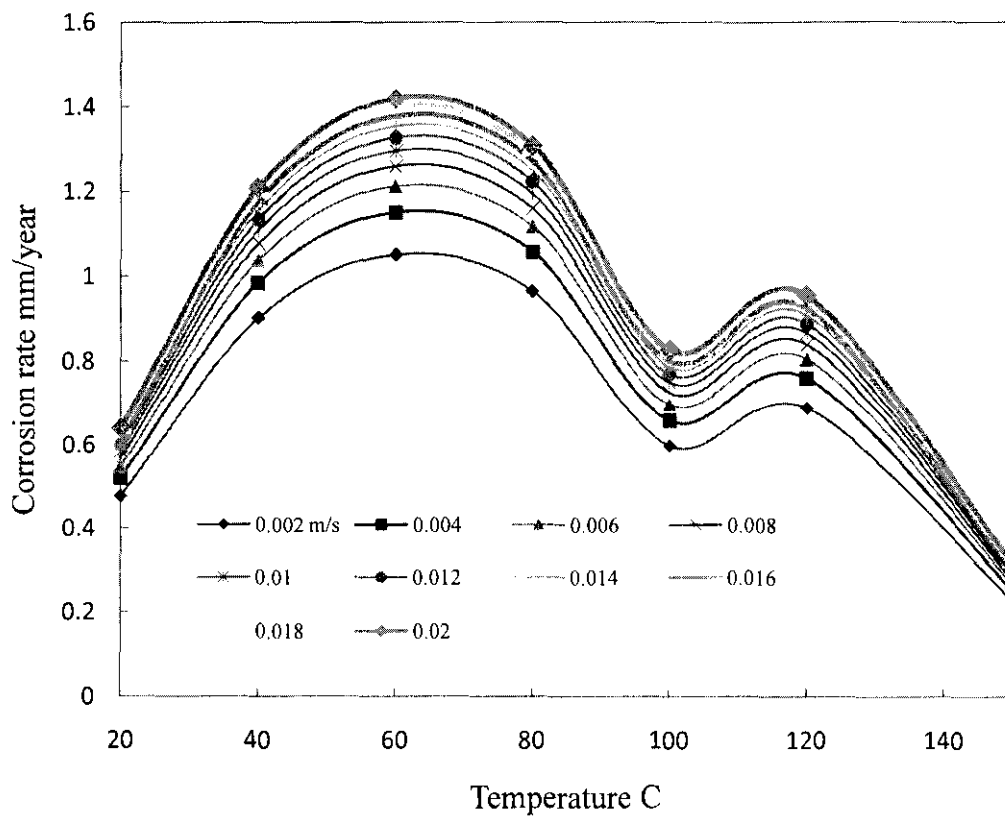


Figure 5-61: Variation of corrosion rate with temperature at different velocity $PCO_2=0.2$ bar, $pH=5$ (laminar flow)

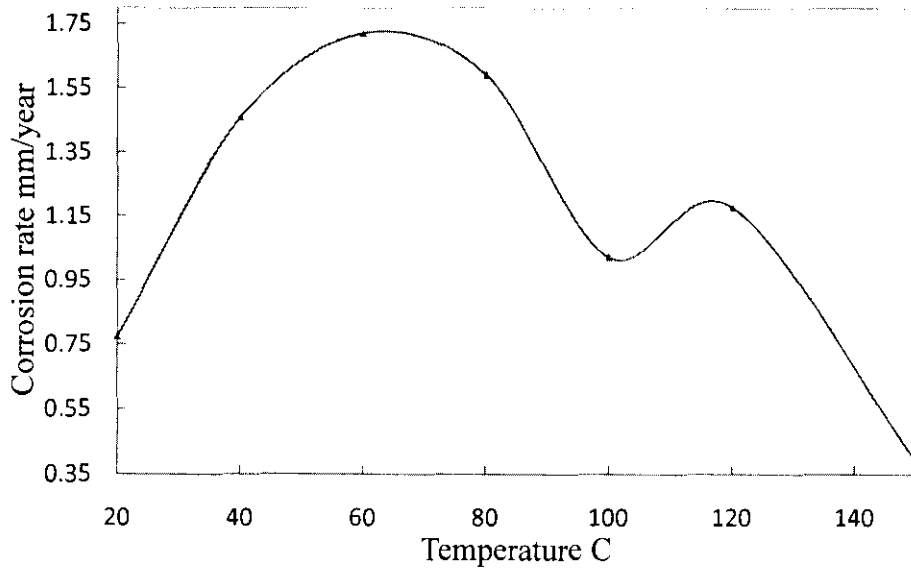


Figure 5-62: Variation of corrosion rate with temperature, $V=0.04$ m/s, $PCO_2=0.2$ bar, $pH=5$ (laminar flow)

5.8.3.7 Comparison of the model results with field data

The results of straight pipe corrosion rate predicted by the NORSOK model have been compared with field data taken from Gunaltun (Gunaltun 1991). The data used for the comparison are shown in Table 5-18. Nestic et al. (Nestic *et al.* 2005) used the same data to validate a corrosion model developed by them in 2005. Their validation result is shown in Figure 5-63. Using the field data shown in the table, the change of corrosion rate with flow velocity is shown in Figure 5-64. It is clear that the corrosion rate predicted by the model lays in the range between 2 to 3.5 mm/year whereas that predicted by the Nestic et al. (Nestic *et al.* 2005) model lays in the range between 1 to 4 mm/year, for the same range of velocity. We can say that the code gives acceptable agreement with Nestic et al. model. Figure 5-65 shows comparison between the predicted data from the code and selected data from Gunaltun field data (Gunaltun 1991). The comparison shows acceptable agreement.

Table 5-18: The field data of Gunaltun (Gunaltun 1991) (from Nesic et al. (Nesic et al. 2005))

	Umm Al Dalkh
WHFP (bars)	20 ~75
WHFT (°C)	30 ~ 70
BHFP (bars)	235 ~260
BHFT (°C)	100
Oil production rate (bopd)	65 ~ 2100
Water cut (%)	Up to 70
Oil density (at 20 °C)	0.872
CO2 content of the well fluid (mole %)	2.5
H2S content of the well fluid (mole %)	nil
GOR (SCF/SB)	70 ~ 200
Gas molar weight	
Tubing size (inch)	2 3/8 ~ 3 1/2
Tubing material	C-75
Deviation (degree)	Up to 40
Water composition (mg/l)	
Na ⁻	59525
Ca ⁻	5890
Mg ⁺⁺	755
K ⁻	270
Fe ⁻	
Ba ⁻	
Sr ⁻	770
Cl ⁻	104425
HCO ₃ ⁻	410
SO ₄ ⁻	260
pH (20 °C)	7.2

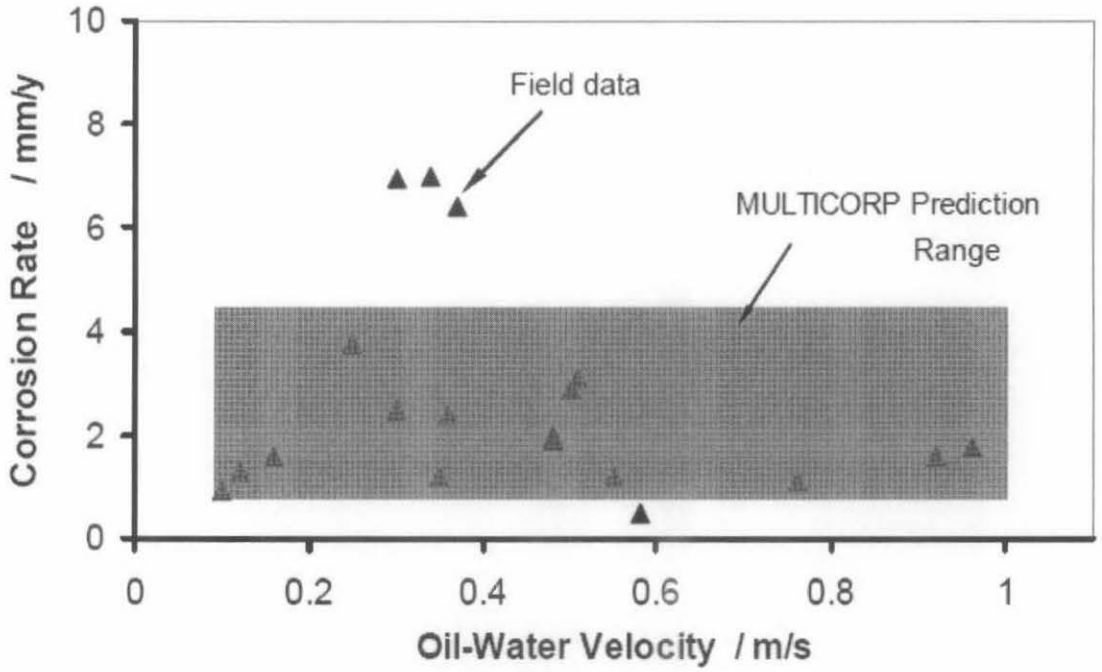


Figure 5-63: Comparison of Nestic et al. model results (Nestic *et al.* 2005) with Gunaltun field data (Gunaltun 1991)

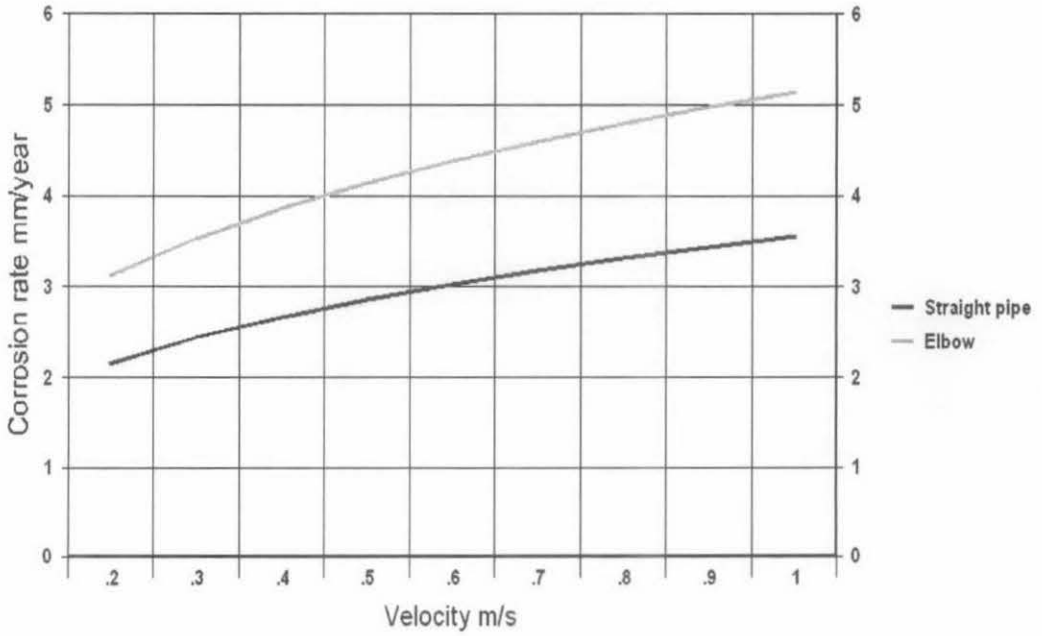


Figure 5-64: Variation of corrosion rate with velocity using Gunaltun field data (Gunaltun 1991)

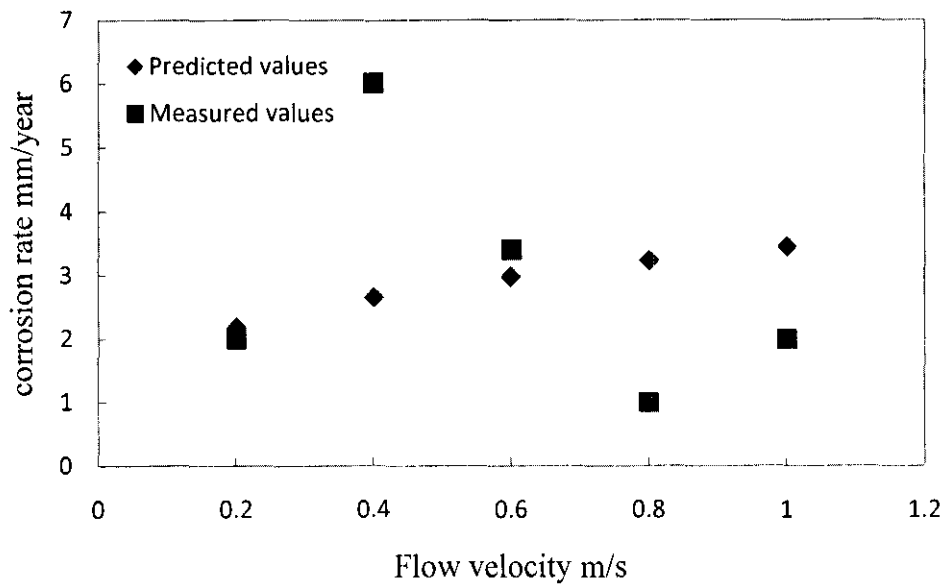


Figure 5-65: Comparizon of the code results with Gunaltun field data (Gunaltun 1991)

Another validation was carried on against data taken from (Wang *et al.* 2006) for a tubing transporting oil and water. The reported field data is in the range of 4.4 to 10 mm/year with no details about the tubing length and the corrosion rate at each point.

The predicted results in Table 5-19 are almost within the range of the reported field data.

Table 5-19: The tubing predicted corrosion rate

T (°C)	P (Bar)	PCO ₂ (Bar)	Qt m ³ /d (°V m/s)	D (m)	pH	WC (%)	CRp
57	270	1.56	800 (1.18)	0.1	5.05	5	5.42
80	250	1.56	1220 (1.8)	0.1	5.05	5	6.776
85	269	1.56	1220 (1.8)	0.1	5.1	47	3.775

- Calculated value

5.8.4 Erosion-corrosion prediction and simulation

Modeling of erosion-corrosion has been done by using the adopted NORSOK model (to account for elbow geometry) for corrosion and Salama model for erosion. The modeling methodology is outlined in section 3.4.1.1. The erosion-corrosion is assumed to be the total of erosion, corrosion, and synergy (erosion-enhanced-corrosion and corrosion-enhanced-erosion) which is predicted using Wood empirical model. One input data form is available for both erosion and corrosion related input data as shown in Figure 5-66.

The screenshot displays the 'EROSION-CORROSION CALCULATION' software interface. It is divided into several sections for data entry:

- Corrosion Input Data:**
 - Temperature C: 30
 - CO2 Partial Pressure Bar: 6
 - pH: 5
 - Total Pressure bar: 10
- Pipe and Fluid Data for Shear Stress Calculation:**
 - Diameter m: 0.08
 - Roughness m: 0
 - Fluid Density kg/m3: 1000
 - Fluid Viscosity Pa.s: 0.001
 - Velocity m/s: 5
- Erosion Input Data:**
 - particle size micron: 300
 - Sand Production Rate kg/Day: 200

On the left side of the interface, there are several control elements: 'Erosion/Corrosion Rate mm/y', a 'varied variable' dropdown menu, a 'Chart Type' dropdown menu, and buttons for 'Draw E/C', 'E/C Table', and 'Pipeline Simulation'.

Figure 5-66: Input data form for erosion-corrosion

Table 5-20 shows the data entered for erosion corrosion prediction and simulation.

Table 5-20: Input data for erosion-corrosion simulation

Parameter	Value
Temperature °C	60
CO ₂ partial pressure (Bar)	0.2*
pH	5
System total pressure (Bar)	10
Diameter (m)	0.075
Roughness (m)	0.0005
Fluid density (kg/m ³)	1000*
Fluid viscosity (Pa.s)	0.0015*
Velocity (m/s)	5*
Particles size (micron)	400
Sand production rate (kg/day)	500

5.8.4.1 The effect of flow velocity on erosion-corrosion

Figure 5-67 shows how wear rate will change when sand is entrained in a fluid containing CO₂. It is clear that the contribution of sand erosion on the overall wear is very low at the conditions listed in Table 5-20. In this condition, the contribution of erosion below velocity of 4 m/s is very low. At high sand production rate, the contribution of sand erosion will increase. Figure 5-68 is a result of a higher sand production rate (1500 kg/day).

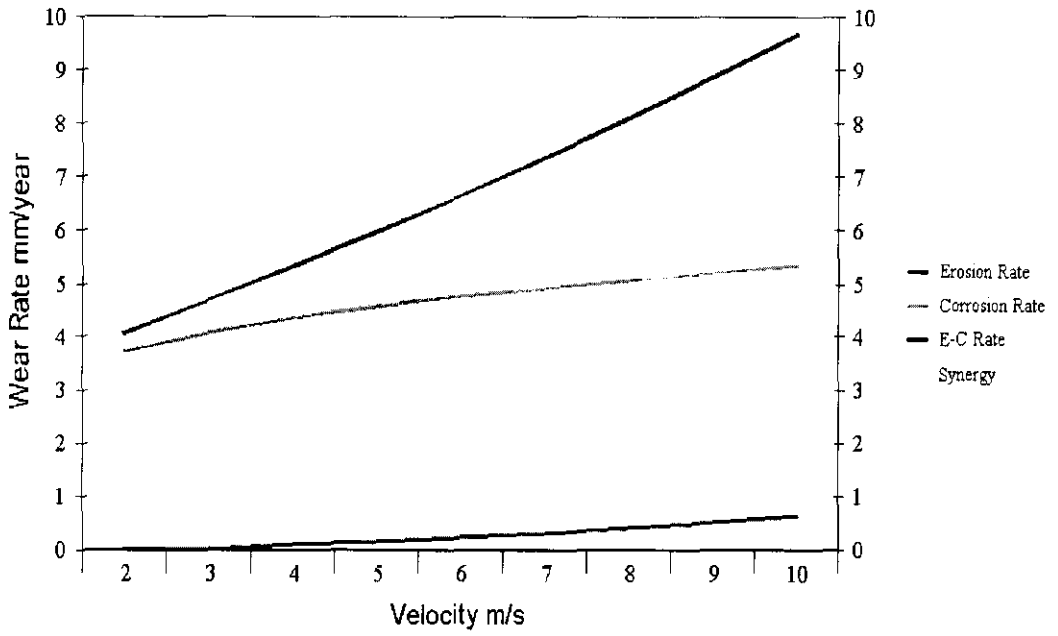


Figure 5-67: Effect of flow velocity on erosion, corrosion and erosion-corrosion rates
(Sand production rate 500 kg/day)

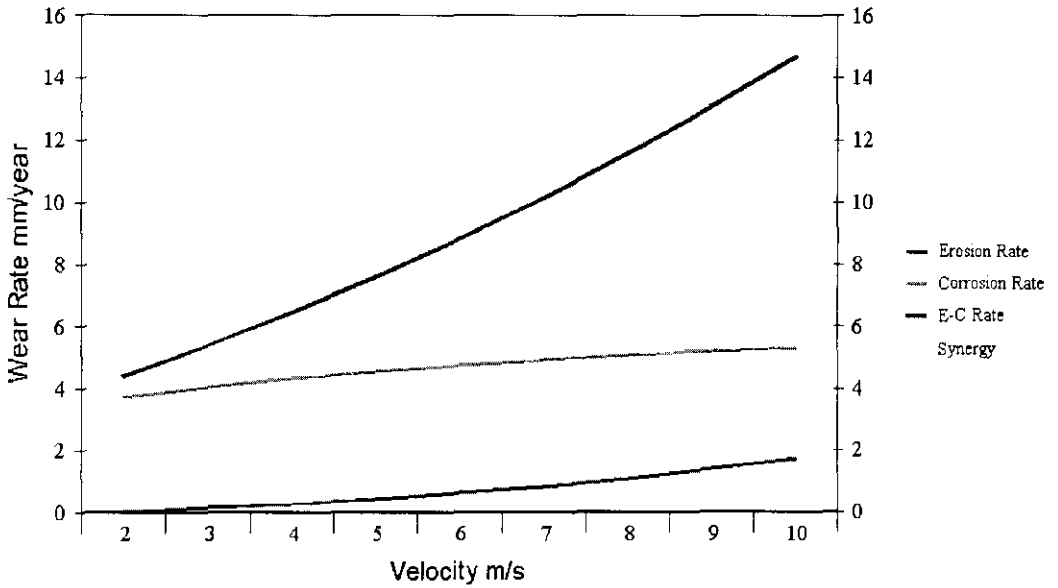


Figure 5-68: Effect of flow velocity on erosion, corrosion and erosion-corrosion rate
(Sand production rate 1500 kg/day)

5.8.4.2 The effect of fluid density on erosion-corrosion

As stated before, the pure corrosion rate increases with fluid density increase. In contrast, the pure sand erosion rate decreases with the increase of fluid density. The effect of fluid density on erosion, corrosion, and erosion-corrosion is shown in Figure 5-69. It can be noted that the erosion-corrosion decreases with density increase. This is because; in this case erosion effect is predominant.

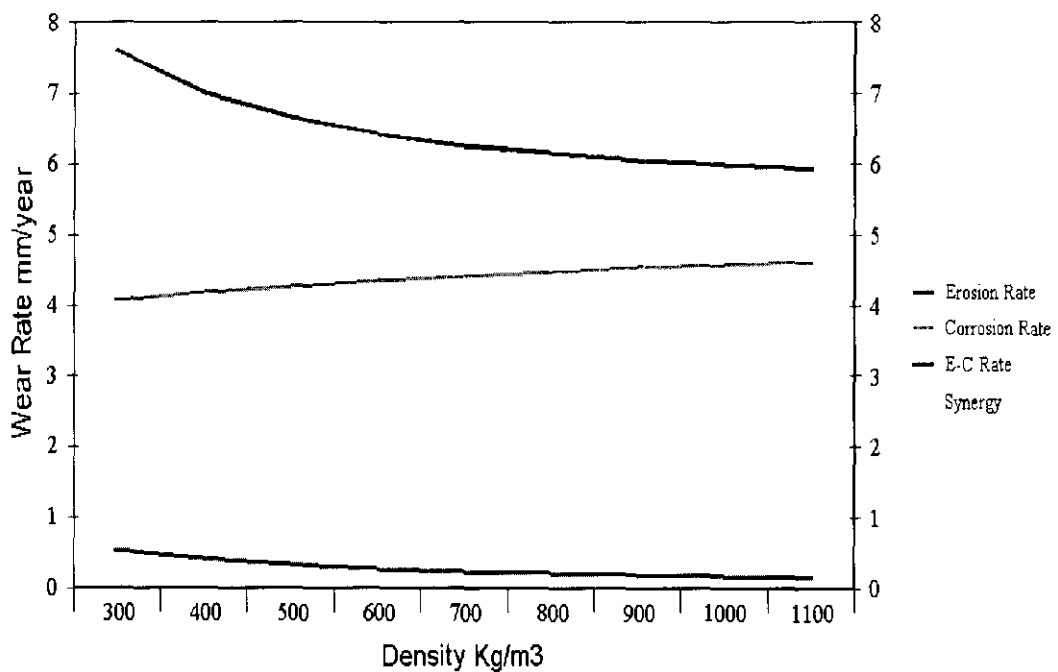


Figure 5-69: The effect of fluid density (kg/m³) on pure corrosion and erosion-corrosion rate (mm/year)

5.8.5 Results of pipeline simulation

In this section corrosion rate is predicted along a pipeline when the fluid is being cooled along the pipeline due to heat loss to the surroundings. The modification of NORSOK model to predict corrosion rate along pipeline has been explained in section 3.4.1.2 and the procedure followed is shown in Figure 3-7.

Figure 5-70 shows the input data form of pipeline simulation. Other required input data are entered in corrosion input data form, from which the user can navigate to this form. From the form, prediction of corrosion rate, temperature, Fugacity, $f(\text{pH})$, wall shear stress, Reynolds number, mixture viscosity, and mixture density at specified distances along the pipeline can be obtained as output in tabular or graphical form.

Input Data	
Inlet Temperature C	80
Surrounding Temperature C	22
Heat Capacity J/kg	2000
Heat Transfer Coefficient	2
Total Length m	200000
Water Cut %	30
Density at 20 C	900
Water Density kg/m ³	1000
Water Viscosity Pa.S	0.0015
Oil density at inlet temperature kg/m ³	850

Draw Table

Parameters
Corrosion Rate
Temperature
CO₂ partial pressure eff.
Wall shear stress
pH effect
Reynolds No
kt
Viscosity

Figure 5-70: Input data form of pipeline simulation.

5.8.5.1 Prediction of corrosion rate and its related parameters along pipeline

The code output includes the variation of temperature, corrosion rate, f_{CO_2} , $f_{(pH)}$, kt , wall shear stress, Reynolds number, mixture density, and mixture viscosity along the pipeline at any conditions. The parameters in Table 5-21 were arbitrary selected as input data to predict corrosion rate along the pipeline and to analyze the effects of different parameters.

Figure 5-71 and Figure 5-72 show the variation of corrosion rate along the pipeline when the flow velocity is 5 and 1 m/s, respectively. A comparison of the two figures indicates that, the effect of velocity on corrosion rate is significantly high; however, the corrosion rate variation in the case of the higher velocity (5 m/s) is not significant. This is due to the fact that temperature declines too slowly as shown in Figure 5-73, and the flow regime is entirely turbulent. For the lower velocity (1 m/s) the temperature declines rapidly as shown in Figure 5-74, which results in increasing fluid viscosity; and the flow regime, therefore, turns from turbulent to laminar flow at distance 125 km where the Reynolds number declines to less than 2000 as shown in Figure 5-75.

At flow velocity of 0.5 m/s, temperature declines more rapidly to reach the soil temperature at 140 km and the flow regime turns from turbulent to laminar at 52 km as shown in Figure 5-76 and Figure 5-77.

Table 5-21: Input data for pipeline simulation

Parameter	Unit	Value
Velocity	m/s	5, 1, 0.5
pH	-log (H ⁺) concentration	5
Inlet temperature	°C	80
Soil temperature	°C	15
Overall heat transfer coefficient	W/m ² C	2
Heat capacity	J/kgm ²	2600
Water cut	%	30
Total length	Km	200
Oil density at 20°C	kg/m ³	900
Pipe diameter	m	0.2
Roughness	m	0.0005

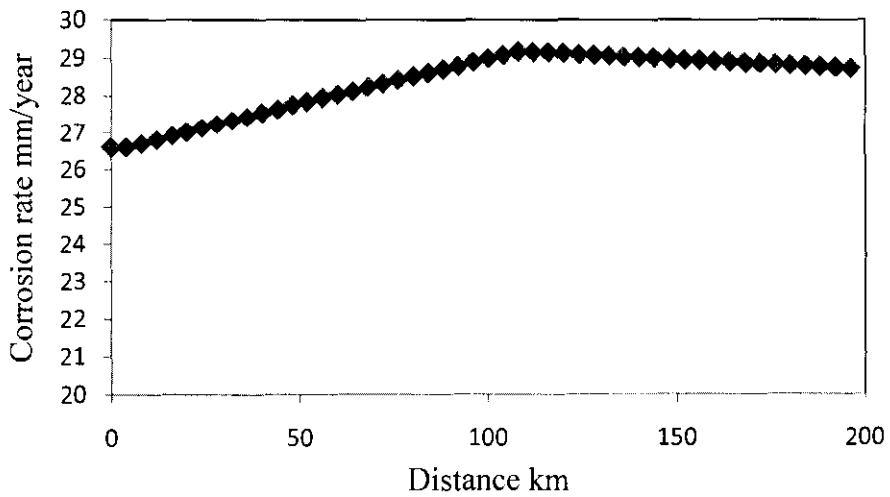


Figure 5-71: Corrosion rate variation along pipeline (velocity=5 m/s)

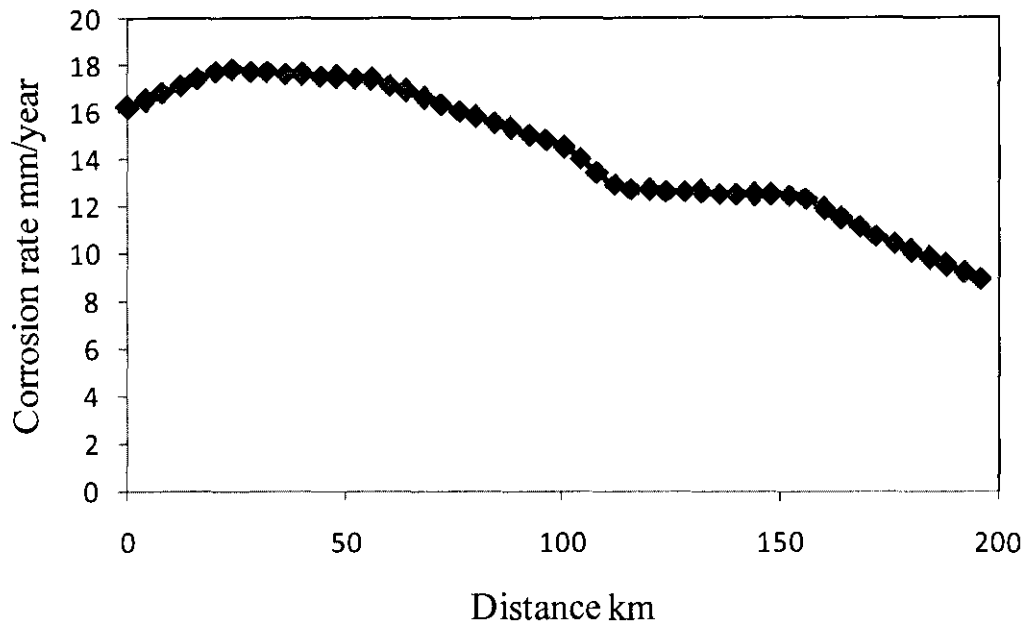


Figure 5-72: Corrosion rate variation along pipeline (velocity=1 m/s)

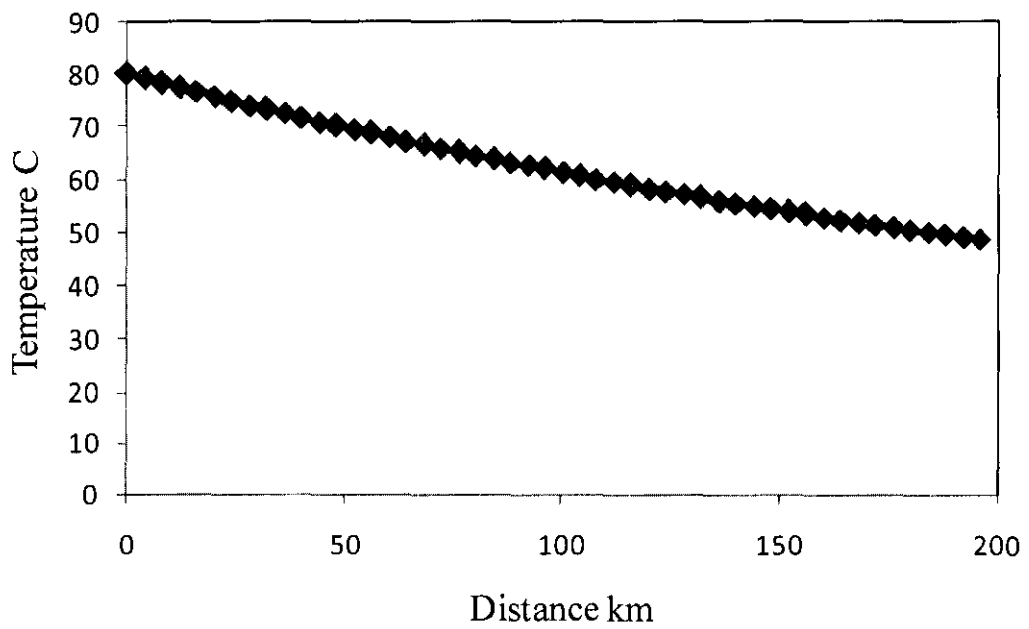


Figure 5-73: Temperature variation along pipeline (velocity=5 m/s)

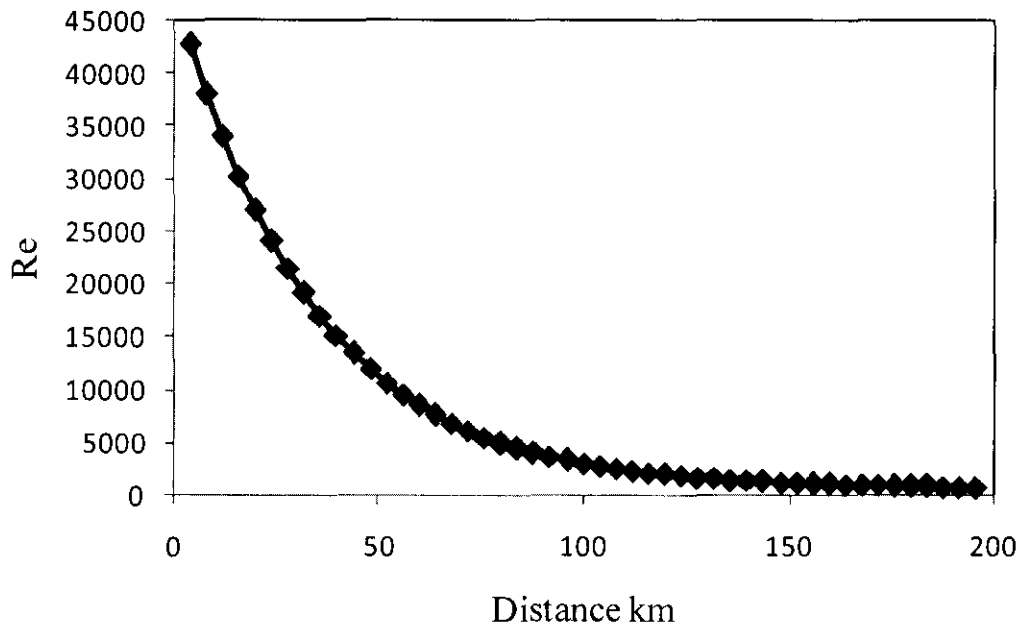
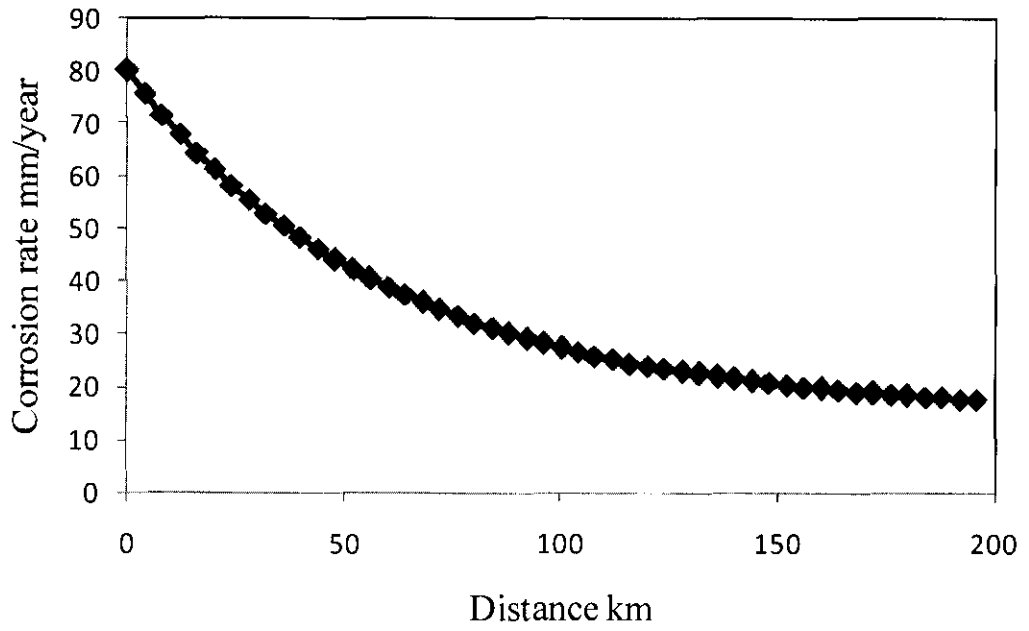


Figure 5-75: Variation of Reynolds no along pipeline (velocity=1 m/s)

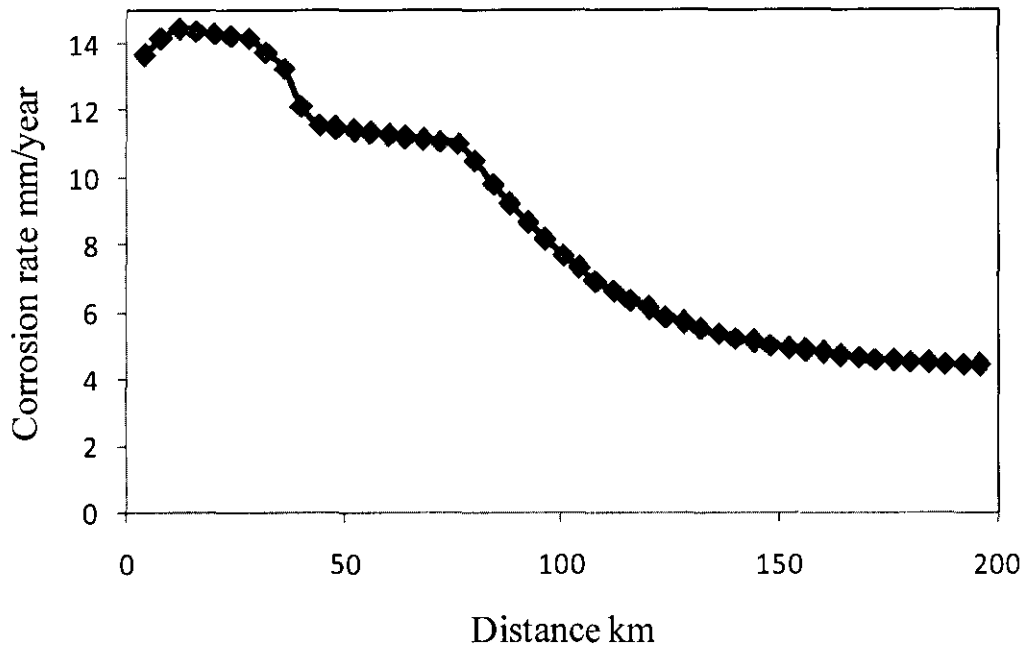


Figure 5-76: Corrosion rate variation along pipeline (velocity=0.5 m/s)

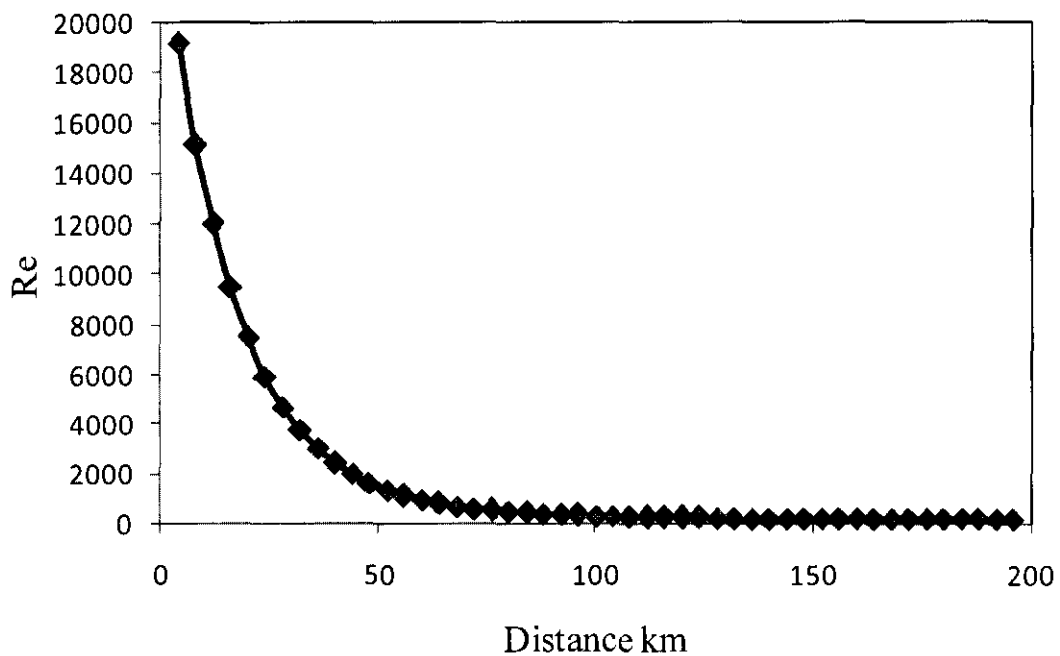


Figure 5-77: Variation of Reynolds no. along pipeline (Velocity=0.5 m/s)

The corrosion rate, temperature, wall shear stress, and Reynolds number variation along the pipeline at the three velocities are shown in Figure 5-78 to Figure 5-81. From Figure 5-78, the corrosion rates for the velocities of 1 m/s and 0.5 m/s are

almost identical after the point of 152 km, where the flow regime is laminar and temperature is very low for both cases.

Figure 5-80 shows that the shear stress for the velocity of 0.5 m/s starts to increase dramatically after the flow regime changes to laminar at the 52 km point. This is due to viscosity increase as temperature decreases, which leads to higher friction factor; and hence, higher shear stress as given by equation 5-32, where $\left[\frac{16\mu}{\rho VD} \right]$ is the friction factor in laminar flow.

$$S = 0.5 \left[\frac{16\mu}{\rho VD} \right] \rho V^2 \quad 5-33$$

The shear stress for the velocity of 0.5 m/s continues increasing until it exceeds that of the velocity of 1 m/s at distance of 90 km and remains constant after the point 140 km, where the flow temperature reaches the surrounding temperature. At distance 125 km, the shear stress of the velocity of 1 m/s starts to increase dramatically in the same manner and continues its increase until it exceeds the shear stress for the case of 0.5 m/s velocity.

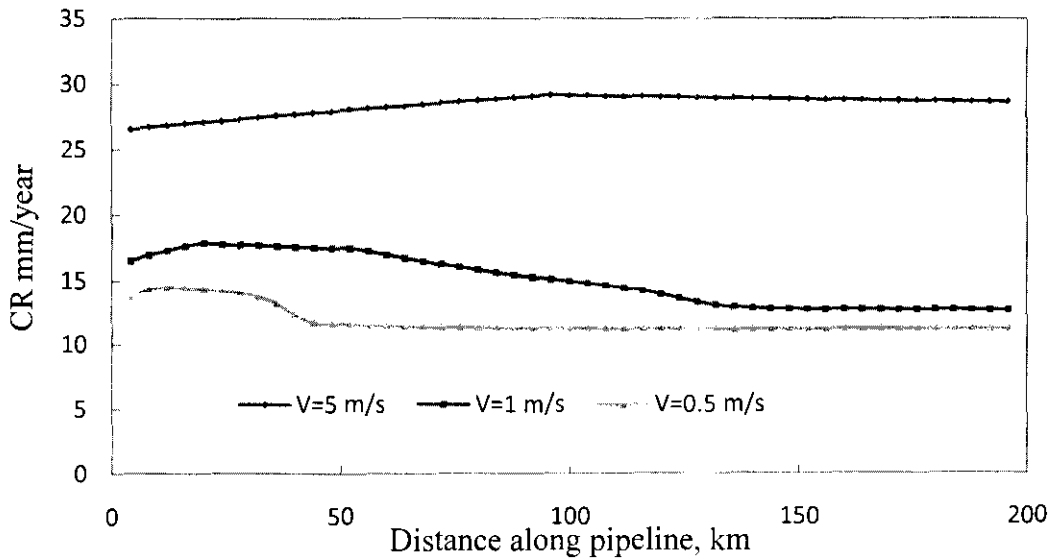


Figure 5-78: Corrosion rate along the pipeline at different velocities (D=0.2, pH=5, WC=30%)

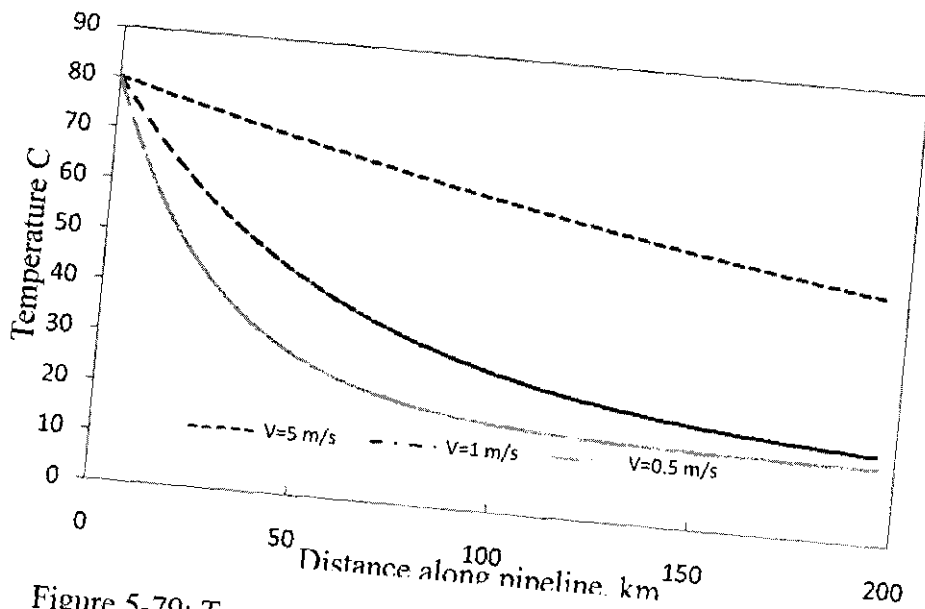


Figure 5-79: Temperature along the pipeline at different velocities

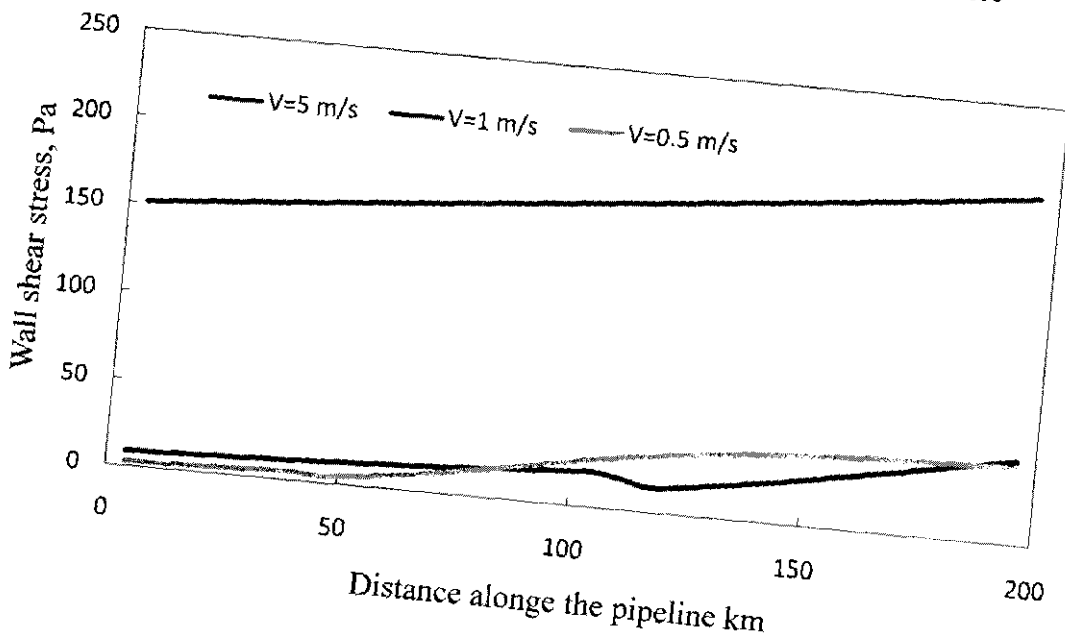


Figure 5-80: Wall shear stress along the pipeline at different velocities

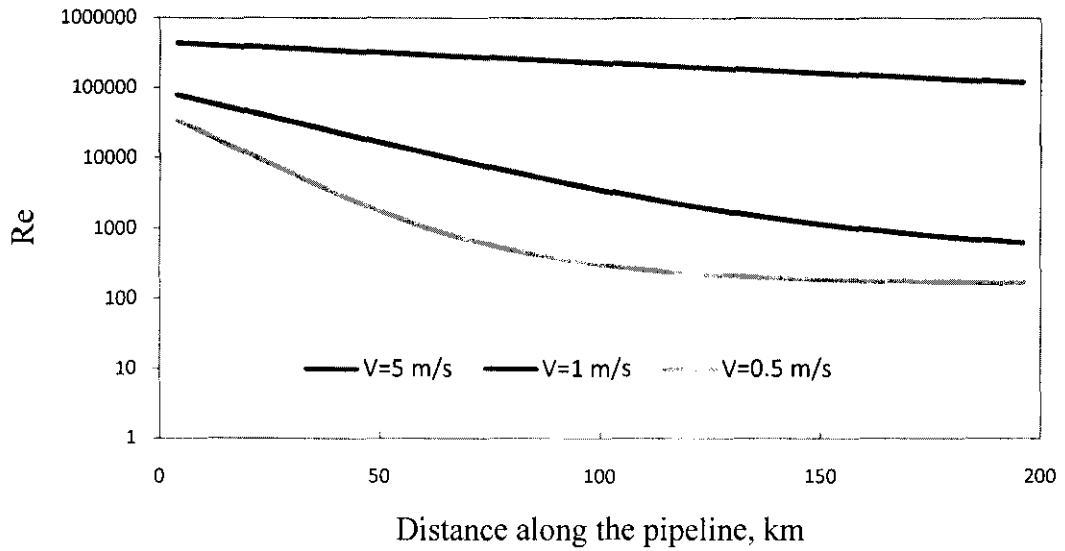


Figure 5-81: Reynolds No. along the pipeline at different velocities

Figure 5-82 and Figure 5-83 show the variation of corrosion rate along pipeline at different CO₂ partial pressure and pH, respectively. It is clear that corrosion rate at any distance increases with the increase of CO₂ partial pressure increase and decrease with the increase of the pH value. In these results both CO₂ partial pressure and pH are assumed constant along the pipeline and the effect of pH (f(pH)) and CO₂ fugacity vary with temperature variation.

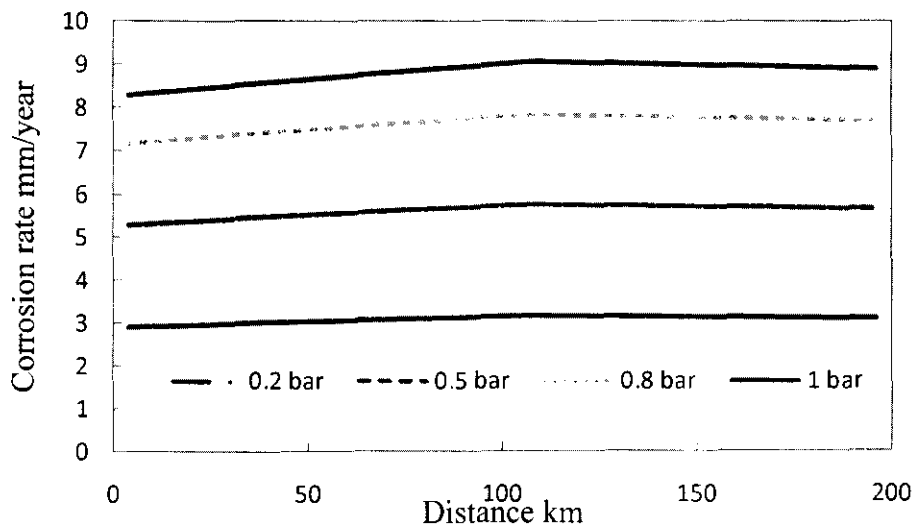


Figure 5-82: Corrosion rate variation along pipeline at different CO₂ partial pressure

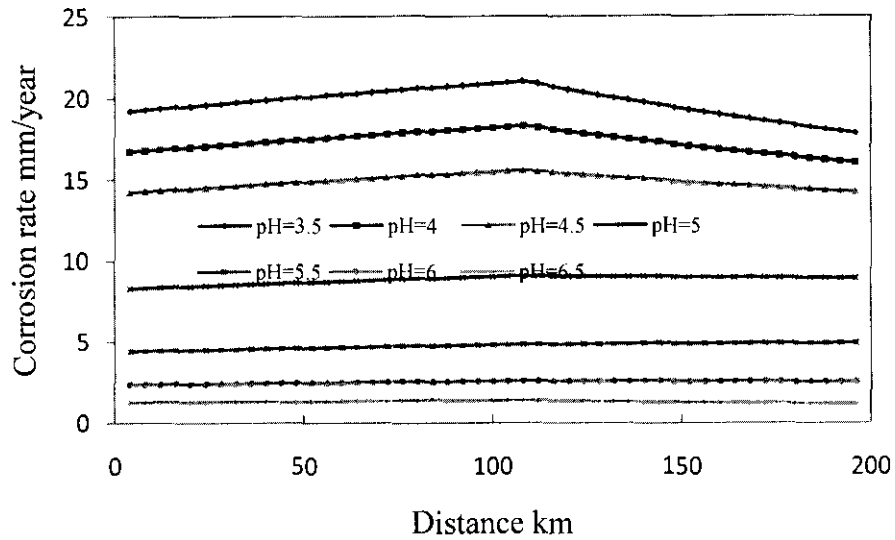


Figure 5-83: Corrosion rate variation along pipeline at different pH

5.9 Analysis of experimental results

5.9.1 Material characterization

Samples were characterized using optical microscope, scanning electron microscope (SEM) and Energy Dispersive X-ray Spectroscopy (EDX).

Figure 5-84 shows the microstructure of the sample material obtained from optical microscope at magnification of 720. Figure 5-85 shows the characterization result using EDX and

Figure 5-86 shows an image of the sample from the SEM. Table 5-22 shows that the samples are high carbon steel with carbon percentage exceeding 11%. In reality, carbon content in high carbon steel does not exceed 6% in worst cases. The result of 11% may results from the presence of this amount in the local point where the measurement was taken

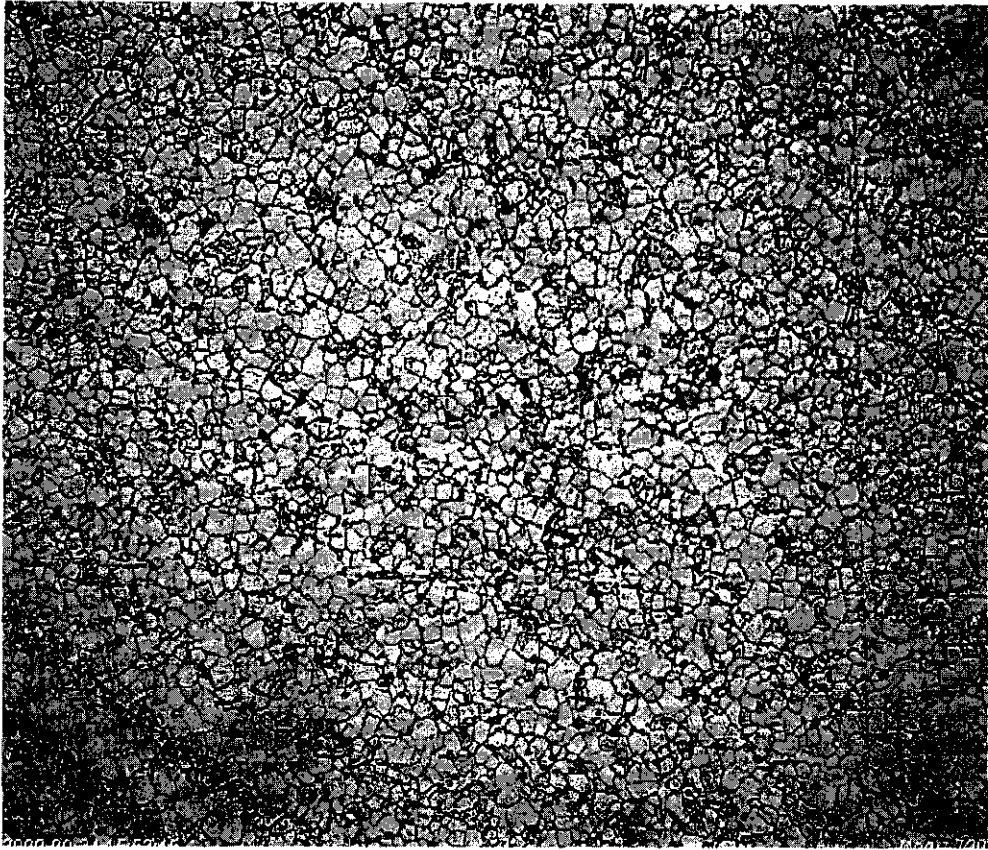


Figure 5-84: The microstructure of the sample material (x720)

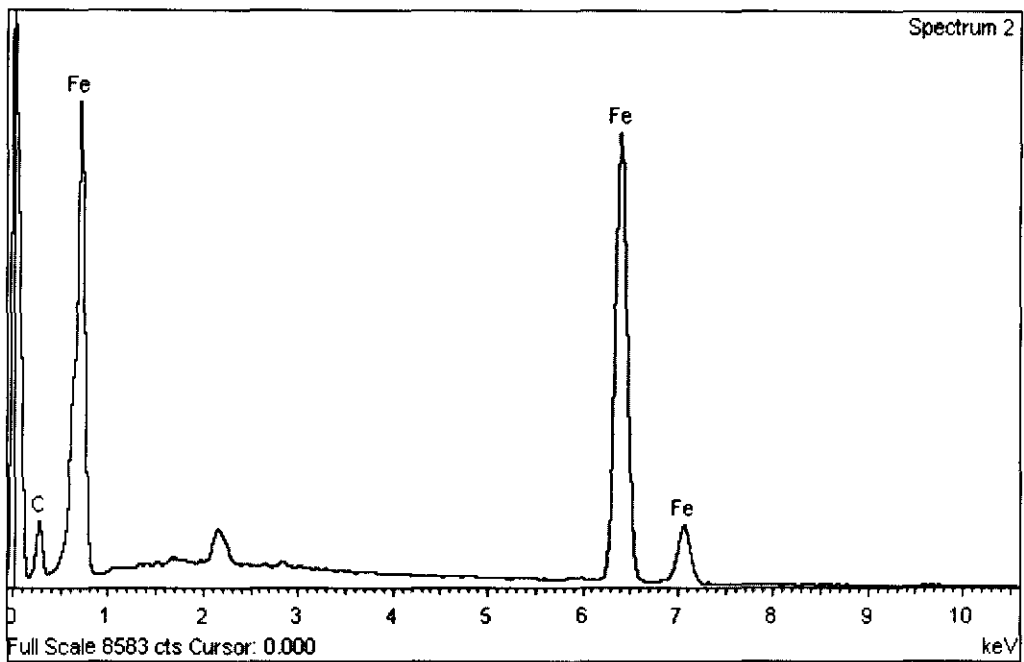


Figure 5-85: The characterization result of a sample (EDX)

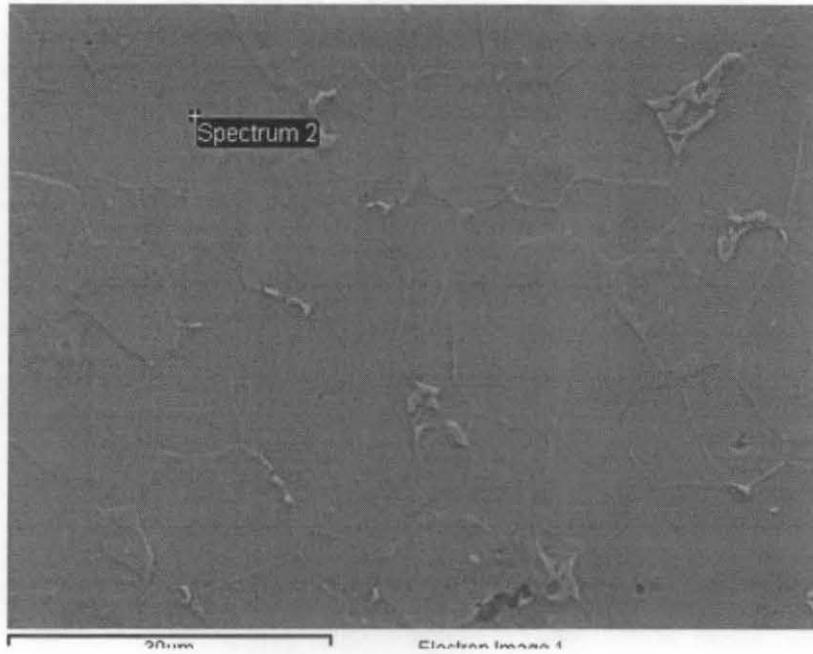


Figure 5-86: The sample surface microstructure using EDX.

Table 5-22: The sample composition (EDX)

Element	Weight%	Atomic%
C	11.13	36.81
Fe	88.87	63.19
Totals	100.00	100.00

5.9.2 Fluid preparation

The fluid used for the experiments was brine with NaCl content ranging from 1% to 3%. The fluid velocity was controlled using a variable speed controller connected to the pump motor.

No additives were used for controlling pH. The pH of the solution varied only depending on the concentration of the dissolved CO₂. CO₂ was injected continuously and pH was measured before every run, using the pH probe shown in Figure 5-87.

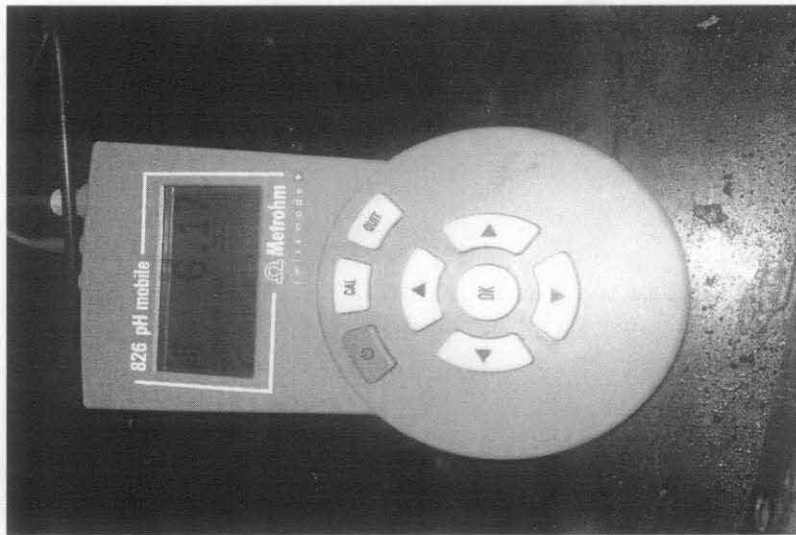


Figure 5-87: The pH probe

Due to the lack of measurement technique for CO_2 partial pressure, the following procedure has been used to estimate the CO_2 partial pressure at any pH.

The change of ocean CO_2 partial pressure (given as concentration) and pH with time is shown in Figure 5-88 (Turley *et al.* 2005)

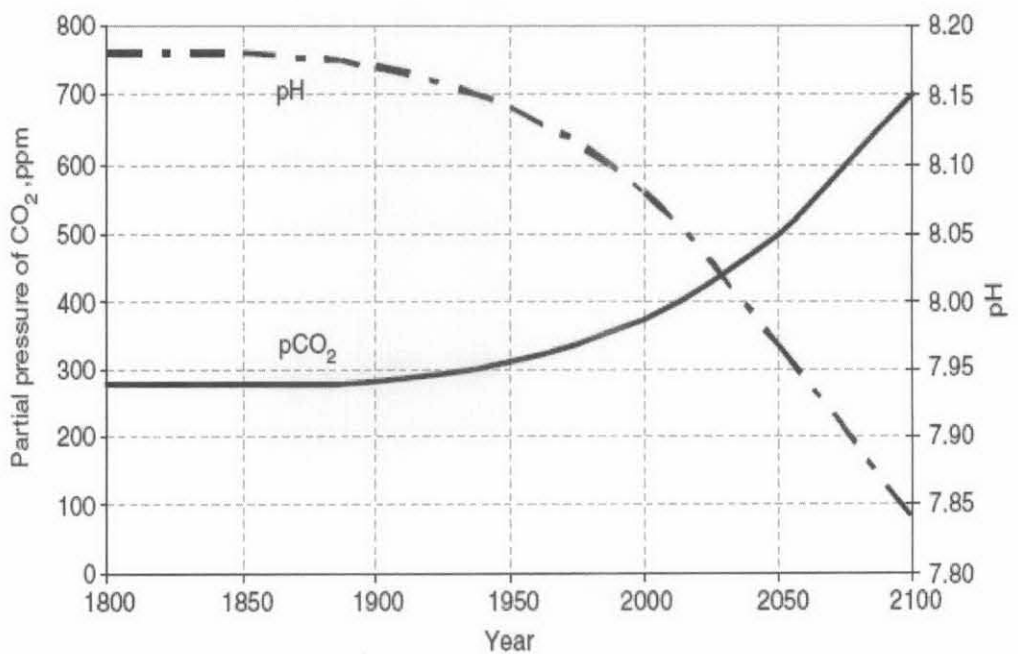


Figure 5-88: The change of ocean CO_2 partial pressure and pH with time(Turley *et al.* 2005)

Based on Figure 5-88, a relationship between pH and CO₂ concentration has been established as shown in Figure 5-89.

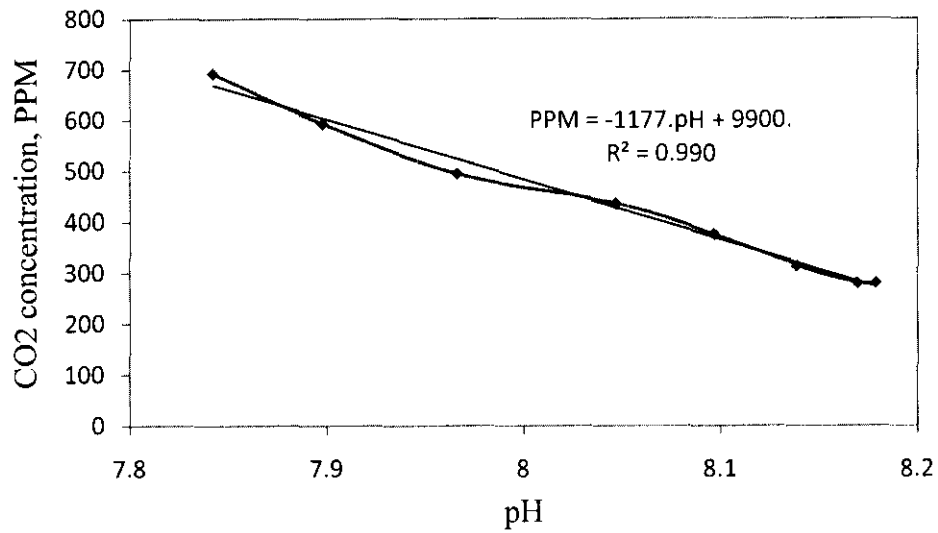


Figure 5-89: The change of CO₂ partial pressure with pH

The CO₂ concentration in PPM can be converted to partial pressure by using Rault's equation as follows:

$$P_{CO_2} = x_{CO_2} \times P_{vCO_2} \quad 5-34$$

Where P_{vCO_2} is the vapor pressure of CO₂ at measurement temperature and x_{CO_2} is the mole fraction of the CO₂ solute in water which is calculated by multiplying CO₂ concentration by the ratio of the molecular weight of water to molecular weight of CO₂.

As the flow loop is open to atmosphere, the system pressure can be calculated as follows:

$$P_{sys} = \Delta P_{losses} + \Delta P_{potential} + P_{atm} \quad 5-35$$

Where ΔP_{losses} is the pressure losses due to friction and fittings, $\Delta P_{potential}$ is the pressure losses due to heights differences, and P_{atm} is the atmospheric pressure (equals to 101325 Pa).

Using Equation 5-34, the system pressures at different flow velocities are shown in Table 5-23.

Table 5-23: Calculated system pressures at different flow velocities

Flow velocity m/s	System pressure Pa
0.1	131154
0.2	132048
0.3	136011
0.4	140604
0.5	146488

Considering CO₂ vapor pressure of 50 bar (at 20 °C) and by using Equation 5-33 and the relationship between pH and concentration, CO₂ partial pressures for different pH have been calculated as in Table 5-24.

Table 5-24: CO₂ Partial Pressure at different flow velocities and pH values

pH	CO ₂ partial pressure (bar)
4	0.106
4.5	0.094
5	0.082
5.5	0.07
6	0.058
6.5	0.046

5.9.3 Corrosion rate measurements

Corrosion rate was measured by connecting the electrodes to their corresponding wires in GillAC potentiostat, which was connected to a computer as shown in Figure 5-90. The potentiostat signals were displayed in the form of simultaneous fluctuations of current and potential with time. A software package called Sequencer was used to display the signals and to analyze the results to obtain the corrosion rate in mm/year.

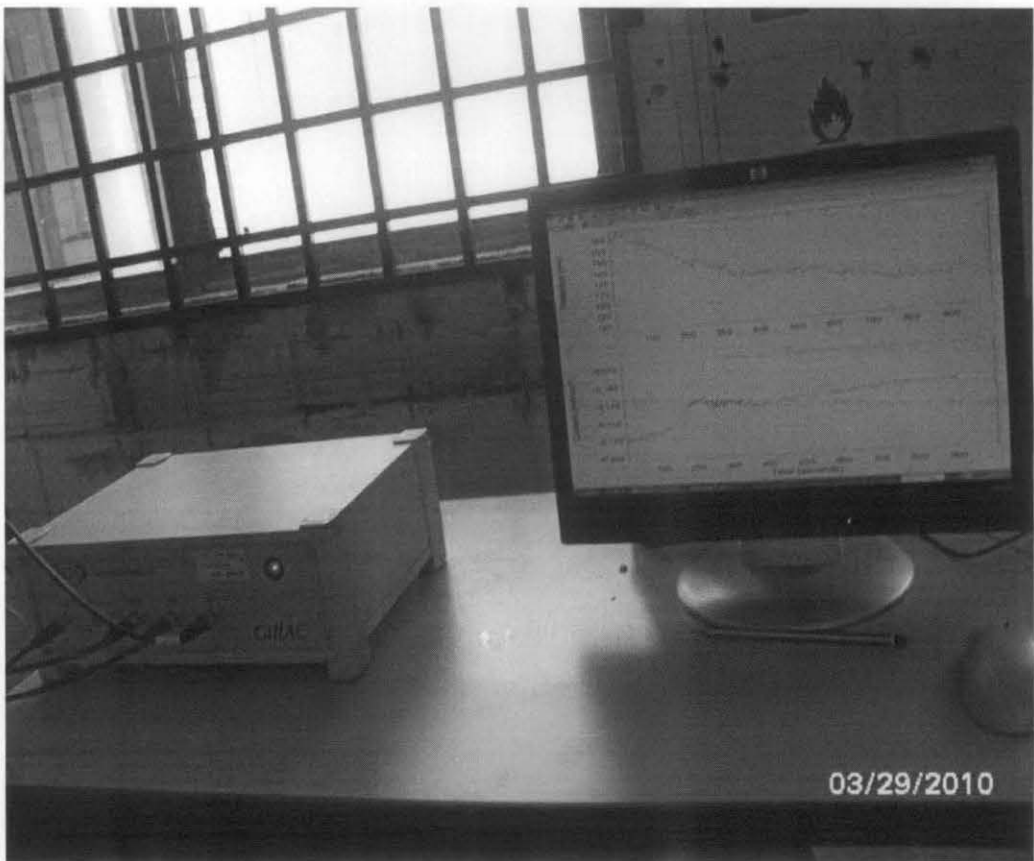


Figure 5-90: GillAC potentiostat

Corrosion rate was measured at five flow velocities (0.1, 0.2, 0.3, 0.4, and 0.5 m/s) and three pH values (5, 5.5, and 6.5). Electrochemical noise measurement (ENM) technique was used for direct measurement and analysis. Some acquired ENM results are given in Appendix B.

Table 5-25 shows the measured and predicted corrosion rate at the five velocities and the three pH values.

Figure 5-91 to Figure 5-93 indicate that, the predicted values agree fairly with the measured values. Figure 5-94 shows a comparison between all measured data set with the predicted values under the same conditions. From the figure, good agreement is observed. The average absolute error is 8.57%.

Table 5-25: Measured and predicted corrosion rates at different velocity and pH

pH	Velocity m/s	Pred. mm/y	Meas. mm/y	Abs error %
6.5	0.1	0.28	0.262	7.25
	0.2	0.32	0.292	9.58
	0.3	0.34	0.326	5.215
	0.4	0.36	0.331	9.36
	0.5	0.38	0.338	12.42
5.5	0.1	0.36	0.29	24
	0.2	0.41	0.352	16.4
	0.3	0.443	0.446	0.67
	0.4	0.468	0.409	14.4
	0.5	0.49	0.454	7.93
5	0.1	0.5724	0.556	2.94
	0.2	0.656	0.604	8.60
	0.3	0.711	0.706	0.70
	0.4	0.753	0.71	6.1
	0.5	0.79	0.815	3.06

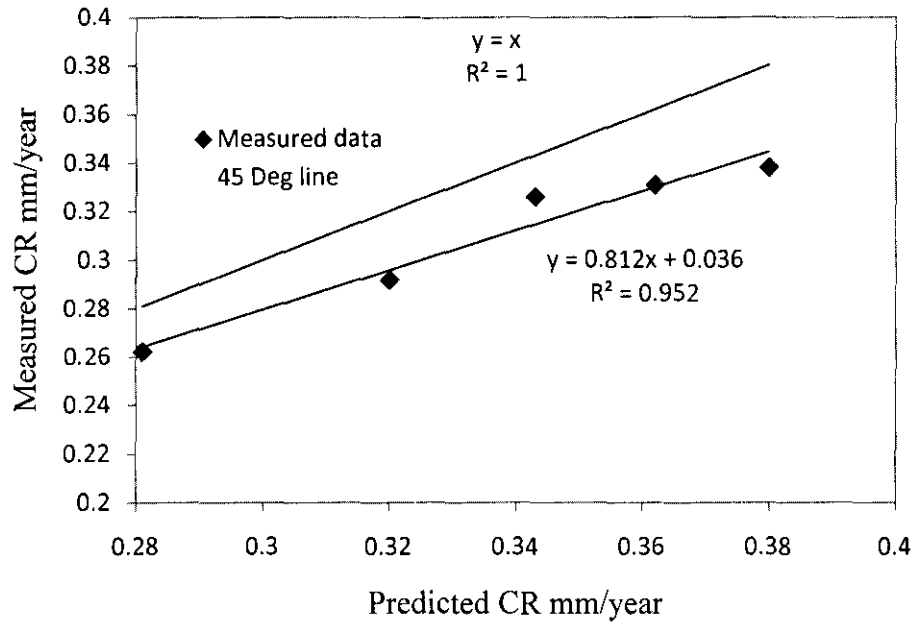


Figure 5-91: Measured and predicted corrosion rate at pH=6.5

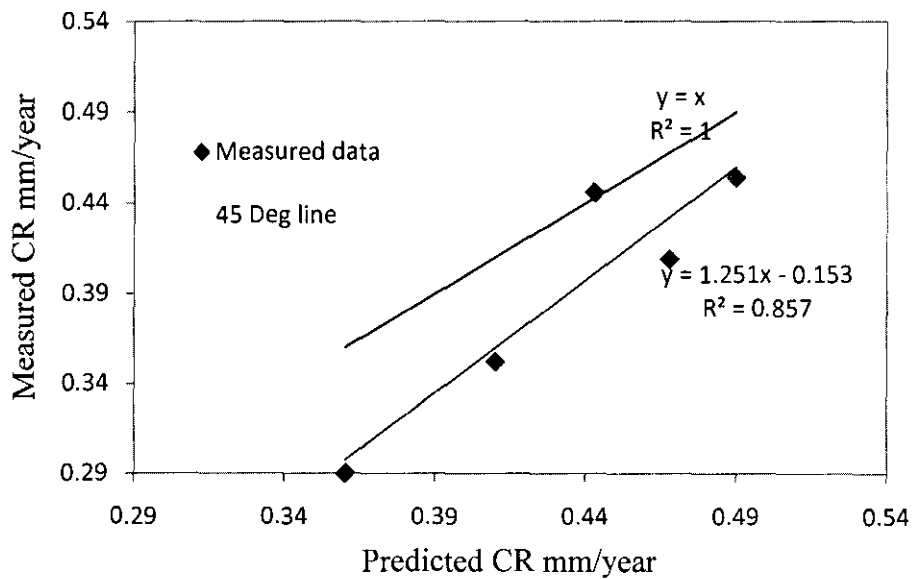


Figure 5-92: Measured and predicted corrosion rate at pH=5.5

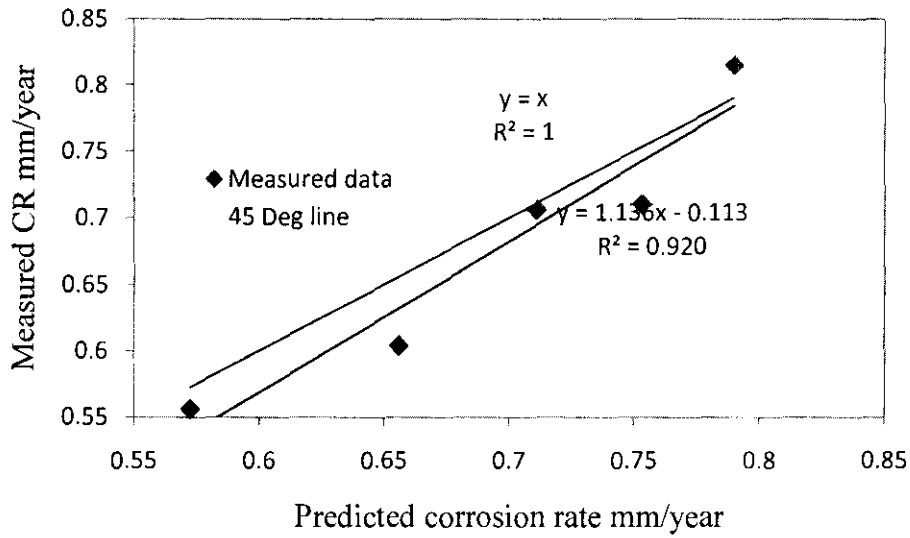


Figure 5-93: Measured and predicted corrosion rate at pH=5

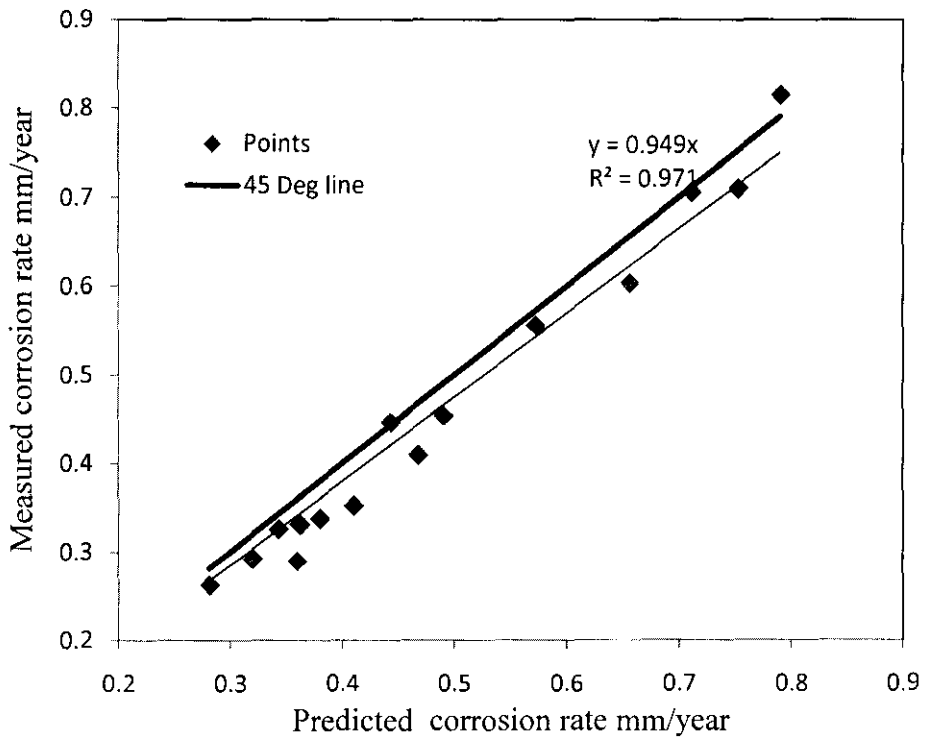


Figure 5-94: Comparison between predicted and measured corrosion rate

5.10 Summary

In this chapter selected results of the whole research have been presented. The results include those obtained from the developed computational code at specified process conditions (input parameters) and those obtained from experimental measurements. A thorough investigation of the code results is made to evaluate the models applicability and accuracy based on comparison with data measured from the flow loop and CFD results. The effect of different parameters on erosion and corrosion rates as predicted by different models were investigated and discussed. The results for erosion rate prediction include those obtained from the developed computational package. Salama empirical model and DIM semi-empirical model, which are used to develop the package, were validated against published measured data and a CFD model developed using the discrete phase model (DPM) in Fluent software. The validation shows good accuracy of the DIM model and lack of accuracy of Salama model. As an improvement of the Salama model, three sub-models have been proposed based on comparison with published measured data categorized according to gas-liquid-ratio. Another improvement to Salama model based on comparison with the DIM model resulted in extending its applicability to oil flow by including the effect of viscosity.

The results of corrosion and erosion-corrosion from the developed package are those obtained from different models employed to the package. Results for CO₂ in straight pipes and elbows were predicted using the original and modified NORSOK CO₂ corrosion rate prediction model. The erosion-corrosion was predicted using a model developed by combining the modified NORSOK model (corrosion) to Salama model (erosion) and Wood model (synergy). Corrosion rate along pipelines with varying temperature were predicted by coupling NORSOK model to pipeline thermal/hydraulic equations. The results of corrosion prediction in straight pipes and elbows were validated using published field data and experimental data measured from a flow loop designed and fabricated by the researcher.

Chapter 6

CONCLUSIONS AND RECOMMENDATIONS

6.1 Conclusions

The main outcome of this research is the development of a computational package for erosion, corrosion, and erosion-corrosion prediction by employing selected empirical and semi-empirical models to Visual Basic programming. The package, serves as a comprehensive erosion/corrosion predictive tool, encompasses the features of accessibility, comprehensiveness, flexibility, simplicity, and accuracy. From the results of this work, the following conclusions are made:

- 1- The erosion rates predicted by the direct impingement model (DIM) agree well with results obtained from the computational fluid dynamics (CFD). The results of the DIM model also agreed with measured data. The DIM model solves for the particle velocity and has the viscosity among its input parameters.
- 2- Salama model does not account for fluid viscosity and is mainly developed for air flow. Erosion rates predicted by Salama model deviate largely from results of DIM and CFD models especially for oil flow.
- 3- Salama model was modified to account for fluid viscosity. Three equations were developed depending on the velocity ranges which are determined by the fluid viscosity. The developed model, termed Mysara-UTP model, gives results comparable to the DIM model. This model exhibits the simplicity of the Salama model and the accuracy of the DIM model.

4- The NORSOK model for CO₂ corrosion prediction is extended to be applicable for corrosion in elbows by introducing the concept of equivalent length. The model was validated using data measured from a lab-scale flow loop constructed at UTP.

5- The effect of different parameters affecting erosion, corrosion, and erosion-corrosion rates were investigated using the computational models. The following effects were found:

- i. Erosion rate is mainly influenced by viscosity. It decreases with the increase of viscosity. The erosion rate is influenced to a lesser degree by the fluid density. It also decreases with the increase of density.
- ii. In laminar flow, corrosion rate increases with the increase in fluid viscosity and velocity and decreases with the increase of pipe diameter.
- iii. In turbulent flow it is mainly affected by velocity. It increases with the increase of velocity. The corrosion rate increases with the increase of viscosity and density to a lesser degree.
- iv. Corrosion rate increases with the increase of CO₂ partial pressure which is directly related to the ppm of CO₂ dissolved in the fluid.
- v. The synergy effect increases with the increase of the fluid velocity and decreases with the increase of the fluid density.

6.2 Recommendations

The recommendations for future work are as follows:

- 1- The code results should be verified with real field data.
- 2- The flow loop should be equipped with a higher speed pump, a heater, and a compressor to simulate sand erosion in multiphase flow at different temperatures.

- 3- The flow loop should be upgraded to a closed system to eliminate the oxidation effects and to enable pressurization of the system.
- 4- More models are to be employed to the code for prediction of corrosion due to other components such as H₂S.
- 5- The prediction of corrosion along pipelines can be extended to well tubing.
- 6- The procedure of adopting NORSOK model to elbow geometries should be extended to other components such as valves and tees.

6.3 Contributions

By the end of this research, the following contributions have been achieved:

1. The Salama erosion empirical model has been modified to improve its accuracy. Three sub-models were introduced for erosion rate prediction in elbows according to the gas-liquid-ratio.
2. The applicability of the Salama erosion empirical model has been extended to oil flow by introducing the effect of viscosity.
3. NORSOK Norwegian standard CO₂ corrosion prediction model has been modified to extend its applicability to elbows geometries.
4. NORSOK Norwegian standard CO₂ corrosion prediction model has been coupled to pipeline thermal/hydraulic models to simulate CO₂ corrosion along pipelines of varying temperature.
5. An ad hoc equation has been used with the equation of particles motion to model the temperature-dependency of particles impingement velocities and erosion rate in oil transportation.
6. A computational package with a user friendly graphical interface has been developed to serve as a tool for erosion/corrosion prediction in elbows, tees and straight pipes.
7. The effect of the different parameters on erosion and corrosion rates are analyzed and discussed.

References

- Aballe, A., Bethencourt, M., Botana, F. J. and Marcos, M. (1999). "Using wavelets transform in the analysis of electrochemical noise data." *Electrochimica Acta* 44: 4805–4816.
- Ahlert, K. (1995). The effects of particle impingement angle and surface wetting on solid particle erosion on AISI 1018 steel, U of Tulsa. M Sc.
- A. and Young, R. D. (2001). A model for calculating rates of general corrosion of carbon steel and 13%Cr stainless steel in CO₂/H₂S environments. CORROSION 2001, Houston, Tx, NACE International.
- Andrews, P., Illson, T. F. and Matthews, S. J. (1999). "Erosion–corrosion studies on 13 Cr steel in gas well environments by liquid jet impingement." *Wear* 568–574.
- Api (1991). API RP 14 E Recommended Practice for Design and Installation of Offshore Production Platform Piping Systems. Washington DC, American Petroleum Institute: p. 22.
- Arnold, K. and Stewartt, M. (1998). surface production operations-design of oil handling systems and facilities. Houston, Gulf Publishing Company. 1.
- Badr, H. M., Habib, M. A., Ben-Mansour, R. and Said, S. A. M. (2002). Effect of Flow Velocity and Particle Size on Erosion in a Pipe with Sudden Contraction. The 6th Saudi Engineering Conference, KFUPM, Dhahran.
- Badr, H. M., Habib, M. A., Ben-Mansour, R. and Said, S. A. M. (2005). "Numerical investigation of erosion threshold velocity in a pipe with sudden contraction." *Journal of Computer and Fluids* 34: 721-742.
- Barton, N. A. (2003). Erosion in Elbows in hydrocarbon production systems: Review document.
- Bitter, J. (1963). "A study of erosion phenomena (Part II)." *Wear* 6.
- Bourgoyne, A. (1989). Experimental study of erosion in divertor systems due to sand production. SPE/AIDC, Louisiana, USA.
- Brown, G. J. (2003). "Erosion prediction in slurry pipeline tee-junctions." *Applied Mathematical Modeling* 26(2): 155-170.
- Carlson, J., Curley, D., King, G., Price-Smith, C. and Waters, F. (October 1992). Sand control: why and how?

- Chen, X., Mclaury, B. S. and Shirazi, S. A. (2004). "Application and experimental validation of a computational fluid dynamics (CFD)-based erosion prediction model in elbows and plugged tees." *Computers & Fluids* 33(10): 1251-1272.
- Chen, X., Mclaury, B. S. and Shirazi, S. A. (2006). "Numerical and experimental investigation of the relative erosion severity between plugged tees and elbows in dilute gas/solid two-phase flow." *Wear* 261: 715–729.
- Churchill, S. W. (1977). "Friction factor equation spans all fluid-flow regimes,." *Chem. Eng.* 84: 91-92.
- Colwart, G., Burton, R. C., Eaton, L. F. and Hodge, R. M. (2007). *Lessons Learned on Sand-Control Failure and Subsequent Workover at Magnolia Deepwater Development*. SPE/IADC Drilling Conference, Amsterdam.
- Crowe, C. T. (2006). *Multiphase Flow Handbook*, Taylor & Francis Group, LLC.
- Deng, T., Chaudhry, A. R., Patel, M., Hutchings, I. and Bradley, M. S. A. (2005). "Effect of particle concentration on erosion rate of mild steel bends in a pneumatic conveyor." *Wear* 258: 480-487.
- Durand, R. and Condolios, E. (1952). *Experimental investigation of the transport of solids in pipes*. Deuxieme Journée de l'hydraulique, Société Hydrotechnique de France.
- Eden, D. A., Hladky, K., John, D. G. and Dawson, J. L. (1986.). *Electrochemical Noise -Simultaneous Monitoring of Potential and Current Noise Signals from Corroding Electrodes*. Corrosion 86, Paper 274, Houston, TX, NACE.
- Fajer, E., Holt, R. M., Horsrud, P., Raaen, A. M. and Risnes, R. (1992). *Petroleum related rock mechanics*. Amstrdam, Elsevier science publishers B. V.
- Faziri, H., Allam, R., Ldd, G., Grose, T., Robinson, P. and Malin, E. (2006). "Sanding: A rigorous examination of the interplay between drawdown, depletion, startup frequency, and water cut." *Society of petroleum engineers (SPE 89895)*.
- Finnie, I. (1972). "Some observations on the erosion of ductile materials." *Wear* 19, 81-90.
- Govier, G. W. and Aziz, K. (1972). *The Flow of Complex Mixtures in Pipes*. Van Nostrand, New York, R. E. Krieger Pub. Co.
- Gunaltun, Y. (1991). "Carbon Dioxide Corrosion in Oil Wells." *SPE 21330*: pp.97-113.
- Gupta, R., Singh, S. N. and Sehadri, V. (1995). "prediction of uneven wear in a slurry pipeline on the basis of measurements in a pot tester." *Wear* 184: 169-178.

- Gupta, R., Singh, S. N. and Sehadri, V. (1995). "Prediction of uneven wear in a slurry pipeline on the basis of measurements in a pot tester " *Wear* 184, 169-178.
- Gupta, R., Singh, S. N. and Seshadri, V. (1992). Accelerated wear rate test rig for the predicting of erosion in slurry pipelines. 19th NCFMFP, Bombay.
- Habib, M. A., Ben-Mansour, R., Badr, H. M. and Said, S. A. M. (2005). "Erosion in the tube entrance region of a shell and tube heat exchanger." *International journal of numerical methods in heat and fluid flow* 15(2): 143-160.
- Haugen, K., Kvernfold, O., Ronold, A. and Sandberg, R. (1995). "Sand erosion of wear-resistant materials: erosion in choke valves." *Wear* 186-187, pp. 179-188.
- Hayashi, K. and Tomiyama, A. (2009). "A drag correlation of fluid particles rising through stagnant liquids in vertical pipes at intermediate Reynolds numbers." *Chemical Engineering Science* 64(12): 3019-3028.
- Huang, Y. and Chong, Z. (1995). *Oil pipelines design and control* (Chinese book). Beijing, China, University of petroelum press.
- Hugget, P. G. and Walker, C. I. (1988). Development of a wear test to simulate slurry erosion. Proc. Hydrotransports, Stratford-upon-Avon, UK.
- Huser, A. and Kvernfold, O. (1998). Prediction of sand erosion in process and pipe components. North American Conference of Multiphase Teknologi, Banff, Canada, BHR group conf. series publ.
- Jepson, W. P., Bhongrde, S. and Gopal, M. (1996). Predictive Model for Sweet Corrosion in Horizontal Multiphase Slug Flow. . NACE International, paper No. 19.
- Jepson, W. P., Stitzel, S., Kang, C. and Gopal, M. (1997). Model for Sweet Corrosion in Horizontal Multiphase Slug Flow, CORROSION/97, paper no. 11, (Houston Texas: NACE International, 1997)
- Jones, L. W. (1992). *Corrosion and Water Technology for Petroleum Products*, Oil and Gas Consultants International, Inc.
- Kabir, M. E. (2005). Numerical investigation of erosion of a pipe protruded in a sudden contraction. Mechanical Engineering, King Fahd University of Petroleum & Minerals. M Sc.
- [Karelin, C. G. D. A. V. Y. (2002). *Abrasive erosion and corrosion for hydraulic machinery* Vol 2, Imprial college press.
- Lowe, A. M., Eren, H. and Bailey, S. I. (2003). "Electrochemical noise analysis: detection of electrode asymmetry." *Corrosion Science* 45 941–955.

- Maniero, R. and Canu, P. (2006). "A model of fine particles deposition on smooth surfaces: I—Theoretical basis and model development." *Chemical Engineering Science* 61(23): 7626-7635.
- Mazur, Z., Campos-Amezcu, R. and G. Urquiza-Beltran, A. G.-G. (2004). "Numerical 3D simulation of the erosion due to solid particle impact in the main stop valve of a steam turbine." *Applied Thermal Engineering* 24: 1877–1891.
- Mazur, Z., Campos-Amezcu, R. and G. Urquiza-Beltr an, A. G.-G. (2004). "Numerical 3D simulation of the erosion due to solid particle impact in the main stop valve of a steam turbine." *Applied Thermal Engineering* 24: 1877–1891.
- Mckibben, M. J. (1992). wall erosion in slurry pipelines. Chemical engineering. Saskatoon, University of Saskatchewan. PhD.
- Mclaury, B. S. (1996). Predicting Solid Particle Erosion Resulting from Turbulent Fluctuations in Oilfield Geometries, University of Tulsa. PhD Thesis.
- Mclaury, B. S. and Shirazi, S. A. (1999). Generalization of API RP 14E for Erosive Service in Multiphase Production. SPE 56812. Houston, Texas.
- Mclaury, B. S., Shirazi, S. A., Shadley and Rybiki, E. (1996). Modelling erosion in chokes. ASME vol. 236, FED conference vol 1, pp. 773-781.
- Mishra, R., Singh, S. N. and Seshadri, V. (1998). "study of wear and solid distribution in constant area and erosion-resistant long-radius pipe bends for the flow of multisized particulate slurries." *Wear* 217: 297-306.
- Morsi, S. A. and Alexander, A. J. (1972). "An Investigation of particle trajectories in two-phase flow systems " *Journal of Fluid Mechanics* 52: 193–208.
- Neilson, J. and Gilchrist, A. (1968). "Erosion by a stream of solid particles." *Wear* 11: 111–122.
- Nesic, S., Cai, J.-Y. and Lee, K.-L. J. (2005). A Multiphase Flow and Internal Corrosion Prediction Model for Mild Steel Pipeline. CORROSION2005, NACE International.
- Norsok (2005). NORSOK standard M-506: CO₂ corrosion prediction model Strandveien.
- Patankar, N. A. and Joseph, D. D. (2001). "Modeling and numerical simulation of particulate flows by the Eulerian-Lagrangian approach." *International journal of multiphase flow* 27: 1659-1684.
- Paul, E. L., Atiemo-Obeng, V. and Kresta, S. M. (2004). *Handbook of Industrial Mixing: Science and Practice*, Wiley

- Rajahram, S. S., Harvey, T. J. and R.J.K.Wood (2009). "Evaluation of a semi-empirical model in predicting erosion-corrosion." *Wear* 267 1883-1893.
- Salama, M. M. (2000). Influence of Sand Production on Design and Operations of Piping Systems. CORROSION 00080. Ponca city, Oklahoma
- Salama, M. M. and Venkatesh, E. S. (1983). Evaluation of Erosional Velocity Limitations in Offshore Gas Wells OTC 15th Annual OTC. Houston, Texas.
- Servant, G., Marchina, P. and Jean-Francoise (November 2007.). "Near-wellbore Modelling: Sand Production Issues." SPE(109894).
- Shah, S. N. and Samyak (2008). "coiled tubing erosion during hydraulic fracturing slurry flow." *Wear* 264: 279-290.
- Shirazi, S. A., Mclaury, B. S., Shadley, J. R. and E.F. Rybicki (1995). "Generalization of the API RP 74E Guideline for Erosive Services." *Journal of Petroleum Technology* (SPE No. 28518): 693-698.
- Sommerfeld, M. (1992). " Modelling of particle-wall collisions in confined gas-particle flows " *Int. J. Multiphase Flow* 18, 6: 905-926.
- Swidzinski, M., Fu, B., Taggart, A. and Jepson, W. P. (2000). Corrosion inhibition of wet gas pipelines under high gas and liquids velocities. corrosion, Orlando.
- Thomas, D. G. (1965). "Transport characteristics of suspensions: VIII. A note on the viscosity of Newtonian suspensions." *J. Colloid Sci.* 20: 267-277.
- Tian, B. (2007). mechanistic understanding and effective prevention of erosion-corrosion of hydrotransport pipes in oil sand slurries, U of Calgary. M Sc. .
- Tolle, G. C. and Greenwood, D. R. (1977). Design of fittings to reduce wear caused by sand erosion, Texas A & M research foundation.
- Trimmer, W. and Hassan, H. (1997). sizing irrigation minerals and fittings.
- Tronvoll, J., Dusseault, M. B., Sanfilippo, F. and Santarelli, F. J. (2001). "The tools of sand management." *Society of petroleum engineers*(SPE No. 71673.).
- Turian, R. M., Hsu, F. L. and Selim, M. S. (1987). "Estimation of the critical velocity in pipeline flow of slurries." *Powder Technol* 51: 35-47.
- Turley, C., Blackford, J. C., Widdicombe, S., Lowe, D., Nightingale, P. D. and Rees, A. P. (2005). Reviewing the Impact of Increased Atmospheric CO₂ on Oceanic pH and the Marine Ecosystem, Plymouth Marine Laboratory, Prospect Place.
- Waard, C. D., Lotz, U. and Dugstad, A. (1995). Influence of liquid flow velocity on CO₂ corrosion: a semi-empirical model. NACE CORROSION, Houston, Texas.

- Ward, C. D. and Milliams, D. E. (1975). Carbonic Acid Corrosion of Steel. Corrosion 31.
- Wang, H., Cai, J.-Y. and Jepson, W. P. (2002). CO₂ Corrosion Modelling and Prediction of Horizontal Slug Flow. CORROSION 2002, NACE International.
- Wang, H., Clariant and Nešić, S. (2006). CO₂ CORROSION MODEL VERIFICATION USING FIELD DATA NACE International. San Diego Ca.
- Wang, J. and Shirazi, S. A. (2003). "A CFD Based Correlation for Erosion Factor for Long-Radius Elbows and Bends." Journal of Energy Resources Technology Vol. 125: 26-34.
- Wang, J., Shirazi, S. A., Shadley, J. R. and Rybicki, E. F. (1996). "Application of Flow Modeling and Particle Tracking to Predict Sand Erosion Rates in Elbows " ASME FED 236: 725-734.
- Wilson, K. C. (1970, 1976). Slip point of beds in solid-liquid pipeline flow. Proc. ASCE J. Hyd.
- Wood, R. J. K. (1992). Erosion-corrosion synergism for multi-phase flowline material., Institution of Mechanical Engineers: 151-158.
- Wood, R. J. K. and Hutton, S. P. (1990). "The synergistic effect of erosion-corrosion: trends in published results." Wear 140: 387-394.
- Wood, R. J. K., Jones, T. F., Ganeshalingam, J. and Miles, N. J. (2004). "comparison of predicted and experimental erosion estimates in slurry ducts." Wear 256: 937-949.
- Wood, R. J. K., Wharton, J. A., Speyer, A. J. and Tan, K. S. (2002). "Investigation of erosion-corrosion processes using electrochemical noise measurements." Tribology International 35: 631-641.
- Www.Dultmeier.Com. "PVC - Equivalent Length Friction Loss in Fittings." 2009, from <http://www.dultmeier.com/pdfs/tech-library/Friction-Loss.pdf>.
- Www.Engineeringtoolbox.Com. (2005). "Resistance and Equivalent Length of Fittings." from www.engineeringtoolbox.com.
- Yao, J., Zhang, B. and Fan, J. (2000). "An experimental investigation of a new method for protecting bends from erosion in gas-particle flows." Wear 240: 215-222.
- Zhang, G. A., Xu, L. Y. and Cheng, Y. F. (2009). "Investigation of erosion-corrosion of 3003 aluminum alloy in ethylene glycol-water solution by impingement jet system." Corrosion Science, Elsevier

Appendix A

The Computational Software

6.4 A.1 Introduction

This appendix discusses the erosion/corrosion prediction computational software which has been developed by the researcher. The function of the software is to predict wear loss of a target component under flow of fluid with sand particles (erosion) and/or CO₂ gas (corrosion or erosion-corrosion). Two models are employed for erosion prediction in elbows and tees and one model is employed for corrosion prediction in straight pipes and elbows.

6.5 A.2 The software requirement and installation procedure

The minimum requirements for the software installation are as follows:

- Operating System: Windows 98/Me/2000/XP
- Hard disk free space > 10 MB
- RAM: 512 MB

Figure A-1 shows the setup of execution icon that is used to install the software. By clicking this icon, the installation starts as shown in Figure A-2. Following the setup instruction, the installation will be completed successfully.



Figure A-1: The installation icon



Figure A-2: The setup of the code

6.6 A.3 The software graphical user interface and navigation forms

Figure A-3 shows the main graphical user interface of the code from which a user can select one of three process calculations, namely erosion, corrosion, or erosion-corrosion calculations. In erosion calculation the user can navigate to an erosion calculation interface as illustrated in

Figure A-4, which enables the navigation to one of the input data forms using either of Salama model, Direct Impingement Model (DIM), modified DIM model (for temperature dependency), or Mysara-UTP model.

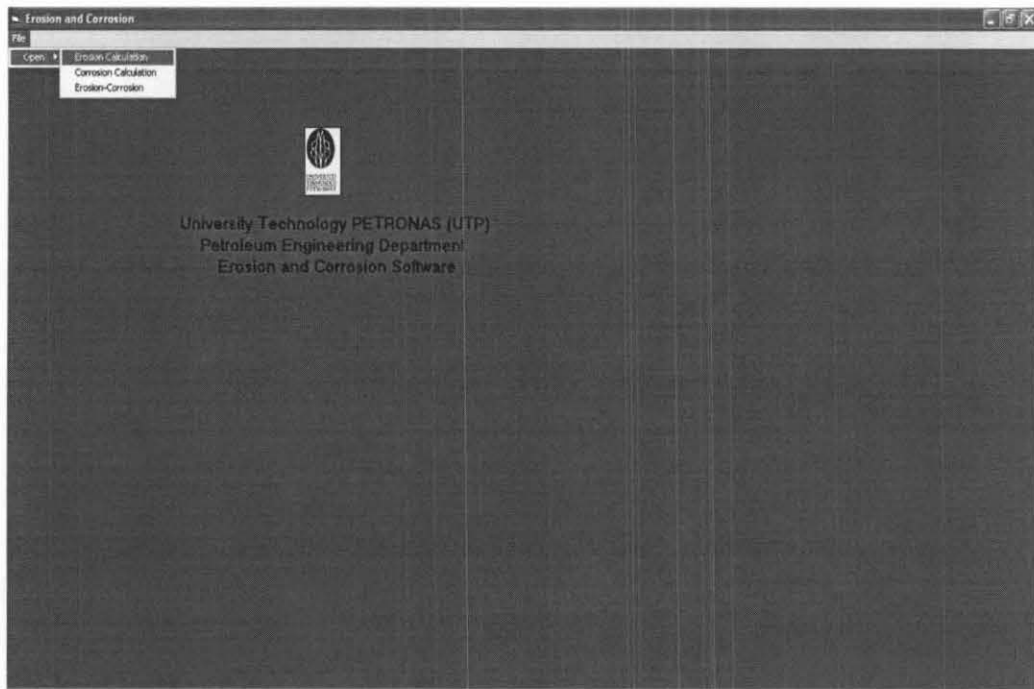


Figure A-3: The main graphical user interface

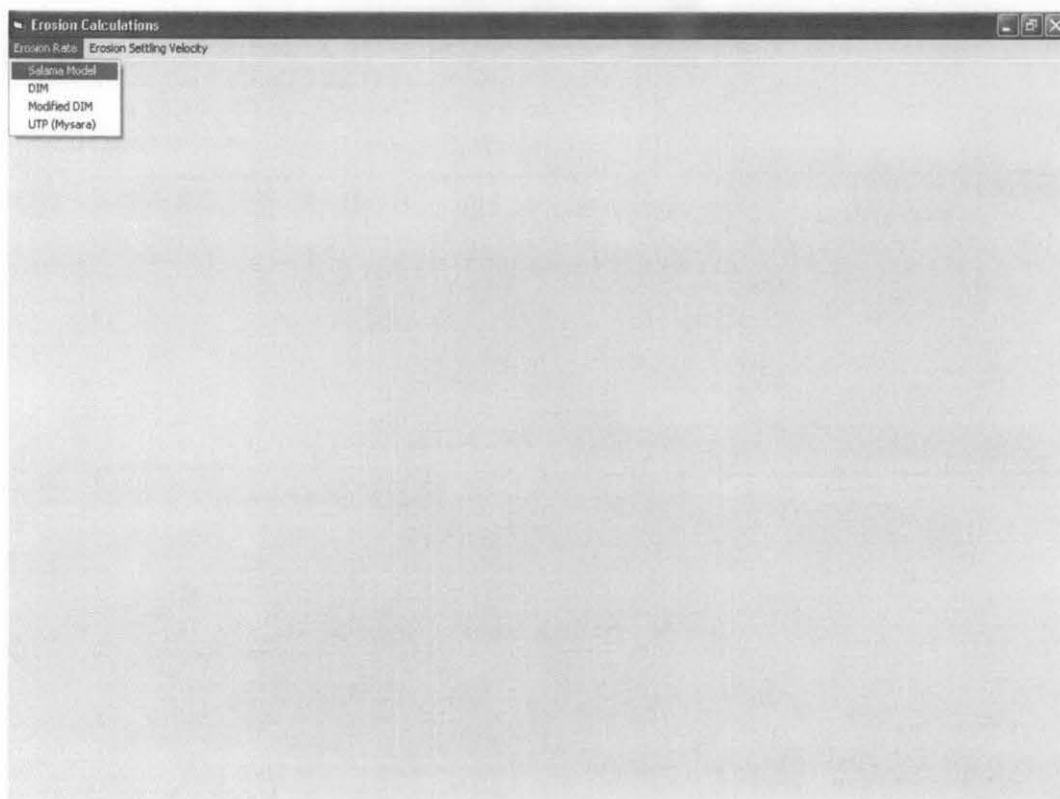


Figure A-4: The erosion graphical user interface

The input data form of Salama model is shown in Figure A-5. The input data for this model include:

- Flow velocity (in m/s)
- Sand production rate (in kg/day)
- Sand size (in micron)
- Pipe diameter (in mm)
- Fluid density (in kg/m^3)

The form also enables the selection of the component geometry.

The screenshot shows a software window titled "Sand Erosion (Salama)". Inside, there are two panels. The "Input Data" panel on the left contains five input fields with the following values: "Flow Velocity m/s" (31), "Sand Production Rate Kg/day" (250), "Sand Size micron" (150), "Pipe Diameter mm" (48), and "Fluid Density Kg/m3" (34.48). The "Geometry" panel on the right contains four radio button options: "Elbow", "Seamless and Cost Elbow", "Plugged Tee (Erosion Liquid)", and "Plugged Tee (Erosion)".

Figure A-5: The input data form of Salama model

The input data form of the Direct Impingement Model (DIM) is shown in Figure A-6. The input data include:

- Flow velocity (in m/s)
- Sand production rate (in kg/s)
- Sand size (in micron)
- Pipe diameter (in mm)
- Fluid density (in kg/m^3)
- Fluid viscosity (in Pa.s)
- Sand density (in kg/m^3)
- The elbow curvature (r/D) (dimensionless)
- Brinell number

Input Parameters		
Sand Production Rate kg/s		0.000086
Fluid Velocity m/s		24.4
Fluid Density kg/m ³		1.2015
Fluid Viscosity Pa.s		0.000182
Pipe Diameter m		0.05
Particle diameter m		0.0003
Brinell Hardness Factor B		140
Elbow r/D		5
Sand Density kg/m ³		2650

Figure A-6: The input data form of DIM model

From the DIM input data form, one of two geometries (elbow or tee), five target materials (carbon steel, 13 Cr annealed, 13 Cr heat treated, 22 Cr 5 Ni Duplex, or 316 SS), and three sand shapes (angular, semi-rounded, or rounded) can be selected.

If the fluid is multiphase, the mixture density and viscosity will first be calculated using parameters of the phases.

The corrosion and erosion-corrosion input data form are shown in Figure A- 7. The input data for corrosion calculation are the data related to wall shear stress calculation, and those related to the CO₂ corrosion calculation. The data related to the shear stress calculation are as follows:

- Flow velocity (in m/s)
- Fluid density (in kg/m³)
- Fluid viscosity (in Pa.s)
- Pipe diameter (in m)
- Pipe roughness (in m)

The data related to the CO₂ corrosion calculations are as follows:

- Temperature (in °C)
- pH
- CO₂ partial pressure (in Bar)
- Total pressure (in Bar)

For erosion-corrosion calculations, in addition to the corrosion calculation data, the following data should be entered:

- Sand size (in micron) and sand production rate (in kg/day)

Figure A- 7: The input data form of corrosion and erosion-corrosion model

A.4 The software output

After the data input, the calculations would be performed by the code and the results would be ready to be presented in digital, graphical, or tabular forms. The digital format is the display of the results of the input data in a message box as shown in Figure A-8.

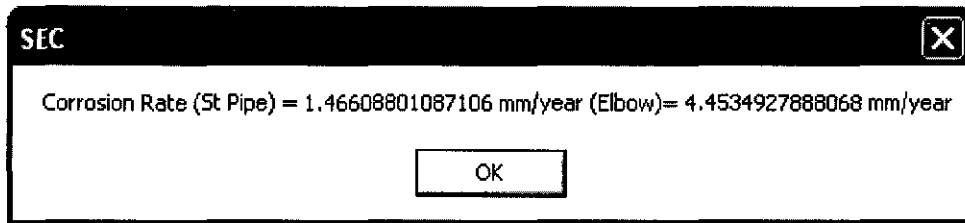


Figure A-8: Digital output

The graphical and tabular outputs illustrate the results variation with a selected variable. For erosion rate calculations in 2-D form, four parameters can be selected as variables. These parameters are flow velocity, pipe diameter, sand production rate, and substrate material as shown in Figure A-9.



Figure A-9: Variables for DIM erosion calculations (for 2-D output)

In 3-D graphical output, the variation of erosion rates can be obtained at different velocities for different sand production rate or sand size as shown in Figure A-10.



Figure A-10: Variables for DIM erosion calculations (for 3-D output)

Figure A-11 is an example of the output of erosion rate (in mm/year) due to variation with pipe diameter (mm).

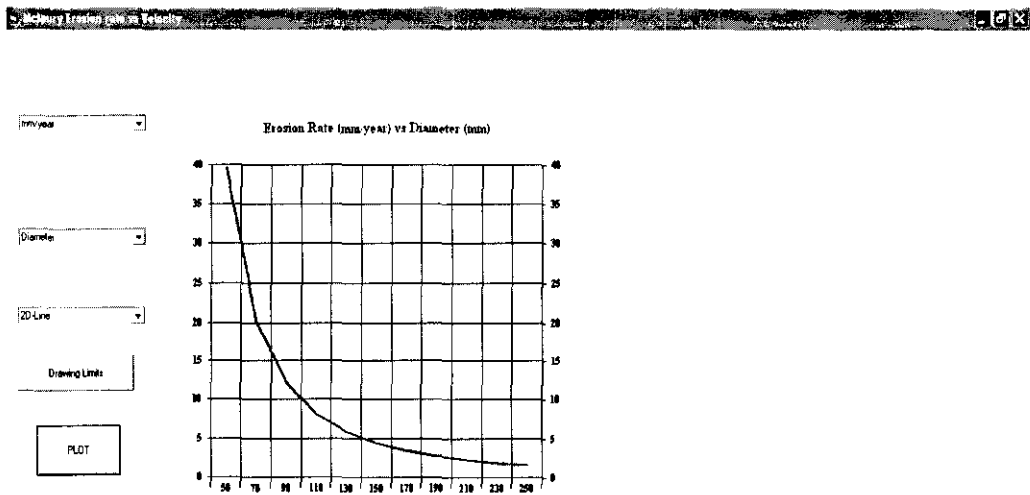


Figure A-11: An example of 2-D graphical output

Different curve types can be selected (select the chart type). For example, the same result in Figure A-11 can be illustrated in the curves' types in Figure A- 12.

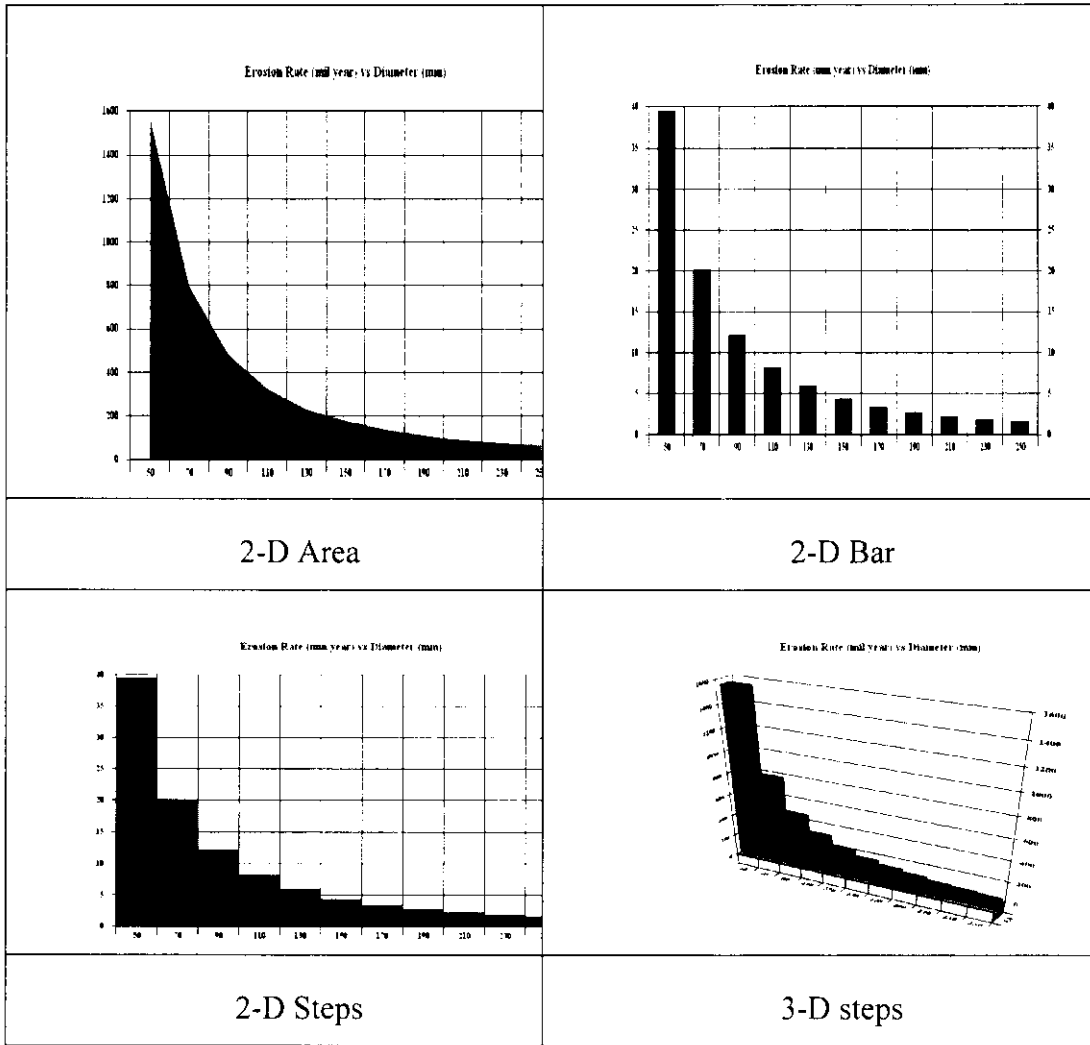


Figure A- 12: Examples of graph shapes (2-D)

For 3-D curves output, two variables would be selected, and their minimum and maximum values are entered as in Figure A-13. The erosion rate unit and curve type can also be selected. Figure A- 14 shows examples of the curve types.

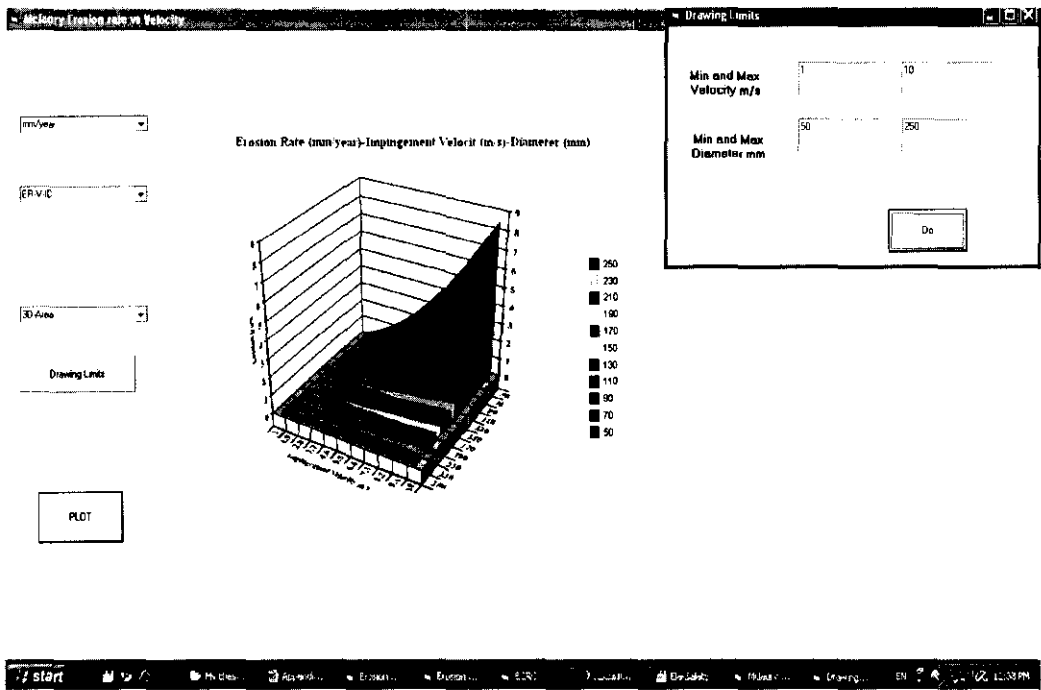


Figure A-13: An example of 3-D graphical output

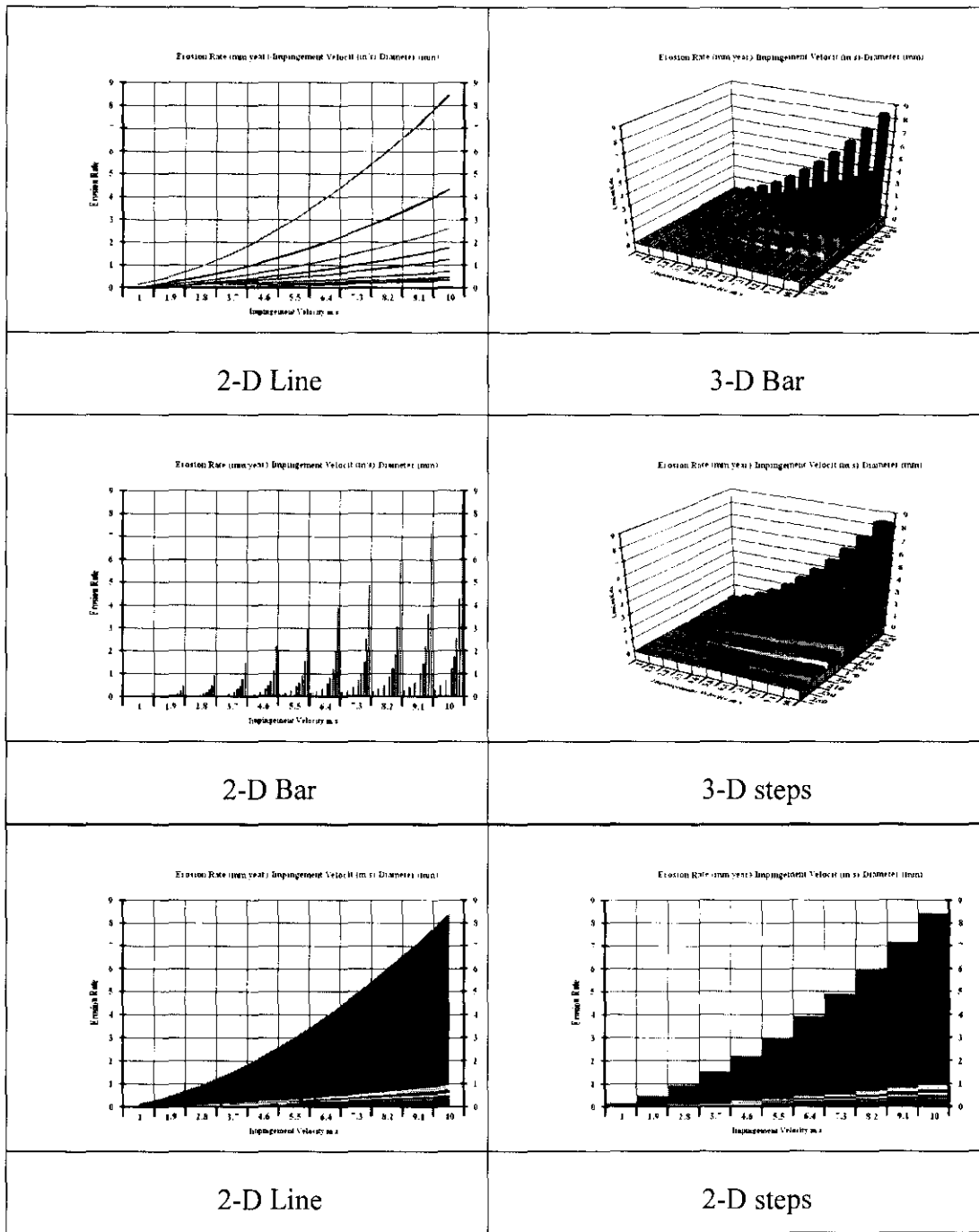


Figure A- 14: Examples of graph shapes (3-D)

All models have the capability of presenting outputs in tabular forms. The table output can be presented in a variation of erosion, corrosion, or erosion-corrosion rate with one variable or two variables. An example of one-variable relationship is shown in Figure A-15, where corrosion (the 2nd column) and erosion-corrosion (the 3rd column) rates are varied with velocity (the 1st column).

Velocity m/s	Corrosion Rate mm/yr	Erosion-Corrosion Rate
0.5	0.035	0.035
1	0.059	0.361
1.5	0.055	0.399
2	0.142	0.145
2.5	0.2	0.211
3	0.266	0.289
3.5	0.346	0.367
4	0.433	0.451
4.5	0.53	0.565
5	0.636	0.679
5.5	0.752	0.803
6	0.876	0.937
6.5	1.009	1.081
7	1.151	1.235
7.5	1.302	1.399
8	1.451	1.57
8.5	1.629	1.752
9	1.806	1.944
9.5	1.99	2.144
10	2.184	2.354
10.5	2.365	2.573
11	2.595	2.801
11.5	2.813	3.039
12	3.04	3.295

Figure A-15: An example of one-variable table output

An example of two-variable relationship is shown in Figure A-16, where erosion rate in elbow with velocity for different diameters is illustrated. The first column contains the velocity values (in m/s) and the first row contains the diameter values (in m).

Diameter m	Velocity m/s	0.025	0.051	0.076	0.101	0.126
1	25.26	11.38	6.44	4.14	2.88	
2	50.94	22.94	12.39	8.35	5.81	
3	83.8	37.73	21.37	13.73	9.56	
4	129.28	55.51	31.43	20.2	14.06	
5	168.99	76.1	43.09	27.69	19.28	
6	220.64	99.36	56.26	36.15	25.17	
7	277.98	125.18	70.88	45.54	31.71	
8	340.81	153.47	86.9	55.83	38.88	
9	408.95	194.15	104.27	67	46.65	
10	482.25	217.16	122.36	79.01	55.01	
11	560.6	252.44	142.34	91.84	63.95	
12	643.86	289.94	164.17	105.48	73.45	
13	731.93	329.6	186.62	119.91	83.49	
14	824.72	371.38	210.28	135.12	94.08	
15	922.13	415.25	235.12	151.08	105.19	
16	1024.1	461.17	261.12	167.78	116.82	
17	1130.55	509.1	288.26	185.22	128.97	
18	1241.4	559.02	316.52	203.38	141.61	
19	1356.59	610.89	345.9	222.25	154.75	
20	1476.1	664.72	376.4	241.84	168.49	

Figure A-16: An example of two-variable table output

The graphical output can be saved as (*.bmp) picture format, whereas the tabular output can be exported to excel. For example, when the table in

Figure A-16 is exported to excel it will appear as shown in Figure A-17.

	A	B	C	D	E	F	G	H	I	J	K	L	M	N	O	P	Q	R	S
1																			
2	Diameter m		0.036	0.051	0.076	0.101	0.136	0.151	0.176	0.201	0.226	0.251	0.276	0.301	0.326	0.351	0.376	0.401	0.426
3	1	25.26	11.38	6.44	4.14	2.88	2.12	1.63	1.25	1.04	0.86	0.73	0.62	0.53	0.46	0.41	0.36	0.32	
4	2	50.94	22.94	12.99	8.35	5.82	4.28	3.28	2.59	2.1	1.74	1.46	1.25	1.08	0.94	0.82	0.73	0.65	
5	3	83.8	37.73	21.37	13.73	9.56	7.04	5.39	4.27	3.46	2.86	2.41	2.05	1.77	1.54	1.36	1.2	1.07	
6	4	123.28	55.51	31.43	20.2	14.06	10.35	7.94	6.28	5.09	4.21	3.54	3.02	2.6	2.27	1.99	1.77	1.58	
7	5	168.99	76.1	43.09	27.69	19.28	14.19	10.89	8.61	6.98	5.77	4.85	4.14	3.57	3.11	2.73	2.42	2.16	
8	6	220.64	99.36	56.26	36.15	25.17	18.53	14.2	11.24	9.11	7.53	6.33	5.4	4.66	4.06	3.57	3.16	2.82	
9	7	277.98	125.18	70.88	45.54	31.71	23.34	17.9	14.16	11.48	9.49	7.98	6.8	5.87	5.11	4.5	3.98	3.55	
10	8	340.61	153.47	86.9	55.63	38.88	28.62	21.94	17.36	14.07	11.64	9.78	8.34	7.2	6.27	5.51	4.88	4.36	
11	9	408.95	184.15	104.27	67	46.65	34.34	26.33	20.83	16.88	13.96	11.74	10.01	8.63	7.51	6.62	5.86	5.23	
12	10	482.25	217.16	122.96	79.01	55.01	40.49	31.05	24.56	19.91	16.47	13.84	11.6	10.18	8.87	7.8	6.91	6.17	
13	11	560.6	252.44	142.94	91.84	63.95	47.07	36.09	28.57	23.14	19.14	16.09	13.72	11.84	10.31	9.07	8.03	7.17	
14	12	643.86	289.94	164.17	105.48	73.45	54.06	41.45	32.79	26.58	21.98	18.48	15.76	13.59	11.85	10.41	9.23	8.23	
15	13	731.93	329.6	186.62	119.91	83.49	61.46	47.12	37.27	30.22	24.99	21.02	17.91	15.45	13.47	11.84	10.49	9.36	
16	14	824.72	371.38	210.28	135.12	94.08	69.25	53.09	42	34.05	28.16	23.68	20.18	17.41	15.17	13.34	11.82	10.55	
17	15	922.13	415.25	235.12	151.08	105.19	77.43	59.37	46.56	38.07	31.49	26.47	22.57	19.47	16.97	14.92	13.22	11.79	
18	16	1024.1	461.17	261.12	167.78	116.82	85.99	65.93	52.15	42.28	34.97	29.4	25.06	21.62	18.84	16.57	14.68	13.1	
19	17	1130.55	509.1	288.26	185.22	128.97	94.93	72.76	57.57	46.67	38.6	32.46	27.67	23.67	20.8	18.29	16.2	14.46	
20	18	1241.4	559.02	316.52	203.38	141.61	104.24	79.92	63.22	51.25	42.39	35.64	30.38	26.21	22.84	20.08	17.79	15.87	
21	19	1356.59	610.89	345.9	222.25	154.75	113.91	87.34	69.08	56.01	46.32	38.95	33.2	28.64	24.96	21.94	19.44	17.35	
22	20	1476.07	664.69	376.36	241.83	168.38	123.94	95.03	75.17	60.94	50.4	42.38	36.13	31.16	27.16	23.88	21.16	18.88	
23	21	1599.77	720.4	407.9	262.09	182.49	134.33	102.99	81.47	66.05	54.62	45.93	39.15	33.77	29.49	25.89	22.93	20.46	
24	22	1727.65	777.96	440.51	283.04	197.08	145.07	113.23	87.98	71.33	58.99	49.6	42.28	36.47	31.78	27.95	24.76	22.09	
25	23	1859.65	837.42	474.17	304.67	212.14	156.15	119.72	94.7	76.78	63.5	54.19	45.51	39.26	34.21	30.08	26.65	23.78	
26	24	1995.73	898.7	508.66	326.97	227.66	167.56	128.48	101.63	82.39	68.14	57.29	48.84	42.13	36.72	32.18	28.4	25.52	
27	25	2135.85	961.8	544.59	349.91	243.64	179.34	137.51	108.77	88.18	72.93	61.12	52.27	45.09	39.29	34.55	30.61	27.31	

Figure A-17: Tabular output exported to excel

Appendix B

Electrochemical Noise Measurements (ENM) results

Introduction to electrochemical measurement of corrosion

In electrochemical measurements, a sample from the target material (normally called working electrode, WE) with surface area of few square centimeters is immersed in a solution while controlling the test parameters to simulate the environment of the system being studied. Other two electrodes, called reference electrode RE and counter electrode CE (or auxiliary electrode AE), are immersed with the working electrode and connected to a device that allows measuring of the working electrode potential while change of potentials.

The output of the most electrochemical measurement techniques is a resistance represents the corrosion current. For linear polarization resistance (LPR), this resistance is called polarization resistance, R_p and is related to corrosion current, I_{corr} , as follows:

$$I_{corr} = \frac{B}{R_p} \tag{B-1}$$

Where B is the Stern-Geary constant with values range 0.02 to 0.03 V/Decade.

The polarization resistance can be calculated from the ratio of potential difference to its corresponding current difference, i. e.,

$$R_p = \frac{\Delta E}{\Delta I} \tag{B-2}$$

Electrochemical noise measurement (ENM)

Electrochemical Noise Measurement (ENM) is one of several electrochemical techniques used to monitor corrosion rate in a real field process or at lab. The technique can be used to measure, and evaluate general and localized corrosion without artificial disturbance of the process under test. Electrochemical noise can be defined as “the naturally occurring fluctuations in the corrosion potential and/or galvanic current of corroding electrodes noise” (Wood *et al.* 2002). The fluctuations of potential lead to so-called electrochemical potential noise (EPN) and the fluctuations in current lead to so-called electrochemical current noise (ECN).

Eden (Eden *et al.* 1986.) proposed the following setup for the measurement of electrochemical noise. The ammeter measures the ECN between the working electrodes 1 and 2. At the same time, EPN with respect to the reference electrode is measured.

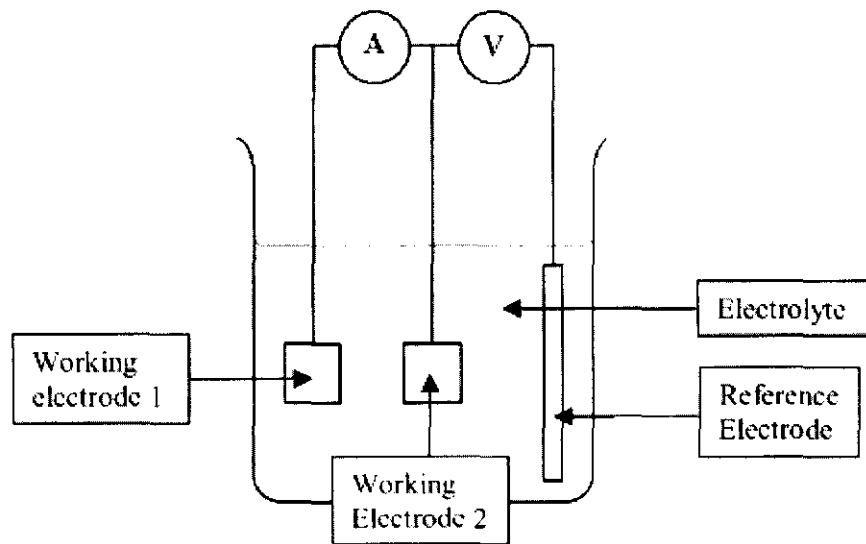


Figure B-1: The ENM setup proposed by Eden (from (Lowe *et al.* 2003))

ENM measures simultaneous fluctuations of current and potential, which can be converted to noise resistance, R_n , as follows:

$$R_n = \frac{\sigma_V}{\sigma_I}$$

Where σ_V and σ_I are standard deviation of potential and current, respectively.

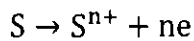
The noise resistance can be used to calculate corrosion current as follows:

$$I_{\text{corr}} = \frac{B}{R_n}$$

B-4

The corrosion current (mAmp) can be converted to corrosion rate (mm/year) using the following principle:

Assume an electrochemical process involving a chemical species S.



B-5

The current flow can be related to mass using Faraday's law as follows:

$$Q = nFM$$

B-6

Where Q is the charge in coulombs due to reaction of the species S.

n is the number of electrons transferred per molecule or atom of S.

F is Faraday's constant (96486.7 coulombs/mole)

M is the number of moles of the species S.

By substituting

$$We = \frac{Aw}{n} \text{ and } M = \frac{Wg}{Aw}$$

Where *We* is the mass of species S that will react with one Faraday of charge.

Aw is the atomic weight of the species

Wg is the mass of the species S.

Then

$$W = \frac{W_g e Q}{F}$$

For general corrosion, in which corrosion rate distributes uniformly over the surface, and by substituting the value of Faraday and $Q = It$, we can attain the final equation of calculating corrosion rate in mm/year as follows:

$$CR = \frac{I_{corr} t K W e}{\rho_m A}$$

6B-8

Where, t is time in s, ρ_m and A are the density and surface area of the material, respectively, and K is a factor that define the unit of corrosion. The value of K for conversion to mm/year is equals to 3720 mm/(amp-cm-year).

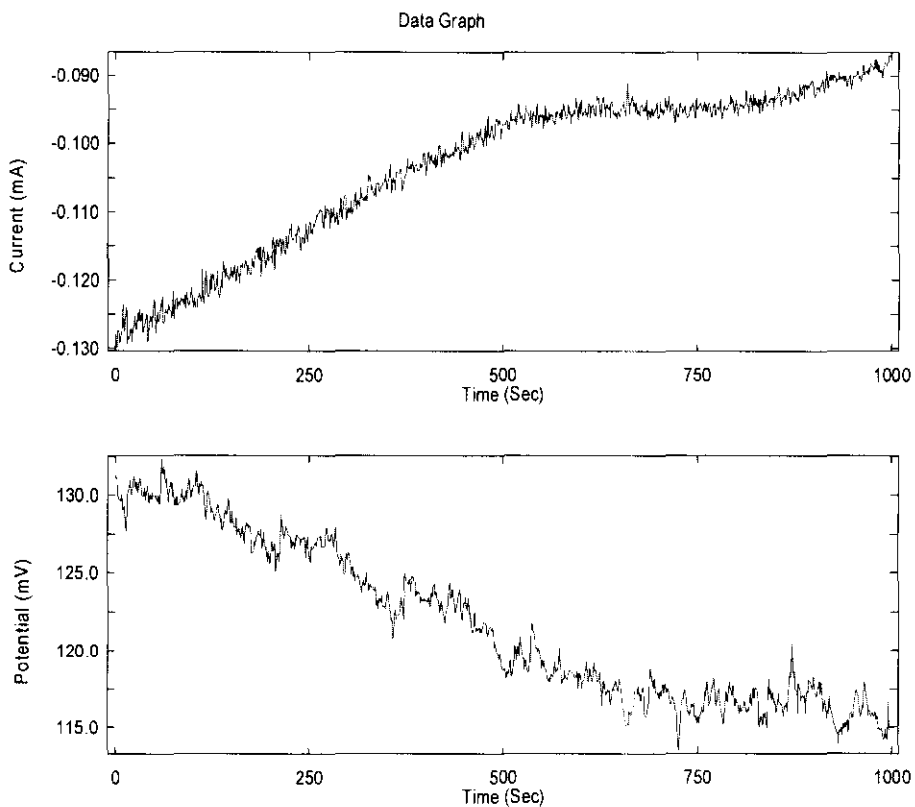


Figure B-2:ENM results at $V=0.2$ m/s, $pH= 5$ ($CR=0.604$ mm/y)

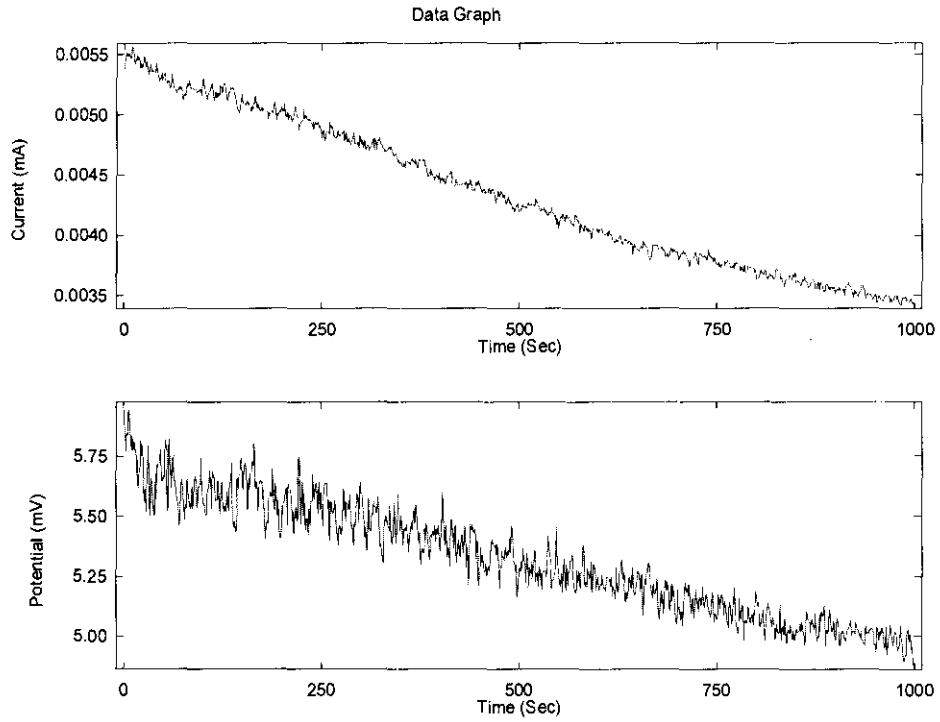


Figure B-3: ENM signal at $V=0.1$ m/s, $pH=6.5$ ($CR=0.262$ mm/year)

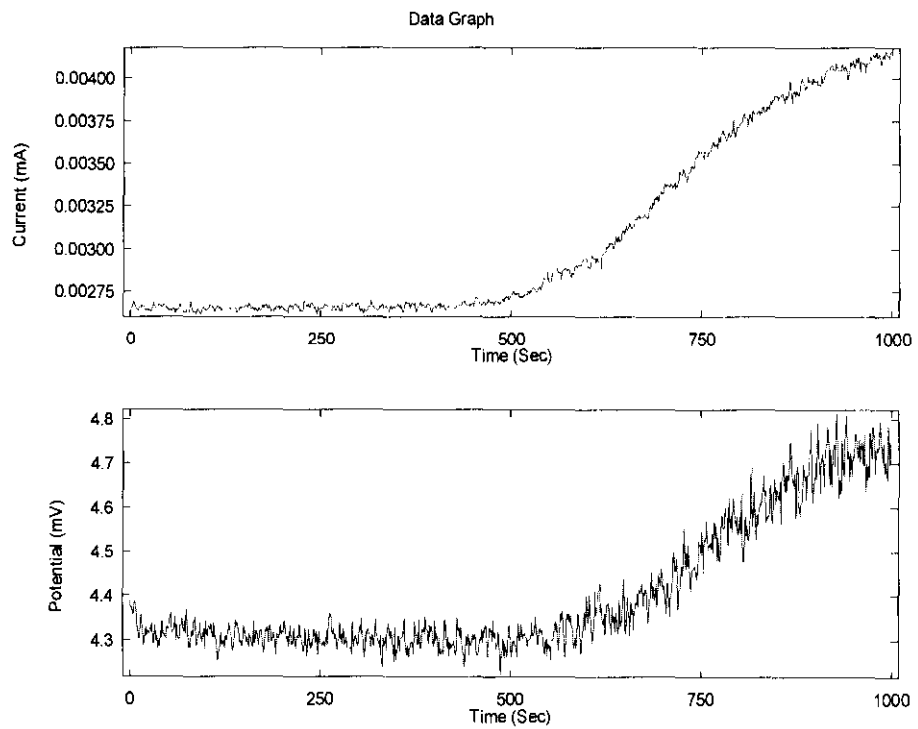


Figure B-4: ENM signal at $V=0.2$ m/s, $pH=5.5$ ($CR=0.352$ mm/y)

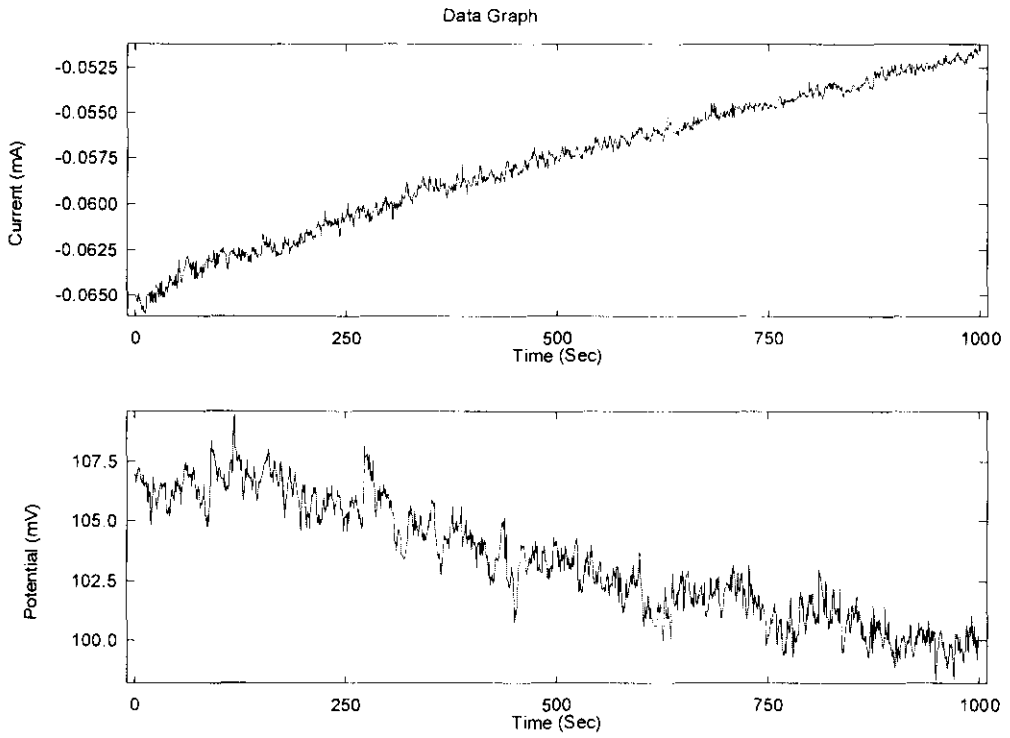


Figure B-5: ENM signal at 0.4 m/s, pH=5.5 (CR=0.409 mm/y)

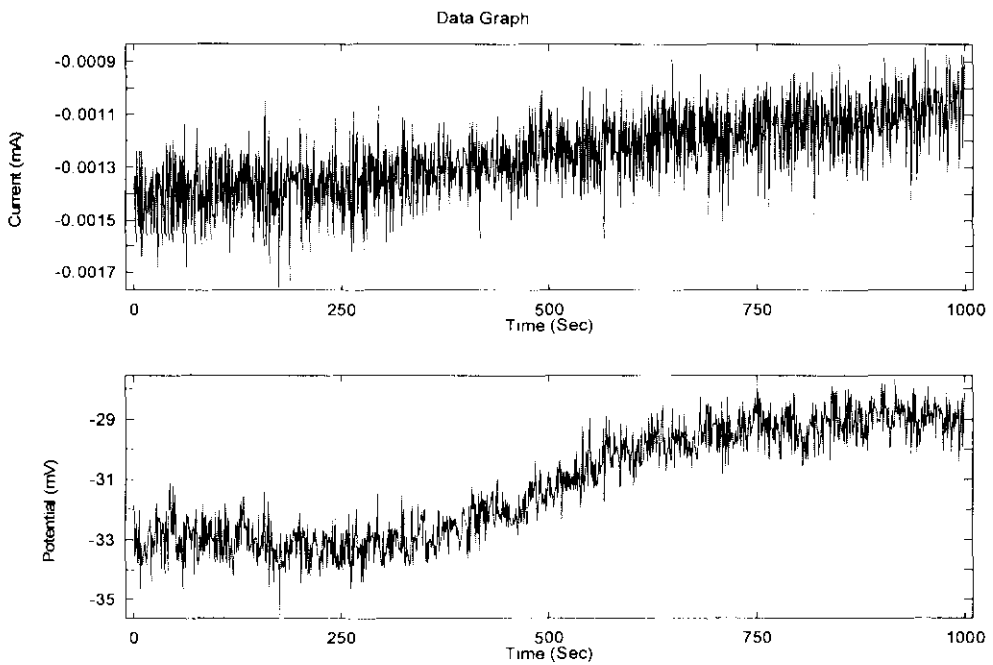


Figure B-6: ENM signals, V=0.5 m/s, pH=6.5 (CR=0.338 mm/y)

Appendix C

The Data used for Salama model improvement

The whole data

Reference	Vsg (m/s)	Vsl (m/s)	Density kg/s	Viscosity pa.s	D m	dp m	ER (mm/ke)
Bourgoyne	32	0	1.2015	0.00018	0.0525	0.00035	8.13E-03
Bourgoyne	47	0	1.2015	0.00018	0.0525	0.00035	4.96E-03
Bourgoyne	72	0	1.2015	0.00018	0.0525	0.00035	1.40E-01
Bourgoyne	93	0	1.2015	0.00018	0.0525	0.00035	2.85E-02
Bourgoyne	98	0	1.2015	0.00018	0.0525	0.00035	3.55E-02
Bourgoyne	111	0	1.2015	0.00018	0.0525	0.00035	1.11E-01
Bourgoyne	141	0	1.2015	0.00018	0.0525	0.00035	2.07E-01
Bourgoyne	141	0	1.2015	0.00018	0.0525	0.00035	1.90E-01
Bourgoyne	148	0	1.2015	0.00018	0.0525	0.00035	2.09E-01
Tolle and Greenwood	9.15	0	1.2015	0.00018	0.05	0.0003	2.13E-03
Tolle and Greenwood	12.2	0	1.2015	0.00018	0.05	0.0003	3.80E-03
Tolle and Greenwood	15.24	0	1.2015	0.00018	0.05	0.0003	7.51E-03
Tolle and Greenwood	18.29	0	1.2015	0.00018	0.05	0.0003	9.20E-03
Tolle and Greenwood	21.34	0	1.2015	0.00018	0.05	0.0003	1.22E-02
Tolle and Greenwood	24.39	0	1.2015	0.00018	0.05	0.0003	1.62E-02

Tolle and Greenwood	27.44	0	1.2015	0.00018	0.05	0.0003	1.80E-02
Tolle and Greenwood	30.49	0	1.2015	0.00018	0.05	0.0003	2.04E-02
Tolle and Greenwood	21.34	0	1.2015	0.00018	0.05	0.0003	1.44E-02
Tolle and Greenwood	30.49	0	1.2015	0.00018	0.05	0.0003	1.56E-02
Salama	30	1	33.4208	0.0000461	0.049	0.00015	5.25E-04
Salama	30	0.5	17.5752	0.0000323	0.049	0.00015	2.46E-03
Salama	20	5.8	225.737	0.000214	0.049	0.00015	5.19E-05
Salama	20	3.1	135.239	0.000135	0.049	0.00015	6.93E-05
Salama	15	1	63.626	0.0000725	0.049	0.00015	1.47E-04
Salama	9	6.2	408.54	0.0003737	0.0265	0.00025	1.80E-04
Salama	14.4	1.5	91.9	0.0000973	0.0265	0.00025	2.30E-04
Salama	14.6	1.5	92	0.0000973	0.0265	0.00025	4.20E-04
Salama	34.4	2.1	59.2	0.0000687	0.0265	0.00025	2.83E-03
Salama	35	1	28.84	0.0000422	0.0265	0.00025	6.56E-03
Salama	34.3	0.5	15.57	0.0000306	0.0265	0.00025	7.20E-03
Salama	37	0.7	19.64	0.0000342	0.0265	0.00025	8.03E-03
Salama	38.5	0.5	14.07	0.0000293	0.0265	0.00025	8.03E-03
Salama	44	1.5	34.024	0.0000467	0.0265	0.00025	1.05E-02
Salama	51	0.6	12.71	0.0000281	0.0265	0.00025	2.27E-02
Salama	15	5	250.9	0.000236	0.049	0.00015	6.38E-05
Salama	10	5	334.13	0.0003087	0.049	0.00015	1.35E-05
Salama	10	0.7	66.54	0.000075	0.049	0.00015	7.01E-05
Salama	8	0.2	25.56	0.0000393	0.049	0.00015	1.23E-04
Salama	3.5	4	500.6	0.000454	0.049	0.00015	4.60E-06
Bourgoyne	86	0.53	7.32	0.0000233	0.0525	0.00035	1.27E-01
Bourgoyne	92	0.53	6.92	0.000023	0.0525	0.00035	1.21E-01
Bourgoyne	89	0.12	2.55	0.0000192	0.0525	0.00035	1.08E-01
Bourgoyne	84	0.53	7.464	0.0000192	0.0525	0.00035	9.34E-02

Bourgoyne	72	0.53	8.5	0.0000244	0.0525	0.00035	5.37E-02
Bourgoyne	84	0.12	2.626	0.0000192	0.0525	0.00035	7.51E-02
Bourgoyne	92	0.12	2.503	0.0000191	0.0525	0.00035	9.94E-02
Bourgoyne	107	0.53	6.124	0.0000223	0.0525	0.00035	1.05E-01

Data used for pure gas

V_{sg}	V_{sl}	ρ_m	μ_m	D	d_p	ER_m	ER_p
32	0	1.2015	0.00018	0.0525	0.00035	6.50E-02	8.13E-03
47	0	1.2015	0.00018	0.0525	0.00035	1.40E-01	4.96E-03
72	0	1.2015	0.00018	0.0525	0.00035	3.30E-01	1.40E-01
93	0	1.2015	0.00018	0.0525	0.00035	5.40E-01	2.85E-02
98	0	1.2015	0.00018	0.0525	0.00035	6.00E-01	3.55E-02
111	0	1.2015	0.00018	0.0525	0.00035	7.80E-01	1.11E-01
141	0	1.2015	0.00018	0.0525	0.00035	1.26E+00	2.07E-01
141	0	1.2015	0.00018	0.0525	0.00035	1.39E+00	1.90E-01
148	0	1.2015	0.00018	0.0525	0.00035	5.00E-03	2.09E-01
9.15	0	1.2015	0.00018	0.05	0.0003	8.93E-03	2.13E-03
12.2	0	1.2015	0.00018	0.05	0.0003	1.39E-02	3.80E-03
15.24	0	1.2015	0.00018	0.05	0.0003	2.00E-02	7.51E-03
18.29	0	1.2015	0.00018	0.05	0.0003	2.73E-02	9.20E-03

21.34	0	1.2015	0.00018	0.05	0.0003	3.57E-02	1.22E-02
24.39	0	1.2015	0.00018	0.05	0.0003	4.52E-02	1.62E-02
27.44	0	1.2015	0.00018	0.05	0.0003	5.58E-02	1.80E-02
30.49	0	1.2015	0.00018	0.05	0.0003	6.50E-02	2.04E-02
21.34	0	1.2015	0.00018	0.05	0.0003	1.40E-01	1.44E-02
30.49	0	1.2015	0.00018	0.05	0.0003	3.30E-01	1.56E-02
18.9	0	1.2015	0.00018	0.025	0.00015	5.40E-01	3.16E-03
27.44	0	1.2015	0.00018	0.025	0.00015	6.00E-01	4.33E-03
34.15	0	1.2015	0.00018	0.025	0.00015	7.80E-01	6.20E-03

Data used for LGLR

V_{sg}	V_{st}	ρ_m	μ_m	D	d_p	V_{st}/V_{sg}	ER_m	ER_p
20	3.1	135.2393	0.000135	0.049	0.00015	0.155	1.24E-04	6.93E-05
20	5.8	225.7376	0.000214	0.049	0.00015	0.29	9.20E-05	5.19E-05
15	5	250.9	0.000236	0.049	0.00015	0.333333	4.98E-05	6.38E-05
10	5	334.13	0.000309	0.049	0.00015	0.5	2.10E-05	1.35E-05
3.5	4	500.6	0.000454	0.049	0.00015	1.142857	3.51E-06	4.60E-06

Data used for HGLR

V_{sg}	V_{sl}	V_{sl}	ρ_m	D	d_p	V_{sl}/V_{sg}	ER_m	ER_p
0.12	92	2.503	1.91E-05	0.0525	0.00035	0.001304	8.84E-02	9.94E-02
0.12	89	2.55	1.92E-05	0.0525	0.00035	0.001348	8.27E-02	1.08E-01
0.12	84	2.626	1.92E-05	0.0525	0.00035	0.001429	7.37E-02	7.51E-02
0.53	107	6.124	2.23E-05	0.0525	0.00035	0.004953	6.00E-02	1.05E-01
0.53	92	6.92	0.000023	0.0525	0.00035	0.005761	3.82E-02	1.21E-01
0.53	86	7.32	2.33E-05	0.0525	0.00035	0.006163	3.34E-02	1.27E-01
0.53	84	7.464	1.92E-05	0.0525	0.00035	0.00631	3.20E-02	9.34E-02
0.53	72	8.5	2.44E-05	0.0525	0.00035	0.007361	2.05E-02	5.37E-02
0.5	30	17.57525	3.23E-05	0.049	0.00015	0.016667	1.60E-03	2.46E-03
1	30	33.42081	4.61E-05	0.049	0.00015	0.033333	9.10E-04	5.25E-04
1	15	63.626	7.25E-05	0.049	0.00015	0.066667	1.25E-04	1.47E-04
0.2	8	25.56	3.93E-05	0.049	0.00015	0.025	8.08E-05	1.23E-04
0.7	10	66.54	0.000075	0.049	0.00015	0.07	5.34E-05	7.01E-05